



The  
University  
Of  
Sheffield.

---

# **Vision-based Measurement for Combustion and Vibration Studies**

---

**Mr Jiansheng Yang**

**Combustion and Flow Diagnostics Research Group**

**Department of Mechanical Engineering**

*This thesis is submitted to the University of Sheffield for the degree of Doctor of Philosophy,*

2016



# **Declaration**

The work presented in this thesis is that of the author and has not been submitted for any other award or degree at the University of Sheffield or any other university or institution. Where other sources of information or help from other parties has been used this has been acknowledged.

# Dedication

~ *For my parents and wife* ~

# Acknowledgements

I would first of all like to express my sincere appreciation to my supervisor, Prof. Yang Zhang, for his continuous encouragement and guidance during my research. I am extremely grateful for everything he taught me, in work and life, for the past four years. I have benefited greatly from his outstanding knowledge in research.

Then I would like to thank my second supervisor, Dr. Swee B. Chin for his additional support, and Dr. Robert Woolley, Dr. Ling Zhao, Prof. Zi-qiang Lang for their valuable guidance during our cooperative research projects.

I would also like to thank Dr. Hua Wei Huang, Dr. Qian Wang, Dr. Li-Wei Chen, Dr. Chloe Jo McDaid, Dr. Hussain Saeed, Mr. Paco Carranza Ch, Mr. Zhen Ma, Mr. Shuida Ji, Mrs. Lukai Zheng, Miss. Yiran Wang, Mr. Hangxu Zhou, Mr. Songyang Yu and Mr. Houshi Jiang, for their helpful comments on my research. Their suggestions helped my research project to be more complete and sound. It has been an honour and pleasure to work with all of them.

I deeply appreciate the support from my beloved family and dearest friends. The achievement of this thesis is both theirs and mine.

The EPSRC, KTA Sheffield and John Crane Ltd have funded some research works. The funding support is essential for the research activities and is gratefully acknowledged. The equipment loan from EPSRC is also acknowledged.

# Publications

## Journal:

1. J. Yang, F. M. S. Mossa, H. W. Huang, Q. Wang, R. Woolley and Y. Zhang, **Oscillating Flames in Open Tubes**, *Proceedings of Combustion Institute*, 35 (2015), 2075-2082;
2. Q. Wang, J. Yang, H. W. Huang, Y. Zhang and C. Zhang, **Three-dimensional Investigation of the Dynamics of a Propane Diffusion Flame**, *Fuel*, 116 (2014), 448-454;
3. H. W. Huang, J. Yang, Q. Wang and Y. Zhang, **Variation of Hydrocarbon Composition and Ignition Locations on the Radiative Flame Initiation Characteristics through Multi-dimensional DFCD Incorporated Image Analysis**, *Fuel*, 103 (2013), 334-346;

## Conference:

1. J. Yang, Z. Ma and Y. Zhang, **A Novel Flame Chemiluminescence Measurement using a Digital Colour Camera**, *25th ICDERS Conference*, 2015, poster presentation;
2. Q. Wang, J. Yang, Y. Wang, Y. Zhang and C. Y. Zhao, **Experimental Investigation of Co-flow Effect on Ignition Process of a Methane Jet Diffusion Flame**, *25th ICDERS Conference*, 2015, oral presentation;

3. J. Yang, F. M. S. Mossa, H. W. Huang, Q. Wang, R. Woolley and Y. Zhang,  
**Oscillating Flames in Open Tubes**, *35th International Symposium on  
Combustion*, 2014, oral presentation.

# Abstract

Vision-based measurement as a useful tool has been applied successfully in many applications. The aim of this thesis is to apply vision-based measurement in both combustion and vibration studies. The purpose is to process and analyse the recorded light information for understanding combustion and vibration conditions. The chemiluminescence emission from a flame contains fundamental information on combustion, and the reflected light from an object's surface can also provide information on the condition of the measured object. These types of information can be recorded quantitatively into images through a camera. Further processing and analysis of the image data can explore useful information. In this work, a high-speed stereo colour imaging system is employed for both combustion and vibration studies. In each study, a suitable methodology is developed.

In a premixed hydrocarbon flame, the blue-green flame colour is mostly attributed to the presence and mixture of chemiluminescence emissions of  $\text{CH}^*$  and  $\text{C}_2^*$ . The modern colour camera with the colour filter array (CFA) scheme inherently encodes with red, green, and blue wide-band wavelength filters. According to the aforementioned principles, a flexible image colour model is proposed to detect flame chemiluminescence emissions of  $\text{CH}^*$  and  $\text{C}_2^*$ . A sensor calibration process is employed to refine the  $\text{CH}^*$  and  $\text{C}_2^*$  concentration expressions based on different camera sensor spectral sensitivities. The detected  $\text{CH}^*/\text{C}_2^*$  ratio is utilised to analogue the fuel/air ratio for combustion diagnostics. Two cases of flame

propagation in tubes and flame ignition to impinging are studied using this proposed image colour-based flame chemiluminescence measurement. Combined with stereo imaging and high-speed imaging, the ability of the proposed method to perform multi-dimensional measurement is demonstrated.

The reflected light from the measured object is the result of the interaction between the incident light and the object's surface. A camera captures the illumination of the reflected light as intensity in an image. When the positions of the light source and camera are fixed, any image intensity variation from the reflected light could indicate the object's movement. Hence, the measured images of a vibrating object would show intensity fluctuations. Based on this, an image intensity fluctuation-based vibration measurement is proposed. Two cases, wind turbine blade vibration monitoring and industrial coupling rotation-vibration testing, are studied using the proposed method. The ability of the image intensity fluctuation-based vibration measurement to perform one-dimensional and two-dimensional measurements is demonstrated successfully.

# Contents

|  |           |
|--|-----------|
| <b>Declaration .....</b>                 | <b>2</b>  |
| <b>Dedication.....</b>                   | <b>3</b>  |
| <b>Acknowledgements .....</b>            | <b>4</b>  |
| <b>Publications .....</b>                | <b>5</b>  |
| <b>Abstract .....</b>                    | <b>7</b>  |
| <b>Contents.....</b>                     | <b>9</b>  |
| <b>List of Figures .....</b>             | <b>15</b> |
| <b>List of Tables .....</b>              | <b>22</b> |
| <b>Nomenclature .....</b>                | <b>23</b> |
| <b>1 INTRODUCTION.....</b>               | <b>28</b> |
| <b>1.1 Motivation.....</b>               | <b>28</b> |
| <b>1.2 Objectives.....</b>               | <b>30</b> |
| <b>1.3 Outline of the thesis .....</b>   | <b>32</b> |
| <b>2 LITERATURE REVIEW .....</b>         | <b>35</b> |
| <b>2.1 Introduction.....</b>             | <b>35</b> |
| <b>2.2 Vision-based measurement.....</b> | <b>35</b> |
| 2.2.1 Introduction .....                 | 35        |
| 2.2.2 Vision systems .....               | 36        |
| 2.2.2.1 Introduction .....               | 36        |
| 2.2.2.2 Human vision system .....        | 36        |
| 2.2.2.3 Digital vision system.....       | 37        |
| 2.2.3 Light.....                         | 40        |
| 2.2.3.1 Introduction .....               | 40        |
| 2.2.3.2 Nature of light.....             | 40        |
| 2.2.3.3 Absorption and emission.....     | 42        |



|  |           |
|--|-----------|
| 2.2.3.4 Human vision perception of light.....      | 45        |
| 2.2.3.5 Summary of light.....                      | 47        |
| 2.2.4 Cameras.....                                 | 47        |
| 2.2.4.1 Introduction .....                         | 47        |
| 2.2.4.2 Properties.....                            | 47        |
| 2.2.4.2.1 Photosensitive sensor.....               | 47        |
| 2.2.4.2.2 Camera noise .....                       | 49        |
| 2.2.4.2.3 Signal-to-noise ratio .....              | 50        |
| 2.2.4.3 Colour imaging.....                        | 52        |
| 2.2.4.3.1 CIE colour model .....                   | 54        |
| 2.2.4.3.2 RGB colour model.....                    | 56        |
| 2.2.4.3.3 HSV colour model.....                    | 58        |
| 2.2.4.4 High-speed imaging .....                   | 60        |
| 2.2.4.5 Stereo imaging.....                        | 62        |
| 2.2.4.5.1 Stereo imaging principles .....          | 62        |
| 2.2.4.5.2 Intrinsic and extrinsic parameters ..... | 64        |
| 2.2.4.5.3 Stereo cameras .....                     | 66        |
| 2.2.4.5.3.1 Two-camera systems.....                | 66        |
| 2.2.4.5.3.2 Single-camera systems .....            | 67        |
| 2.2.4.6 Summary of cameras .....                   | 70        |
| 2.2.5 Summary of vision-based measurement .....    | 71        |
| <b>2.3 Combustion diagnostics.....</b>             | <b>73</b> |
| 2.3.1 Introduction .....                           | 73        |
| 2.3.2 Combustion definition .....                  | 73        |
| 2.3.2.1 Flame classification.....                  | 73        |
| 2.3.2.1.1 Diffusion flames .....                   | 74        |
| 2.3.2.1.2 Premixed flames.....                     | 75        |
| 2.3.2.1.3 Equivalence ratio .....                  | 76        |
| 2.3.3 Flame colour.....                            | 77        |

|  |            |
|--|------------|
| 2.3.4 Chemiluminescence of hydrocarbon flames .....  | 78         |
| 2.3.5 Flame chemiluminescence measurements .....   | 80         |
| 2.3.6 Summary of combustion diagnostics .....  | 84         |
| <b>2.4 Vibration diagnostics .....</b>   | <b>86</b>  |
| 2.4.1 Introduction .....   | 86         |
| 2.4.2 Preliminary Considerations.....  | 86         |
| 2.4.2.1 Maintenance.....   | 86         |
| 2.4.2.2 Vibration monitoring.....  | 87         |
| 2.4.2.3 Vibration signals.....   | 89         |
| 2.4.2.3.1 Frequency analysis .....   | 89         |
| 2.4.3 Vibration measurement .....  | 90         |
| 2.4.4 Summary of vibration diagnostics.....  | 92         |
| <b>2.5 Conclusion of the literature review.....</b>  | <b>94</b>  |
| <b>3 IMAGING SYSTEM AND CALIBRATION PROCESSES .....</b>                                    | <b>97</b>  |
| <b>3.1 Introduction.....</b>   | <b>97</b>  |
| <b>3.2 High-speed stereo colour imaging system .....</b>                                   | <b>97</b>  |
| 3.2.1 Introduction .....   | 97         |
| 3.2.2 High-speed colour camera .....   | 99         |
| 3.2.3 Stereo adapter .....   | 99         |
| <b>3.3 Calibration processes .....</b>   | <b>102</b> |
| 3.3.1 Introduction .....   | 102        |
| 3.3.2 SNR calibration .....  | 103        |
| 3.3.3 Sensor spectral sensitivity calibration.....   | 104        |
| 3.3.4 Camera parameters calibration .....  | 108        |
| 3.3.4.1 Camera parameters of the employed high-speed stereo colour imaging system<br>..... | 108        |
| 3.3.4.2 Parameter calibration process .....  | 108        |
| <b>3.4 Conclusion of imaging system and calibration processes .....</b>                    | <b>113</b> |

|   |            |
|---|------------|
| <b>4 IMAGE COLOUR-BASED FLAME CHEMILUMINESCENCE MEASUREMENT</b>     | <b>115</b> |
| <b>4.1 Introduction</b>   | <b>115</b> |
| <b>4.2 Methodology</b>  | <b>115</b> |
| 4.2.1 Introduction  | 115        |
| 4.2.2 Camera image colour   | 117        |
| 4.2.3 CH* and C <sub>2</sub> * chemiluminescence                    | 117        |
| 4.2.4 Relationship between image colour and flame chemiluminescence | 118        |
| 4.2.5 Advantages and disadvantages                                  | 120        |
| <b>4.3 Experimental estimation</b>                                  | <b>122</b> |
| 4.3.1 Introduction  | 122        |
| 4.3.2 Experimental setup and process                                | 122        |
| 4.3.2.1 CH* and C <sub>2</sub> * expressions                        | 123        |
| 4.3.2.2 Image processing  | 124        |
| 4.3.3 Results and analysis  | 126        |
| 4.3.4 Comparison with a colour-modelled method                      | 130        |
| 4.3.5 Conclusion  | 132        |
| <b>4.4 Case 1: flame propagation in open/closed tubes</b>           | <b>134</b> |
| 4.4.1 Introduction  | 134        |
| 4.4.2 Experimental setup  | 136        |
| 4.4.3 Results and analysis  | 138        |
| 4.4.3.1 Flame position analysis                                     | 140        |
| 4.4.3.2 Flame structure analysis                                    | 144        |
| 4.4.3.3 Flame chemiluminescence analysis                            | 146        |
| 4.4.4 Conclusions   | 152        |
| <b>4.5 Case 2: flame ignition to impinging</b>                      | <b>154</b> |
| 4.5.1 Introduction  | 154        |
| 4.5.2 Experimental setup  | 155        |
| 4.5.3 Image processing  | 157        |

|  |            |
|--|------------|
| 4.5.4 Results and discussion.....  | 160        |
| 4.5.4.1 Structures analysis .....  | 160        |
| 4.5.4.2 Signal analysis .....  | 164        |
| 4.5.4.3 3D structures .....  | 169        |
| 4.5.4.4 3D CH <sup>*</sup> /C <sub>2</sub> <sup>*</sup> ratio .....  | 172        |
| 4.5.4.4 Conclusion.....  | 175        |
| 4.5.5 Conclusion of image colour-based flame chemiluminescence measurement<br>.....                          | 178        |
| <b>5 IMAGE INTENSITY FLUCTUATION-BASED VIBRATION MEASUREMENT</b>   | <b>180</b> |
| <b>5.1 Introduction.....</b>   | <b>180</b> |
| <b>5.2 Methodology .....</b>   | <b>180</b> |
| 5.2.1 Introduction .....   | 180        |
| 5.2.2 Surface orientation.....   | 181        |
| 5.2.3 Light scattering .....   | 183        |
| 5.2.4 Reflectivity .....   | 184        |
| 5.2.5 Image intensity fluctuation-based vibration measurement.....   | 187        |
| 5.2.5.1 Measured position.....   | 189        |
| 5.2.5.2 Measured size.....   | 193        |
| 5.2.6 Conclusion.....  | 195        |
| <b>5.3 Case 1: wind turbine blade vibration monitoring.....</b>  | <b>197</b> |
| 5.3.1 Introduction .....   | 197        |
| 5.3.2 Experimental setup.....  | 198        |
| 5.3.3 Image processing .....   | 201        |
| 5.3.4 Results and discussion.....  | 202        |
| 5.3.4.1 Comparison between the intensity fluctuation-based method and feature<br>tracking-based method ..... | 202        |
| 5.3.4.2 Blade condition monitoring.....  | 204        |
| 5.3.4.3 Damage detection .....   | 207        |
| 5.3.5 Conclusion.....  | 214        |

|  |            |
|--|------------|
| <b>5.4 Case 2: membrane coupling rotation-vibration measurement .....</b>        | <b>216</b> |
| 5.4.1 Introduction .....   | 216        |
| 5.4.2 Experimental setup and process .....                                       | 217        |
| 5.4.3 Results and analysis .....   | 221        |
| 5.4.3.1 Vibration frequency identification .....                                 | 221        |
| 5.4.3.2 Steady torque effect .....   | 223        |
| 5.4.3.3 Cyclic torque and its frequency effect .....                             | 226        |
| 5.4.4 Conclusion .....   | 229        |
| <b>5.5 Conclusion of intensity fluctuation-based vibration measurement .....</b> | <b>231</b> |
| <b>6 CONCLUSION AND FUTURE WORK .....</b>  | <b>233</b> |
| <b>6.1 Conclusion .....</b>  | <b>233</b> |
| <b>6.2 Scope of future work .....</b>  | <b>236</b> |
| <b>References .....</b>  | <b>240</b> |

# List of Figures

|  |    |
|--|----|
| Figure 1. 1: Outline of the thesis.....  | 32 |
| Figure 2. 1: A schematic of human vision system.....   | 37 |
| Figure 2. 2: A schematic of digital vision system. ....  | 38 |
| Figure 2. 3: The electromagnetic spectrum (EM) and the visible spectrum (VIS). ...   | 41 |
| Figure 2. 4: Absorption and emission of line spectra.....  | 43 |
| Figure 2. 5: Normalized spectral sensitivity of retinal rod and cone cells of the human eyes [adapted from (Dowling, 1987)]. ....                  | 46 |
| Figure 2. 6: The CCD and CMOS configurations.....  | 49 |
| Figure 2. 7: Bayer's CFA pixel filter arrangement.....   | 53 |
| Figure 2. 8: 1931 CIE chromaticity chart [redrawn from (Smith & Guild, 1931)].....   | 55 |
| Figure 2. 9: 3D representation of the RGB colour model.....  | 57 |
| Figure 2. 10: The HSV model.....   | 59 |
| Figure 2. 11: Images of a galloping horse by Edward Muybridge (Newhall, 1949). 61  |    |
| Figure 2. 12: Optical geometry between a read object and its corresponding two images.....   | 63 |
| Figure 2. 13: Relations among the world coordinate system, camera coordinate system, image coordinate system, and computer coordinate system. .... | 65 |
| Figure 2. 14: A single camera stereo imaging system with two outer fixed mirrors and a rotating mirror.....  | 67 |
| Figure 2. 15: A single camera stereo imaging system with a glass plate. ....   | 68 |
| Figure 2. 16: A stereo imaging system proposed by Gosthasby and Gruver.....  | 69 |
| Figure 2. 17: Signal camera with a four-mirror stereo adapter imaging system.....  | 70 |

|   |     |
|---|-----|
| Figure 2. 18: Schematic of Bunsen burner flames: (a) diffusion flames and (b) premixed flames [adapted from (Kuo, 2005)].   | 75  |
| Figure 2. 19: Scheme of machine life [adapted from (Bilosova & Bilos, 2012)].   | 87  |
| Figure 3. 1: Configuration of a high-speed stereo colour imaging system.  | 98  |
| Figure 3. 2: Asahi Pentax stereo adapter.   | 100 |
| Figure 3. 3: Dimensions of the four-mirror stereo adapter.  | 101 |
| Figure 3. 4: The camera with the four-mirror adapter and its two-virtual-camera system.   | 101 |
| Figure 3. 5: Image samples captured with different connections of the stereo adapter: (a) left/right connection for measuring a vertical flame and (b) up/down connection for measuring a horizontal blade. | 102 |
| Figure 3. 6: SNR results for the employed high-speed stereo colour imaging system using different shutter speeds.   | 104 |
| Figure 3. 7: (a) Dimensions and (b) internal structure of the Newport Manual Mini Monochrometer.  | 106 |
| Figure 3. 8: R, G, and B colour channels spectral sensitivities of the employed high-speed camera.  | 107 |
| Figure 3. 9: Standard calibration board.  | 109 |
| Figure 3. 10: Images of a calibration board captured from four different directions.  | 110 |
| Figure 3. 11: 3D Reconstruction of the calibration board images taken from four different directions in Figure 3.10.  | 112 |
| Figure 4. 1: The relationship between image colour and radiation.   | 119 |
| Figure 4. 2: Sensitivity ratios of the B and G channels at 430 nm and 516 nm.   | 123 |

|   |     |
|---|-----|
| Figure 4. 3: Processed $C_3H_8$ premixed flame images at equivalence ratio $\Phi$ ranging from 0.93 to 1.53; the R, G, and B intensities of each image are enhanced 10 times. ....  | 126 |
| Figure 4. 4: Colour-calculated $CH^*/C_2^*$ ratio maps at equivalence ratio $\Phi$ ranging from 0.93 to 1.53. ....  | 127 |
| Figure 4. 5: $CH^*/C_2^*$ histogram of a typical single frame at $\Phi = 1.53$ . ....   | 128 |
| Figure 4. 6: Calculated $\mu_e$ values at different $\Phi$ along with an error bar denoting the 99% CI range. ....  | 129 |
| Figure 4. 7: Comparison between developed and conventional modelled $CH^*/C_2^*$ ratios. ....   | 131 |
| Figure 4. 8: Difference between the developed and conventional modelled $CH^*/C_2^*$ ratios. ....   | 132 |
| Figure 4. 9: A schematic of the experimental configuration. ....  | 137 |
| Figure 4. 10: Examples of images in closed and open tubes at different equivalence ratios ( $\Phi=0.8-1.6$ , with a 0.1 interval). ....   | 139 |
| Figure 4. 11: Flame propagation in both closed and open tubes at $\Phi = 1.2$ . ....  | 141 |
| Figure 4. 12: Images of a $\Phi = 1.2$ propane/air flame recorded at 3000 fps. The numbers on the frames is the time after the camera trigger: (a) beginning of the tube: from 38 to 42.3 ms after trigger and (b) centre of the tube: from 88 to 92.3 ms after trigger. .... | 142 |
| Figure 4. 13: Leading points plotted against time: (a) flame position, (b) flame front position after subtraction of the FFT filtered flame position, and (c) the measured flame speed. These relate to the image sequences of Figure 4.12. ....                              | 143 |



|   |     |
|---|-----|
| Figure 4. 14: (a) $\text{CH}^*$ , $\text{C}_2^*$ , and $\text{CH}^*/\text{C}_2^*$ values against flame area in open tubes at $\Phi = 1.2$ ; (b) flame visualisation at 59, 63, 66, 71, and 72 ms corresponding to Figure 4.13. ....   | 146 |
| Figure 4. 15: Processed $\text{CH}^*/\text{C}_2^*$ ratio maps of $\Phi = 1.2$ with propane/air flame recorded at 1000 fps. ....   | 148 |
| Figure 4. 16: The colour-calculated $\Phi$ of the real $\Phi = 1.2$ propane/air flame propagation in both closed and open tubes. ....   | 150 |
| Figure 4. 17: Colour-calculated $\Phi$ and flame front position against time from the beginning of the recording. ....  | 151 |
| Figure 4. 18: Schematic of the experimental setup. ....   | 156 |
| Figure 4. 19: Image processing procedure. ....  | 157 |
| Figure 4. 20: Samples of images: (a) original image and (b) blue colour-enhanced image. ....  | 158 |
| Figure 4. 21: Samples of (a) processed 2D image pairs and (b) their 3D reconstruction structure. ....   | 159 |
| Figure 4. 22: A sample of a 3D $\text{CH}^*/\text{C}_2^*$ ratio map. ....   | 160 |
| Figure 4. 23: 2D flame appearance of 16.8L/min $\text{C}_3\text{H}_8$ diffusion flame with bottom ignition location. ....   | 161 |
| Figure 4. 24: 2D Flame structure visualisation of $\text{C}_3\text{H}_8$ and $\text{CH}_4$ 100 ms after ignition at the bottom, middle, and top, respectively. ....   | 163 |
| Figure 4. 25: $\log(I_D/I_P)$ signal ratio of the $\text{C}_3\text{H}_8$ flame ignition process under different flow rates (4.2 L/min plotted in red, 8.4 L/min plotted in blue, and 16.8 L/min plotted in black) and different ignition locations at the (a) bottom, (b) middle, and (c) top. .... | 166 |
| Figure 4. 26: $\log(I_D/I_P)$ signal ratio of the $\text{CH}_4$ flame ignition process under different flow rates (4.2 L/min plotted in red, 8.4 L/min plotted in blue, and 16.8 L/min  |     |

|  |     |
|--|-----|
| plotted in black) and different ignition locations at the (a) bottom, (b) middle, and (c) top.....   | 168 |
| Figure 4. 27: Premixed blue flame 3D structures of 16.8L/min CH <sub>4</sub> diffusion with ignition at the bottom location. ....                                      | 170 |
| Figure 4. 28: Yellow diffusion flame 3D structures of 16.8L/min CH <sub>4</sub> diffusion with ignition at the bottom location. ....                                   | 170 |
| Figure 4. 29: Premixed blue flame 3D structures of 16.8L/min C <sub>3</sub> H <sub>8</sub> diffusion with ignition at the bottom location. ....                        | 171 |
| Figure 4. 30: Yellow diffusion flame 3D structures of 16.8L/min C <sub>3</sub> H <sub>8</sub> diffusion with ignition at the bottom location. ....                     | 171 |
| Figure 4. 31: 3D CH <sup>*</sup> /C <sub>2</sub> <sup>*</sup> ratio map of 16.8 L/min C <sub>3</sub> H <sub>8</sub> diffusion with bottom ignition for Fig. 4.29. .... | 173 |
| Figure 4. 32: 3D CH <sup>*</sup> /C <sub>2</sub> <sup>*</sup> ratio map of 16.8 L/min CH <sub>4</sub> diffusion with bottom ignition for Fig. 4.27. ....               | 173 |
| Figure 5. 1: Front view and side view measurements of an object during rotation. ....  | 181 |
| Figure 5. 2: Definition of a plane. ....   | 182 |
| Figure 5. 3: Surface orientation of a curved object. ....  | 183 |
| Figure 5. 4: Light reflection from a glossy surface. ....  | 184 |
| Figure 5. 5: Light geometry, using a single-point light source. ....   | 185 |
| Figure 5. 6: $\varphi(i, e, g)$ changed by object motion. ....   | 186 |
| Figure 5. 7: A sample stereo image in the employed image sequence. ....  | 188 |
| Figure 5. 8: Different measured positions. ....  | 189 |
| Figure 5. 9: Comparison of measured positions: (a) obvious features on object surface, (b) unobvious features on object surface and (c) outside of object. ....        | 190 |

|   |     |
|---|-----|
| Figure 5. 10: Different measured sizes of measured position a in Figure 5.8; a) 1 pixel, b) 3×3 pixels, c) 5×5 pixels, d) 7×7 pixels, e) 9×9 pixels, and f) 11×11 pixels..... | 194 |
| Figure 5. 11: The schematic of blade vibration measurement. ....  | 199 |
| Figure 5. 12: A sample stereo image and the markers' locations on the blade.....  | 200 |
| Figure 5. 13: Vibration signal results samples derived by (a) intensity fluctuation and (b) marker displacement in the (1) time domain and (2) frequency domain. ....         | 203 |
| Figure 5. 14: Intensity fluctuation derived vibration frequency spectra of the Marker 1 position on the undamaged blade at input settings of 6.0–6.4 Hz and 3 V. ....         | 204 |
| Figure 5. 15: Intensity fluctuation-derived vibration frequency spectra of the Marker 1 position on the undamaged blade at input settings of 6.3 Hz and 3–5V....              | 206 |
| Figure 5. 16: Measured intensity variation of undamaged and damaged blades at 6.3 Hz and 4V. ....   | 208 |
| Figure 5. 17: Measured displacement variation of undamaged and damaged blades at 6.3 Hz and 4V by the photogrammetry method. ....   | 209 |
| Figure 5. 18: Intensity variation-derived frequency spectra of undamaged and damaged blades at the input settings of 6.3 Hz and 4V.....                                       | 212 |
| Figure 5. 19: Displacement variation-derived frequency spectra of undamaged and damaged blades at the input settings of 6.3 Hz and 4V.....                                    | 213 |
| Figure 5. 20: Schematic of a membrane coupling connected with pipes.....  | 217 |
| Figure 5. 21: Schematic of testing setup. ....  | 218 |
| Figure 5. 22: Six-bolt membrane coupling (GA/118640). ....  | 219 |
| Figure 5. 23: A sample image of bowing occurred in the 2000 rpm and 5500 Nm steady torque test case. ....   | 220 |

|  |     |
|--|-----|
| Figure 5. 24: Intensity variation tracked window position. ....  | 220 |
| Figure 5. 25: A sample frequency spectrum.....   | 221 |
| Figure 5. 26: Intensity variation-derived frequency spectra for increasing steady torque from 1000 to 5000 Nm.....   | 224 |
| Figure 5. 27: Intensity variation-derived frequency spectra (sub-synchronous portion) for increasing steady torque from 1000 to 5000 Nm. ....  | 225 |
| Figure 5. 28: $f_v$ change during a steady torque increase.....  | 226 |
| Figure 5. 29: Image intensity variation gained frequency spectra of coupling rotation-vibration under 2000 rpm and 4000 Nm steady torque with 10 Hz cyclic torques at 500, 1000, and 1500 Nm. .... | 228 |
| Figure 5. 30: Image intensity variation-derived frequency spectra of coupling rotation-vibration under 2000 rpm and 4000 Nm steady torque with 1500 cyclic torques at 5, 10, and 15 Hz. ....       | 229 |
| Figure 6. 1: Enhanced colour images combined with Schlieren images for flame ignition measurement. ....  | 238 |
| Figure 6. 2: Images of an industrial gas turbine combustor: (a) side view and (b) front view. ....   | 239 |

## List of Tables

|   |     |
|---|-----|
| Table 2. 1: Guidelines for interpreting the SNR in terms of the subjective image quality (Constant, 2009).....                | 50  |
| Table 2. 2: Example of operation parameters monitoring (ISO 17359).....   | 88  |
| Table 4. 1: $\text{CH}^*$ and $\text{C}_2^*$ emission expressions using the developed and conventional modelled methods. .... | 130 |

# Nomenclature

| Abbreviation | Definition   |
|--------------|--|
| 1D           | One-Dimension/Dimensional  |
| 2D           | Two- Dimension/Dimensional   |
| 3D           | Three- Dimension/Dimensional   |
| API 671      | American Petroleum Institute standard 671  |
| B            | Blue   |
| CAD          | Computer-Aided Design (computer program)   |
| CCD          | Charge-Coupled Device  |
| CFA          | Colour Filter Array  |
| CI           | Confidence Interval  |
| CIE          | Commission Internationale de l'Eclairage<br>(the International Commission on Illumination) |
| CMOS         | Complementary Metal Oxide Semiconductor  |
| CV           | Computer Vision  |
| DDT          | Deflagration to Detonation Transition  |
| DSN          | Dark Shot Noise  |
| EM           | Electro-magnetic wave  |
| FFT          | Fast Fourier Transform   |
| fps          | Frames per second  |
| FOV          | Field of view  |
| FOS          | Factor of Safety   |
| G            | Green  |

|         |   |
|---------|---|
| HSV     | Hue, Saturation and Value Colour Model                                    |
| IR      | Infrared  |
| ISO     | International Standards Organisation                                      |
| LabVIEW | Laboratory Virtual Instrument Engineering Workbench<br>(computer program) |
| LDV     | Laser Doppler Velocimetry   |
| LIF     | Laser-induced Fluorescence  |
| Matlab  | Matrix Laboratory (computer program)                                      |
| MIT     | Massachusetts Institute of Technology                                     |
| MV      | Machine Vision  |
| NIR     | Near-infrared   |
| PFV     | Photron FASTCAM Viewer (computer program)                                 |
| RMS     | Root-Mean-Square  |
| PSN     | Photon Shot Noise   |
| R       | Red   |
| RGB     | Red, Green and Blue Colour Model  |
| RN      | Readout Noise   |
| SNR     | Signal-to-Noise Ratio   |
| UV      | Ultraviolet   |
| VIS     | Visible light   |
| XYZ     | CIE tri-stimulus values   |

| Symbol                  | Definition                                   | Unit                             |
|-------------------------|--|----------------------------------|
| $A$                     | Intrinsic parameter                          |                                  |
| $b$                     | Distance between two optical axes            | mm                               |
| $c$ (Section 2.2.3.3)   | Speed of light                               | 299792458m/s                     |
| $c$ (Section 2.2.4.6)   | Principle points                             |                                  |
| $c'$ (Section 2.2.4.6)  | Optical centre                               |                                  |
| $Dev_N$                 | Standard deviation of image background noise | dB                               |
| $E$                     | Energy of photon                             | $eV$                             |
| $E_1$                   | Ground state (First energy level)            | $eV$                             |
| $E_2$                   | Second energy level                          | $eV$                             |
| $E_3$                   | Third energy level                           | $eV$                             |
| $E_4$                   | Fourth energy level                          | $eV$                             |
| $E_f$                   | Finial energy stage                          | $eV$                             |
| $E_i$                   | Initial energy state                         | $eV$                             |
| $eV$                    | Electron-voltage                             |                                  |
| $f$ (Section 2.2.4.6)   | Focus length                                 | mm                               |
| $f$ (Section 2.3.2.2.3) | Fuel-to-oxidiser ratio                       |                                  |
| $f$ (Chapter 5)         | Frequency                                    | Hz                               |
| $f_c$                   | Cyclic torque frequency                      | Hz                               |
| $f_r$                   | Rotation frequency                           | Hz                               |
| $f_{st}$                | Stoichiometric fuel-to-oxidiser ratio        |                                  |
| $f_v$                   | Vibration frequency                          | Hz                               |
| $h$                     | Planck' constant                             | $6.6262 \times 10^{-34}$ joule/s |



|                       |   |       |
|-----------------------|---|-------|
| $H$                   | Hue   |       |
| $I$                   | Intensity                                     |       |
| $I_B$                 | Blue intensity                                |       |
| $I_G$                 | Green intensity                               |       |
| $I_R$                 | Red intensity                                 |       |
| $I_D$                 | Intensity amount of diffusion flame           |       |
| $I_P$                 | Intensity amount of premixed flame            |       |
| $I_{SAT}$             | Intensity amount of an image                  |       |
| $l$                   | distance between nozzle and ignition position | mm    |
| $m_1(m_2)$            | point in image                                |       |
| $m_f$                 | Mass of fuel                                  | g     |
| $m_{os}$              | Mass of stoichiometric oxidiser               | g     |
| $M$                   | point in 3D world                             |       |
| $M_f$                 | Molecular weight of fuel                      | g/mol |
| $M_o$                 | Molecular weight of oxidiser                  | g/mol |
| $n_f$                 | Mole of fuel                                  | mol   |
| $n_{os}$              | Mole of stoichiometric oxidiser               | mol   |
| $R$                   | Rotational parameter                          |       |
| $S$                   | Saturation                                    |       |
| $s$                   | second  |       |
| $s$ (Section 2.2.4.6) | Arbitrary scale factor                        |       |
| $t$                   | Translation parameter                         |       |
| $(u, v)$              | Computer coordinate system                    |       |

|              |  |
|--------------|--|
| $(u_0, v_0)$ | Principle point of computer coordinate |
| V            | Value                                  |
| (X, Y, Z)    | World coordinate system                |
| $(x, y, z)$  | Camera coordinate system               |
| $(x', y')$   | Image coordinate system                |

| Chemical Symbols | Definition                      |
|------------------|---------------------------------|
| $C_2^*$          | $C_2$ radical chemiluminescence |
| $CH^*$           | CH radical chemiluminescence    |
| $CH_4$           | Methane                         |
| $C_3H_8$         | Propane                         |
| $CO_2$           | Carbon Dioxide                  |
| $O_2$            | Oxygen                          |
| $OH^*$           | OH radical chemiluminescence    |
| $H_2O$           | Water                           |

| Greek Symbols        | Definition  | Unit |
|----------------------|---|------|
| $\alpha$ (Chapter 2) | Scale factor for $u$                                |      |
| $\alpha$ (Chapter 4) | Camera sensor light conversion rate                 |      |
| $\beta$              | Scale factor for $v$                                |      |
| $\gamma$             | Skew parameter of physical image and computer image |      |
| $\lambda$            | Wavelength  | nm   |
| $\Phi$               | Equivalence ratio                                   |      |

# 1

---

## INTRODUCTION

---

### 1.1 Motivation

*‘One Look is Worth a Thousand Words’*

--- *American proverb* (Mieder, 1992)

The American proverb ‘One look is worth a thousand words’ indicates that sight makes it possible to record huge amounts of information in a very short period (Mieder, 1992). As Davies (1997) stated, each glance can provide megabits of information, and continuous viewing could probably receive information exceeding even 10 megabits per second. Up to 80% of the total information that we receive from the world is because of vision (McMains, 2000). Undoubtedly, among the five conscious senses of natural human ability – vision, hearing, smell, taste, and touch – vision is the one that people depend on most.

The illumination, colour, shape, and position of a measured object can be observed through the visual system. In fact, light is what we are measuring directly, regardless of whether the object is self-illuminated or illuminated by reflection. Light is a type of energy that carries information about the measured object. Visual perception, thus, is the ability to process and analyse received light information to understand our

surroundings. However, the large amount of information carried by light exceeds the limitations of the brain's ability to process it. A part of light information is reduced by the brain automatically so that only a small portion of the total light information is abstracted and interpreted for us to understand the world.

Human vision comprehends light's colour and intensity in a relative sense, so it is difficult for us to observe the absolute information from light, such as detecting the received light wavelengths and quantifying light illumination, while a digital camera, as a light detector, can capture light in absolute measurement (Sonka, Hlavac, & Boyle, 1999). Through the camera, a scene can be photographed into a 2D digital-format image. The light information can then be measured quantitatively by processing the image via a computer. The combination of a digital camera and a computer is referred to as a digital vision system. Such a vision system has been successfully applied as a useful measurement tool in many applications, such as medical imaging, industrial inspection, visual surveillance, and autonomous vehicles (Steger, Ulrich, & Wiedemann, 2007). Some researchers have also employed vision-based measurement in combustion diagnostics (Huang & Zhang, 2008; Hossain, Lu, Sun, & Yan, 2013) and vibration monitoring (Giergiel & Kohut, 2011).

Combustion and vibration are two fundamental research fields in the energy industry. They are very different subjects: combustion is referred to as a chemical reaction that involves fluid dynamics with heat transfer and self-luminous light emission, while vibration is a mechanical phenomenon with solid dynamics that requires an

additional light source to assist in the imaging. Measurements of both phenomena are essential for fundamental research, production improvement, and process maintenance. For combustion, it can provide a better understanding of fundamental information that can benefit fuel utilization efficiency and pollutant emission reduction. For vibration, it usually refers to machine condition monitoring to detect failures or damage to arrange maintenance.

Conventionally, the measurement of combustion often employs optical devices because the flame is a light emission fluid, while the measurement of vibration usually uses different mechanical sensors (Bilosova & Bilos, 2012). Recently, some researchers have begun to employ high-speed camera to measure vibration phenomena (Ozbek, Rixen, Erne, & Sanow, 2010; Giergiel & Kohut, 2011). It seems that both combustion and vibration can be measured using the same optical imaging technique. The work described in this thesis attempts to use the same vision system in both combustion and vibration diagnostics studies. Since vision-based measurement is still case dependent, there is no general processing method that can be used for different applications. The same is true here for both combustion and vibration. Therefore, different methodologies must be developed in both combustion and vibration studies.

## 1.2 Objectives

The main objectives of this thesis are as follows:

- To review vision-based measurement, combustion, and vibration.

- To choose a flexible vision-based system for both combustion and vibration studies.
- To analyse the employed imaging system.
- To develop suitable methodologies for combustion and vibration measurements.

- **For combustion:**

- To explore the relationships among flame chemiluminescence, camera sensor spectral sensitivity, and image colour model and, based on the relationships, to develop a flexible model presenting flame chemiluminescence by image colour analysis.
- To estimate the proposed colour-based flame chemiluminescence measurement and compare it with the conventional method.
- To apply colour-based flame chemiluminescence measurement for combustion case studies.
- To apply the method for flame multi-dimensional analysis.

- **For vibration:**

- To explore the relationships between object vibration and image intensity fluctuations.
- To compare the developed image intensity fluctuation-based vibration measurement with the conventional feature tracking-derived vibration displacement.

- To apply intensity-based vibration measurement for vibration case studies.

## 1.3 Outline of the thesis

This thesis includes three main subjects: vision-based measurement, combustion diagnostics, and vibration diagnostics. A mind map is used to describe their relations in this thesis, as shown in Figure 1.1.

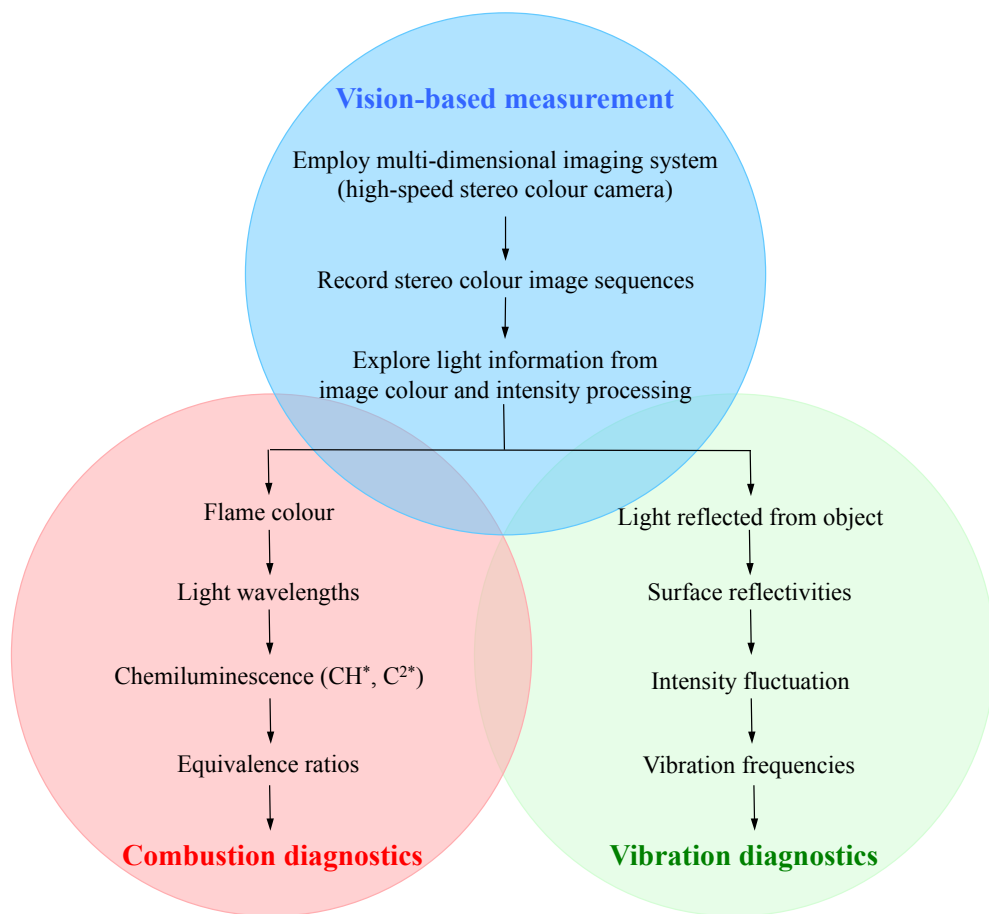


**Figure 1. 1: Outline of the thesis.**

The thesis consists of six chapters. Apart from the introduction and conclusion chapters, all chapters begin with an introduction and end with a conclusion. The references are placed at the end of the thesis.

Chapter 1 outlines the motivation of the research study and points out the aims of the work. The objectives are also presented in this chapter.

Chapter 2 is the literature review, which is divided into three main sections. The first part reviews fundamental information on vision-based measurement, including vision systems, light properties, and digital imaging. The second part introduces background knowledge on combustion, and measurements of flame chemiluminescence. The last part addresses vibration. The purposes for vibration monitoring are introduced. The measured parameters and methods are reviewed.

Chapter 3 is divided into two main sections. The first section gives details of the employed vision-based measurement system, including descriptions of the main camera device, lens, and stereo adapter. The second section addresses the camera signal-to-noise ratio, camera sensor spectral sensitivity, and camera 3D reconstruction parameter calibrations.

Chapter 4 proposes a developed image colour-calculated flame chemiluminescence measurement. This method is validated by an experimental test and compared with the conventional colour-model method. Then, the method is applied to two case studies. One is flame propagation in tubes; the other is the flame ignition-to-flame propagation phenomenon.

Chapter 5 investigates an image intensity fluctuation-based vibration measurement. The proposed method is compared with the conventional feature-tracking method in



monitoring blade vibration. The method is also applied to an industrial membrane coupling rotation-vibration test measurement.

Chapter 6 concludes the work and gives the scope of future work.

# 2

---

## LITERATURE REVIEW

---

### 2.1 Introduction

This chapter consists of three major sections. The first part introduces vision-based measurement. In this part, the components and principles of the vision system are described. Fundamental knowledge on light properties and digital cameras are also reviewed. The second portion reviews combustion diagnostics. Combustion properties, flame classification, flame colour, flame chemiluminescence, and chemiluminescence measurements are discussed. The last part addresses vibration. The role of vibration monitoring, vibration signals, and vibration measurements are introduced. This literature review is not intended to cover all the literature that has been produced in the fields mentioned above. It presents the states of the art of vision-based measurement in both combustion and vibration research, and the knowledge gaps that need further study are highlighted.

### 2.2 Vision-based measurement

#### 2.2.1 Introduction

Vision-based measurement is reviewed here in three parts:

- i. Vision system: the overall principles, configuration of the human vision system, and an analogue digital vision system.
- ii. Light: the nature of light, the principles of light absorption, emission, reflection, and refraction, and human vision perception of light.

- iii. Camera: the photosensitive sensor and digital imaging techniques, including colour imaging, high-speed imaging, and stereo imaging.

## **2.2.2 Vision systems**

### **2.2.2.1 Introduction**

Vision is the ability to build a representation of the physical world through receiving, processing, and interpreting useful light information. The various components of vision are corporately known as the vision system. The most common but powerful vision system is the human vision system, which is composed of biological components. Another type that differs from the human vision system is called a digital vision system, in which digital camera and computer components simulate the eyes and brain. Human vision is good at extracting useful meaning from a scene observed for a short period, while digital vision can measure absolute quantitative light information directly.

### **2.2.2.2 Human vision system**

The human vision system allows individuals to assimilate information from the physical world through light. A sample schematic of this process is shown in Figure 2.1. The light reflected from the surface of the butterfly passes through the human eye. In the eye, the front curved surface of the cornea assists the internal lens to focus the light onto the retina. The retina comprises two types of receptor cells, rods and cones. The functions of these two cells are discussed in Section 2.2.3.4. These receptors can convert light into neural signals. Then the converted signals travel into

the brain via the optic nerve. The image of the butterfly is formed in the mind. After the brain analyses and understands this image, the characteristics of the butterfly can be identified.

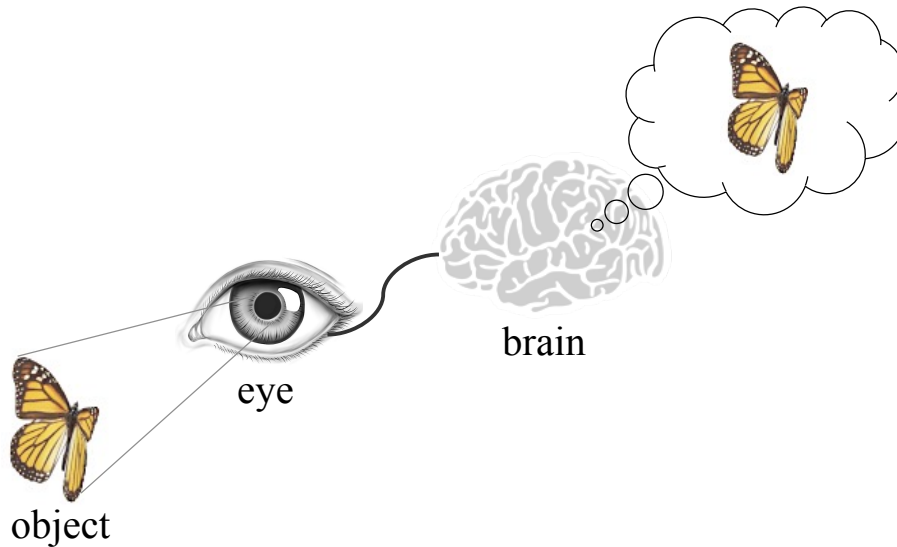


**Figure 2. 1: A schematic of human vision system.**

The human vision system makes it easy to extract meaningful information from the received light. With each glance, human eyes can receive megabits of information, and continuous viewing can probably receive information exceeding 10 megabits per second (Davies, 1997). However, some information is filtered and reduced by our brain automatically, so only a small portion of the light information is comprehended.

### **2.2.2.3 Digital vision system**

A digital vision system is analogous to the human vision system, but it consists of digital components such that the camera and the computer replace the eye and the brain. Compared to human vision, an advantage of digital vision system is that it

records light information with absolute measurement. The recorded data, an image, can be processed and analysed conveniently via a computer. A sample of the digital vision system is shown in Figure 2.2.

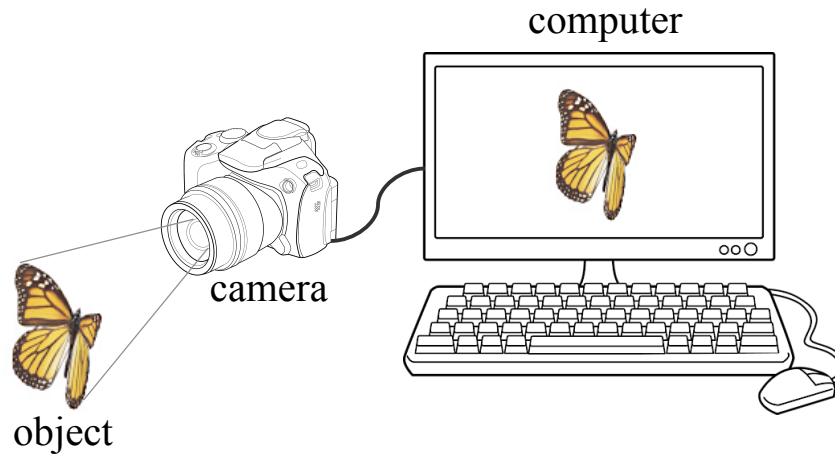


**Figure 2. 2: A schematic of digital vision system.**

The digital vision system can be regarded as having four parts (Heavens & Ditchburn, 1991):

- i. Optic system, which receives and focuses the incident light.
- ii. Photoreceptor, which converts the incident light to electrical signals.
- iii. Information transmission, which transfers the converted electrical signals to the processor.
- iv. Processor, which processes and analyses signals to assist in decision-making.

The optic system and photoreceptor are the imaging inputs. Generally, they include a lens and a photosensitive sensor in a camera. The lens focuses the incident light, while the photosensitive sensor converts the received photon signals into digital

signals. The computer, as the processor, serves the functions of the brain to process and analyse the signals. In the digital vision system, the light is recorded from the 3D scene to the 2D matrix of an image.

With the development of the digital camera and computer, digital vision systems have been successfully applied in many applications, such as medical imaging, industrial inspection, visual surveillance, and autonomous vehicles (Steger, Ulrich, & Wiedemann, 2007). Vision-based measurement has also played an essential role in combustion diagnostics (Huang & Zhang, 2008; Hossain, Lu, Sun, & Yan, 2013) and showed potential in vibration diagnostics (Giergiel & Kohut, 2011).

For combustion diagnostics, the flame profile, radical emissions, and temperature are important parameters to reveal the combustion physics, such as flame dynamics and chemical reaction. A digital vision system can measure this information to guide intuition into the complex combustion phenomena and inspiring the formulation of theories for engineering designs. In contrast, for vibration diagnostics, digital vision systems are also useful for machine condition monitoring. The obtained results can provide important vibration signals of machine condition. Since the human vision system cannot perceive these types of information, employing digital vision systems in these two applications seems necessary. However, few researchers used the same vision system in both combustion and vibration studies.

## **2.2.3 Light**

### **2.2.3.1 Introduction**

In a vision system, light is the directly measured object. Generally, light is referred to as electromagnetic (EM) radiation. As a type of energy, light is accompanied by information. This information is useful for researchers to understand the physics phenomenon such as combustion. To understand light, background knowledge on it is discussed here, including light's dual wave and particle nature; principles of light absorption, emission, reflection, and refraction; and human visual perception of light.

### **2.2.3.2 Nature of light**

Over the past hundred years, physics experiments have demonstrated that light has a dual nature (Hecht, 2002). Light behaves like both a wave and particles; these two behaviours can explain how the vision system responds to light.

The first nature of light is the wave phenomenon, which means that light can vary in frequency and wavelength. Visible light covers the wavelength range to which human vision is sensitive, called the visible spectrum (VIS) (CIE, 1987). The VIS is a tiny part of the total EM between the long radio waves and the short X-rays/gamma rays. The former oscillate and propagate in an electric field, while the latter are energetic particles. Usually, the VIS refers to the wavelength range from approximately 400 nm to 700 nm (Buser & Imbert, 1992), as shown in Figure 2.3. However, this is only an approximate range for most people and does not represent the limit of human vision. Some definitions of the VIS are as narrow as 420 nm to

680 nm (Smith, 2006; Kumar, 2008) and as broad as 380 nm to 800 nm (Laufer, 1996; Bradt, 2004). Light is often described in terms of wavelength during colour perception; the reason is discussed in Section 2.2.3.6.1.

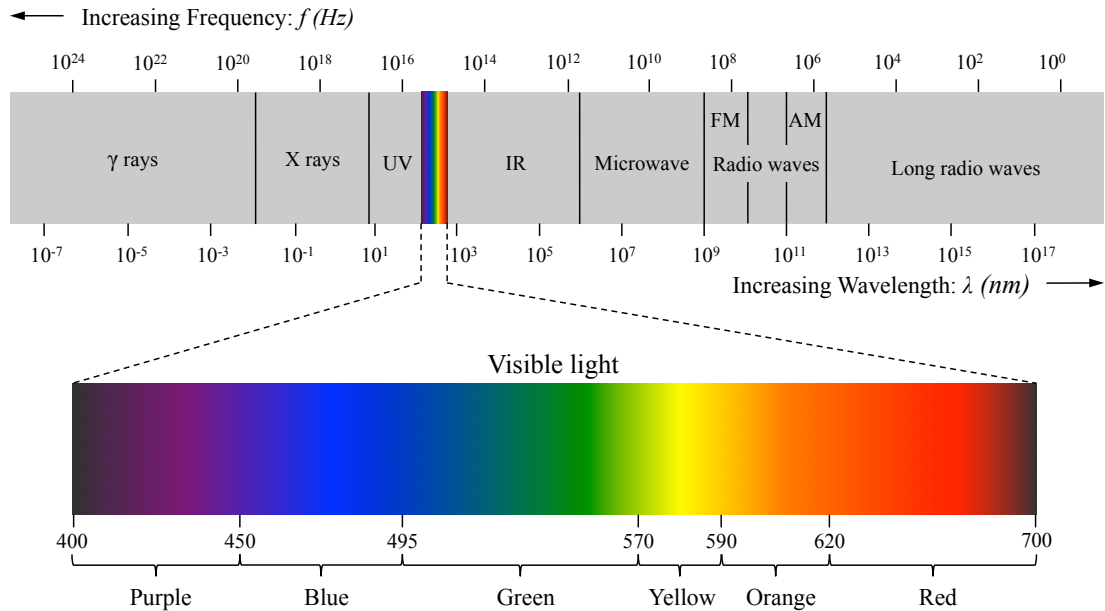


**Figure 2. 3: The electromagnetic spectrum (EM) and the visible spectrum (VIS).**

In other cases, it is convenient to represent light as a particle phenomenon: photons. When determining the sensitivity of a vision system to light, such as the minimum threshold of light detection, it is normal to refer to light in these terms. A photon is defined as the smallest quantity (quantum) of energy, and it is a massless particle that travels at the speed of light. However, not all photons have the same energy. For example, an ultraviolet light (UV) photon contains more energy than an infrared light (IR) photon.

According to Maxwell's (1865) theory, light is an EM wave that consists of two mutually perpendicular electric and magnetic fields. Since no medium is required for



it to travel in, the EM wave velocity is always equal to the speed of light ( $c$ ), which is a product of the wavelength ( $\lambda$ ) and frequency ( $f$ ):

$$c = \lambda f. \quad (2.1)$$

As mentioned before, light is also a discrete packet of photon energy. Hence, the relationship between the photon energy ( $E$ ) and the corresponding frequency is

$$\Delta E = hf, \quad (2.2)$$

where  $h$  is Planck's constant of  $6.6262 \times 10^{-34}$  joule/s, which is a constant numerical value for any wavelength within EM radiation. According to Eqs. 2.1 and 2.2, different portions (wavelengths) of the EM can serve as useful diagnostic tools to relate various atomic and molecular processes.

### **2.2.3.3 Absorption and emission**

When incident light passes through matter, the light absorption and emission phenomena occur. The natural absorption and emission of radiant energy is attributed to the mechanism of the electrons confined within atoms. In this case, the absorption and emission behaviours of light can be explained by a quantum model. Figure 2.4 demonstrates the phenomena with an atom model.

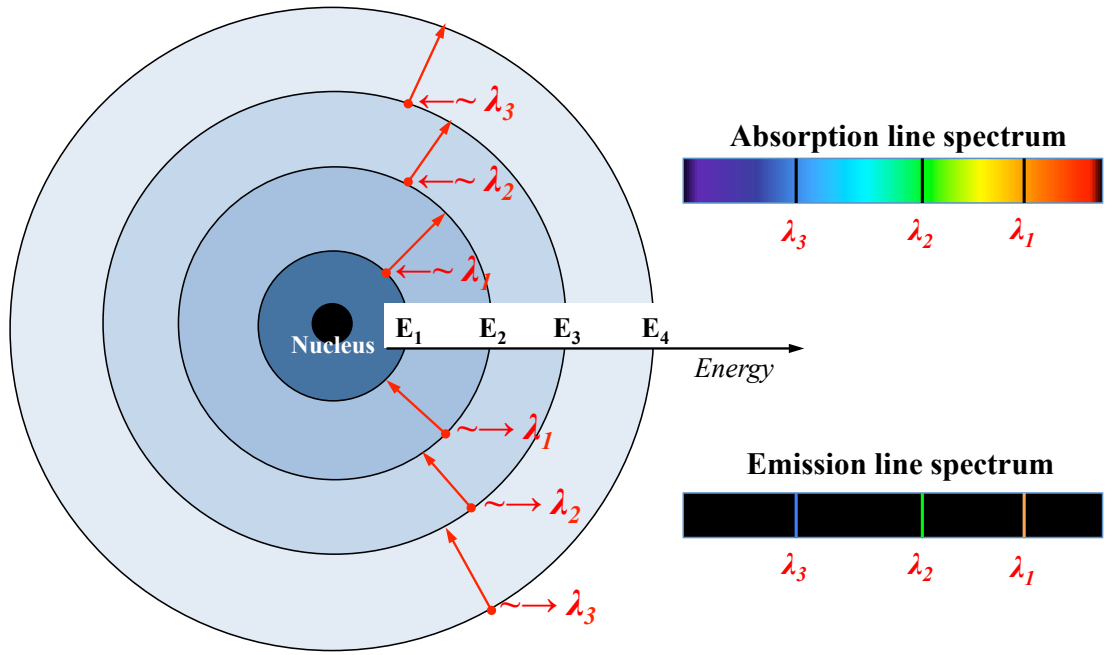


Figure 2. 4: Absorption and emission of line spectra.

The massive positive nucleus of an atom is located in the centre, with minute negative electrons surrounding it at specific energy levels. In a stable configuration, electrons stay at the lowest energy level of the atom, such as  $E_1$  in the model shown in Figure 2.4. This energy state is called the ground state. The atom's ground state could change if energy is pumped into the atom. Based on quantum mechanical theory, an atom can only exist as long as its electrons stay at certain energy levels. Outside the ground state, there are higher energy levels with specific well-defined energy, such as  $E_2$ ,  $E_3$ , and  $E_4$  shown in Figure 2.4. If the atom absorbs additional photon energy, the electrons could jump to other energy levels, which excites the atom. The amount of absorbed energy equals the energy gap between the two energy levels:

$$\Delta E = |E_i - E_f|, \quad (2.3)$$

where the subscripts  $i$  and  $f$  indicate the initial and final energy states, respectively. If the gap between the initial and final energy states is known, the wavelength of the absorbed photon at this particular energy gap can be obtained according to Eqs. 2.1 and 2.2. For instance, an electron jumping from  $E_1$  to  $E_2$  needs to absorb the photon at wavelength  $\lambda_1$ . If the absorbed energy is high enough, it will cause an electron to become unbound from the atom; this process is called ionization.

Usually, after about  $10^{-8}$  or  $10^{-9}$  s, the excited atom spontaneously relaxes back to a lower state; this is called de-excitation (Zajac, 1987). When the atom de-excites, the excess energy is emitted as a photon. For example, an electron decaying from  $E_4$  to  $E_3$  will emit a photon at wavelength  $\lambda_3$ . An electron jumping to a higher energy level or returning to a lower energy level needs to absorb or emit the particular energy of a photon related to a specific wavelength. A photon at the specific wavelength is referred to as the line spectra. Several absorption and emission lines could be associated with a particular atom or molecule; for example, the model atom in Figure 2.4 can absorb and emit photons at  $\lambda_1$ ,  $\lambda_2$ , and  $\lambda_3$ .

By combining Eqs. 2.1 and 2.2, the released photon energy can be quantified by

$$\Delta E = \frac{hc}{\lambda}. \quad (2.4)$$

Based on Eq. 2.4, the light emitted can be treated as an energetic wave. The light emissions at the end of violet towards the 400 nm wavelength have much more energy than those at the end of red towards 700 nm. Thus, more energy is needed for the production of UV emissions than what is required to thermally excite atoms to

emit photons in the IR. The photon energy of atomic emissions in the VIS is between  $1.8\text{ eV}$  and  $3.0\text{ eV}$ . In dense gases, liquids, and solids, absorption could occur over a range or band of wavelengths.

#### **2.2.3.4 Human vision perception of light**

The white light from the sun is a combination of the radiation of all VIS spectra. Newton observed that the white light could be separated into ‘rainbow’ colours through a prism. However, the colour is not a natural property of light but a perception of human vision.

There are two groups of light receptor cells in the human retina, called rods and cones. Colour perception is attributed to the presence of the cone cells. According to the Young-Helmholtz theory (Young, 1802; Svaetichin, Negishi, & Fatehchand, 1965), there are three types of cones, and different types of cones are sensitive to different wavelength ranges. Based on these different spectral sensitivities, cones are sub-categorised as short, medium, and long wavelength cones, sometimes referred to as blue (B), green (G), and red (R) pigment cones (Guild, 1931; Wright, 1928). As shown in Figure 2.5, the peaks of the bell-shaped spectral sensitivity responses of B, G, and R cones are at 437 nm, 533 nm, and 564 nm, respectively (Dowling, 1987).

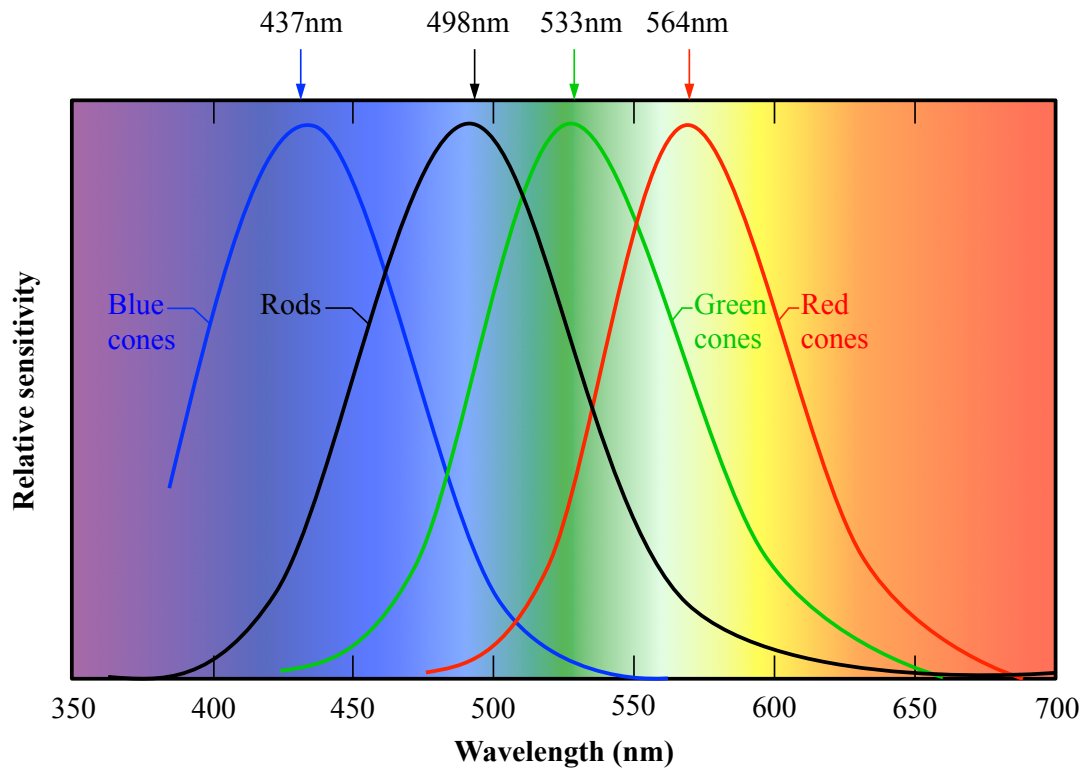


Figure 2. 5: Normalized spectral sensitivity of retinal rod and cone cells of the human eyes

[adapted from (Dowling, 1987)].

In contrast, rods are in charge of gathering light intensity. They are primarily used in low-light conditions with a spectral sensitivity peak at about 498 nm. In a largely black and white context, they are often inactive in sufficiently lit conditions.

To discriminate between colours, one must have two or more different types of cones (Tovee, 2008) because the changes in wavelengths cannot be discriminated by a single cone pigment. For example, a blue cone responds strongly to a 430 nm light but weakly to a 560 nm light. However, a single cone class can signal the number of photons absorbed by its pigment.

### **2.2.3.5 Summary of light**

The light described in this thesis refers to the VIS spectrum portion of EM radiation. Light is a wave that contains wavelengths and frequencies. Different light wavelengths are represented as colours in human vision perception. Thus, different flame colours can be utilised to detect emission wavelengths. Light is also photons that contain energy. According to the quantum mechanics, photon energy is emitted at a certain wavelength by specific species. This information could further relate flame colours to specific chemical radicals.

## **2.2.4 Cameras**

### **2.2.4.1 Introduction**

There are many types of light detectors that can measure different proportions of EM radiation. Since the topic of this thesis is focused on visible light, only the direct camera imaging is reviewed here. First, the properties of a camera's photosensitive sensor, its exposure, and image noise are introduced. Then, three types of imaging methods, colour imaging, high-speed imaging, and stereo imaging, are reviewed.

### **2.2.4.2 Properties**

#### **2.2.4.2.1 Photosensitive sensor**

The photosensitive sensor is the key component that contributed to the camera's evolution. Nowadays, two types of photosensitive sensors are used in modern cameras, photo-emission-based sensors and photovoltaic-based sensors. The former

is based on the photoelectric effect of ionisation. The latter is widely used in the development of semiconductors. The energy carried by a photon could cause an electron to leave its valence band and change to a conduction band. The amount of incident photons affects macroscopic conductivity. Excited electrons, referring to a type of electric voltage, manifest as an electric current, which depends on the amount of incident photons (Sawicki, 2007).

The charge-coupled device (CCD) and complementary metal oxide semiconductor (CMOS) are two types of widely used semiconductor photosensitive sensors. They were both invented in the 1960s; CCD became mature in the 1970s, while CMOS became popular twenty years later. The CCD and CMOS both have a 2D array of solar cells, and their capturing media are similar. The media are pixelated metal oxide semiconductors made from silicone. Therefore, their spectral sensitivities in the VIS and NIR (near-infrared) range are highly similar.

The difference between these two techniques is the means of digital signal transfer. Comparison configurations are shown in Figure 2.6. For a CCD sensor, the charge of a pixel is transported to the next pixel in the same array. The output is an analogue signal at the end of that array. The analogue signal is converted into voltage first. Then, it is amplified and digitised off the chip. Since only the photon-to-electron process is performed in CCD itself, each pixel in CCD is devoted to light capture.

In contrast, in CMOS, each pixel is processed by both photon-to-electron and electron-to-voltage conversions within the chip. The CMOS sensor often includes

amplifiers and digitisation circuits so that its output is in digital format. Although the inclusion of individual transistors leaves less room for light acquisition, this design opened a door to the ‘smart camera’, in which imaging and image processing can be performed on the same chip (Sonka, Hlavac, & Boyle, 2015).

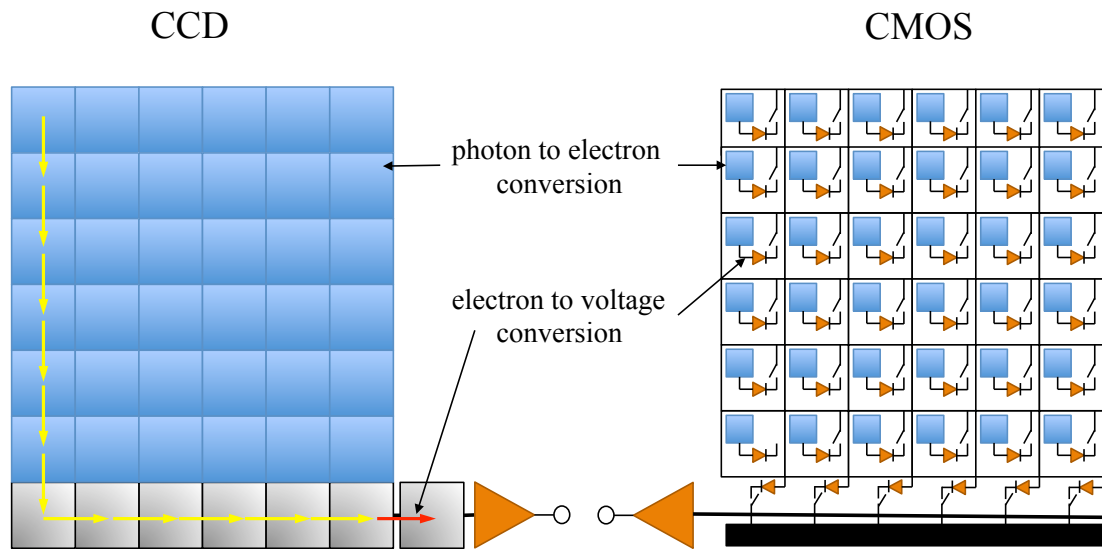


Figure 2.6: The CCD and CMOS configurations.

#### 2.2.4.2.2 Camera noise

The sensor within a camera determines the majority of the noise generation in an image while converting photons to digital signals. In the final obtained image, there are three types of noise: photon shot noise (PSN), dark shot noise (DSN), and readout noise (RN) (Payri, Pastor, Garca, & Pastor, 2007).

PSN and DSN are attributed to the discrete nature of photons and electrons (Seitz, 1997). PSN exists when photoelectrons are created, which affects the statistics of the actual photons. While DSN occurs when dark current electrons are generated, it usually appears in the region of the image without actual photons, creating noise in



black background areas. For a well-designed camera sensor, the amount of DSN is very low, and it is easy to reduce by calculating the root mean square (RMS) of the DSN so that each pixel subtracts the mean noise intensity. When the charge is read, the reset noise and amplifier noise are added. When the signals are transformed into digital signals, the quantisation noise may be considered. The RN is a combination of the reset noise, amplifier noise, and quantisation noise (Demler, 1991). It can exist at each pixel location.

#### 2.2.4.2.3 Signal-to-noise ratio

In a camera, the signal-to-noise ratio (SNR) refers to the level of a desired intensity in relation to the level of background noise. The SNR is often used to evaluate an imaging system or image quality. Table 2.1 shows the SNR levels with their corresponding image quality.

**Table 2. 1: Guidelines for interpreting the SNR in terms of the subjective image quality**

(Constant, 2009)

| SNR (dB) | SNR: 1 | Image quality  |
|----------|--------|--|
| 60       | 1,000  | Excellent: no noise apparent.  |
| 50       | 316    | Good: a small amount of noise but good image quality.                |
| 40       | 100    | Reasonable: fine grain or snow in the image, some fine details lost. |
| 30       | 32     | Poor image with a great deal of noise.                               |
| 20       | 10     | Unusable image.  |

One way of measuring the SNR is to employ an oscilloscope: SNR is mathematically defined by

$$SNR = 20(\log \frac{Signal}{Noise}). \quad (2.5)$$

The measured signal and noise are based on their RMS values. This RMS noise contains the shot-noise, which is relative to the light intensity falling on the camera sensor. In addition, optical filters are needed to reject frequencies that are too high or too low. This evaluation method requires additional devices and involves a complex calibration process, including changing optical settings, camera orientations, and examination time. This method employs filters to evaluate noise in one layer, but the sensor in a colour camera generates signals and noise in three layers. This difference in evaluation will cause deviation between the tested and actual performance.

Another method can evaluate the SNR without exposing the camera to light to obtain the black-level signal distribution in absolutely dark conditions. This method is known as dark framing. It calculates the combination of DSN and RN, without PSN. It is assumed that modern camera sensors are well calibrated for optimum performance in the VIS spectrum, so the PSN does not affect noise generation significantly. The mathematical definition of this method is

$$SNR = 20(\log \frac{I_{SAT}}{Dev_N}), \quad (2.6)$$

where  $I_{SAT}$  is the intensity amount of an image, typically equalling 255 and 65,535 for 8-bit and 16-bit images, respectively, and  $Dev_N$  is the standard deviation of the image background noise.

### **2.2.4.3 Colour imaging**

In the past, the conventional colour imaging method employed different wavelength range filters placed in front of a monochromatic camera. The different recorded monochromatic images were then combined to create a colour image. The advantage of this method is that the recorded image can provide the light intensity at a specific wavelength range and even at a certain narrow wavelength. This method has been applied in combustion diagnostics to measure flame radical emission concentration (Nori & Seitzman, 2007; 2008). In this method, the camera and the measured object should be relatively static during the measurement. Therefore, it is not suitable for measuring a fast moving object.

Therefore, another method was introduced by Bayer (1976) that used a colour filter array (CFA) on the photosensitive sensors. A schematic of a CFA is shown in Figure 2.7. Each sensor pixel is covered with an individual colour (wavelength range) filter that can be implemented either on a cover glass on the chip package or directly on the silicon and captures only one colour (Sawicki, 2007). With this CFA arrangement, the result patterns are shown in R, G, and B colour channels. In a colour camera, a filtered colour pixel in the sensor is a sub-pixel for a real image pixel. In Bayer's CFA, each real image pixel is a combination of four sub-pixel colours, one red, one blue, and two green. The number of green sub-pixels is two times to those of the red and the blue sub-pixels because the peak of human vision spectral sensitivity in the VIS is in the green wavelength range.

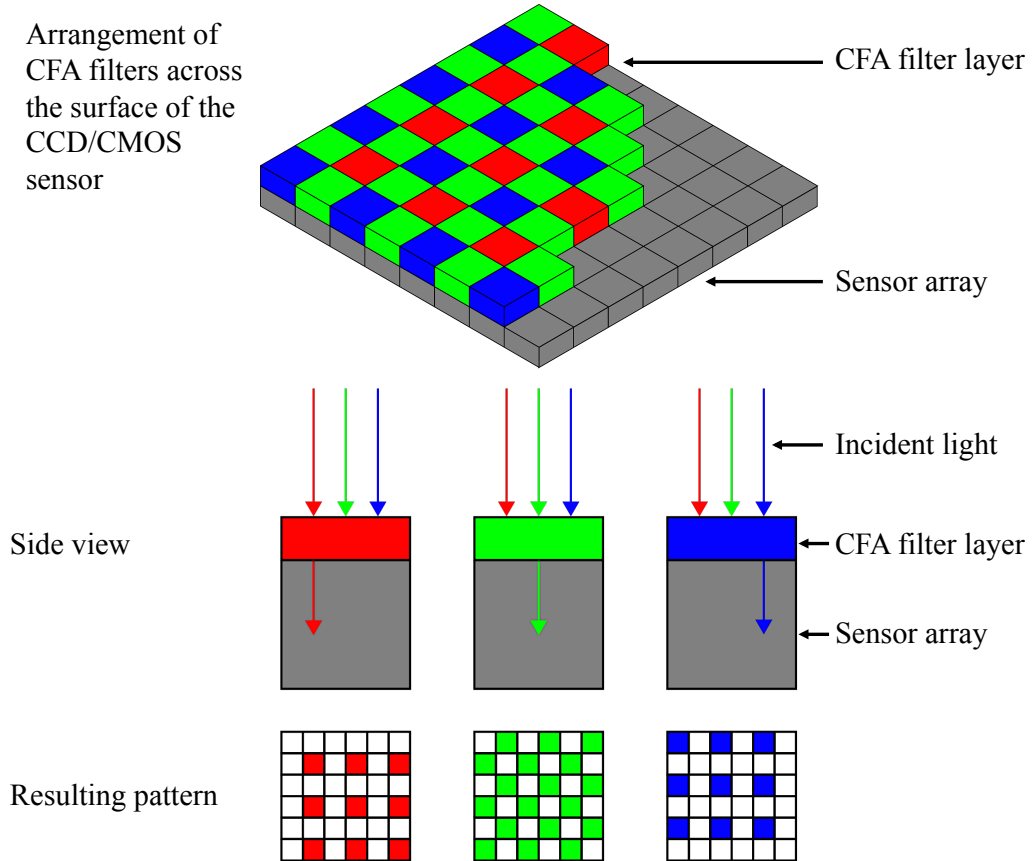


Figure 2.7: Bayer's CFA pixel filter arrangement.

In combustion diagnostics, colour imaging was applied in distinguishing diffusion yellow flame and premixed blue flame (Huang & Zhang, 2008); the image red and green intensities have been used to detect flame temperature of sooty flame (Hossain, Lu, Sun, & Yan, 2013; Ma & Zhang, 2014); the image blue and green intensities have been used to measured the related fuel/air ratio in a premixed flame (Huang, Yang, Wang, & Zhang, 2013; Yang, Mossa, Huang, Wang, Woolley, & Zhang, 2015). As the author's knowledge, the colour imaging was not applied for vibration diagnostics so far (at least the colour information was not used). However, the colour

information must be useful in both combustion and vibration diagnostics, due to it can offer additional light information such as light wavelengths.

#### **2.2.4.3.1 CIE colour model**

In designing a colour imaging system and colour encoding, it is necessary to identify colours with standardisation. The most important colour model is the CIE (Commission Internationale de l'Eclairage – the International Commission on Illumination) chromaticity coordinate system. In essence, this was the first mathematical standardisation connecting colour vision physics with arbitrary colorimetric reproduction (Smith & Guild, 1931). In accordance with the colour perception mechanism of human vision, the CIE model employs the three monochromatic primary colour wavelengths to build a model known as the XYZ colour space. In this model, the values of the three primary colour wavelengths are called tri-stimulus values, which can describe a particular colour.

Although the tri-stimulus values can be assigned to any arbitrary wavelength within the VIS spectrum, the standard values given by the CIE model are  $X = 700.0$  nm,  $Y = 546.1$  nm, and  $Z = 435.8$  nm (Smith & Guild, 1931). These values depend on the average human vision sensitivity peaks in the VIS corresponding to the various primary colours. In particular, the XYZ values are presented as tri-stimulus ratios, known as chromaticity coordinates:

$$x = \frac{X}{X+Y+Z} \quad , \quad (2.7)$$

$$y = \frac{Y}{X+Y+Z} \quad , \quad (2.8)$$

$$z = \frac{Z}{X+Y+Z} \quad . \quad (2.9)$$

The summation of the three tri-stimulus ratios is equal to one:

$$x + y + z = 1. \quad (2.10)$$

Therefore, only two chromaticity values are needed. Based on this, the most common CIE chromaticity diagram is composed using the x and y coordinates, as shown in Figure 2.8.

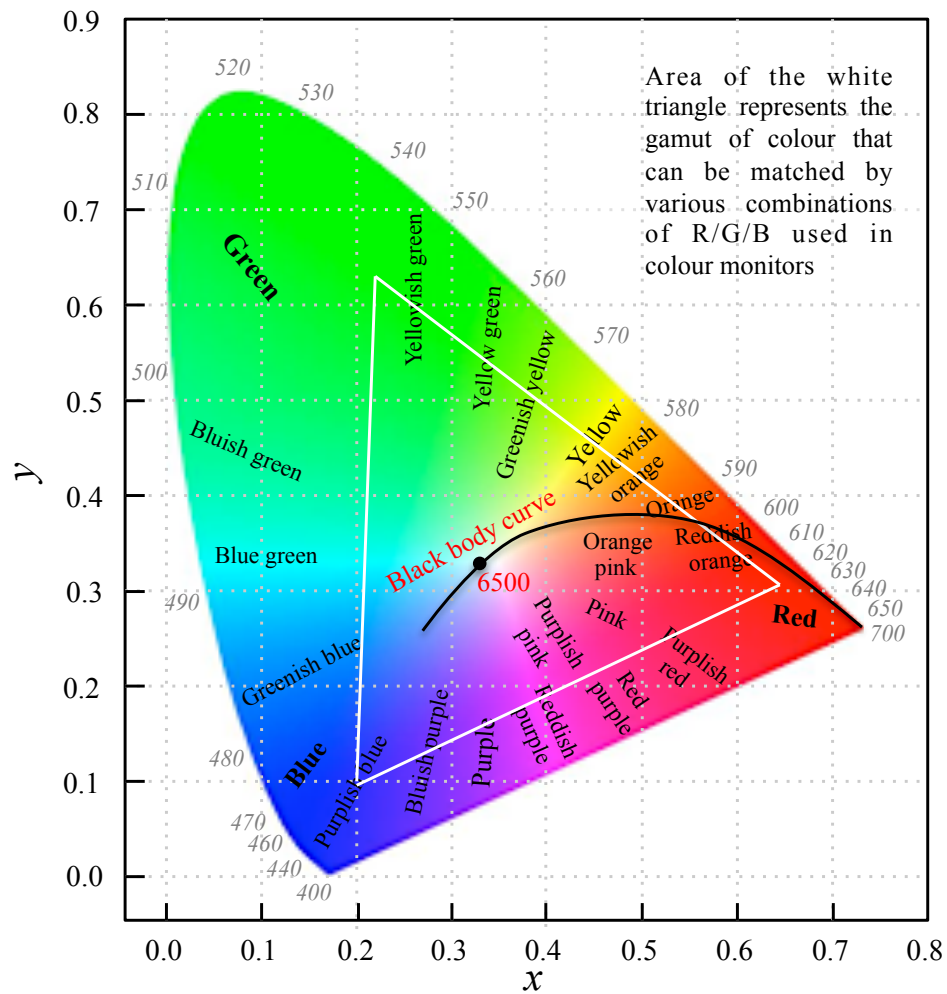


Figure 2. 8: 1931 CIE chromaticity chart [redrawn from (Smith & Guild, 1931)].

This horseshoe-like shape model can denote all the colours for human visual perception. The boundary of the model indicates the VIS spectrum, and their wavelengths are shown on the curve. The white triangular shape within the colour gamut denotes the limitation of reproducible colours from the selected RGB wavelengths. Therefore, any colour within this triangle can be replicated by filtered RGB radiation intensities. Depending on the different applications, this triangle is defined differently. Several colour models are employed for different applications. In theory, these models can all be converted into the others without losing any information. Two common colour spaces, the RGB model and HSV (hue, saturation, and value) model, are introduced in the following sections. The black curve from red to white is called the black body curve, which connects particular colours with their corresponding temperatures; details are discussed in Section 2.3.3.

### **2.2.4.3.2 RGB colour model**

The RGB colour model is a relative colour standard, and it is often used for colour display, such as the colour displayed in cameras and on computers. The RGB colour model can be presented in a 3D space; see Figure 2.9. In this model, the choice of primary colours is based on the Young-Helmholtz theory (Young, 1802; Svaetichin, Negishi, & Fatehchand, 1965). The primary colours are red, green, and blue along the x, y, and z axes of a 3D coordinate system. The secondary colours are combinations of two pure primary colours. For example, yellow is red combined with green, cyan is green combined with blue, and magenta is red combined with

blue. All colours can be described by combinations of the three primary colours. Therefore, a particular colour of the captured visible radiation is specified by the coordinate of

$$Colour = [I_R, I_G, I_B], \quad (2.11)$$

where  $I$  indicates the intensity of each primary colour.

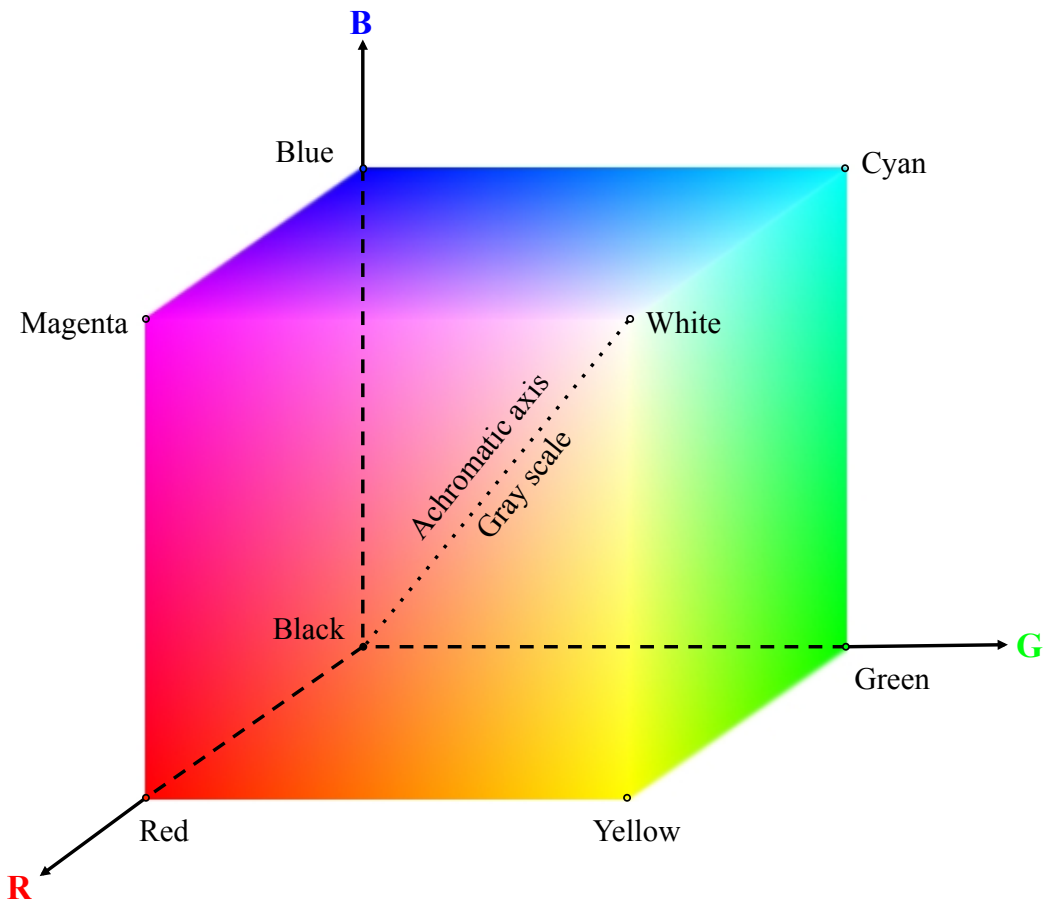


Figure 2. 9: 3D representation of the RGB colour model.

The intensity is used to describe a colour from darkness to brightness. The level of intensity, named grey scale, is defined as the achromatic axis of the RGB model from black towards white. Three primary values of a particular colour along the grey scale axis are always the same. Outside this axis, different coordinates within the RGB



model indicate a multitude of colours. A colour's saturation depends on the difference between the minimum and maximum contribution of the primary colours. In terms of perception, when one primary colour value has a maximum, the displayed colour will be closer to that primary colour. If two primary colour values are at their peak intensities, the resultant colour will be a shade of the secondary colour.

### **2.2.4.3.3 HSV colour model**

Colour is easy to link with the physical property of light (i.e., spectral wavelengths) in the CIE model and display in the RGB model. However, it is not easy to describe colour with either model. A more convenient model for thinking about colour is called the HSV model (Simth, 1978). This model is derived from the RGB model by looking down the grey scale axis from white to black. In Figure 2.10, the HSV model is specified in a cone coordinate system.

In the HSV model, colours are defined by hue, saturation, and value (synonymous with colour, brightness, and intensity, respectively). Within the conical plane, the hue is measured by the angular coordinate. For instance, green is at  $120^\circ$  and blue is at  $240^\circ$ . The saturation is measured as the radial distance from the achromatic axis. The value is given as the depth along the achromatic line. Therefore, in the HSV model, colours can be easily denoted by degrees from  $0^\circ$  to  $360^\circ$ . Because the colour is presented in a circle, the red colour both begins and ends in the hue circle. This means that the red covers roughly both  $0^\circ$  to  $30^\circ$  and  $330^\circ$  to  $360^\circ$ .

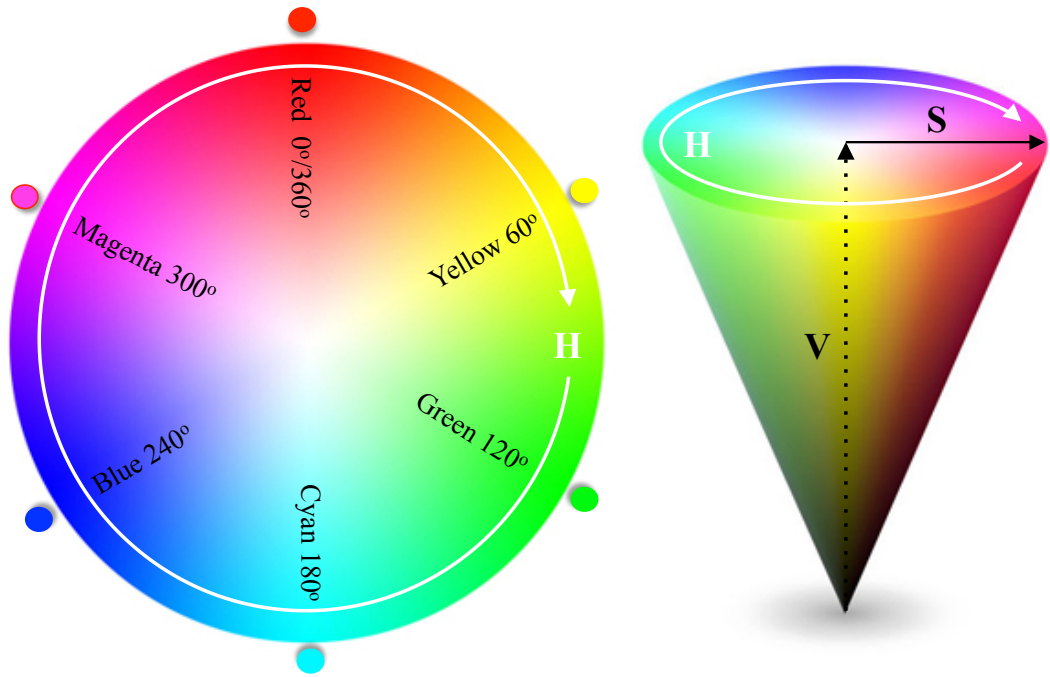


Figure 2. 10: The HSV model.

Based on above principle, the hue is related to the absolute colour. It can be considered the approximate psychosensorial equivalent to the dominant wavelength (Gonzalez & Woods, 2002). Smith (1978) presented the standard transformation algorithms to convert the RGB model into the HSV model:

$$H' = \begin{cases} \frac{G-B}{Max-Min} & \text{if } R = Max \\ 2 + \frac{B-R}{Max-Min} & \text{if } G = Max, \\ 4 + \frac{R-G}{Max-Min} & \text{if } B = Max \end{cases} \quad (2.12)$$

$$H' = \frac{H'}{6} \times 360, \quad (2.13)$$

$$H = \begin{cases} H' & \text{if } H' > 0 \\ H' + 360 & \text{if } H' < 0 \end{cases} \quad (2.14)$$

$$S = \begin{cases} 0 & \text{if } Max = 0 \\ 1 - \frac{Min(R,G,B)}{Max(R,G,B)} & \text{Otherwise} \end{cases} \quad (2.15)$$

$$V = \text{Max}(R, G, B). \quad (2.16)$$

#### **2.2.4.4 High-speed imaging**

A high-speed camera is designed to capture fast motion. In addition, it can record the motion dynamics in an image sequence. Therefore, this device can not only freeze a movement that is too fast for human vision but also show the dynamic details of the motion.

In 1851, William Henry Fox Talbot performed the first attempt at high-speed imaging (Arnold, 1977). He photographed a fast-rotating wheel with a camera shutter speed of 1/2000 s. A newspaper was attached to the wheel, and the captured picture showed a readable part of the newspaper. In 1886, Austrian physicist Peter Salcher used a high-speed imaging technique to take the first photograph of a supersonic flying bullet (Endelman, 1988). These experiments only used high-speed imaging to capture non-blurry images with a short exposure time.

In the 1870s, Edward Muybridge applied high-speed imaging in investigations of animal locomotion (Newhall, 1949). His most famous study depicts a galloping horse, shown in Figure 2.11. He employed a sequence of still cameras to photograph the horse as it ran. The aim was to see whether all the horse's feet left the ground while it was galloping. This was the first time that a high-speed imaging technique was employed to capture image sequences to explore complex dynamics.

The above experiments all relied on film-based cameras. Although a film-based camera can capture images at relatively high frame rates, its operation is too

complex. With the development of CCD and CMOS, images can now be captured by digital cameras at very high frame rates, and the results can be seen immediately. The ability to measure at high frame rates is more important than a short exposure time. The ability to use a short exposure time is essential for capturing an image of fast motion, only high frame rates can enable us to understand phenomena with complex dynamics, such as combustion (Sick, 2012).

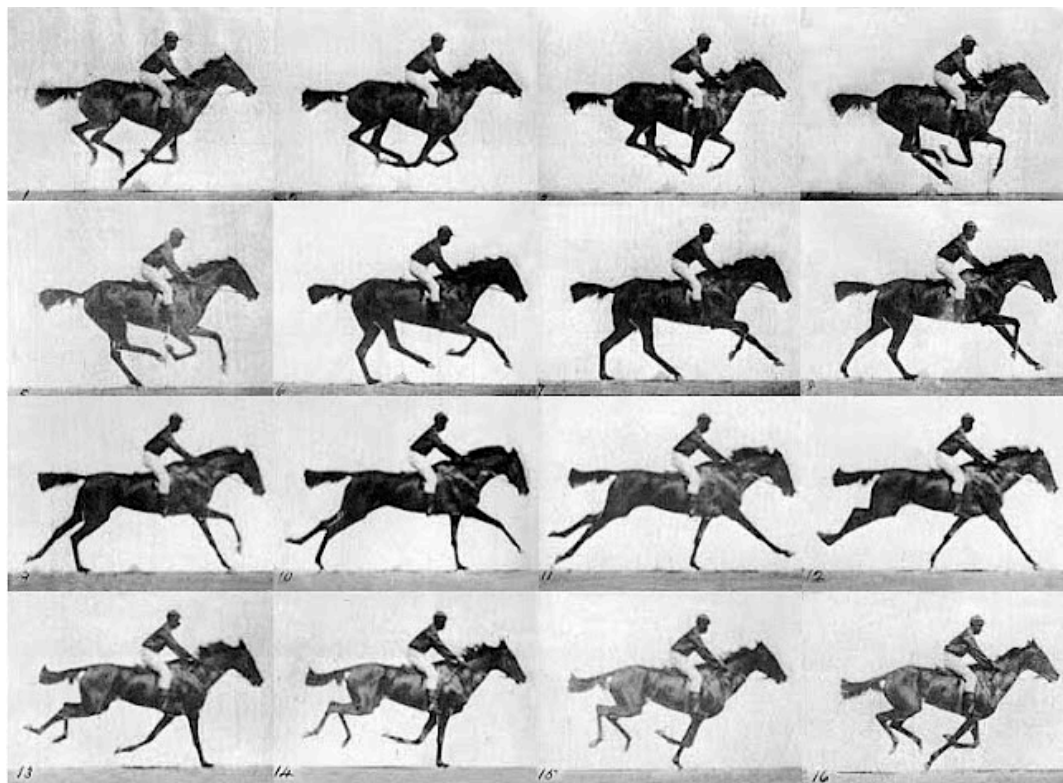


**Figure 2. 11: Images of a galloping horse by Edward Muybridge (Newhall, 1949).**

The development of high-speed imaging is continuing to lead to cameras with higher frame rates, better pixel resolution, and bigger storage capacities, which gives scientists greater insights and usability for research (McDaid, 2013). Recently, the MIT Media Lab developed a high-speed imaging system that can capture an image

within a picosecond or move with a frame rate of  $5 \times 10^{11}$  frames per second (fps) (Velten, Raskar, & Bawendi, 2011). In this way, high-speed imaging can even visualise photons in motion.

#### **2.2.4.5 Stereo imaging**

The stereo imaging technique was invented by Charles Wheatstone in 1838 for entertainment applications (Wheatstone, 1838). At that time, 3D perception could be generated only in the mind by viewing the two images directly. After the 1960s, with the development of digital cameras and digital image processing techniques, the object's depth information could be obtained by processing the two images in a computer. After that, the stereo imaging techniques, as an advanced 3D measurement tool, became increasingly important in scientific research and industrial applications.

##### **2.2.4.5.1 Stereo imaging principles**

Digital stereo imaging is an extension of the conventional 2D digital imaging. The aim is to obtain depth information from 2D images. The basic principle of stereo imaging is the use of two slightly different views of 2D images of the same measured object to capture depth information. Figure 2.12 shows the optical geometry between a real butterfly and its two 2D images.

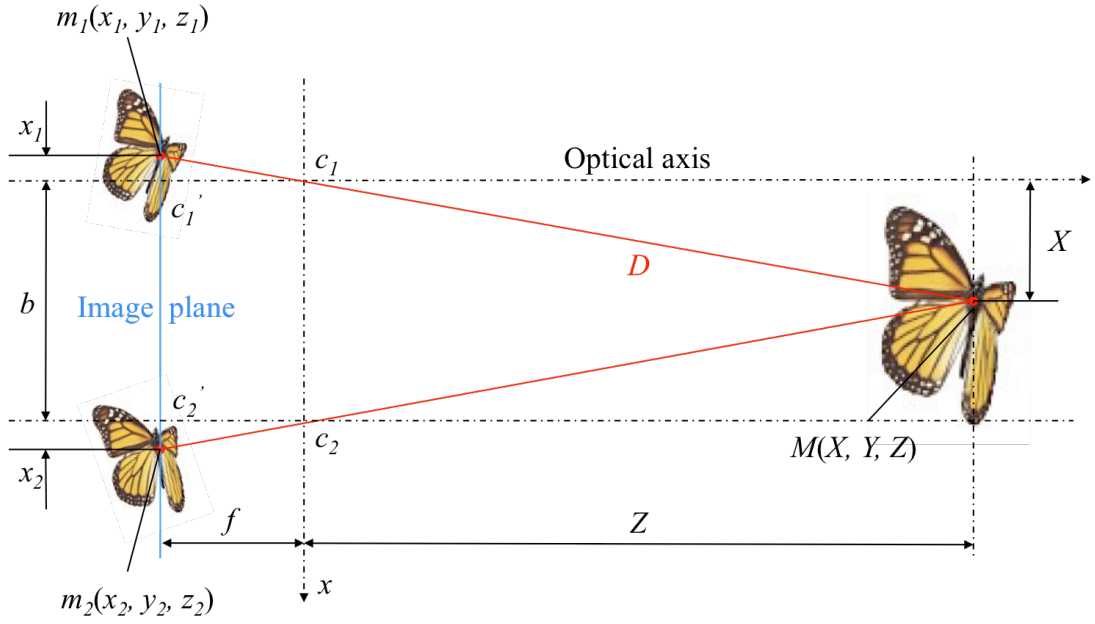


**Figure 2.12: Optical geometry between a real object and its corresponding two images.**

Two parallel optical axes represent the optical paths of the two images. The focus length of the two cameras is  $f$ ;  $b$  denotes the distance between these two optical axes. The two optical centres are represented by  $c_1'$  and  $c_2'$ , respectively, and their corresponding principle points are indicated by  $c_1$  and  $c_2$ . Point  $M$  in the 3D world is denoted by  $M(X, Y, Z)$ , and its corresponding points on the two image views are  $m_1(x_1, y_1, z_1)$  and  $m_2(x_2, y_2, z_2)$ . Based on the principle of the similar triangles, we have

$$x_1 = -X \frac{f}{Z}, \quad (2.17)$$

$$x_2 = (b - X) \frac{f}{Z}, \quad (2.18)$$

$$y_1 = y_2 = Y \frac{f}{Z}. \quad (2.19)$$

Combining Eqs. 2.17 and 2.18, we get

$$Z = \frac{bf}{x_2 - x_1}, \quad (2.20)$$

where  $(x_2 - x_1)$  is called the disparity. When  $b$  and  $f$  are fixed,  $Z$  is inversely proportional to the disparity.  $D$  (the distance from the origin  $c_l$  to point  $M$ ) is then given by

$$D = \frac{b\sqrt{f^2 + x^2 + y^2}}{x_2 - x_1}. \quad (2.21)$$

This is called the true range equation, and it can be worked out by matching corresponding points in both views (Li, Lu & Yan, 2014).

#### **2.2.4.5.2 Intrinsic and extrinsic parameters**

Figure 2.13 demonstrates the relations between an object in the 3D world and its corresponding image on a computer. There are four coordinate systems in the relationships: the world coordinate system  $(X, Y, Z)$ , camera coordinate system  $(x, y, z)$ , image coordinate system  $(x', y')$ , and computer coordinate system  $(u, v)$ . The model in Figure 2.13 can describe the relationships among these coordinate systems. The object, camera, and image can be composed using a pinhole model. In this model, the camera is reduced to a point,  $c$ . For convenience, the image plane is placed in front of the camera.

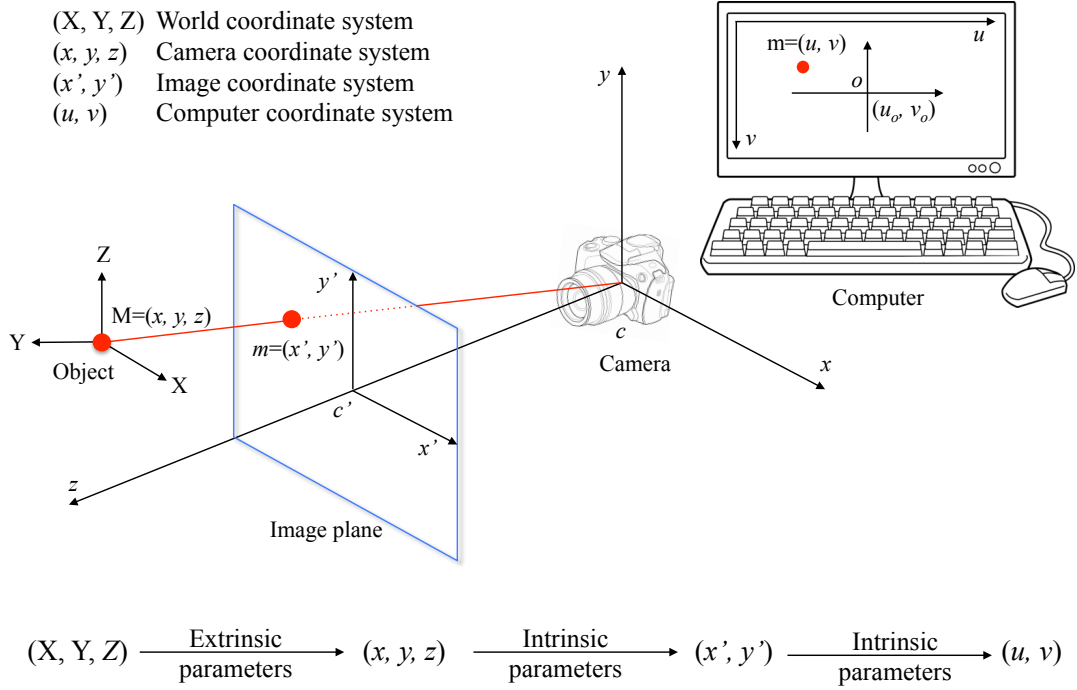


**Figure 2. 13: Relations among the world coordinate system, camera coordinate system, image coordinate system, and computer coordinate system.**

The camera coordinate system is rotated and translated from the world coordinate system; its relation can be described by the extrinsic parameters, which include the rotational parameter  $R$  and translation parameter  $t$ . The transfer from the camera coordinate system to the computer coordinate system can be described by the intrinsic parameters, which consist of the principal point  $(u_0, v_0)$  for the computer coordinate,  $\alpha$  and  $\beta$  for the scale factor of  $u$  and  $v$ , respectively, and the skew parameter  $\gamma$  of two image (the physical image and the computer image) axes. Therefore, the mathematical expression for the 3D world point  $M$  and its 2D image projection point  $m$  in a computer is

$$sm = A[R, t]M, \text{ with } A = \begin{bmatrix} \alpha & \gamma & u_o \\ 0 & \beta & v_o \\ 0 & 0 & 1 \end{bmatrix}, \quad (2.22)$$



where  $s$  is an arbitrary scale factor. To obtain these parameters, the camera calibration is needed (the calibration process is described in Section 3.3.4).

### **2.2.4.5.3 Stereo cameras**

In the 1950s, David Brewster was the first to create a real stereo camera with two lenses. Then Barnard built a stereo camera with a multi-mirror system in front of a single lens. Since then, different styles of stereo cameras have been invented and various stereo adapters for single-lens cameras have been built. Nowadays, stereo camera systems can be divided into two groups, two-camera and single-camera systems.

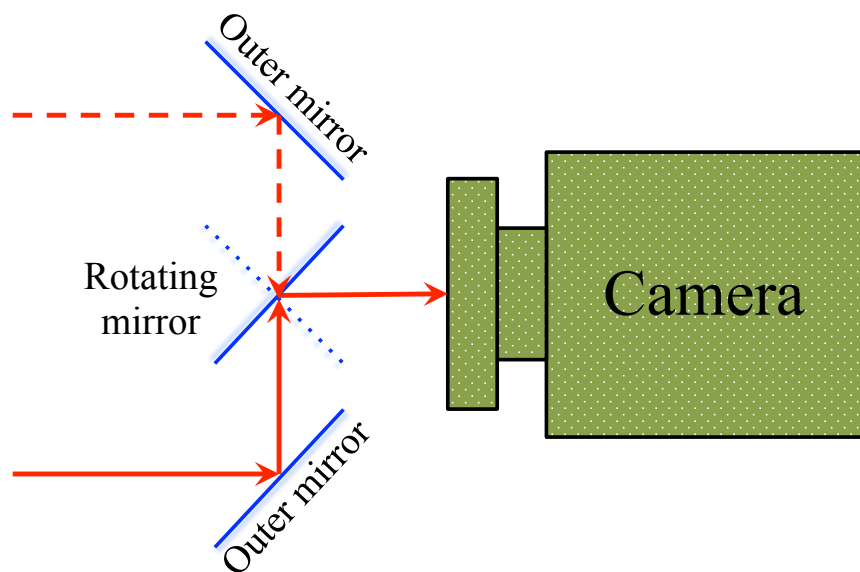
#### ***2.2.4.5.3.1 Two-camera systems***

To capture two images with different views of the same object simultaneously, the conventional method employs two cameras. The advantage of the two-camera system is that it has better spatial resolution and a larger common FOV (field of view) than a single-camera system. However, because of the discrepancy between the two cameras employed, the characteristics of the cameras (i.e., zoom level, focal length, and exposure time) may not be exactly the same. These discrepancies will increase the difficulty of image processing, such as ensuring corresponding features, which would increase error in 3D reconstruction (Lee & Kweon, 2000). Furthermore, employing an extra camera costs more money, and synchronisation between cameras is also a complicated job. Regarding the synchronisation mechanism among cameras, one camera is as the master, which sends a signal to control the others. In this case, a signal

time delay would also affect the reconstruction accuracy, especially in measuring a fast motion (Wang, 2009).

#### 2.2.4.5.3.2 *Single-camera systems*

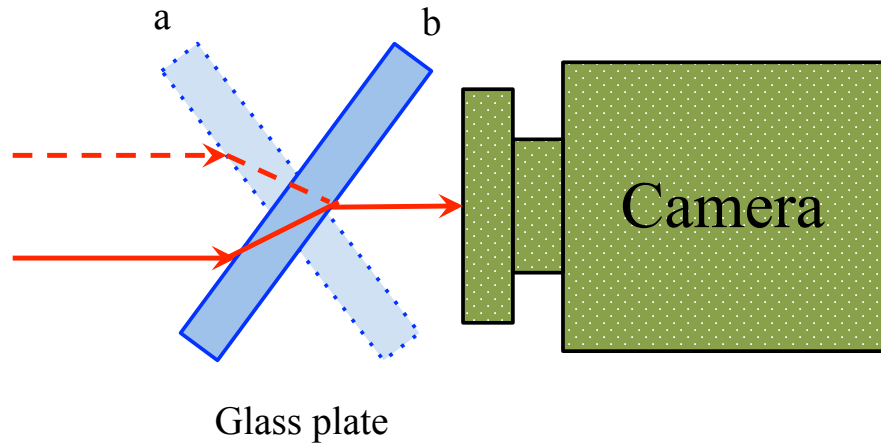
To avoid the weakness of two-camera systems, researchers have designed various adapters for a single camera to capture two views simultaneously. In 1984, Teoh and Zhang (1984) proposed an adapter structure with three pieces of mirrors (see Figure 2.14). Two mirrors are fixed outside and placed at  $45^\circ$  angles to the camera's optical axis. The third one is placed in the middle and can be rotated. Because the third mirror can be rotated in different directions, this imaging system can capture different views of the measured object.



**Figure 2. 14: A single camera stereo imaging system with two outer fixed mirrors and a rotating mirror.**

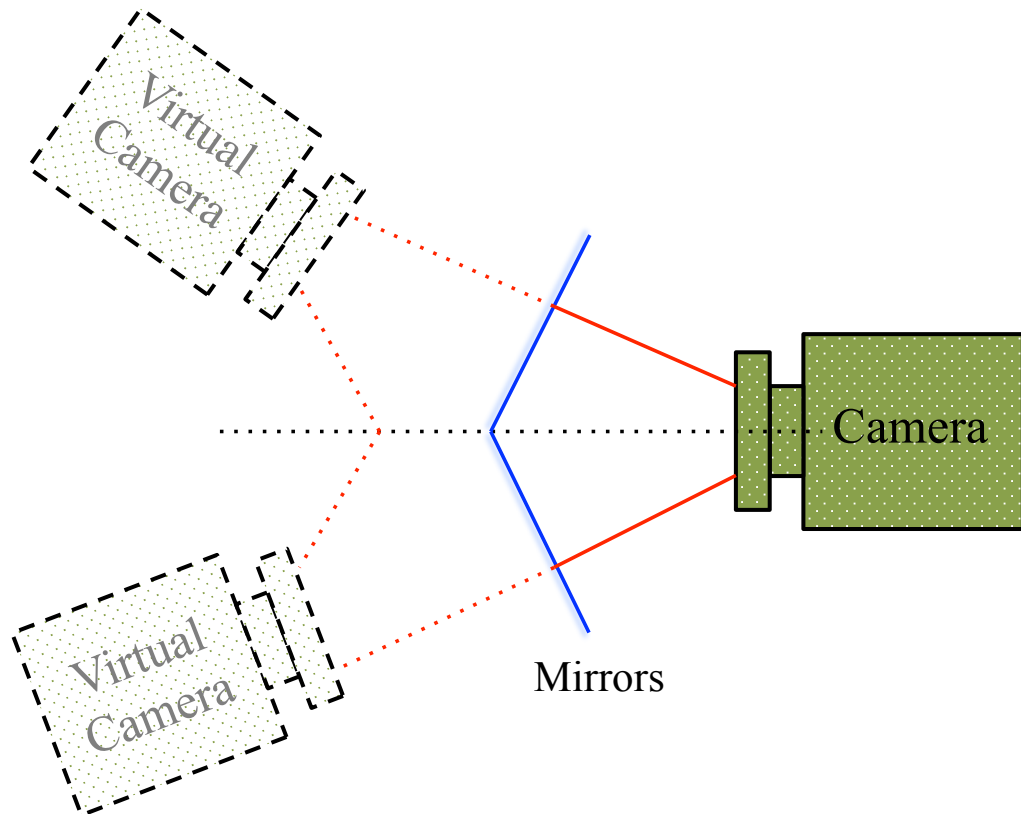
Nishimoto and Shirai (1987) proposed another configuration adapter with a single glass plate (see Figure 2.15). Because the incident rays passing through the glass

plate will change paths, rotating the glass plate can capture different views of the measured object. However, these two systems cannot capture images simultaneously. They are only suitable for measuring still objects.



**Figure 2.15: A single camera stereo imaging system with a glass plate.**

In some conditions, the measured object is in motion. For this purpose, Gosthasby and Gruver (1993) presented a new structure to measure object without changing settings, as shown in Figure 2.16. Two symmetrical mirrors are placed in front of the camera. In this way, two virtual cameras are formed in a rotational displacement. Hence, the camera can capture two views of the measured object at the same time. However, aligning the mirrors with the camera is complicated. In addition, handling and relocating the whole system during measurement to keep all parts in the same position is a difficult job.



**Figure 2. 16: A stereo imaging system proposed by Gosthasby and Gruver.**

Nowadays, a mature four-mirror configuration designed by Inaba et al. (1993) is widely used for stereo applications. The structure of the adapter is shown in Figure 2.17. In contrast to the systems described above, this design can capture two different views simultaneously, and it is flexible for implementation in practical experiments. An investigation of this adapter can be found in the work of Wang (Wang, Li, & Zhang, 2008).

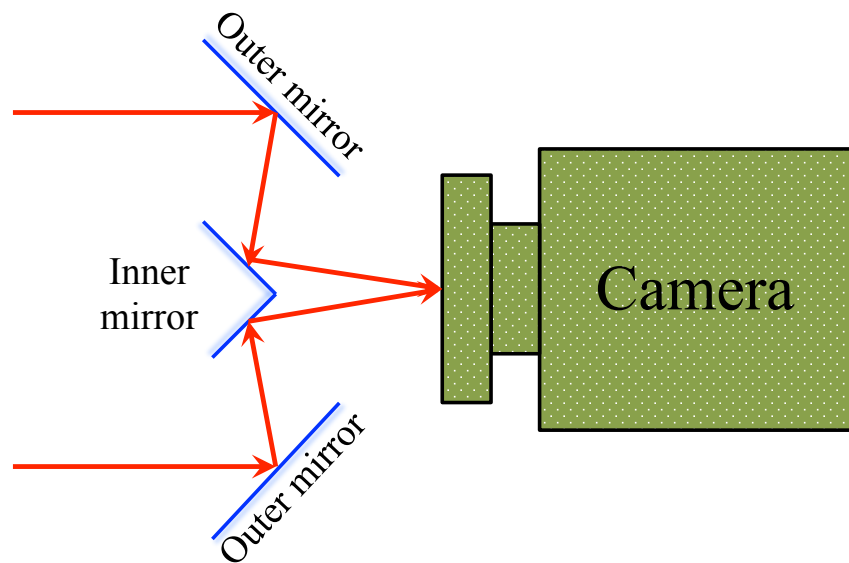


**Figure 2. 17: Signal camera with a four-mirror stereo adapter imaging system.**

Based on above stereo systems, the obtained stereo images and their reconstruction can only explore the missed depth information from the common view of the image pairs. Thus, the reconstruction is not in a real 3D but a 2.5D. In order to obtain the whole 3D reconstruction, more cameras need to be employed or a more complex stereo system should be designed to capture all views of the measured object.

#### **2.2.4.6 Summary of cameras**

Digital cameras are widely used in research today as light detectors. The CCD/CMOS are the most common photon-to-voltage converters employed in modern cameras. In cameras, light information is converted into a 2D matrix as an image. The quality of the sensors primarily determines the image noise level, which is usually evaluated by SNR. Various imaging methods have been designed to measure different light information. Colour imaging can record light colour

information. High-speed imaging can capture fast motion and provide information on dynamics. Stereo imaging is used to obtain depth information. Therefore, in order to record different light information, the corresponding specific imaging methods should be used. Furthermore, various imaging methods can be combined in a vision system to record enough light information in one shot.

### **2.2.5 Summary of vision-based measurement**

Digital vision systems are analogues to the human vision system. Vision-based measurement has been applied successfully in many fields. The principle is to record light information and then process and comprehend the information in the recorded images. Light, whether it is emitted from a flame or reflected from an object's surface, can be recorded in images through camera. The flames have different colours, and colour is a human perception of the light's wavelength. Thus, colour imaging could be a useful tool for flame radical emission wavelength measurement. By combining high-speed and stereo imaging techniques, the flame wavelength dynamics in the temporal and spatial domains can be analysed. The light reflected from an object's surface depends on the light and the object's surface properties. The recorded image intensity of a measured object is the amount of photons reflected by the object's surface. The object's surface condition can be explored by analysing the recorded image intensity. With high-speed imaging, the dynamics of the object's surface can also be obtained. To record as much as light information as possible for

the analysis of different applications, a multi-dimensional imaging system that features colour imaging, high-speed imaging, and stereo imaging is needed.

## **2.3 Combustion diagnostics**

### **2.3.1 Introduction**

Fire has been utilised by human beings for around 600,000 years. Since then, combustion has been an essential process for heat and power, and it still plays a critical role in modern industry. Although combustion is widely used today, the combustion phenomenon is not well understood because of its complexity. Combustion diagnostics is a measurement and analysis process that can provide better understanding of the combustion phenomenon. Through fundamental research on combustion, the explored knowledge can enhance fuel energy efficiency and reduce pollutant emission.

### **2.3.2 Combustion definition**

Combustion is defined as an exothermic chemical reaction between fuels and an oxidiser. During the reaction, the active intermediates, such as atoms or free radicals, release electromagnetic radiation energy in the forms of light and heat. These radicals are involved in complex reaction chains during the combustion process. Consequently, particular reactant molecules are consumed and the released energy is transferred to the next stage of the reaction mechanism.

#### **2.3.2.1 Flame classification**

Based on whether the fuel and oxidiser are mixed or not prior to combustion, the flames can be classified into three categories: diffusion, premixed, and partially



premixed flames (Warnatz & Dibble, 2006). Diffusion flames and premixed flames will be discussed below in detail.

#### **2.3.2.1.1 Diffusion flames**

For a diffusion flame, the fuel and oxidant are not mixed homogeneously before the reaction. It involves the burning of pure fuel along with the flame fronts contacting the surrounding air directly. In this case, the mixing rate is lower than the chemical reaction rate (Kuo, 2005). Thus, the reaction is controlled by the diffusion mixing process. A candle flame is one of the most well-known examples of a diffusion flame; the wax evaporates to form a zone containing reactants burning to form a yellow-red flame. In the reaction zone, a diffusion flame occurs between the reactants and the surrounding air. This process is slower than the reaction process, causing a wide region where the gas composition and amount of reactants are variable (Glassman, 1977).

The Bunsen burner, which was invented by Robert Bunsen in 1855 (Kuo, 2005), is a device that can produce both diffusion and premixed flames by adjusting the air input. A schematic of a Bunsen burner is shown in Figure 2.18. A diffusion flame is shown in Figure 2.18(a) with the air hole closed. The flows of fuel and air are plotted by the red and blue arrows, respectively.

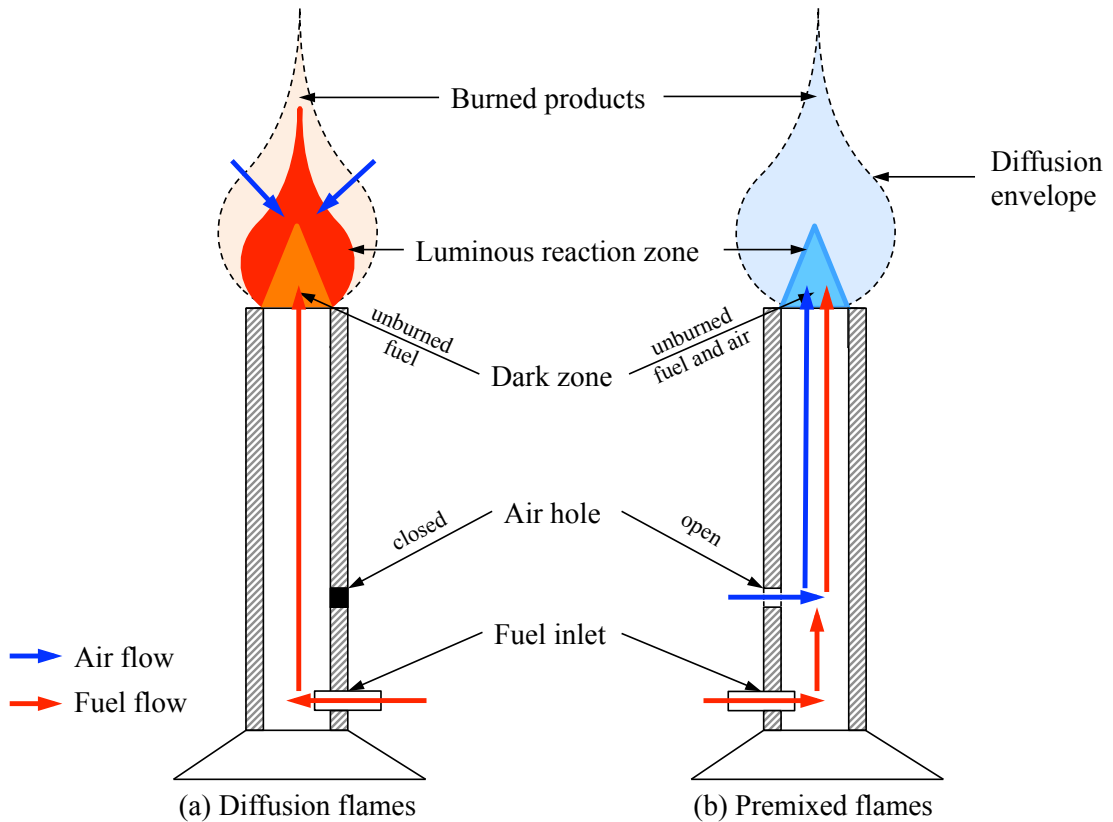


Figure 2. 18: Schematic of Bunsen burner flames: (a) diffusion flames and (b) premixed flames

[adapted from (Kuo, 2005)].

#### 2.3.2.1.2 Premixed flames

In a premixed flame, the fuel and air are mixed homogeneously before combustion, and the reaction occurs within the fuel and air mixture. A Bunsen burner can also produce a premixed flame with the air hole open, as shown in Figure 2.18(b). Air enters the air hole of the burner and mixes with the fuel. Then the mixing fuel/air ascends towards the exit of the burner. The premixed flame propagation is stabilised by the fuel flow velocity in the opposite direction. In this case, the flame exists between the burned reaction products and unburned fuel-air mixture. In contrast to diffusion flames, the reaction rate is dominated by the chemical reaction.

If the unburned mixture of a flame does not contain enough oxidiser, the diffusion of the fuel-air mixture and the surrounding air will cause the combustion to create a flame with characteristic premixed and diffusion flame features. This flame is a so-called partially premixed flame.

### 2.3.2.1.3 Equivalence ratio

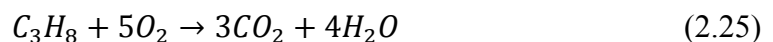
In premixed flame analysis, it is usually express the degree of mixing between the fuel and oxidiser in a dimensionless parameter known as equivalence ratio ( $\Phi$ ). The fuel and oxidiser mixture can be described by the fuel-to-oxidiser ratio  $f$ . The  $\Phi$  is defined as the ratio of the proportion of the actual  $f$  to the stoichiometric  $f_{st}$ . The latter term expresses the required proportion of fuel and oxidiser to enable the process of complete combustion. Hence, the mathematic expression of  $\Phi$  is (Lefebvre, 1999) as follows:

$$\Phi = \frac{f}{f_{st}}, \quad (2.23)$$

where  $f_{st}$ ,

$$f_{st} = \frac{m_f}{m_{os}} = \frac{M_f n_f}{M_o n_{os}} \quad (2.24)$$

where  $m_f$  and  $m_{os}$  presents the mass of the fuel and the stoichiometric oxidiser respectively.  $M_f$  and  $M_o$  are the molecular weights of the fuel and oxidiser respectively.  $n_f/n_{os}$  is the number of moles of fuel to the moles of stoichiometric oxidiser, calculated from the stoichiometric chemical balance equation. For example, propane ( $C_3H_8$ ) reacts with oxygen ( $O_2$ ), the stoichiometric chemical balance equation is given by:



Therefore, in this equation, the  $n_f/n_{os}$  equals to 1/5. This means that 1 mole of propane is needed to react 5 moles of oxygen stoichiometrically.

$\Phi$  is used as an important indicator to describe burning conditions. When the actual fuel to oxidiser ratio is changed, the value of the equivalence ratio changes accordingly;  $\Phi = 1$  means that it is the combustion stoichiometric. If  $\Phi$  is below 1, the combustion occurs in fuel-lean conditions, and if  $\Phi$  is above 1, the combustion is fuel-rich.

### 2.3.3 Flame colour

Flame colour depends on the radiation energy released during a combustion reaction. Therefore, the colour is attributed to the photons emitted from species under excitation. For hydrocarbon flames, the most important factor in flame colour is the mixture of the fuel and oxidiser because it determines the rate of the combustion reaction.

When there is no air supply in a Bunsen burner (see Figure 2.18a), the flame is in diffusion condition and turns a yellowish-red colour because of the incandescence of unburned soot particles in the flame. The flame colour is dominated by the black/grey body radiation, which has a specific spectrum and intensity depending only on the body's temperature. Therefore, colder parts of the diffusion flame are red and turn from orange to yellow and to then white during temperature increases.

When the oxygen supply increases, more complete combustion leads to less unburned soot, and it releases more energy to excite gas molecules in the flame, with

colour become green-blue. The change is attributed to excited molecules emitting photons in the green and blue wavelength ranges of the VIS spectrum. A green-blue flame occurs only when the excited molecular radicals become dominant; thus, the flame colour is attributed to flame chemiluminescence.

### 2.3.4 Chemiluminescence of hydrocarbon flames

During a combustion reaction, the reactant conversion to the product does not happen in a single step. In fact, many sub-reactions occur that produce many short-lived intermediate chemical species. When the short-lived chemical radicals return from excited states to lower but steady states, they release energy and emit photons. This process is known as flame chemiluminescence.

For example, during a combustion process, there is a chemical reaction:



where  $D^*$  is the excited species generation. Through the collision quenching process,



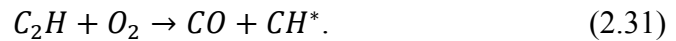
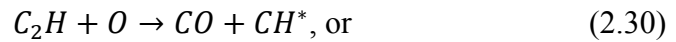
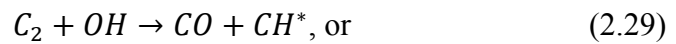
Or, because of the spontaneous emission of photon energy,



The excited molecule  $D^*$  will decay to a lower energy level and emit photons (Barnard & Bradley, 1985). According to the amount of energy released, it emits photons at certain wavelengths. This specific emission spectrum could be a characteristic of the particular fuel type and its chemical transition process. For a

premixed hydrocarbon flame, the emission spectrum is mainly attributed to  $\text{OH}^*$ ,  $\text{CH}^*$ , and  $\text{C}_2^*$  (Gaydon, 1974). Since the work of the thesis is focused on the visible spectrum, only  $\text{CH}^*$  and  $\text{C}_2^*$  chemiluminescence are discussed here.

$\text{CH}^*$  chemiluminescence generation is commonly considered to result from the chemical reactions (Devriendt, Van Look, Ceusters, & Peeters, 1996; Wu, Fuh, & Wang, 2015):



In contrast, the sources of  $\text{C}_2^*$  chemiluminescence are relatively uncertain (Smith, Luque, Park, Jeffries, & Crosley, 2002). However, most studies refer to the following reactions (Bulewica, Padley, & Smith, 1970; Kojima, Ikeda, & Nakajima, 2005):



The reaction described by Eq. 2.32 lacks the exothermic energy to form excited  $\text{C}_2^*$ . Although the reaction described by Eq. 2.33 is fairly exothermic, its dependency on CH is disputability. It is based on the acceptance of stable  $\text{C}_2$  formed from  $\text{CH}^*$ . However, acceptance of both mechanisms occurred because the carbon atom taking part in the reaction is drawn from different hydrocarbon sources. Clearly, further research is needed to study the  $\text{CH}^*$  and  $\text{C}_2^*$  generation. Furthermore, the  $\text{CH}^*$  and

$C_2^*$  are only parts of CH and  $C_2$  that are excited and emitted photons. The relationship between  $CH^*$  and CH or  $C_2^*$  and  $C_2$  are still less understood. More studies on this could contribute to deep understanding of the combustion condition from its flame chemiluminescence.

Generally, peak in the  $CH^*$  emission spectrum occur only at the 430 nm wavelength, while the  $C_2^*$  emission spectrum consists of several sequences of vibrational bands scattered throughout the VIS spectrum. Normally, its emission spectrum peaks occur at 473.7 nm, 516.5 nm, and 563.5 nm. This is well known as the  $C_2^*$  Swan-band system, named for the Scottish physicist William Swan, who first recognised this phenomenon in 1856 (Swan, 1857). The highest peak of  $C_2^*$  emissions is usually at 516.5 nm, which is marked as  $C_2^*(0,0)$ . Thus, the peaks of 473.7 nm and 563.5 nm are named  $C_2^*(1,0)$  and  $C_2^*(0,1)$ , respectively. The  $C_2^*$  Swan band structure is related to the excitation temperature. Robert King (1948) found that the first band head of  $C_2^*$  begins to occur at 516.5 nm from about 2,800° K to 3,000° K. Above 3,000° K, more energy released causes more band heads, such as  $C_2^*(1,0)$  and  $C_2^*(0,1)$ , to occur. Since  $C_2^*(0,0)$  is the first observed emission spectrum peak, and because it has the strongest amplitude of the  $C_2^*$  Swan-band system in most conditions, it is often considered the relative concentration of  $C_2^*$  chemiluminescence.

### **2.3.5 Flame chemiluminescence measurements**

The industry is interested in monitoring flames' local equivalence ratio and the reacting mixture's premixedness degree, as these parameters are related to pollutant

emissions and combustion oscillations in gas turbines (Hardalupas & Orain, 2004). For many years, the concentrations of various species in flames have been measured by sampling probes to estimate the fuel/air mixture (Taylor, 1993). However, there are two drawbacks of probe-based measurement. First, this method cannot identify the spatial and temporal information about the reaction. Second, it disturbs the flow. This issue could increase measurement uncertainties, especially in the high-concentration gradient regions. Because of the above reasons, optical measurements have been developed. Particular emphasis has been placed on the utilisation of these optical flame signatures to detect the global and local equivalence ratio condition of the reactant flow. Unlike probes, optical measurements do not obstruct the flame's natural mass flow, heat transfer, and propagation.

Lasers are widely used in optical measurement. Laser-based methods have been developed and used since the 1960s. The most simplest and direct method for fuel concentration detection is the absorption of laser light (Kiefer & Ewart, 2011). This method involves passing a laser containing a specific spectrum through a flame; the result is an absorption spectrum. Any missed spectrum line in the obtained absorption spectrum is attributed to the species within the flame. However, this method does not provide spatial and temporal information. Laser-induced fluorescence (LIF) is another very popular method for fuel vapour concentration measurement (Hardalupas & Orain, 2004). In the LIF technique, the molecules are excited by specific wavelengths of laser light because of the absorption of EM radiation. Then the



photon emissions from the excited molecules are recorded quantitatively for concentration analysis (Bartaud & Heinze, 1992; Ni. & Melton, 1993). This method requires various corrections before measurement. Because of the effect of the dopant vapour, the obtained results may not stand for the real fuel vapour correctly (Hardalupas & Orain, 2004). Therefore, uncertainties may persist after corrections. Furthermore, although the LIF method can detect the fuel/air ratio, it is unable to distinguish between reacting and non-reacting mixtures. However, information on the fuel/air ratio in a reacting mixture is desired, as it can describe the chemical reaction between fuel and air to understand the combustion conditions. Because of the complex setup and safety issue, the laser-based techniques still are not widely used in the industrial measurement.

Flame chemiluminescence is related to the equivalence ratio; thus, it is also possible to obtain information on a flame's stoichiometry (Hardalupas & Orain, 2004). As suggested by various studies (Chou & Patterson, 1995; Higgins, McQuay, Lacas, & Candel, 2001), the measurement of  $\Phi$  could be considered the intensity ratio of radical chemiluminescence. Not surprisingly  $\text{OH}^*$ ,  $\text{CH}^*$ , and  $\text{C}_2^*$  chemiluminescent emissions are the most interesting optical properties in flame chemiluminescence diagnostics. Clark (1958) used a grating monochrometer to illustrate discrepancies in  $\text{OH}^*$ ,  $\text{CO}^*$ ,  $\text{CH}^*$ , and  $\text{C}_2^*(0,0)$  emissions between propane/air and ethylene/air flames. He demonstrated that the  $\text{C}_2^*(0,0)/\text{CH}^*$  ratio can be applied to indicate the global fuel/air mixture of flames at  $\Phi = 0.6 - 1.5$  conditions. In addition, studies have shown

that the chemiluminescence emission concentrations of  $\text{CH}^*$  and  $\text{C}_2^*$  show non-monotonic dependence on the equivalence ratio in flames (Kojima, Ikeda, & Nakajima, 2000). Haber also confirmed that the  $\text{CH}^*/\text{C}_2^*$  chemiluminescence ratio has a linear response to  $\Phi$  (Haber, 2000). Nowadays, chemiluminescence-based equivalence ratio detection is becoming a standard combustion condition monitoring method in industrial applications such as gas turbine combustors and internal combustion engines (Docquier & Candel, 2002).

Spectroscopy is a conventional method used to measure flame chemiluminescence concentration directly. Because of its simplicity, this method is still common and a standard tool for combustion diagnostics. However, it is a line-of-sight method, so it inherently lacks spatial resolution (Kiefer & Ewart, 2011). To overcome this problem, later researches have focused on obtaining the spatial/local variance of radical chemiluminescence. Kojima et al. (2000; 2005) developed specially designed Cassegrain optics to measure local chemiluminescence emissions. Other studies used narrow-wavelength interference filters combined with a monochrome camera to detect local chemiluminescence based on different radicals, such as detecting  $\text{CH}^*$  and  $\text{C}_2^*$  emissions using  $430 \pm 5$  and  $516 \pm 5$  nm narrow-wavelength filters, respectively (Stadler, Forster, & Kneer, 2007; Migliorini, 2014). However, with this method, the radical chemiluminescence emissions must be captured separately. It is not suitable for measuring fast movements, such as explosions.

With the development of modern colour camera and computer processing techniques, the colour camera played an important role in laboratory research and industrial measurement. Recently, Huang (2011) found that the average blue and green intensity of the colour image were well matched with the global chemiluminescence concentrations of  $\text{CH}^*$  and  $\text{C}_2^*$  in a premixed methane flame, respectively. In this way, both  $\text{CH}^*$  and  $\text{C}_2^*$  concentrations could be detected simultaneously by using a single-colour camera. However, because of the difference in spectral sensitivities within different camera sensors, the model cannot be used directly when using other cameras (Migliorini, 2014).

### **2.3.6 Summary of combustion diagnostics**

Combustion is a complex chemical reaction between fuel and an oxidiser that releases heat and light. The fuel and air mixture determines the combustion conditions and flame colour. Flame colours are attributed to the soot black/grey body radiation-derived yellow-red colour and the radical chemiluminescence emissions-derived green-blue colour. In a hydrocarbon premixed flame, the green-blue colour is related to the flame chemiluminescence of  $\text{CH}^*$  and  $\text{C}_2^*$  emissions in the visible spectrum. The concentrations of  $\text{CH}^*$  and  $\text{C}_2^*$  exhibit non-monotonic dependence on the  $\Phi$  of flames. The  $\text{CH}^*/\text{C}_2^*$  ratio exhibits a linear response to  $\Phi$ , which can be utilised to analyse the combustion reaction conditions. With the development of cameras, it plays an important role in the flame chemiluminescence measurement. Conventional method needs to put narrow-band ( $430 \pm 5$  and  $516 \pm 5$  nm) filters in

front of a monochromatic camera lens to measure  $\text{CH}^*$  and  $\text{C}_2^*$  concentrations. Due to this method needs different filters to measure different wavelengths, it cannot detect different wavelengths at the same time. The colour camera is inherently encoded with three wide-band filters. As Huang's finding, the image's average blue and green intensities in a colour image match the  $\text{CH}^*$  and  $\text{C}_2^*$  global concentrations in a premixed methane flame, respectively. However, this finding cannot be applied to all colour cameras, due to Migliorini cannot get the result as good as Huang did. The reason could be the spectral response difference in different camera sensors. Therefore, a more precise image colour to flame chemiluminescence model needs to be developed considering the sensor spectral sensitivity difference.

## **2.4 Vibration diagnostics**

### **2.4.1 Introduction**

Vibration has always occurred within machines, especially because motors have been used to power them. The causes of vibrations could be attributed to the dynamic effects of manufacturing tolerances, clearances, rolling and rubbing contact between machine parts, and unbalanced forces in reciprocating and rotating components (Bruel & Kjaer, 1982). All machines vibrate to some degree during their operation, but most vibration is not expected (Bilosova & Bilos, 2012). Vibration diagnostics is used to measure vibration signals to estimate a machine's condition. The goal is to detect faults and arrange maintenance in a timely manner.

### **2.4.2 Preliminary Considerations**

#### **2.4.2.1 Maintenance**

All machines need to be maintained if they are to work reliably in their planned lifetime. A scheme for a standard machine life is described in Figure 2.19. As illustrated, the operational life is an essential factor that accounts for most of the total machine life. Especially for large and expensive equipment, appropriate maintenance during operation is as important as suitable design, manufacturing, and assembly in reliable machine operation (Bilosova & Bilos, 2012). Maintenance not only refers to repairing damage to a machine but also preventing any damage. The aims of maintenance are to achieve maximum productivity, optimise machine performance, and ensure operation safety.

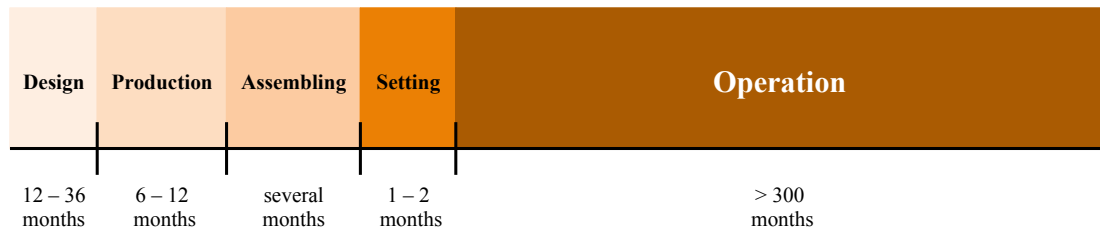


**Figure 2. 19: Scheme of machine life [adapted from (Bilosova & Bilos, 2012)].**

In the past, the common maintenance type was preventive maintenance, which is time-based maintenance that depends on the failure rate (mean time to failure) of similar equipment. However, it is not easy to decide the period between maintenance, as some machines will remain in good condition, while some machines become faulty before the planned maintenance.

Another type of condition-based maintenance is called predictive maintenance. This type of maintenance depends on the condition that requires repair. In this case, it can avoid unplanned shutdown and unexpected failure. Although the machine is still shut down during the repair machine, the planned shutdown is usually shorter and safer, which could avoid serious accidents. The essential factor is that information is needed to indicate when a machine is going to fail. Therefore, it is necessary to identify this condition, so the condition of the machine requires diagnosis.

#### **2.4.2.2 Vibration monitoring**

All machines vibrate during operation. In general, all uncontrolled vibration is undesirable and could result in structural failure. However, vibration signals contain information about a machine's condition. Based on an analysis of this information,

different machine faults can be detected. For a rotating machine, most faults will change the amount and the spectral content of machine vibrations. Different types of damage and their corresponding symptoms are shown in Table 2.2. As indicated, different types of damage in pumps can be represented by vibration signals. Therefore, monitoring vibration is essential for detecting damage.

**Table 2. 2: Example of operation parameters monitoring (ISO 17359).**

| Pumps              | Symptom or parameter change |                    |       |          |       |           |             |                 |            |             |
|--------------------|-----------------------------|--------------------|-------|----------|-------|-----------|-------------|-----------------|------------|-------------|
| Faults             | Fluid leakage               | Length measurement | Power | Pressure | Speed | Vibration | Temperature | Coast down time | Oil debris | Oil leakage |
| Damaged impeller   |                             | ●                  | ●     | ●        | ●     | ●         | ●           | ●               | ●          |             |
| Damaged seals      | ●                           | ●                  |       | ●        | ●     | ●         |             |                 |            |             |
| Eccentric impeller |                             |                    | ●     | ●        | ●     | ●         | ●           | ●               |            |             |
| Bearing damage     |                             | ●                  | ●     |          | ●     | ●         | ●           | ●               | ●          | ●           |
| Bearing wear       |                             | ●                  |       |          |       | ●         | ●           | ●               | ●          |             |
| Mounting fault     |                             |                    |       |          |       | ●         |             |                 |            |             |
| Unbalance          |                             |                    |       |          |       | ●         |             |                 |            |             |
| Misalignment       |                             | ●                  |       |          |       | ●         |             |                 |            |             |

● Indicates symptom may occur or parameter may change if faults occur.

In addition, vibration monitoring is a testing programme as a part of engineering design. The vibration testing results can indicate the performance of a component in different vibration environments. Generally, it is likely to be encountered in a real-life situation, which could then contribute to better design.

### 2.4.2.3 Vibration signals

Vibration refers to a body motion that oscillates around a reference position. In mechanics, the vibration movement behaviour in the time domain can be described by three parameters: displacement  $x$ , velocity  $v$ , and acceleration  $a$ . Since vibration is a type of motion, displacement refers to the changes in position caused by forces; while, velocity is the first derivative of displacement; and acceleration is the second derivative of displacement. These three parameters can be linked by the following mathematical relationships (Bilosova & Bilos, 2012):

$$x(t) = X \cdot \sin(2\pi ft), \quad (2.34)$$

$$v(t) = \frac{dx}{dt} = X \cdot 2\pi f \cdot \cos(2\pi ft), \quad (2.35)$$

$$a(t) = \frac{dv}{dt} = -X \cdot (2\pi f)^2 \cdot \sin(2\pi ft), \quad (2.36)$$

where  $X$  is the amplitude of vibration and  $f$  is the frequency of vibration. If one of the three parameters is known, the others can be simply calculated using the above equations. Therefore, in vibration measurements, only one parameter needs to be monitored. In addition, all these parameters can be transferred into the frequency domain; the frequency can describe the complete cycle of vibration in one second.

#### 2.4.2.3.1 Frequency analysis

Usually, after vibration monitoring, the vibration signals can be analysed in the frequency domain (Serridge & Licht, 1987). Frequency analysis is a tool that can identify different contributions directly, and the contributions are related to the



individual vibrating parts. Hence, a machine fault can also occur in the vibration frequency spectrum as a frequency component (Bilosova & Bilos, 2012). To obtain useful information from a spectrum to detect a machine's condition, it is worth knowing which frequency components are likely to occur in the obtained frequency spectrum.

### **2.4.3 Vibration measurement**

Conventional vibration measurements employ various types of sensors. Some sensors have direct contact on the measured object's surface to measure the strain induced by the object's deformation. A strain gauge is one device used to measure strain caused by an object's vibration. The gauge needs to be attached to the measured object. When the measured object vibrates, the foil within the gauge is deformed. This deformation causes the electrical resistance to change. This change is related to the vibration characteristics.

A piezoelectric accelerometer is a widely used vibration transducer. Similar to deformation based strain measurement, the principle of the accelerometer is also attributed to the deformation of the piezoelectric material, which leads to an electrical charge. This method can be used at a very wide frequency range (Serridge & Licht, 1987). However, these two methods both require contact with the measured object. Unfortunately, the extra structures add mass loading, affecting the original dynamics of the measured object, especially in measuring small and light objects.

Nowadays, more and more non-contact sensors are being developed. A proximity probe is an often-employed non-contact sensor. The method is based on the measurement of eddy currents. The measured currents are related to the distance between the probe and the conductive surface of the measured object (Bilosova & Bilos, 2012). For example, when this distance becomes larger during vibration, the reduced electromagnetic coupling causes a lower magnitude of eddy currents, so less energy is gained by the probe. Of course, the vibrating surface must be electrically conductive. Therefore, the vibration displacement is observed by measuring the currents. In this method, a specified factor that models distance with voltage must be calibrated. However, this factor is sensitive to the temperature and pressure around the probe; any environmental change during measurement will affect the accuracy of the result (Maurice & Adams, 2001).

Another non-contact method is laser Doppler vibrometry (LDV). This method employs a laser vibrometer as a single-point transducer. The principle is based on the Doppler effect. When the laser light is scattered from the surface of the vibrating object, interference occurs between the outgoing and reflected laser beams. The Doppler frequency shift can be converted to the corresponding vibration velocity (Drain, 1980). The laser-based vibration measurement can be very accurate if the measured surface is reasonably reflective and the laser beam is properly aligned (Kon, Oldham, & Horowitz, 2007). However, this method usually has a bulky and complex setup.

With the development of the camera, direct imaging also offers the possibility of vibration measurement. Generally, this method requires pre-placed markers on the measured object, or the object should have an obvious feature that can be easily tracked. The markers/features are tracked in the captured image sequences to indicate the changes in vibration displacements. Then it can provide vibration displacement information in 2D or 3D depending on the camera systems employed. The advantage is that the setup of this method is easy and flexible. The measurement accuracy depends greatly on the shutter speed and image resolution, so it is usually employed in low-frequency and large-displacement applications. The direct imaging method is now widely applied in wind turbine condition monitoring (Sabel, 1996; Ozbek, Rixen, Erne, & Sanow, 2010). However, this vibration measurement by tracking points is only suitable to measure an object that has clear markers, and the markers must be captured in all the measured images. Therefore, a marker-free tracking technique should be developed. The colour imaging, high-speed imaging and stereo imaging can offer additional colour, dynamics and depth information, which can promote the application and ability of vision-based measurement in vibration diagnostics.

### **2.4.4 Summary of vibration diagnostics**

Vibration is usually measured to explore the condition of a machine to arrange maintenance before it suffers damage or during the product testing process. The vibration signals of displacement, velocity, and acceleration are often measured in

the time domain. The analysis of vibration signals is usually considered in the frequency domain, as each frequency component is attributed to a vibrating part or damage. Several vibration measurements are available, ranging from contact sensor-based methods to non-contact optical-based methods. With the development of camera and computer processing ability, the direct imaging, as a non-contact vision-based method, has also shown its potential for measuring the vibration signals during machine operation. Conventional vision-based measurement in vibration detection is based on the feature-tracking technique, which needs a clear marker to be measured in all captured images. In some case, the marker cannot be tracked in all images. Thus, a marker-free tracking technique is necessary to be developed.

## 2.5 Conclusion of the literature review

The fundamental information of vision-based measurement, combustion, and vibration are as follows:

- For vision-based measurement:
  - A digital vision system is a good tool for quantitative optical measurement. Light, as the information carrier, is the directly measured object in vision-based measurement. Light consists of photons as well as waves, containing energy and emitting at different wavelengths. These two characteristics in an image are referred to as the intensity and colour. Flame chemiluminescence and the reflected light from an object's surface could be used to explore combustion information and an object's condition, respectively.
  - A camera, as an optical measurement device, is widely used in research. Various imaging techniques have been developed to capture different light information; colour imaging is used to measure light's colour information, high-speed imaging is to freeze fast phenomena and record its dynamics, and stereo imaging is used to recover depth information. In this work, a combination imaging system should be employed to capture as

much as light information as possible for combustion and vibration studies.

➤ For combustion:

- A combustion reaction emits photons from excited radicals. In premixed hydrocarbon flames, flame chemiluminescence is primarily attributed to  $\text{CH}^*$  and  $\text{C}_2^*$  emissions at 430 and 516.5 nm in the VIS spectrum. The  $\text{CH}^*/\text{C}_2^*$  ratio has a linear relationship to the flame equivalence ratio, which could be used to measure the fuel/air mixture. Various chemiluminescence measurements have been reviewed. One method uses a colour camera to detect  $\text{CH}^*$  and  $\text{C}_2^*$  emissions by modelling with average blue and green image intensities, respectively. However, this method is not flexible and cannot be used in different cameras directly. In this work, a more flexible model needs to be developed for measuring  $\text{CH}^*$  and  $\text{C}_2^*$  concentrations.

➤ For vibration:

- Vibration occurs in almost all machine operations and can reflect a machine's condition. Based on this, vibration diagnostics are utilised in condition-based maintenance and product testing. Vibration diagnostics are often based on vibration frequency spectrum analysis. The direct imaging

method is a non-contact vibration measurement method. However, in this method, an obvious marker should be placed on the vibration object, and this marker must be observed in all captured images. In this work, a more flexible vibration measurement without tracking markers/features should be developed.

# 3

---

## IMAGING SYSTEM AND CALIBRATION PROCESSES

---

### 3.1 Introduction

One aim of this thesis is to apply the same vision-based measurement system in both combustion and vibration studies. For this purpose, a high-speed stereo colour imaging system is employed. The system includes a high-speed colour camera and a stereo adapter; the details are introduced in Section 3.2. Three types of calibration processes are applied to estimate the imaging system; details are discussed in Section 3.3.

### 3.2 High-speed stereo colour imaging system

#### 3.2.1 Introduction

The camera is the main component of a vision-based measurement system. Generally, commercial cameras are designed for high pixel resolution to obtain a high-precision image. Conversely, some cameras focus on other information, such as high-speed cameras used to capture high dynamics and stereoscopic cameras for detecting depth information. To obtain sufficient pixel resolution, high dynamics, and



3D spatial information via a single device, a high-speed stereo colour imaging system is employed; the configuration is shown in Figure 3.1.



**Figure 3. 1: Configuration of a high-speed stereo colour imaging system.**

This imaging system consists of a high-speed colour camera combined with a four-mirror stereo adapter. Through this system, the recorded image data can be written mathematically as follows:

$$Image = f(x, y, z, \begin{bmatrix} R \\ G \\ B \end{bmatrix}, t), \quad (3.1)$$

where  $x$  and  $y$  are image pixel coordinates and  $z$  is the depth information;  $R$ ,  $G$ , and  $B$  are the three primary colours of each pixel; and  $t$  is the measured time. The  $z$  (depth) information cannot be measured directly. To obtain the depth information, intrinsic and extrinsic camera parameter calibration and 3D reconstruction processes are required; the details are discussed in Section 3.3.4.

### **3.2.2 High-speed colour camera**

The main device used in the imaging system is a Photron FASTCAM SA-4 high-speed colour camera. This camera is connected to a Sigma 24-70 mm, f/2.8 EX DG zoom lens. The camera's CMOS sensor can provide operation at 3,600 fps (frames per second) at a maximum 1,024×1,024 colour pixel resolution. Its frame rates can range up to 500,000 fps, but with reduced pixel resolution. The light sensitivity is constant at ISO 4000 with low noise. In addition, the camera is easy to connect to a computer via the Gigabit Ethernet interface. Through the PFV (Photron FASTCAM Viewer) software, it captures 12-bit uncompressed data that can be saved as 16-bit TIFF format colour images to avoid any distortion. This camera can provide not only high-quality colour resolution but also high dynamics information.

### **3.2.3 Stereo adapter**

As discussed in prior reviews, 3D reconstruction requires at least two images of the same measured object from different views with a slight angle difference. To obtain two views simultaneously during measurement using the employed high-speed camera, an Asahi Pentax four-mirror structure stereo adapter is employed. The adapter is shown in Figure 3.2. It can be connected to the camera lens with a step-out ring.



**Figure 3. 2: Asahi Pentax stereo adapter.**

The stereo adapter includes two inner mirrors and two outer mirrors. The dimensions are given in Figure 3.3. The two inner mirrors are placed at about  $45^\circ$  angles to the lens plane and orthogonally to each other. Corresponding inner mirrors and outer mirrors are fixed almost parallel, with a discrepancy angle of  $3.5^\circ$ . The incident light emitted from the measured object enters the outer mirrors. Then, the ray is reflected to the inner mirrors. After that, it is reflected again and passes through the camera lens. Last, a pair of views is formed on the imaging screen with slightly different angles. The adapter has been thoroughly investigated and analysed; more details can be found in the work of Wang et al. (2008). The high-speed camera connected with the stereo adapter can be considered a two-virtual-camera system, as shown in Figure 3.4.

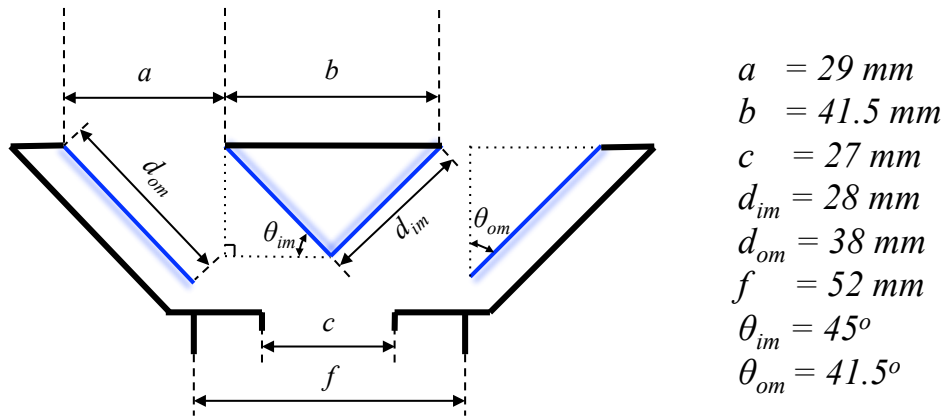


Figure 3.3: Dimensions of the four-mirror stereo adapter.

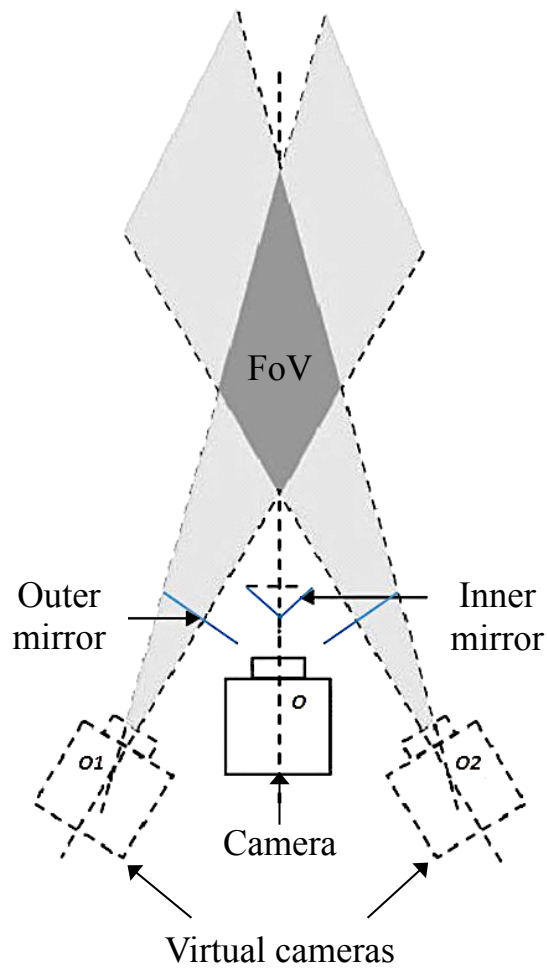
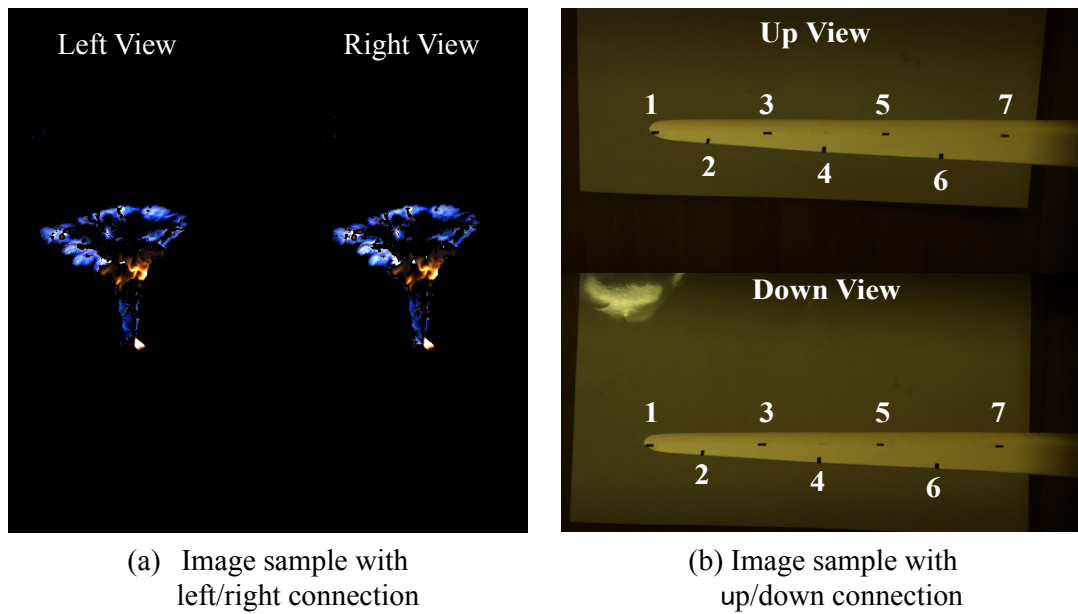


Figure 3.4: The camera with the four-mirror adapter and its two-virtual-camera system.

The adapter can be connected to the camera lens in a left/right configuration or an up/down configuration. To fully use the image pixel resolution, the configuration employed in the measurement depends on the shape of the measured object. Some image samples captured with different configurations of the stereo adapter are shown in Figure 3.5 (a) in the left/right configuration to measure the vertical flame profile and (b) in the up/down configuration to measure a horizontal blade.



**Figure 3. 5: Image samples captured with different connections of the stereo adapter: (a)**

**left/right connection for measuring a vertical flame and (b) up/down connection for measuring a horizontal blade.**

## 3.3 Calibration processes

### 3.3.1 Introduction

For the employed imaging system, three calibration processes are applied: SNR calibration, sensor spectral sensitivity calibration, and intrinsic and extrinsic camera

parameter calibration. The SNR results are used to estimate the quality of the captured images, while the sensor spectral calibration provides the relationship between the camera colour channel responses and their corresponding spectral wavelengths. This step is necessary in developing a flexible colour-wavelength model for flame chemiluminescence measurement in the next chapter. Furthermore, the intrinsic and extrinsic camera parameter calibration is a preliminary step for 3D reconstruction.

### 3.3.2 SNR calibration

To assess the employed high-speed stereo colour imaging system, its SNR was calibrated. The SNR is used to evaluate the quality of an image captured by a camera. As discussed in Section 2.2.4.3.4, the SNR can be calculated using Eq. 2.8.

Since the ISO of the Photron SA-4 camera is constant at 4000, the SNR was calibrated by varying the shutter speeds at 1/50, 1/60, 1/125, 1/200, 1/250, 1/300, 1/400, 1/500, 1/600, 1/700, 1/800, 1/900, and 1/1000 s. The overall standard deviation of the dark background noise was calculated using the following Matlab function:

$$s = \text{std}(X(:)) . \quad (3.2)$$

The input  $X$  only needs one layer vector, but the original image data are in the RGB space containing three layers. Therefore, before using Eq. 3.2, the images were converted to the HSV model using the `rgb2hsv` Matlab function. Then, the hue vector

in the HSV model was employed as the input  $X$ . The final calibrated results are plotted in Figure 3.6.

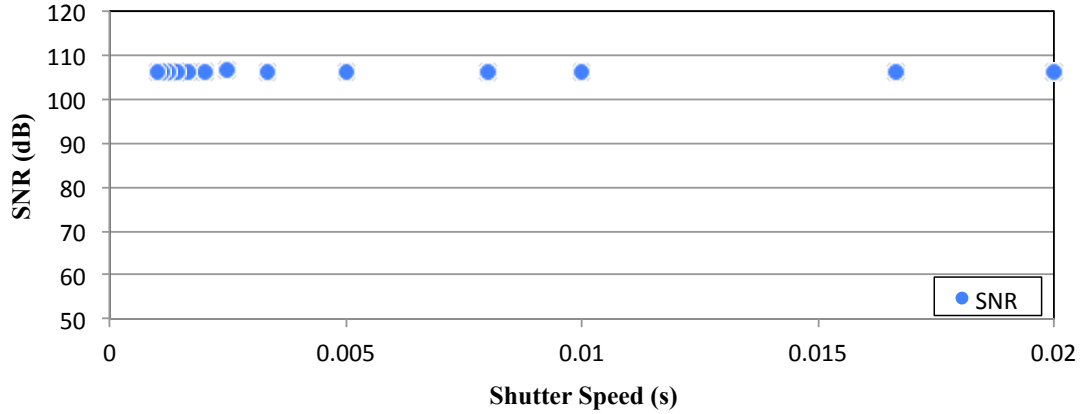


**Figure 3. 6: SNR results for the employed high-speed stereo colour imaging system using different shutter speeds.**

As shown, the SNR results are almost constant and above 100 dB, which is much higher than the standard SNR requirement of 50 dB for a modern camera. These SNR results demonstrate that the image data recorded by the employed high-speed stereo colour imaging system is of high quality. Thus, it can be utilised later to analyse the combustion and vibration information from the measured images.

### 3.3.3 Sensor spectral sensitivity calibration

An image's colour is usually described in the RGB model for display purposes. To determine the relationship between image colour and flame chemiluminescence, the camera sensor's spectral sensitivity must be verified. Therefore, the spectral sensitivity of the R, G, and B channels were calibrated.

The setup for calibrating the employed camera sensor sensitivity is similar to that presented by Takeuchi et al. (1999) and Simonini et al. (2001). This setup requires a standard light source and a monochromator to allow rays to pass through to the camera sensor at each specific wavelength. The standard light source used here was an approximated blackbody radiator in the form of a 150 W tungsten lamp powered by a 12 V battery. The temperature of the tungsten ribbon can be varied from 1300 °C to 2200 °C. The Newport Manual Mini Monochromator (Model 78022) was used to produce monotonic spectral variations for photographs.

The dimensions and internal structure of this monochromator are shown in Figure 3.7. As shown in Figure 3.7(b), the incident light passes through the entrance slit and is reflected by a folding mirror to a focusing mirror with a 74 mm focus length. Then the light is focused on a rotatable diffraction grating. As the grating rotates, radiation centred at a particular wavelength is isolated and reflects back to the exit slit by another folding mirror. Last, the corresponding spectral colour is acquired by capturing the light emitted from the exit.



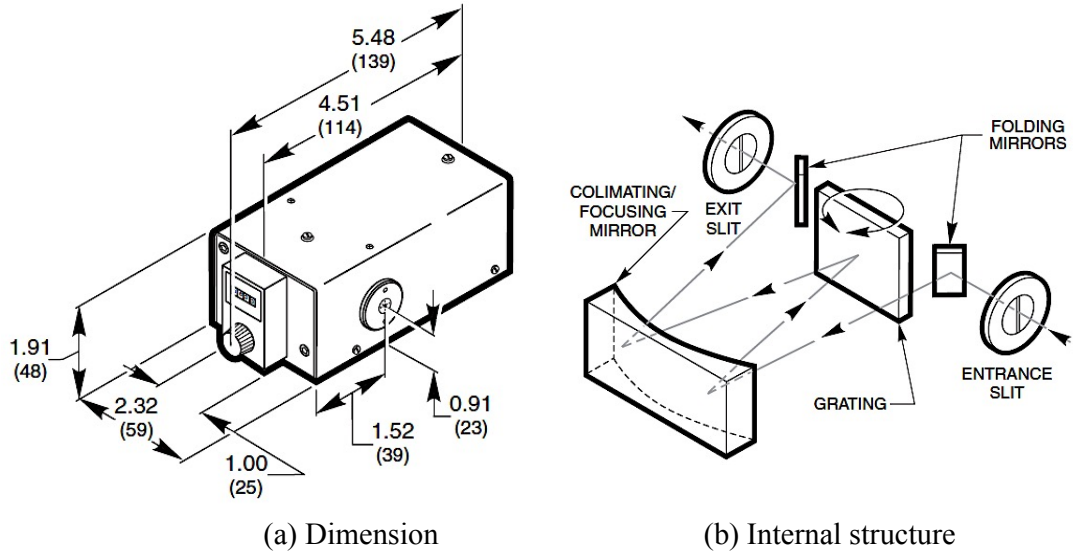
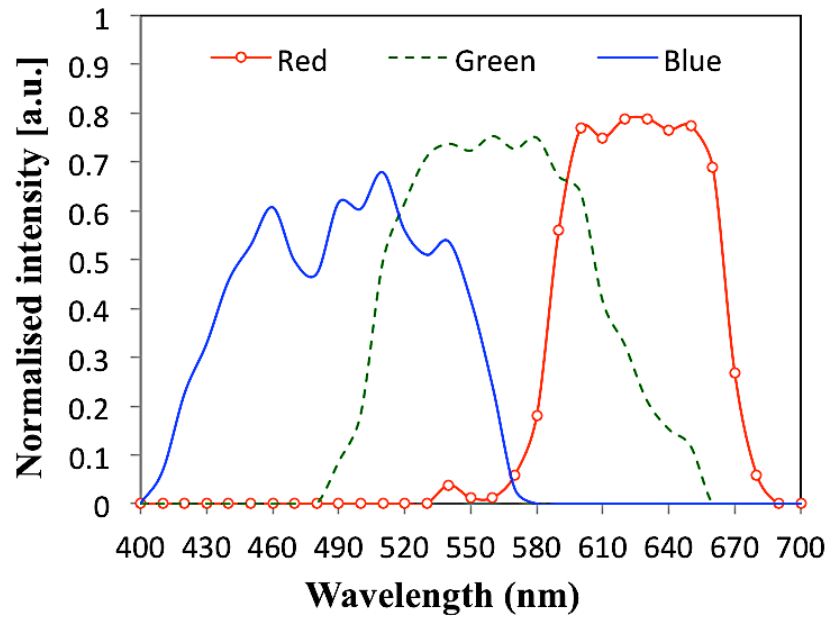


Figure 3. 7: (a) Dimensions and (b) internal structure of the Newport Manual Mini

#### Monochrometer.

Using the setup mentioned above, the spectral responses of the R, G, and B colour channels of the employed camera are calibrated from 400 nm to 700 nm with a 10 nm interval. The measured tungsten radiance is fixed at the temperature of 2200 °C. The captured image data are saved in 16-bit TIFF format. For each image, the average intensity of each colour channel is calculated and recorded. The results of the three channels are normalised by dividing the maximum pixel value by  $(2^{16}-1)$  and plotted in Figure 3.8.



**Figure 3. 8: R, G, and B colour channels spectral sensitivities of the employed high-speed camera.**

The R, G, and B channels spectral sensitivities are plotted by the red, green, and blue lines, respectively. The figure shows that the B channel is sensitive to wavelengths from 400 nm to 580 nm; the G channel is sensitive from 480 nm to 660 nm; and the R channel is sensitive from 530 nm to 690 nm. The sensitivity response of each channel shows an approximately in normal distribution. The distribution peaks of the B, G, and R channels are at about 510 nm, 570 nm, and 630 nm, respectively. This figure will be further discussed in Section 4.3.2.1 to model  $\text{CH}^*$  and  $\text{C}_2^*$  flame chemiluminescences.

### 3.3.4 Camera parameters calibration

#### 3.3.4.1 Camera parameters of the employed high-speed stereo colour imaging system

The transformation of a 3D scene to a 2D image can be described by the camera's extrinsic and intrinsic parameters. The corresponding mathematical expression, Eq. 2.23, was introduced in Section 2.2.4.6.2. The employed stereo imaging system can be considered a two-virtual-camera system. If we use one virtual camera coordinate system as the world coordinate system, then another virtual camera coordinate system can be transferred to the world coordinate system via the extrinsic parameter  $[R, t]$ . Thus, we have

$$m_1 = A_1[1 \quad 0]M, \quad (3.3)$$

$$m_2 = A_2[R \quad t]M. \quad (3.4)$$

Since only one camera is employed in the high-speed stereo system, the intrinsic matrices  $A_1$  and  $A_2$  of the two virtual cameras can be related by

$$A_2 = A_1 - \begin{bmatrix} 0 & 0 & n/2 \\ 0 & 0 & 0 \\ 0 & 0 & 0 \end{bmatrix}, \quad (3.5)$$

where  $n$  is the number of pixels per row of the processing image.

#### 3.3.4.2 Parameter calibration process

To calculate the camera parameters, there are four different calibration methods: 3D reference object-based calibration, 2D plane-based calibration, 1D line-based

calibration, and self-calibration (Zhang, 2004). In this work, the 2D plane-based calibration process is applied.

In 2D plane-based calibration, a graphic template is needed. The intrinsic and extrinsic parameters are calibrated using a known calibration board, which is shown in Figure 3.9. The calibration board consists of  $8 \times 8$  squares with 256 corner points. The standard distance between two neighbouring points in each square is 14 mm, and the gap between two squares is 10 mm. The board is drawn by CAD software, so it is easy to print out and adhere to a plane. The size of the calibration board can be adjusted for different applications. For example, if measuring a large object, a large calibration board is needed to cover the whole object's occupied space.

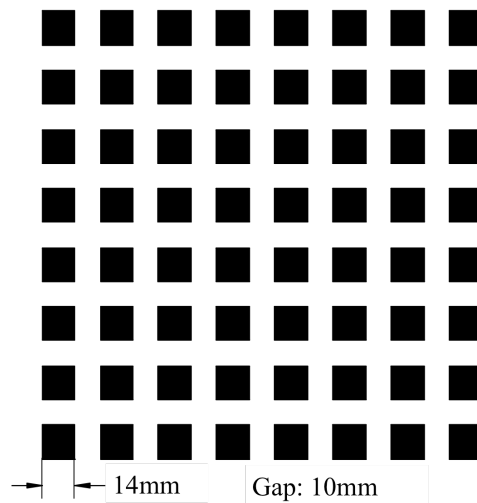


**Figure 3. 9: Standard calibration board.**

When the experimental setup is completed, the calibration board must be placed at the position where the measured object will be placed during the experiments. At least three images of the calibration board at different directions must be captured. In

general, the more images are captured and employed, the higher the accuracy will be. However, using more than five images would not enhance the accuracy significantly but cost more calculation time (Wang, 2009). Therefore, three to five images are usually used for calibration. Figure 3.10 shows an example of four images of a calibration board from different directions.

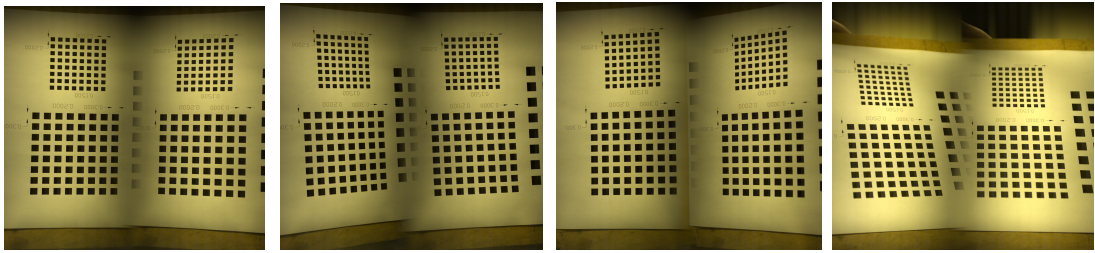


**Figure 3. 10: Images of a calibration board captured from four different directions.**

To calculate the camera parameters, eight steps are needed:

- i. Load at least three images of the calibration board captured from different directions.
- ii. Transfer the colour image data to grey scale.
- iii. Detect the edges of squares by using a Canny edge detector and improvement with Hough transform.
- iv. Detect each corner of the pre-detected squares based on a Harris detector.
- v. Estimate the homography based on the maximum likelihood criterion.
- vi. Estimate the intrinsic and extrinsic parameters using the closed-form solution.
- vii. Calculate the radial distortion coefficients by solving the linear least squares.

viii. Refine all parameters by minimising.

This process can be performed with the Matlab software by using a pre-written programme by Wang (2009). After calibration, the camera's intrinsic and extrinsic parameters can be obtained. For example, the calculated parameter results from Figure 3.10 are listed below:

$$A_1 = \begin{bmatrix} 2276.1 & 2.032 & 950.74 \\ 0 & 2294.2 & 545.26 \\ 0 & 0 & 1 \end{bmatrix}, \quad (3.6)$$

$$A_2 = \begin{bmatrix} 2276.1 & 2.032 & 330.74 \\ 0 & 2294.2 & 545.26 \\ 0 & 0 & 1 \end{bmatrix}, \quad (3.7)$$

$$R = \begin{bmatrix} 0.9325 & 0.018937 & 0.39356 \\ -0.0012481 & 0.99982 & -0.038753 \\ -0.3574 & 0.048732 & 0.97482 \end{bmatrix}, \quad (3.8)$$

$$t = [-0.97654 \ 0.082734 \ 0.18836]^T. \quad (3.9)$$

To verify the obtained parameter results, the 3D reconstruction of images in Figure 3.10 are plotted in Figure 3.11. The calibration board images taken from four directions are plotted in different colours. As indicated, the different colour points are placed on flat plates with very little distortion, demonstrating good results from the 3D calibration board reconstruction. Since the distance between the neighbouring points in the calibration board is known, a comparison with the calculated results shows that the error is less than 5%.

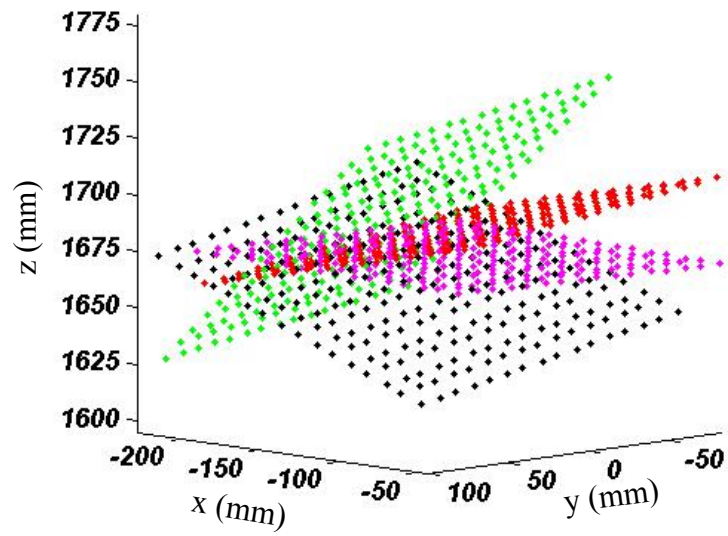


**Figure 3. 11: 3D Reconstruction of the calibration board images taken from four different directions in Figure 3.10.**

### **3.4 Conclusion of imaging system and calibration processes**

- A high-speed stereo colour imaging system is employed in this work that includes a Photron SA-4 high-speed colour camera and an Asahi Pentax four-mirror stereo adapter. This system can provide high-quality colour image pairs in both high dynamics and 3D space.
- The calculated SNR results are always above 100 dB at shutter speed from 1/1000 to 1/50 s, which is higher than the standard SNR requirement of 50 dB for a modern camera. Hence, the employed imaging system can provide high-quality images with low noise.
- The R, G, and B colour channels' spectral sensitivity responses in the employed camera sensor were obtained after the careful calibration. This spectral sensitivity is essential to indicate the relationship between image colour and light wavelength.
- An Asahi Pentax stereo adapter was connected to the camera lens to provide two slightly different views of the measured object to reconstruct the depth information. A calibration board was employed in 2D plane-based calibration. At least three images of the calibration board taken from different directions are required for calibration. The image processing and parameter calculation were produced on Matlab. After selecting and matching the corresponding points in each view of the captured image data,



the parameters can be calculated. The system error is less than 5%, so the reconstructed 3D results are credible.

# 4

---

## IMAGE COLOUR-BASED FLAME CHEMILUMINESCENCE MEASUREMENT

---

### 4.1 Introduction

In this chapter, the relationship between image colour and flame chemiluminescence is discussed. Based on the relationship, a theoretical model correlating image colour with the chemiluminescence emissions of  $\text{CH}^*$  and  $\text{C}_2^*$  is proposed. The details of the methodology are introduced in Section 4.2. The estimation of this method in flame equivalence ratio detection is discussed in Section 4.3. Last, the proposed colour-based flame chemiluminescence measurement is applied in case studies of flame propagation in tubes and of flame ignition to impinging in Sections 4.4 and 4.5, respectively.

### 4.2 Methodology

#### 4.2.1 Introduction

Flame chemiluminescence occurs when excited molecules within a combustion reaction return to their ground state and emit photons. According to quantum mechanics, specific molecules will emit photons at certain wavelengths. Based on the above principle, if the wavelengths of the emitted photons are known, then the

species within the flame can be detected and identified. To human vision perception, the light is presented in different colours in the VIS spectrum. Therefore, the flame colour can be related to certain light wavelengths, and these wavelengths can be further used to determine the species in the measured flame.

As stated previously, human vision is sensitive to colours depending on the three types of cones in the retina. These cones are sensitive differently to short-, middle-, and long-wavelength ranges of light in the VIS spectrum. Based on this principle, modern colour cameras are built in a CFA scheme, so the camera sensor is categorised into R, G and B three colour channels. Therefore, the colour camera can be considered as a three wide-band filters combined light detector. Therefore, the image colour could indicate radical emission concentrations in flames.

With respect to this assumption, Huang (2008; 2011) proposed a experimental model that used average B and G image intensity to present the global  $\text{CH}^*$  and  $\text{C}_2^*$  emission concentrations in a premixed hydrocarbon flame. However, Migliorini (2014) found that he could not repeat the result as well as Huang did when using Huang's model by different camera. It is because the spectral sensitivities of the R, G, and B channels in different cameras are not the same. The researchers employed different cameras with different sensor spectral sensitivities, so Migliorini could not apply Huang's model directly in his test. Therefore, a flexible theoretical colour-to-wavelength model is proposed in this work.

### 4.2.2 Camera image colour

In the CFA scheme, a colour camera sensor includes three primary colour channels, R, G, and B, respectively. The colour displayed in a pixel is the combination of the intensity values in the R, G, and B channels. Therefore, the apparent colour of the visible light striking a pixel could be defined as

$$C = [I_R, I_G, I_B], \quad (4.1)$$

where  $C$  indicates the colour presented by a pixel.  $I$  is the intensity of each pixel. R, G, and B denote each colour channel in a pixel. The intensity of each colour channel for a pixel is the amount of the radiations from all their sensitive wavelengths. Thus, the intensities of three colour channels can be defined as

$$\begin{cases} I_R = \int_{R_{\lambda Min}}^{R_{\lambda Max}} dI_{R\lambda} \\ I_G = \int_{G_{\lambda Min}}^{G_{\lambda Max}} dI_{G\lambda}, \\ I_B = \int_{B_{\lambda Min}}^{B_{\lambda Max}} dI_{B\lambda} \end{cases} \quad (4.2)$$

where  $\lambda$  denotes the wavelength in nanometres, subtitles Max and Min indicate the maximum and minimum of  $\lambda$  range in R, G, and B channels.

### 4.2.3 $\text{CH}^*$ and $\text{C}_2^*$ chemiluminescence

For a premixed hydrocarbon flame, the flame chemiluminescences are mainly attributed to the presence and the mixture of  $\text{OH}^*$ ,  $\text{CH}^*$ , and  $\text{C}_2^*$  radical emissions in the UV-VIS spectrum (Gaydon, 1974). Most modern digital colour cameras capture light in the VIS spectrum, while the  $\text{OH}^*$  emissions are in the UV spectrum. Because

the  $\text{OH}^*$  cannot be measured directly by most normal colour cameras, only the flame chemiluminescence emissions of  $\text{CH}^*$  and  $\text{C}_2^*$  are discussed in the proposed model.

Various experiments have demonstrated that the  $\text{CH}^*$  and  $\text{C}_2^*(0,0)$  emissions are dominant at the 430 nm and 516.5 nm wavelengths, respectively (Gaydon, 1974). Although  $\text{C}_2^*$  also emits at many other wavelengths, such as 473.7 nm and 563.5 nm, the emission of  $\text{C}_2^*(0,0)$  at 516.5 nm is the strongest one, and exists in most of the temperature range (King, 1948). In conventional narrow wavelength filter-based flame chemiluminescence measurement, researchers employed a filter at the wavelength of  $516 \pm 5$  nm to measure  $\text{C}_2^*$  emissions (Migliorini, 2014). Therefore, in this method, it is assumed that the colour of a premixed hydrocarbon flame is only attributed to the photons emitted at the 430 and 516 nm wavelengths because the emissions at other wavelengths are very weak when compared with the  $\text{CH}^*$  and  $\text{C}_2^*(0,0)$  emissions. Based on this assumption, Eq. 4.2 could be simplified as

$$\begin{cases} I_R = I_{R_{430}} + I_{R_{516}} \\ I_G = I_{G_{430}} + I_{G_{516}} \\ I_B = I_{B_{430}} + I_{B_{516}} \end{cases} \quad (4.3)$$

#### **4.2.4 Relationship between image colour and flame chemiluminescence**

The relationship between the radiation at a certain wavelength and its intensity on an image colour channel is plotted in a model shown in Figure 4.1. The radiation of  $\text{CH}^*$  emission at 430 nm wavelength passes through the camera lens. The radiation transfers to illumination depending on the lens transmission rate. Then, its

illumination is converted by camera sensor to different intensities on the R, G, and B colour channels. Here, it is assumed that the transmission rates in our camera lens at all wavelengths are equal to 1. Hence, in the proposed model, the relation between flame chemiluminescence and its intensity in image channels is only depended on the camera sensor conversion rate.

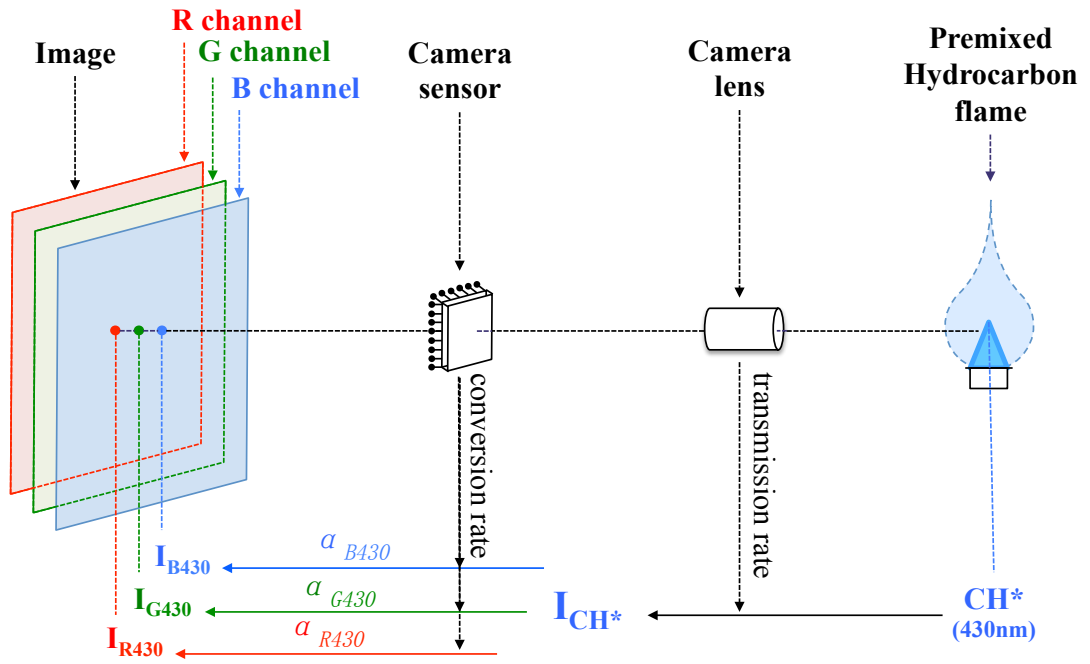


Figure 4. 1: The relationship between image colour and radiation.

Therefore, the relationship between  $CH^*$  and  $C_2^*$  emission illumination and their intensity in R, G, and B colour channels can be defined as

$$I_{CH^*} = \frac{I_{R430}}{\alpha_{R430}} = \frac{I_{G430}}{\alpha_{G430}} = \frac{I_{B430}}{\alpha_{B430}}, \quad (4.4)$$

$$I_{C_2^*} = \frac{I_{R516}}{\alpha_{R516}} = \frac{I_{G516}}{\alpha_{G516}} = \frac{I_{B516}}{\alpha_{B516}}, \quad (4.5)$$

where  $\alpha$  is the radiation conversion rate from chemiluminescence emission to image intensity. Considering Eqs. 4.4 and 4.5, Eq. 4.3 can be rewritten as

$$\begin{cases} I_R = \alpha_{R_{430}} I_{CH^*} + \alpha_{R_{516}} I_{C_2^*} \\ I_G = \alpha_{G_{430}} I_{CH^*} + \alpha_{G_{516}} I_{C_2^*} \\ I_B = \alpha_{B_{430}} I_{CH^*} + \alpha_{B_{516}} I_{C_2^*} \end{cases} \quad (4.6)$$

The intensities on R, G, and B channels can be directly read from the image via software such as Matlab. The conversion rates of R, G, and B channels at 430 nm and 516 nm wavelength can also be obtained after the camera sensor calibration. Therefore, the  $I_{CH^*}$  and  $I_{C_2^*}$  can be detected.

### 4.2.5 Advantages and disadvantages

The equipment for the proposed method is very simple, as only a normal colour digital camera is required. The sensitivity ratio values of the B and G channels at 430 and 516 nm are the only parameters that must be known. These sensitivity ratios can be obtained by calibrating the camera sensor using a standard light source and a monochromator. The monochromator can be replaced by two narrow-wavelength filters at the  $430 \pm 5$  and  $516 \pm 5$  nm wavelengths, respectively.

Compared to LIF, this method is easier to set up and safer for the operators. Compared with the narrow filter-based monochrome camera method, the proposed method requires less equipment because it uses the embedded R, G, and B wide-wavelength band filters instead of narrow-wavelength filters. Compared with Huang's colour-modelled method, this proposed model is more flexible. Because an additional sensor calibration process is used, the effect caused by different sensor spectral sensitivities could be reduced.

Since camera imaging is inherently a 2D measurement method, the captured  $\text{CH}^*$  and  $\text{C}_2^*$  results are already in 2D. By combining the results with dynamics and depth information, the results could be analysed in 1D to 4D (1D: global radical concentration by calculating the mean intensity; 2D: global emission concentration dynamics or 2D local concentration; 3D: 2D local concentration dynamics or 3D concentration distribution; 4D: 3D distribution dynamics).

However, there are still some disadvantages. This method can only measure  $\text{CH}^*$  and  $\text{C}_2^*$  emissions because it assumes that the captured image colours are only attributed to radiation at the 430 and 516 nm wavelengths. In fact, there is still some radiation at other wavelengths that would contribute to the captured image colour. Furthermore,  $\text{C}_2^*$  emissions are not emitted only at 516 nm. In the  $\text{C}_2^*$  Swan bands, emission peaks of  $\text{C}_2^*$  also exist at 473.7 nm and 563.5 nm. However, compared to emissions at the 430 and 516 nm wavelengths, other emissions are very inconspicuous, so the error level is acceptable.



## 4.3 Experimental estimation

### 4.3.1 Introduction

The proposed colour-based  $\text{CH}^*$  and  $\text{C}_2^*$  chemiluminescence measurement was introduced in the previous section. This method is based on the hypothesis that hydrocarbon premixed flame chemiluminescences are only attributed to the radical emissions of  $\text{CH}^*$  and  $\text{C}_2^*$  at the 430 and 516 nm wavelengths, respectively. According to the sensor spectral sensitivities and the sensitivity ratios of the B and G channels at the 430 and 516 nm wavelengths in the employed camera, the relative  $\text{CH}^*$  and  $\text{C}_2^*$  emission concentrations can be calculated. In this section, the accuracy of the method is estimated by analysing premixed  $\text{C}_3\text{H}_8$  flames from  $\Phi = 0.93$  to 1.53. The results are also compared with the conventional colour-modelled method.

### 4.3.2 Experimental setup and process

The experiments were performed using a free-burning atmospheric burner with an inner nozzle diameter of 10 mm. The premixed  $\text{C}_3\text{H}_8$  flames are measured at equivalence ratios from 0.93 to 1.53 (12 cases with a constant fuel flow rate of 0.105 L/min by varying the premixing air flow rates from 1.7 to 2.8 L/min at 0.1 L/min intervals to obtain the desired equivalence ratio states). Typically, five measurements were performed for each condition.

A high-speed stereo colour imaging system is employed to test the proposed method. In each case, 2000 image frames were captured at steady burning states (five-minute interval between data acquisition), with the camera settings of 125 fps and a 1/125s

shutter speed in order to capture clear blue flame profiles at every measured equivalence ratios.

#### 4.3.2.1 $\text{CH}^*$ and $\text{C}_2^*$ expressions

The sensor spectral sensitivity of the R, G, and B channels are different in different cameras. To further calculate the  $\text{CH}^*$  and  $\text{C}_2^*$  chemiluminescence concentrations at 430 and 516 nm, the spectral sensitivity ratios of the B and G channels at these two wavelengths must be known. Therefore, the camera sensor spectral sensitivity calibration is a necessary step. Based on the sensor calibration described in Section 3.3.3, the spectral sensitivity responses of the employed camera are plotted in Figure 4.2.

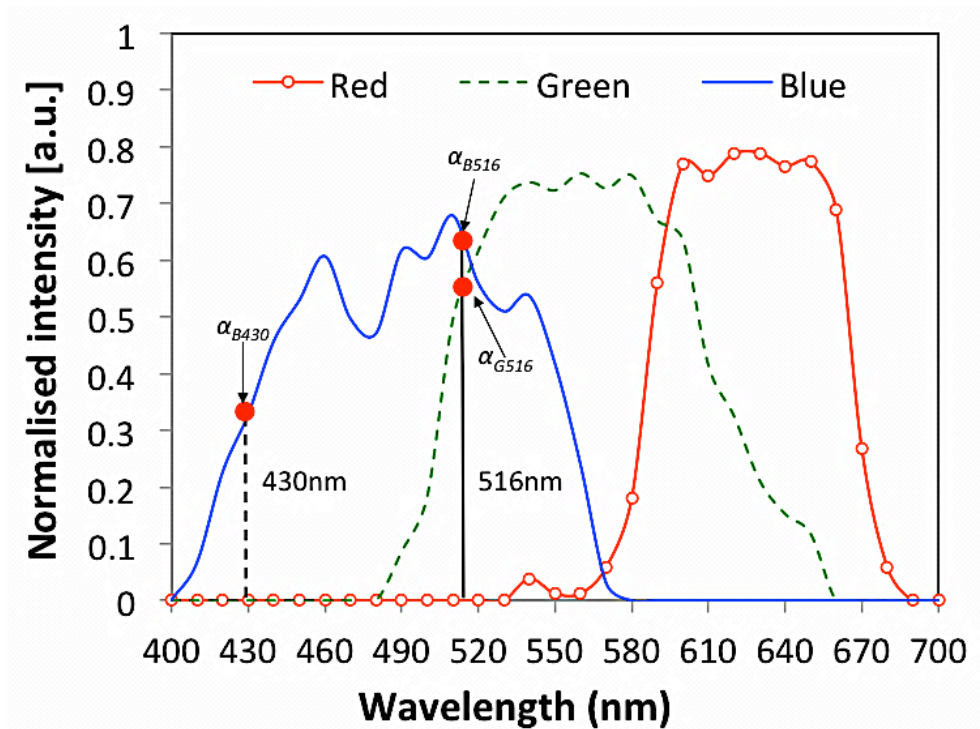


Figure 4. 2: Sensitivity ratios of the B and G channels at 430 nm and 516 nm.

According to the plot, the  $\text{CH}^*$  emission at 430 nm is only sensed by the B channel, whereas the  $\text{C}_2^*$  emission at 516 nm can be sensed by both the B and G channels. Channel R does not cover either 430 nm or 516 nm. The figure shows that the G channel of the employed camera is not sensitive to the 430 nm wavelength. Then the Eq. 4.6 for the employed camera can be simplified as

$$\begin{cases} I_G = \alpha_{G_{516}} I_{C_2^*} \\ I_B = \alpha_{B_{430}} I_{CH^*} + \alpha_{B_{516}} I_{C_2^*} \end{cases} \quad (4.7)$$

According to Figure 4.2, the normalised spectral sensitivity ratio  $\alpha_{B_{430}}$ ,  $\alpha_{B_{516}}$ , and  $\alpha_{G_{516}}$  are about 0.33, 0.62 and 0.56, respectively. Hence, the  $\text{CH}^*$  and  $\text{C}_2^*$  chemiluminescence expressions based on the employed camera are

$$\begin{cases} I_{C_2^*} = 1.79 I_G \\ I_{CH^*} = 3.03 I_B - 3.3 I_G \end{cases} \quad (4.8)$$

It is necessary to emphasise here that Eq. 4.8 is only satisfactory for the camera employed in this work. Since the spectral responses of the R, G, and B channels are different in different cameras, the sensitivity ratio  $\alpha$  is also a camera-specific parameter. For different cameras, this parameter can be obtained through camera sensor calibration. This may also explain the cause of Migliorini's failure to reproduce Huang's results using the same method (Migliorini, 2014).

#### 4.3.2.2 Image processing

The image processing was conducted using Matlab software. After the original image data (Image 1) were loaded, the image noise was reduced by two steps. Since we are only interested in the flame profile, any intensity outside of the flame profile

had to be reduced. Before flame ignition, a background image (Image 2) was captured. The flame profile of interest (Image 3) could be detected from the original image data (Image 1) by subtracting the background image (Image 2). After that, the partial-noise-reduced colour flame profile image (Image 3) was converted to black and white format (Image 4). Hence, in Image 4, each pixel coordinate containing intensity was set as 1; otherwise, it was set as 0. Then a  $3 \times 3$ -pixel window was applied to each pixel in the partial-noise-reduced black and white flame profile image (Image 4). If the intensity amount in the  $3 \times 3$ -pixel window was greater than 3, this pixel intensity remained a part of the flame; otherwise, it was removed as noise. The reason of choosing 3 as the threshold of the applied window is because the threshold at 3 can detect the complete flame profile with the lowest noise level from setting different thresholds from 0 to 9. After this processing, the noise outside the flame profile could be filtered. Then, this all-noise-reduced black and white flame profile image (Image 5) was multiplied by the part-noise-reduced colour flame profile image (Image 3) to obtain the all-noise-reduced colour flame profile image (Image 6).

The image colour is in the RGB colour space. To select the blue colour of a premixed flame easily, the all-noise-reduced colour flame profile image (Image 6) was converted from the RGB model to the HSV model (Image 7). According to the previous investigation by Huang (Huang & Zhang, 2008), the digital colour representative of hydrocarbon premixed flame chemiluminescence is in the range of

120°–240° within hue layer in the HSV model. Therefore, only colour values within this region were selected (Image 8). The selected flame image (Image 8) in the HSV model was then converted back to the RGB model (Image 9). However, the detected flame signals in Image 9 were weak. To visualise the flame's blue profile clearly, the R, G, and B intensity values of the processed image (Image 9) were enhanced. The enhancement time depends on the original intensity in the R, G, and B channels. The enhanced intensity should not exceed the maximum intensity of each pixel; otherwise, the colour is saturated and turns white. Figure 4.3 shows the processed image data at different equivalence ratios, where the images' R, G, and B intensities are enhanced 10 times.

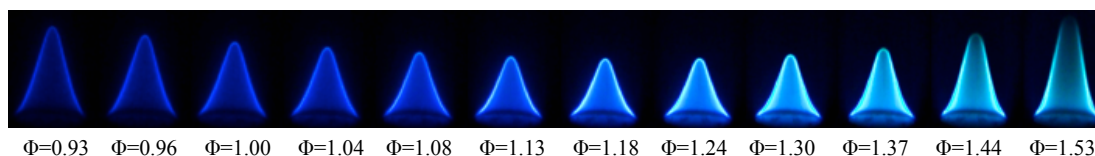


**Figure 4. 3: Processed  $C_3H_8$  premixed flame images at equivalence ratio  $\Phi$  ranging from 0.93 to 1.53; the R, G, and B intensities of each image are enhanced 10 times.**

### 4.3.3 Results and analysis

As shown in Figure 4.3, from left to right, as  $\Phi$  increases, the flame colour changes from pure blue to green-blue because more  $C_2^*$  is emitted in high equivalence ratio conditions. Since the  $CH^*/C_2^*$  ratio has a linear response to the equivalence ratio (Haber, 2000), the corresponding local  $CH^*/C_2^*$  chemiluminescence emission ratio maps of Figure 4.3 are calculated by Eq. 4.8 and plotted in Figure 4.4 using jet colourmap. The colour from blue to red indicates the  $CH^*/C_2^*$  ratio from 0 to 5.

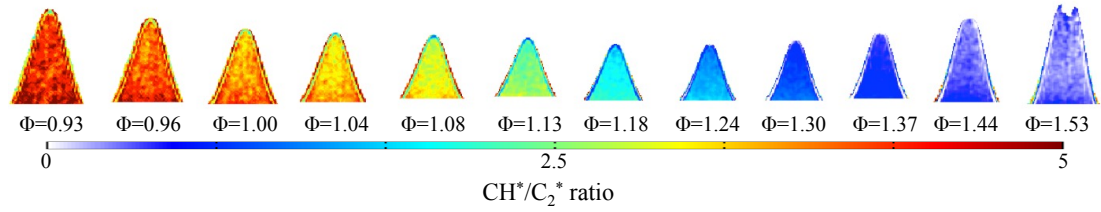


**Figure 4. 4: Colour-calculated  $\text{CH}^*/\text{C}_2^*$  ratio maps at  $\Phi$  ranging from 0.93 to 1.53.**

The colours of the different parts within the flame profile at a certain  $\Phi$  are almost the same. This means that the colour-calculated local  $\text{CH}^*/\text{C}_2^*$  ratio is almost constant for a certain  $\Phi$ . Since the fuel and air are well premixed in the current study, the Figure 4.4 also demonstrates that the proposed colour-calculated chemiluminescence method has the potential to measure the relative fuel/air mixture accurately.

A quantitative parametric investigation has been further analysed to assess the variation between the  $\Phi$  and the corresponding image colour distributions. A typical histogram of the computed local  $\text{CH}^*/\text{C}_2^*$  ratio at  $\Phi = 1.44$  is shown in Figure 4.5. The difference between the minimum and maximum values of the local  $\text{CH}^*/\text{C}_2^*$  ratio is less than 0.5.

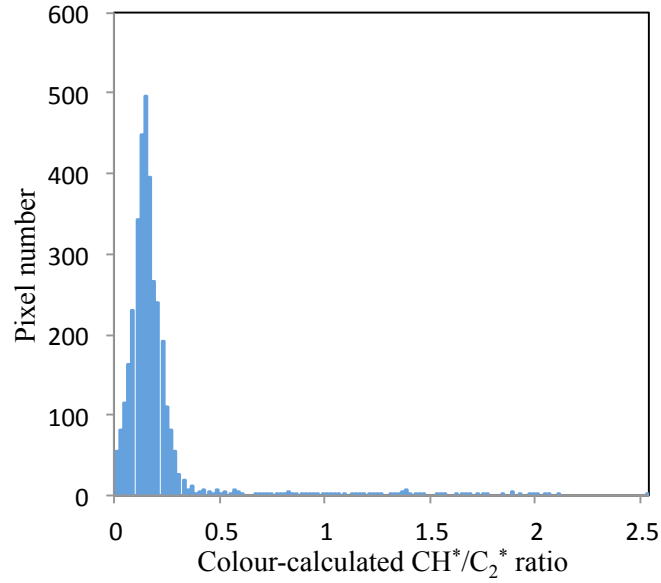


**Figure 4. 5:  $\text{CH}^*/\text{C}_2^*$  histogram of a typical single frame at  $\Phi = 1.53$ .**

The distributions of all  $\Phi$  cases were then fitted by the Gaussian distribution to calculate the acquired mean and variance ( $\mu_e$  and  $\sigma^2$ , respectively):

$$f(x; \mu, \sigma^2) = \frac{1}{\sigma\sqrt{2\pi}} e^{-\frac{1}{2}\left(\frac{x-\mu}{\sigma}\right)^2} \quad (4.9)$$

The observed discrete variation of the  $\mu_e$  values suggests that a curve-fitting algorithm can be applied to compute the corresponding  $\Phi$  states based on the statistical  $\mu_e$  of the  $\text{CH}^*/\text{C}_2^*$  ratio distributions. To facilitate the accuracy of  $\mu_e$  and its range of deviation by considering the broadness of its distribution means, 500 frames from each dataset (comprising 2000 images per dataset) were used as training data to predict the average  $\mu_e$  as well as its upper and lower limits at a CI (confidence interval) of 99%. From the remaining 1500 frames, the  $\mu_e$  from five data groups (each an ensemble of 300 random image frames) were calculated and compared with the training data. The computed  $\mu_e$  peaks and their predictions ranging from  $\Phi = 0.93$  to 1.53 are shown in Figure 4.6.

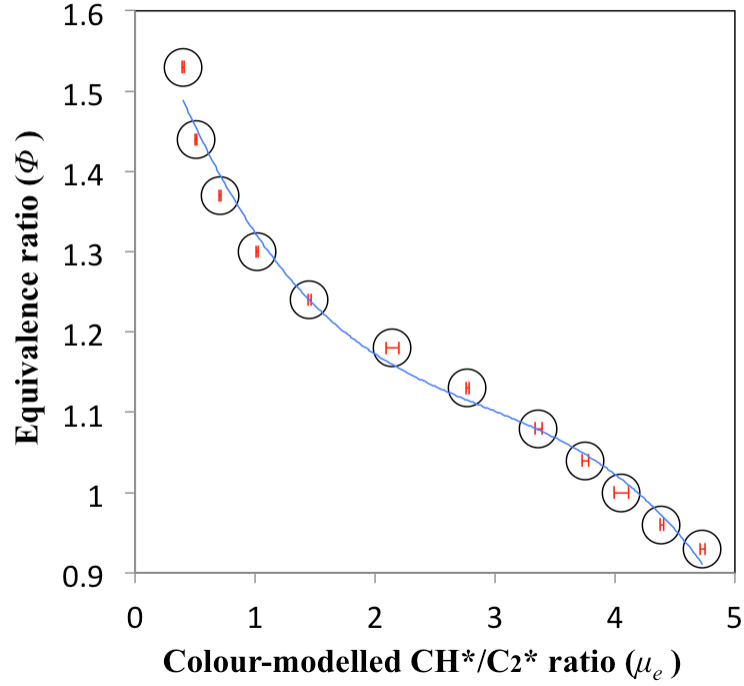


Figure 4. 6: Calculated  $\mu_e$  values at different  $\Phi$  along with an error bar denoting the 99% CI range.

The trend of the characteristic  $\mu_e$  corresponding to the different  $\mu_e$  varies almost linearly from  $\Phi = 0.93$  to  $1.53$ . As shown, even at a 99% CI, the variation of the computed  $\mu_e$  is small; the upper and lower limits are typically less than 1% from each characteristic  $\mu_e$  at different  $\Phi$ . The maximum  $\mu_e$  deviation is no greater than 2% from its characteristic  $\mu_e$  predicted from the training data, meaning a maximum of a 1% deviation from the 99% CI range. Therefore, the actual fluctuation of the average  $\mu_e$  value is small. Thus, for the employed camera, the relationship between  $\Phi$  and the measured  $\mu_e$  is as follows:

$$\Phi = -0.0145\mu_e^3 + 0.1268\mu_e^2 - 0.43\mu_e + 1.6413. \quad (4.10)$$



The  $\text{CH}^*$  and  $\text{C}_2^*$  concentrations can be calculated by image colour using Eq. 4.8. Then, the calculated  $\text{CH}^*/\text{C}_2^*$  ratio can be used to obtain the equivalence ratio by using Eq. 4.10.

#### 4.3.4 Comparison with a colour-modelled method

The same experimental data were also processed by Huang's conventional modelled chemiluminescence measurement method for comparison. In this discussion, the proposed method is called the developed model, while Huang's method is called the conventional model. According to Huang's work, the image average B and G intensities can be used directly to model the global  $\text{CH}^*$  and  $\text{C}_2^*$  chemiluminescence concentrations, respectively (Huang & Zhang, 2008). Hence, the conventional modelling of  $\text{CH}^*$  and  $\text{C}_2^*$  emission concentrations are simply indicated by the mean values of the image's blue and green intensities, respectively. The  $\text{CH}^*$  and  $\text{C}_2^*$  chemiluminescence concentration expressions using two methods based on the employed camera are shown in Table 4.1.

**Table 4. 1:  $\text{CH}^*$  and  $\text{C}_2^*$  emission expressions using the developed and conventional models.**

|                | Developed model    | Conventional model |
|----------------|--------------------|--------------------|
| $\text{CH}^*$  | $3.03I_B - 3.3I_G$ | $I_B$              |
| $\text{C}_2^*$ | $1.79I_G$          | $I_G$              |

The compared results from the two methods under different equivalence ratios are plotted in Figure 4.7. The developed modelled  $\text{CH}^*/\text{C}_2^*$  ratio results are shown by the red circles. According to Eq. 4.8, the developed modelled ratio values were

calculated by  $(3.03I_B - 3.3I_G)/1.79I_G$ . The conventional modelled  $\text{CH}^*/\text{C}_2^*$  chemiluminescence results are plotted in blue squares. Since the conventional modelled results were simply indicated by the mean blue and green intensities, the ratio value is equal to  $I_B/I_G$ .

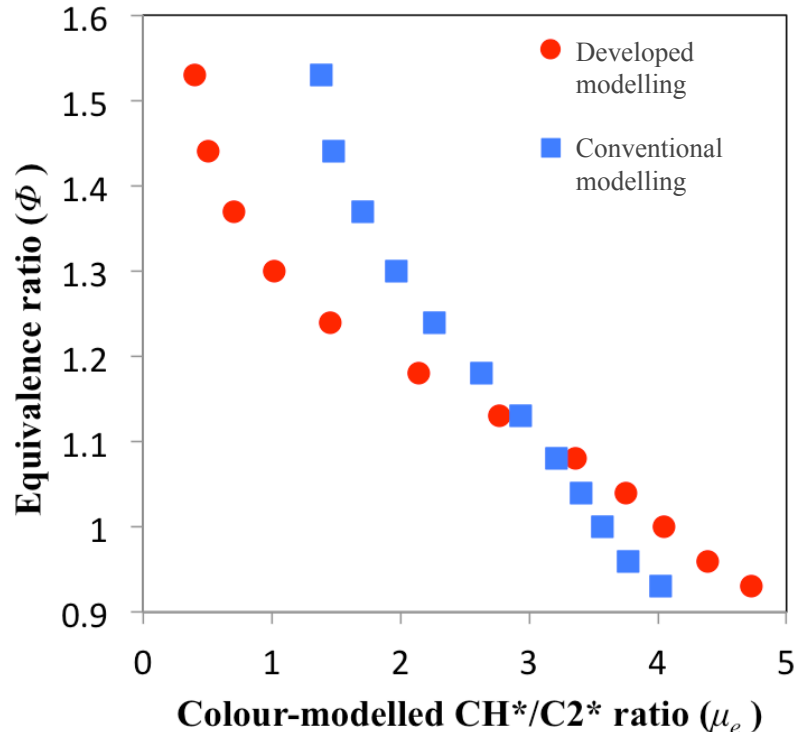


Figure 4. 7: Comparison between developed and conventional modelled  $\text{CH}^*/\text{C}_2^*$  ratios.

As shown in the figure, the trends of the results for the two models are similar: the ratio drops with an increase in the equivalence ratio from 0.93 to 1.53. In this equivalence ratio range, the conventional modelled ratios are from 1 to 4, while the developed modelled ratios turn from 0 to 5. The developed model is more sensitive than the conventional model in colour variation, hence it is more precise in obtaining equivalence ratio. Using the conventional modelled  $\text{CH}^*/\text{C}_2^*$  ratio value divided by the developed modelled  $\text{CH}^*/\text{C}_2^*$  ratio value, we obtain Figure 4.8.

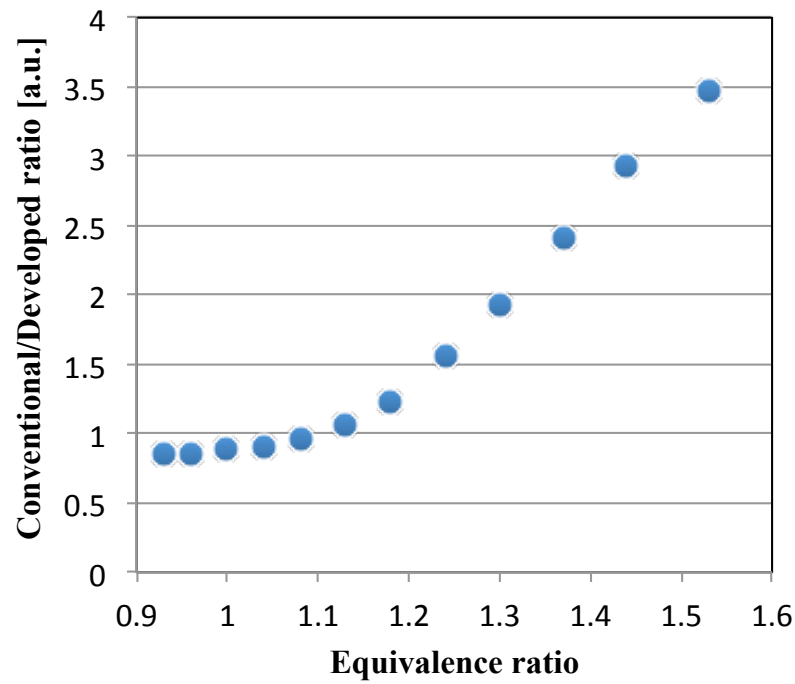


Figure 4. 8: Difference between the conventional and developed modelled  $\text{CH}^*/\text{C}_2^*$  ratios.

The figure indicates the trend of the difference between the two models. As shown, the ratio value difference between the two models increases when  $\Phi$  increases. The reason could be that, in the conventional model, the  $\text{CH}^*$  is modelled by the mean B intensity without reducing the  $\text{C}_2^*$  illumination effect. When  $\Phi$  increases, the flame colour turns greener. This means that the  $\text{C}_2^*$  concentration becomes dominant. Hence, the  $\text{C}_2^*$  illumination effect becomes stronger, which increases the error in the obtained ratio. Therefore, the difference increases because the error increases.

### 4.3.5 Conclusion

- A flame  $\text{CH}^*$  and  $\text{C}_2^*$  chemiluminescence measurement method using a digital colour camera is proposed. This method is based on the assumption that premixed flame chemiluminescence is only attributed to  $\text{CH}^*$  emissions

at 430 nm and  $C_2^*$  emissions at 516 nm. A camera sensor calibration is needed to determine different specific parameters for correcting the spectral sensitivity difference in different cameras. The theoretical modeling of image colour to  $CH^*$  and  $C_2^*$  chemiluminescence is

$$\begin{cases} I_R = \alpha_{R_{430}} I_{CH^*} + \alpha_{R_{516}} I_{C_2^*} \\ I_G = \alpha_{G_{430}} I_{CH^*} + \alpha_{G_{516}} I_{C_2^*} \\ I_B = \alpha_{B_{430}} I_{CH^*} + \alpha_{B_{516}} I_{C_2^*} \end{cases}$$

- For the high-speed stereo colour imaging system employed in this work, the expressions of the colour-calculated  $CH^*$  and  $C_2^*$  are

$$\begin{cases} I_{C_2^*} = 1.79 I_G \\ I_{CH^*} = 3.03 I_B - 3.3 I_G \end{cases}$$

This method has been estimated by measuring a  $C_3H_8$  premixed flame from  $\Phi = 0.93$  to 1.53. The maximum global  $CH^*/C_2^*$  deviation is no greater than 2% from the characteristic  $CH^*/C_2^*$  predicted from the training data, meaning a maximum of a 1% deviation from the 99% CI range. The measured global  $CH^*/C_2^*$  ( $\mu_e$ ) can be related to the  $\Phi$  of a premixed  $C_3H_8$  flame as follows:

$$\Phi = -0.0145\mu_e^3 + 0.1268\mu_e^2 - 0.43\mu_e + 1.6413.$$

Compared to the conventional colour-modelled flame chemiluminescence measurement, the trends of the results obtained from the methods are similar in the beginning, but the difference between them increased at higher  $\Phi$  conditions.

## **4.4 Case 1: flame propagation in open/closed tubes**

### **4.4.1 Introduction**

In combustion science, the transition from a flame ignition to detonation is still a challenging issue. A detonation wave is a shock wave that is sustained by the energy released from a chemical reaction in the highly compressed explosive medium existing in the wave (Glassman, 1977). Generally, a combustion wave is related as the deflagration only. To form a detonation wave, the initial deflagration must be accelerated sufficiently. In this process, the mechanisms of cellular flames resulting from laminar instabilities, obstacles creating turbulent flames, flame–shockwave interactions, and acoustic flame instabilities are involved (Ciccarell & Dorofeev, 2008). The acoustic flame instability is significant in spaces without obstructions and has often been observed in flames in tubes.

The investigation of flame propagation in tubes can be traced to the beginning of combustion science. The pioneering works by Mallard and Le Chatelier are often considered some of the earliest attempts to characterise premixed flames (Mallard & Le Chatelier, 1883). In the 1920s and 1930s, Richard Vernon Wheeler captured flame movement by high-speed imaging in Sheffield (Coward & Hartwell, 1932). Later, Gerstein et al. (Gerstein, Levine, & Wong, 1951) refined this work with respect to mine gas explosions and measured the maximum laminar burning velocity. Furthermore, Guénoche (Guenoche & Pergampn, 1964) did some experiments to

examine the range of phenomena that can be observed within tubes in order to better understand non-steady flame propagation.

Its complex behaviour can be demonstrated by changing the fuel/air properties, tube boundary conditions (e.g., closed or open at ends), and tube diameter. Flames travel steadily and are subjected to violent vibrations. During flames oscillation, the flame front becomes distorted and wave amplification may appear, created by the coherence between the heat release and the acoustic wave (Ciccarell & Dorofeev, 2008). The problem is important for understanding flame acceleration, flame hazards and also miniaturised combustion devices.

More recently, flame propagation in tubes has drawn interest for improving the understanding of the deflagration to detonation transition (DDT) process for safety and pulse detonation. In order to solve this issue, researchers have focused on numeric solutions, typically with simplified chemistry. In a recent study (Akkerman, Law, Bychkov, & Eriksson, 2010), flame oscillation was demonstrated in tubes with no slip walls and open ends, the trigger being the increasing flame surface area resulting from interaction with the walls. It is noteworthy that an assumption in this work was that the boundary conditions at the ends were non-reflective to avoid the influence of sound waves and weak shocks. This can be achieved experimentally by placing orifice plates or similar obstructions at the ends of the tubes, in which case flames are observed to travel down the tubes steadily (Guenoche & Pergampn, 1964).

In this case study, propane/air flames propagating down a 1200 mm tube with a 20 mm internal diameter were imaged using high-speed cameras. Experiments were conducted under two different tube boundary conditions, open and closed at the ends. When the tube was open at ends, acoustic waves were created as the flame propagated. In some circumstances, in the central length of the tube, a fluctuating velocity/pressure field was created. The action of the waves on the propagating flame was observed. The results were analysed using the previous proposed colour-based flame chemiluminescence measurement.

### 4.4.2 Experimental setup

A schematic of the experimental rig is shown in Figure 4.9. It consists of two connected parallel pipes. The tubes are connected together in a loop.  $C_3H_8$  was injected through the injection hole; after that, two fans were used to mix  $C_3H_8$  with air. The mixed propane/air mixture was ignited at the ignition point. Then, the flame would propagate from the ignition point to the other end. The central part of the tube is made from quartz to visualise the flame. Both ends of the tube can be closed or opened to the atmosphere by arranging the two three-way valves.

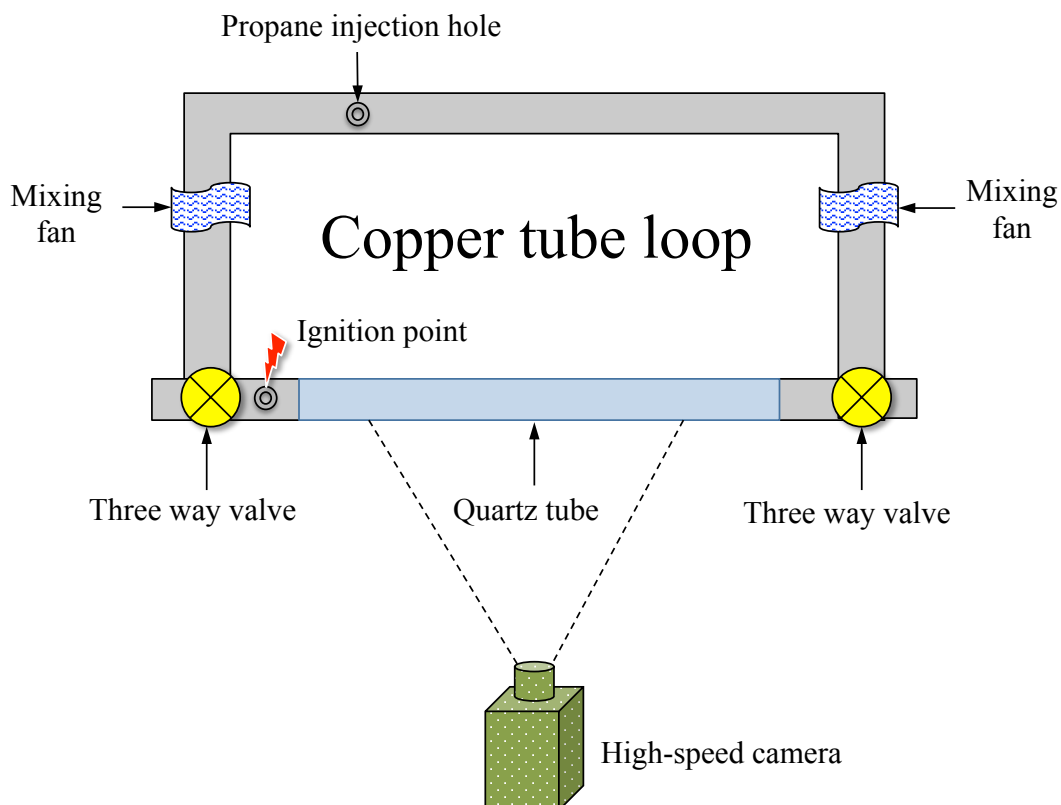


Figure 4. 9: A schematic of the experimental configuration.

For each condition, five measurements were performed. To capture colour images of the flame propagation for chemiluminescence analysis, a high-speed stereo colour imaging system (the details are discussed in Section 3.2) was employed. It was set at a framing rate of 1000 fps and a 1000  $\mu$ s shutter speed. In this imaging system, a shutter speed shorter than 1000  $\mu$ s would cause lower colour intensity. Thus, to measure the dynamics of the flame oscillation, a Photsonics Phantom V210 was employed to capture grey images at 3000 fps and a 332  $\mu$ s shutter speed. Both devices were connected to a computer and controlled using the PFV software.

The initial temperature was typically 293 K. Experiments were performed across the range of  $0.8 \leq \Phi \leq 1.6$  with 0.1 interval. Ignition was performed using a flame



directly into the tube by opening the ignition point at one end of the tube. To minimise gravitational effects, the tube was mounted horizontally. Because the tube was mounted horizontally, to fully use the image pixel resolution, the stereo adapter was placed perpendicular to the SA-4 camera body, and the views appeared at the top and bottom side of the recorded image. In this case study, because of serious distortion caused by the curved boundary of the quartz tube, the 3D reconstruction of the flame surface was not good. However, the flame was still visualised in 3D via the software of NVIDIA 3D Vision viewer. As a result, the flame can be visualised more realistically in this study.

The proposed colour-based flame chemiluminescence was applied to measure the  $\text{CH}^*$  and  $\text{C}_2^*$  flame chemiluminescence concentrations. In this stereo imaging system, each set of image data includes two views of the measured flame in the top and bottom parts of the image. Although the two views were captured with a slight angle difference, their intensities on image are almost the same. To analyse the chemical dynamics during flame propagation, only the top side of the stereo image data was processed via the aforementioned proposed method.

### 4.4.3 Results and analysis

For both tube boundary conditions (closed and open), flames were measured over the ignitable range of equivalence ratios. For convenience, these two boundary conditions are simply called ‘closed tubes’ and ‘open tubes’ in the following

discussion. Examples of captured images in the two boundary conditions at different equivalence ratios (0.8 to 1.6, with 0.1 interval) are shown in Figure 4.10.

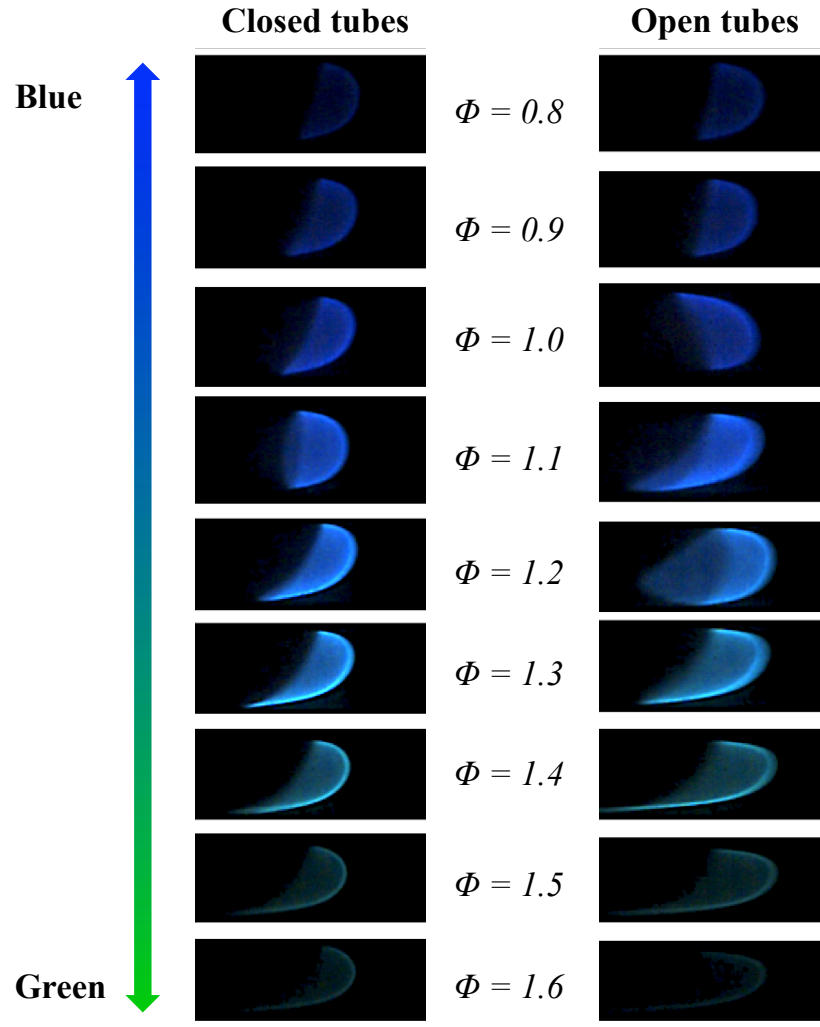


Figure 4. 10: Examples of images in closed and open tubes at different equivalence ratios

( $\Phi=0.8-1.6$ , with a 0.1 interval).

To visualise the flame structure clearly, the image's R, G, and B pixel intensities were enhanced 15 times after the noise reduction (the image processing was the same as that described in Section 4.3.2.2). As indicated, in both conditions from  $\Phi = 0.8-1.6$ , the flame colour changes from blue to green because  $\text{CH}^*$  (430 nm) emissions

dominate in lower  $\Phi$  conditions and  $C_2^*$  (516 nm) emissions dominate in higher  $\Phi$  conditions. This phenomenon is similar to that shown in Figure 4.3.

The steady flame profiles observed in tubes are shown in Figure 4.10. The flame is convex relative to the burned gases and slightly tipped forwards (Guenoche & Pergampn, 1964). Some flame profiles in open tubes are blurred in the captured images, for example at  $\Phi = 1.1$ – $1.3$ . This is because the flame propagation speed in open tubes is higher than that in closed tubes at the same  $\Phi$ . Further analysis based on the movement is discussed in the next section.

#### **4.4.3.1 Flame position analysis**

In closed tubes, flames propagated steadily in all  $\Phi$  cases, while in open tubes condition, flames were only steady in low and high  $\Phi$  cases. For  $1.1 < \Phi < 1.4$ , the flame oscillated in the central portion of the tube. Examples of flame propagation at  $\Phi = 1.2$  in both tube conditions are shown in Figure 4.11. These image sequences were captured at the beginning part of the tube. The leading points of flames in the images were tracked and connected by dashed lines, red for closed tubes and blue for open tubes. For closed tubes, the red line is straight, which means that the flame propagation is linear and its speed is constant. For open tubes, the red line is the translation of the red line from the closed tube case. It is clear that most of flame fronts exceed the red line, which indicates that the flame propagates faster in open tubes. Compared with the other conditions of  $\Phi = 0.8$ ,  $0.9$ , and  $1.0$ , the measured stable flame speeds in open tubes were  $1.3$ ,  $1.9$ , and  $2.3$  m/s, respectively. Compared

to the measured laminar burning velocities of 0.27, 0.35, and 0.38 m/s for  $\Phi = 0.8$ , 0.9, and 1.0, the obtained steady flame speeds are much higher.

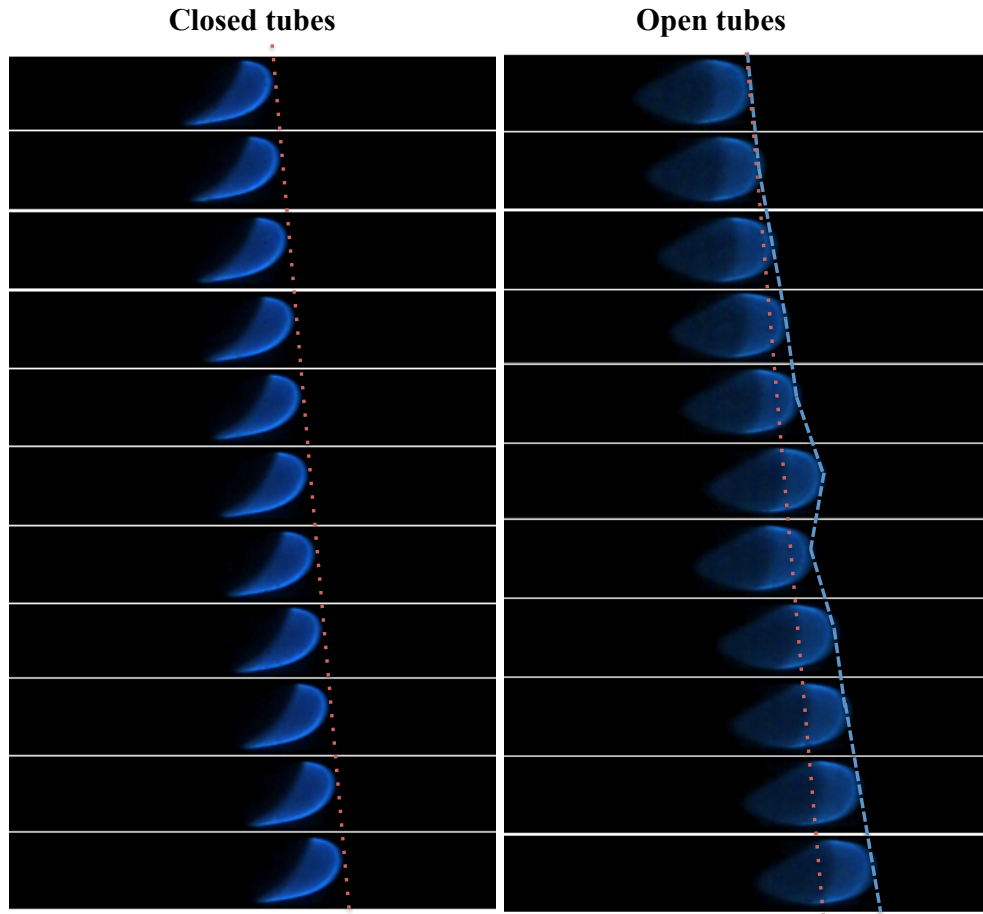


**Figure 4. 11: Flame propagation in both closed and open tubes at  $\Phi = 1.2$ .**

The blue line in the open tube case shows that the flame propagation is not linear. The flame propagation is in the beginning of the transition from steady to oscillating. At the centre of the tube, rapid oscillatory (vibrational) behaviour can be observed. The framing rates of 3000 fps were set to capture the progress details of these flames. Images of the flames at two different measured positions (at the beginning of tube and the centre of the tube) in the open tubes are shown in Figure 4.12.

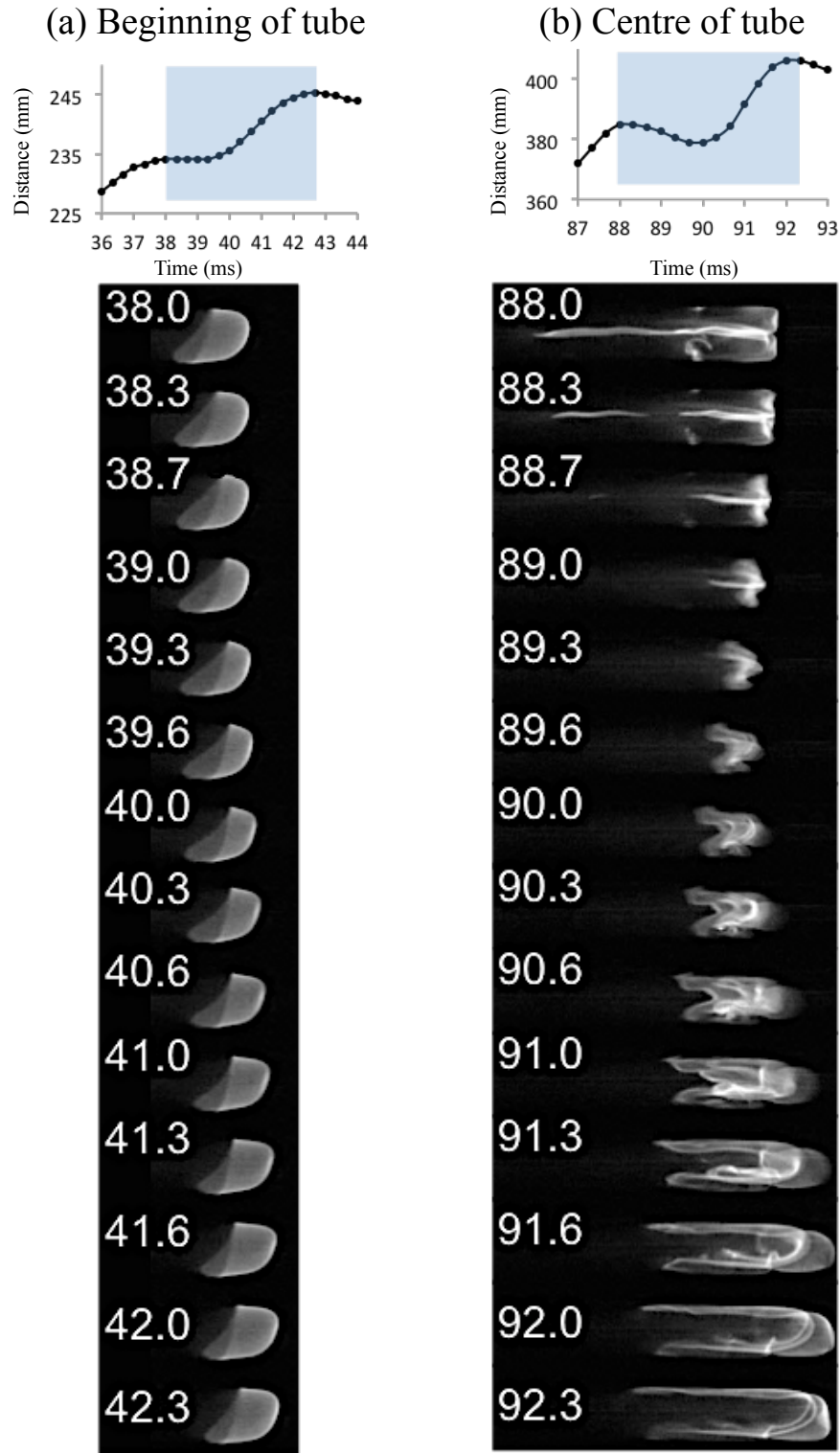
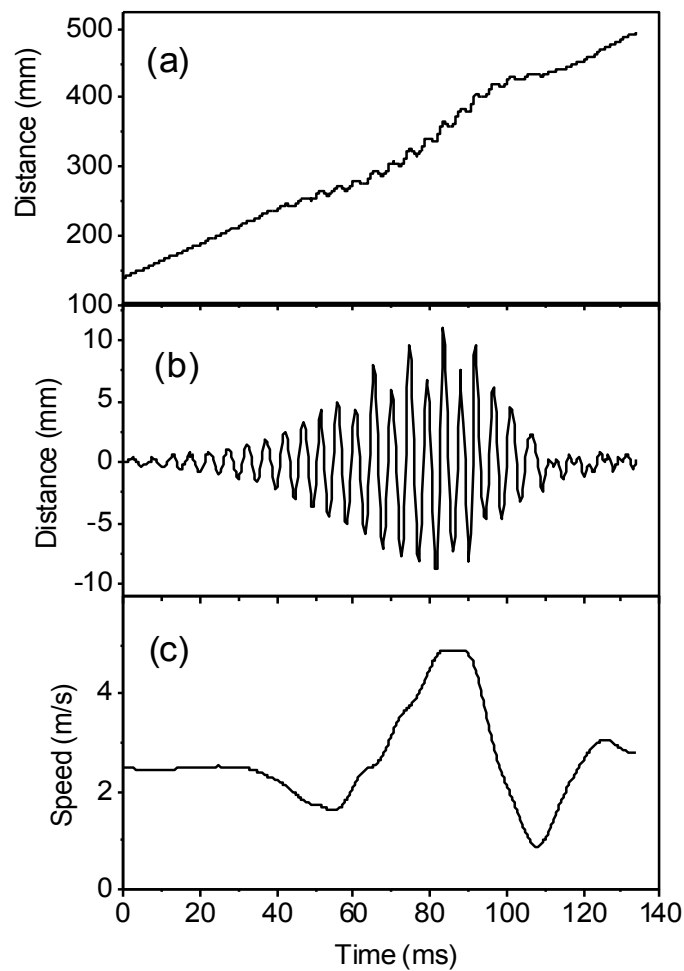


Figure 4. 12: Images of a  $\Phi = 1.2$  propane/air flame recorded at 3000 fps. The numbers on the frames is the time after the camera trigger: (a) beginning of the tube: from 38 to 42.3 ms after trigger and (b) centre of the tube: from 88 to 92.3 ms after trigger.

The flame leading point was used to characterise the position and propagation of the flame. The ignition was out of the FOV of the camera with a pilot flame and its occurrence was not monitored. This meant it was not straightforward to define a consistent time zero. The times shown on images are related to the moment of the camera triggered rather than to any specific event. Figure 4.13 shows the flame position in the tube plotted against time for the flame depicted in Figure 4.12.



**Figure 4. 13: Leading points plotted against time: (a) flame position, (b) flame front position after subtraction of the FFT filtered flame position, and (c) observed flame speed. These relate to the images of Figure 4.12.**

As it shown in Figure 4.13(a), clear flame position oscillation is found from time at 50 to 110 ms. To determine the magnitude of the oscillations separately from the distance of flame travel, a low-pass FFT filter was applied to the data in Figure 4.13(a). The deviation from the filtered flame position is shown in Figure 4.13(b). From this it can be seen that oscillations were present throughout the time that the flame was recorded. Initially, its amplitude grew until it reached a maximum of  $\pm 10$  mm from the filtered flame position. After that, its amplitude decreased rapidly. The oscillation frequency throughout the first 100 ms was found to be 220 Hz. The oscillation frequencies measured for all unstable flames in the range  $1.1 < \Phi < 1.4$  were found similar.

Shown in Figure 4.13(c) is the flame speed derived from the filtered flame position data in Figure 4.13(b). The mean speed was initially constant, and then it slowed to about 1.6 m/s before accelerating and reaching a peak mean flame speed at 4.9 m/s, corresponding with the maximum oscillation. After that, the speed decayed quickly down to around 0.9 m/s. The maximum flame speed is about 10 times higher than quoted values for the laminar burning velocity.

#### **4.4.3.2 Flame structure analysis**

To monitor the flame oscillation frequency and amplitude in experiments, the phenomenon of flame oscillation was found to be repeatable. As measured 10 experiments for  $\Phi = 1.1$  to 1.3, the frequency was 227 Hz (standard deviation: 6 Hz) and the maximum oscillation amplitude was  $\pm 12.1$  mm (standard deviation: 1.2

mm). Therefore, the differences in flame properties had no further influence once the acoustic field was generated. According to this, only two events are discussed in this case study.

As shown in Figure 4.12, the first series (a) indicates that the flame propagated from 38 ms to 42.3 ms in the beginning part of the tube. It can be seen that relatively slight oscillation could be detected in the flame position, with the flame front moving approximately  $\pm 2$  mm from the filtered flame position. In the first six frames, from 38 ms to 39.6 ms, the flame front is motionless. In that time, the flame width (the distance from the flame leading point to its back close to the tube wall) decreases. In the latter portion of the images, from 40 ms to 42.3 ms, the back of the flame remains motionless, but the front of the flame moves forward. Both the flame shape and area are continually changing during the flame propagation. A zoological analogy of such movement might be a caterpillar that begins each crawl by a step of the insect's rear legs followed by a forward moving wave of steps by its middle legs.

The second image sequence in Figure 4.12(b) was taken around 89 ms and relates to the peak flame speed and the flame oscillation. Here, the flame oscillation was  $\pm 10$  mm about the filtered flame position. In the image at 88 ms, the front of the flame is approximately planar. For the first seven frames, the whole flame is moved back to the burned gases. This seems to occur firstly at the walls. The flame develops forward from 89.6 ms onwards. The front edge of this development is diffuse and dim at the beginning but turns into sharper and brighter. When this front decelerates



down, the front of the flame flattens. All the time that the flame moves forward, it is drawn backward to the burned gases as well, but this occurs at the walls. Therefore, only half of the oscillation the flame travels forward.

#### 4.4.3.3 Flame chemiluminescence analysis

High-speed colour camera was also employed during flame oscillations for flame chemiluminescence analysis, although the data were captured at a separated event with a lower framing rate of 1000 fps. The  $\text{CH}^*$  and  $\text{C}_2^*$  emission concentrations were obtained by using Eq. 4.8, and the  $\text{CH}^*/\text{C}_2^*$  ratio was also calculated. Figure 4.14 shows an example of the colour-calculated  $\text{CH}^*$ ,  $\text{C}_2^*$ , and  $\text{CH}^*/\text{C}_2^*$  values against their flame area at the captured moment in the open tube case at  $\Phi = 1.2$ .

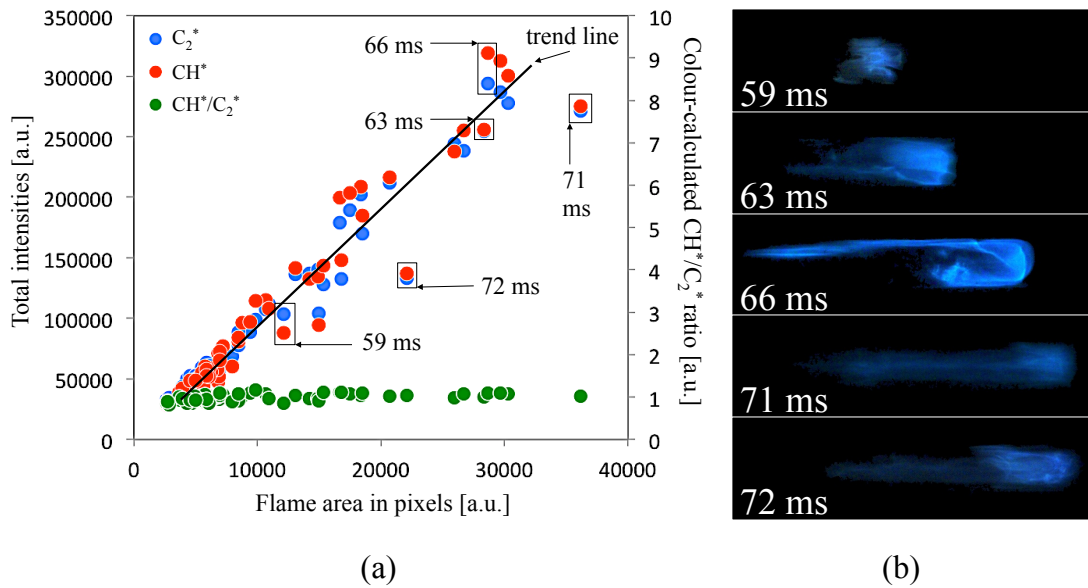


Figure 4. 14: (a)  $\text{CH}^*$ ,  $\text{C}_2^*$ , and  $\text{CH}^*/\text{C}_2^*$  values against flame area in open tubes at  $\Phi = 1.2$ ; (b)

flame visualisations at 59, 63, 66, 71, and 72 ms corresponding to Figure 4.13.

The  $\text{CH}^*$  and  $\text{C}_2^*$  are plotted by red and blue dots, respectively. Each dot indicates the total intensities of measured  $\text{CH}^*$  or  $\text{C}_2^*$  for a particular flame area. For convenient,

an approximate trend line is added for demonstrating their relationship; both their intensities increase when flame area grows. In Figure 4.14a, the dots at 71 and 72 ms are below and a bit away from the trend line, hence their flame visualisation are dim than others in Figure 4.14b. At 66 ms, the flame intensity is much brighter than others, thus the dots in Figure 4.14a is above the trend line.

Although the values of  $\text{CH}^*$  and  $\text{C}_2^*$  rise along with flame area increasing, this phenomenon is not linear. For example in Figure 4.14a, at 59 ms, the  $\text{CH}^*$  value is lower than  $\text{C}_2^*$ ; at 63 ms, their values are similar; while at 66 ms,  $\text{CH}^*$  is much higher than  $\text{C}_2^*$ . The difference also can be seen from the flame visualisation in Figure 4.14b, flame colour at 59 ms is shown in a green-blue profile due to  $\text{C}_2^*$  was dominated, while at 66 ms, the colour turned more blue due to  $\text{CH}^*$  was dominated.

The  $\text{CH}^*/\text{C}_2^*$  ratios are plotted by green dots. The green plot is expected to remain constant because the unburned gases were well mixed before measurement. As anticipated, the ratio is almost constant at around 1 (standard deviation: 0.1). The deviation is attribute to  $\text{CH}^*$  and  $\text{C}_2^*$  value variation which discussed previously.

Fig. 4.15 shows the processed local  $\text{CH}^*/\text{C}_2^*$  ratio maps of flame propagation at  $\Phi = 1.2$  in open tubes. Series a indicates the flame captured at the beginning part of the tube, while series b shows the flame measured at the centre part of the tube. The time on each image is a reference to the particular frame of the image sequences. The  $\text{CH}^*/\text{C}_2^*$  ratios are plotted in colours; blue indicates a low ratio and red a high ratio.

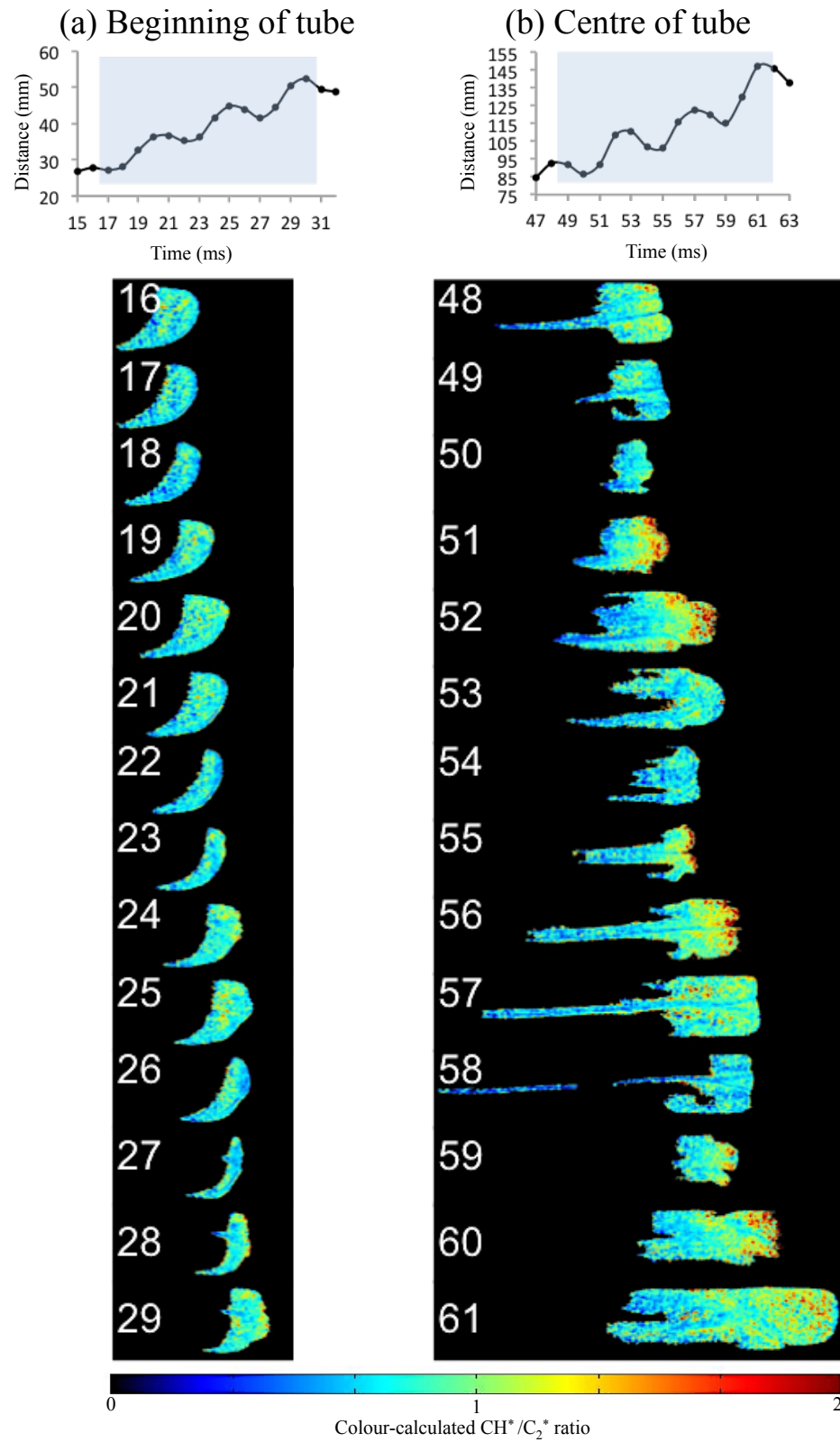
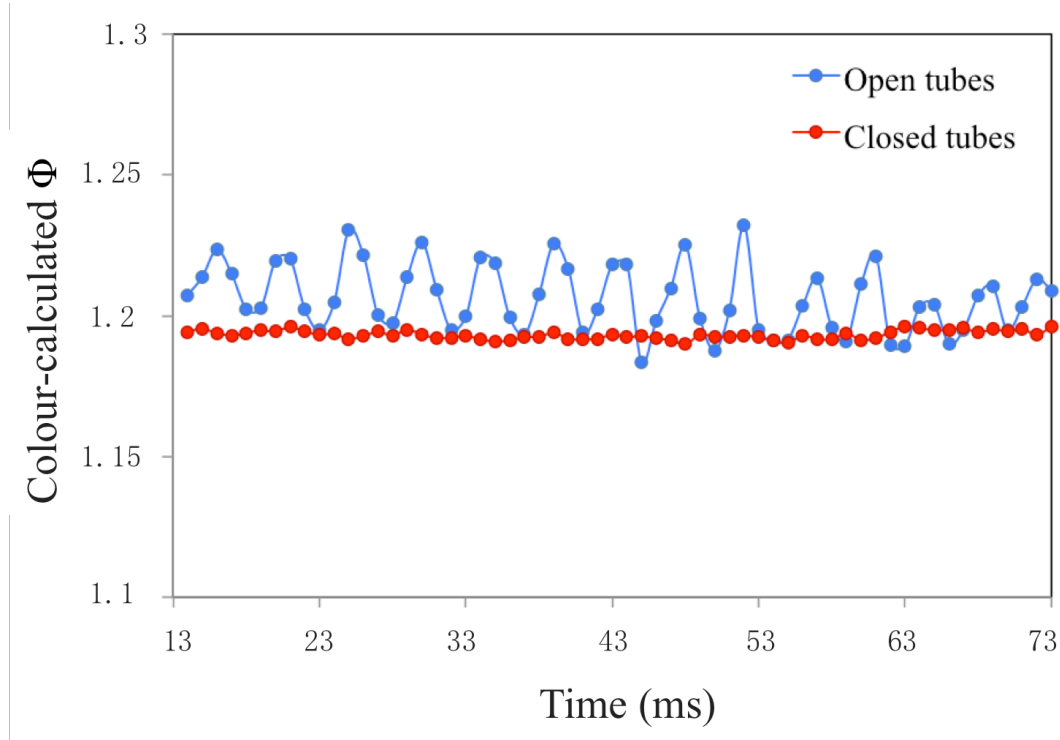


Figure 4. 15: Processed  $\text{CH}^*/\text{C}_2^*$  ratio maps of  $\Phi = 1.2$  with propane/air flame recorded at 1000

fps.

As shown, dramatic changes in the  $\text{CH}^*/\text{C}_2^*$  ratio can be measured. These are particularly apparent in the images from 51 to 54 ms. At 51 and 52 ms, the flame is moved forward the unburned gases. There is a very clear red colour dominating at the flame front, meaning the  $\text{CH}^*/\text{C}_2^*$  ratio at the flame front increases. After that, at 53 and 54 ms, the flame is moved back to the burned gases, causing the colour to return to blue because the  $\text{CH}^*/\text{C}_2^*$  decreases. This phenomenon indicates a modification of the reaction mechanism at the flame front. This chemical change could be related to the oscillation phenomenon. No oscillation occurs during the flame propagation in closed tubes; its colour remains blue during propagation, so the  $\text{CH}^*/\text{C}_2^*$  ratio maps of closed tube cases are not shown. According to the previous study described in Section 4.3.3, the  $\text{CH}^*/\text{C}_2^*$  ratio can be related to the equivalence ratio to identify the flame fuel/air mixture. For the camera employed in this case study, the measured equivalence ratio can be calculated by Eq. 4.10. The colour-calculated  $\Phi$  of the real  $\Phi = 1.2$  propane/air flame propagation in both closed and open tubes are plotted in Figure 4.16.



**Figure 4. 16: The colour-calculated  $\Phi$  of the real  $\Phi = 1.2$  propane/air flame propagation in both closed and open tubes.**

The colour-calculated  $\Phi$  of the closed tube case is shown by red dots. The values are nearly constant at about 1.19 (standard deviation: 0.007), which is quite close to the real  $\Phi = 1.2$ . This proves the accuracy of the proposed colour-based flame chemiluminescence measurement and indicates that it has potential for measuring equivalence ratio dynamics. For the open tube case (plotted in blue dots), the values fluctuate around 1.21 with  $\pm 0.02$  amplitudes. Since the fuel/air was well mixed beforehand, the real  $\Phi$  should be constant. Therefore, it should be stated here that the named colour-calculated  $\Phi$  is not suggested as the real  $\Phi$ . However, it can indicate fuel/air reaction within the flame. The reason for the fluctuation in the colour-calculated  $\Phi$  still needs further investigation.

The fluctuation frequency of colour-calculated  $\Phi$  in the open tube case is 226.7 Hz, as calculated by FFT. This matches the frequency derived by tracking the flame leading point as discussed in the previous section. To find the relationships between flame position oscillation and colour-calculated  $\Phi$  fluctuation, a comparison is plotted in Figure 4.17.

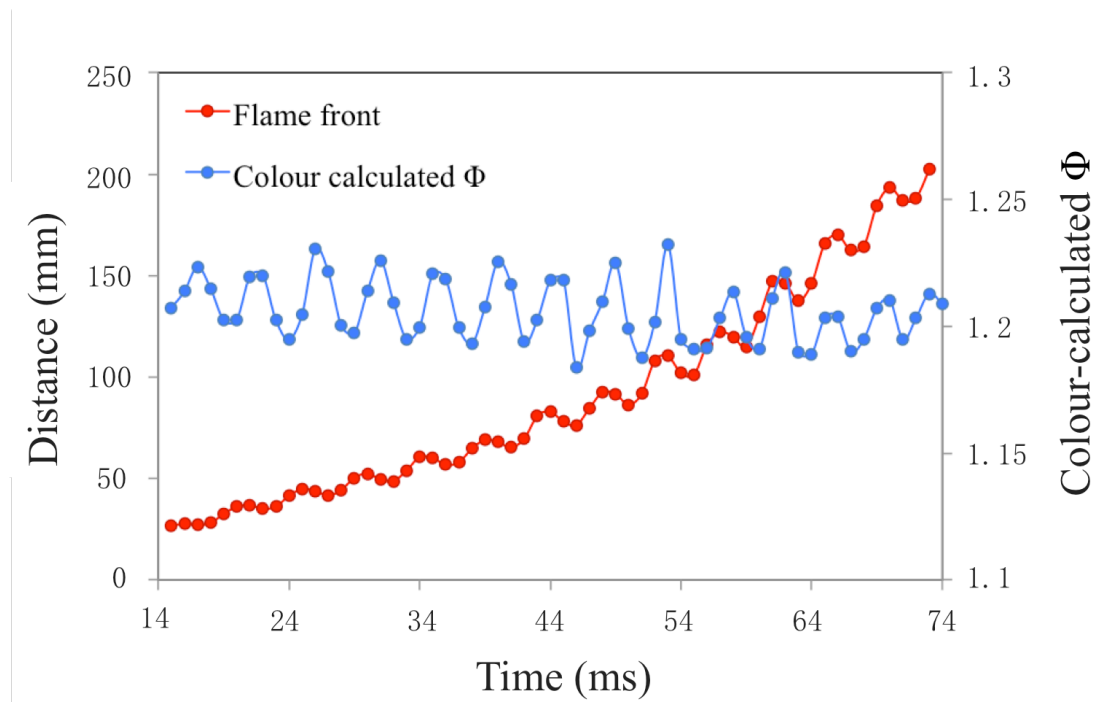


**Figure 4. 17: Colour-calculated  $\Phi$  and flame front position against time from the beginning of the recording.**

This figure indicates the relations between the flame front position and the calculated equivalence ratio. The flame front is plotted in red dots and the colour-calculated equivalence ratio is plotted in blue dots. Changes in the colour-calculated  $\Phi$  can be seen throughout. The fluctuation amplitude in the colour-calculated  $\Phi$  increases slightly at the beginning and reaches its peak at about 40 ms; then it decreases. The

flame front position curve shows that oscillations are presented throughout the filming. However, its oscillation amplitude increases from the beginning to the end, which is different from the colour-calculated  $\Phi$  fluctuation. The flame front position is in phase with the colour-calculated  $\Phi$  as the flame moves backwards into the burned gases, the colour-calculated  $\Phi$  decreases, and vice versa.

### 4.4.4 Conclusions

In this case study, a high-speed stereo colour imaging system was employed in the measurement of premixed propane/air flame propagation under different equivalence ratios  $0.8 < \Phi < 1.6$  in both closed and open tubes:

- In the closed tube case, the flame was steady during propagation. However, when the flame passed down the open tube, a self-induced fluctuating flow/pressure field was generated that the flame had to move back. Oscillations in the flame's progress were found at  $1.1 < \Phi < 1.4$ . The maximum oscillation amplitude of  $\pm 10$  mm occurred at the centre of the tube. The oscillation frequency was constant at 220 Hz. There is no further influence on the flame oscillation by different flame properties, once the acoustic field was generated.
- For small fluctuation, it propagates with caterpillar-like movement. The noticeable changes in the flame structure could be distinguished during oscillations amplified. The unburned gases moved into the burned gases and rapid accelerations of the flame into the unburned gases. When it reached its

peak oscillation amplitude, the unfiltered flame velocity attained 4.9 m/s. It was twice higher than the flame oscillation was small, and that was an order of magnitude higher than the laminar burning velocity.

- The influence of the pressure fluctuations on the flame chemistry was measured by the  $\text{CH}^*$  and  $\text{C}_2^*$  emissions using the proposed colour-based flame chemiluminescence measurement. The  $\text{CH}^*/\text{C}_2^*$  ratio was modelled to obtain  $\Phi$ . The colour-calculated  $\Phi$  was constant in closed tubes but fluctuated in open tubes. The  $\text{CH}^*/\text{C}_2^*$  fluctuation was in phase with the flame front position oscillation, as the flame moved back to the burned gases, the colour-calculated  $\Phi$  decreased, and vice versa. The  $\text{CH}^*/\text{C}_2^*$  fluctuation frequency matched with the flame structure oscillation frequency.
- Observation of the  $\text{CH}^*/\text{C}_2^*$  maps might show that, the higher its value was, the ‘better’ the local burn was; these are fuel-rich flames and higher  $\text{CH}^*/\text{C}_2^*$  values are typical of a leaner  $\Phi$ . Although the colour-calculated  $\Phi$  fluctuated during propagation in open tubes, this does not suggest that there are variations in the real  $\Phi$ , as the unburned gases were fully mixed. Further work is necessary to determine the meaning of the colour-calculated  $\Phi$  or the obtained  $\text{CH}^*/\text{C}_2^*$  ratio, although it is clear that significant alterations in the flame chemistry might have occurred in the flames observed here.



## **4.5 Case 2: flame ignition to impinging**

### **4.5.1 Introduction**

The ignition process is a vital issue in the study of combustion. The burning characteristics of different reactant mixtures are important elements that can affect the flame optical profile through their characteristic combustion behaviours. A better understanding of these processes is important to estimate burning characteristics, combustion efficiency, and interaction between flame and wall in many combustor devices.

The ignition position has a significant effect in forming different flame patterns. In a premixed impinging flame, many flame modes can be established within the same reactant mixture by changing the ignition location (Zhang & Bray, 1999; Foat, Yap, & Zhang, 2001). The observed flame modes are very different in their visible radiations as well as spatial burning behaviours. These differences would significantly affect the flame to wall impingement and heat transfer.

A phenomenon of ignition delay is widely observed during flame ignition. Usually, the first sign of flame does not appear at the time of ignition. Dec and Espey observed that yellow-red flame occurs after ignition, and the length of this period depends on the fuel, mixture, temperature, and density (Dec & Espey, 1998). In addition, Nagase and Funatsu (Nagase & Funatsu, 1989) demonstrated that signs of radical chemiluminescence emission signals were presented before the soot radiation. Many studies have successfully measured some radical emissions at the beginning of the

flame ignition, such as  $\text{OH}^*$ ,  $\text{CH}^*$ , and  $\text{C}_2^*$  (Chou & Patterson, 1995; Aleiferis, Hardalupas, Taylor, Ishii, & Urata, 2004). Therefore, in the initial diffusion combustion reaction process of different combustion conditions, there exists an apparent and quantifiable physical flame property.

Obviously, visualising the ignition process of combustion is an important research orientation to analyse variances in the multi-spectral flame radiation signal behaviours, which is useful for combustion diagnostics and optimisation. Here, different fuels, methane ( $\text{CH}_4$ ) and propane ( $\text{C}_3\text{H}_8$ ), were ignited under different flow rates at different ignition positions. A high-speed stereo colour imaging system was employed to measure the flame ignition-to-impinging behaviour. The previous proposed colour-based flame chemiluminescence method was applied for data analysis from 1D to 4D. To analyse the 3D chemical reaction, the colour-based flame chemiluminescence was incorporated with the 3D reconstruction method.

### 4.5.2 Experimental setup

The schematic of the experimental setup is shown in Figure 4.18. The experiments on the flame ignition-to-impinging process were conducted on a free-burning atmosphere impinging burner with a nozzle diameter of  $4.57 \times 10^{-3}$  m, the same as that used by Wang et al. (2012) and Huang et al. (2012). A steel plate 300 mm in diameter was used for flame impingement, placed in a vertical traversing system, as described by Huang (2012), with a distance of 150 mm above the nozzle. The  $\text{CH}_4$  and  $\text{C}_3\text{H}_8$  fuels were stored individually in cylinders and were supplied at standard

volumetric flow rates of 4.2, 8.4, and 16.8 L/min, respectively. The flow rates were controlled by an electronic digital mass flow controller using the LabView programme. In addition, the ignition positions were assigned at the bottom (near the nozzle,  $l \approx 0$  mm), middle ( $l = 75$  mm) and top (near the plate,  $l \approx 150$  mm);  $l$  is the distance between the nozzle and the ignition position. Typically, five measurements were performed for each condition.

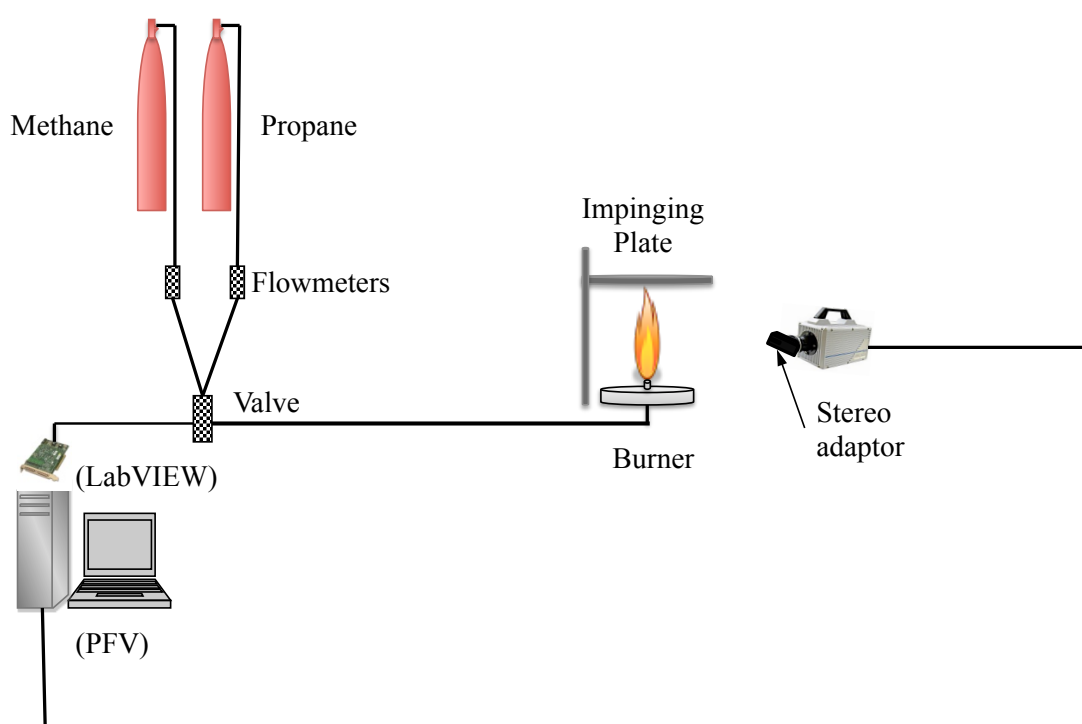


Figure 4. 18: Schematic of the experimental setup.

For data acquisition, a high-speed stereo colour imaging system was employed to record stereo colour image sequences. The system comprised a Photron SA-4 high-speed colour camera with a stereo adaptor placed in the left/right configuration. As mentioned by Gaydon and Wolfhard (1979), there is a radiation emission strength difference between  $\text{CH}_4$  and  $\text{C}_3\text{H}_8$ . The higher-order the hydrocarbon is, the more

intense the flame emission is. Therefore, a higher frame rate of 1000 fps was set for  $C_3H_8$  measurements and 500 fps for  $CH_4$  cases.

### 4.5.3 Image processing

To obtain useful information for analysis, the image data were processed. The image processing procedure includes several steps, as shown in Figure 4.19.

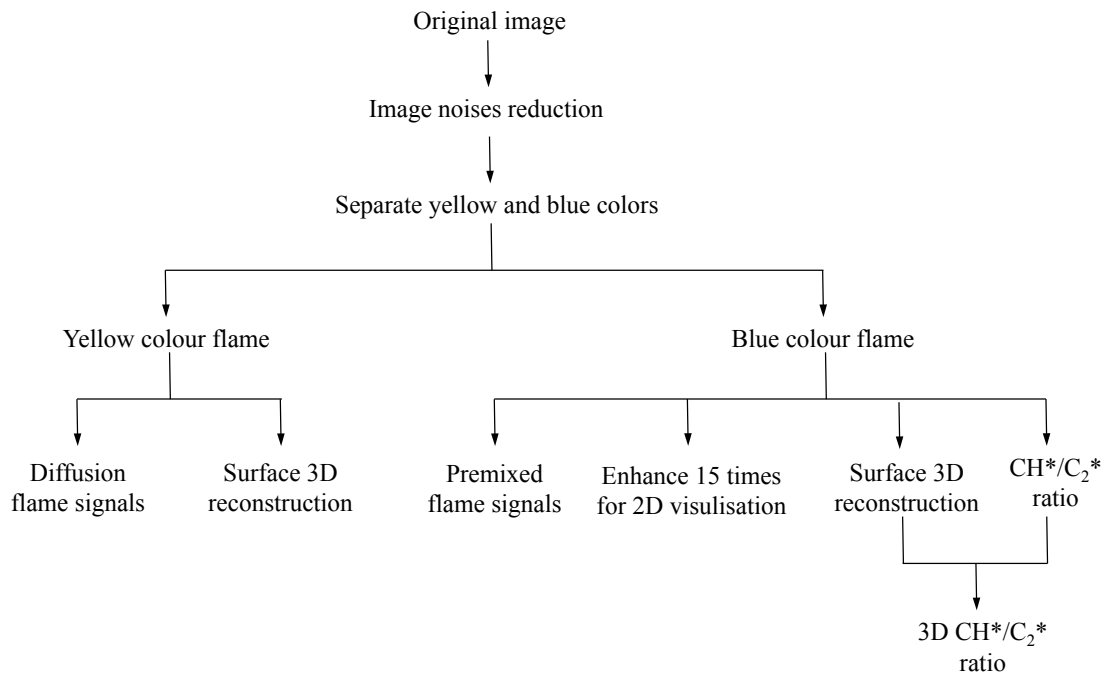


**Figure 4. 19: Image processing procedure.**

First, the original colour image data were processed to remove unexpected noise; the processing details are the same as those discussed in Section 4.3.2.2. Second, the blue flame profile and the yellow flame profile were segmented. For segmentation, the images were converted from the RGB to the HSV model. The hue layer values were multiplied by 360. According to Huang's (2008) investigation, the value range

from  $120^\circ$  to  $240^\circ$  was selected as the blue flame profile, while the yellow flame profile was set at  $1^\circ$  to  $60^\circ$ .

After the colour segmentation, the selected blue flame signals were enhanced by enhancing its RGB values by 15 times (to see the signals clearly and without saturation). Then the enhanced blue flame image was added to the selected yellow flame image; samples are shown in Figure 4.20. It should be noted that the enhanced images were only used for visualisation; any calculation processes related to the quantifying of intensity values utilised the non-enhanced data.

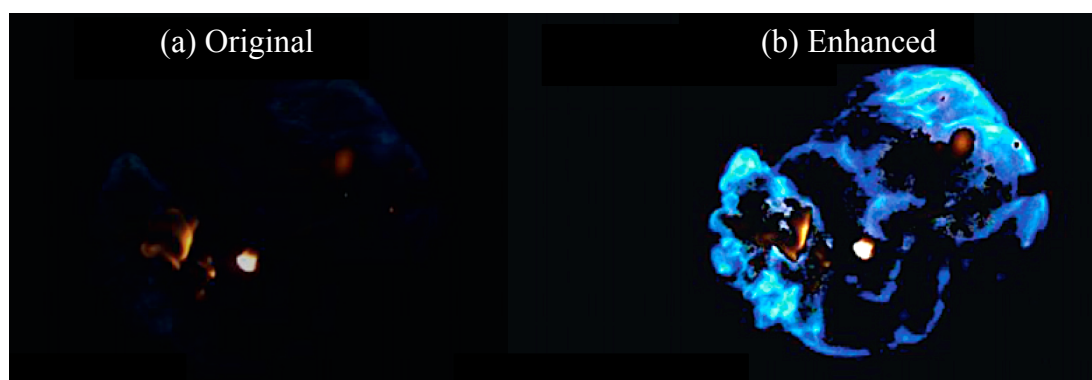


**Figure 4. 20: Samples of images: (a) original image and (b) blue colour-enhanced image.**

The intrinsic and extrinsic camera parameter calibration is a key step for 3D reconstruction. Therefore, before the experiments, the camera parameters were calibrated. The calibration board was photographed in five different positions. The five captured images were then loaded and processed in the Matlab software. After the corner points in both left and right views were selected and the corresponding points on left and right views matched, the intrinsic and extrinsic camera parameters were worked out (details are discussed in Section 3.3.4.2).

For the 3D reconstruction, pairs of corresponding points between the left and the right views in the pre-processed image data were selected. The distance (the y-coordinate difference between the selected pixel in the left view and its corresponding pixel in the right view) was selected as the disparity (the difference between the projected locations between different views). Using Eq. 2.21, the depth information can be calculated. The 3D reconstruction process was conducted using a pre-written Matlab programme (Wang, 2009). Figure 4.21 shows samples of processed 2D image pairs and their 3D reconstruction structure.

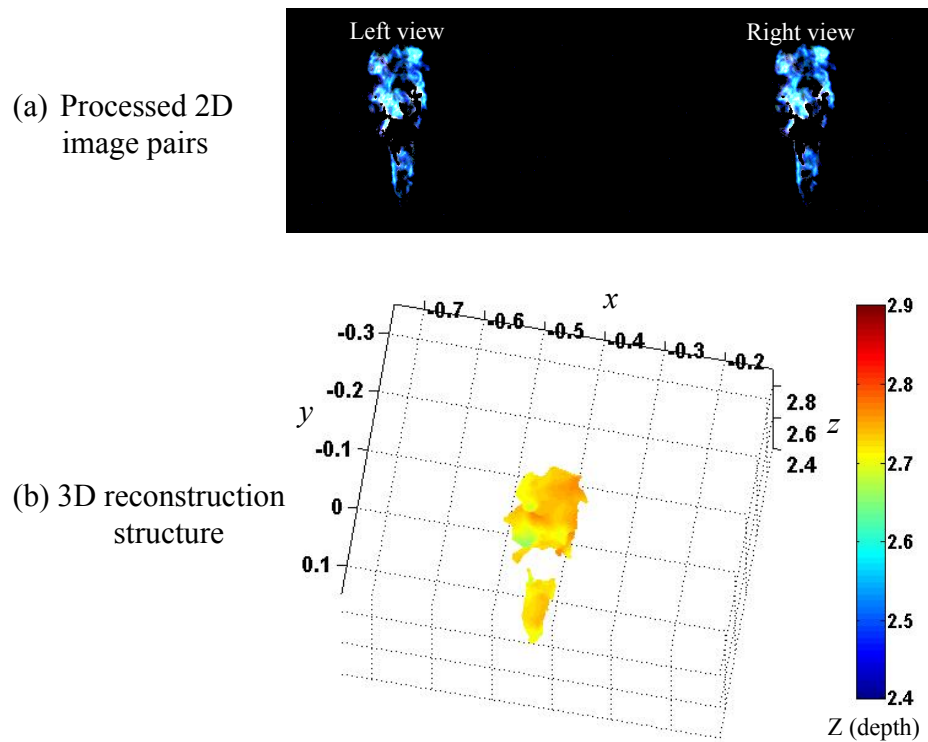


**Figure 4. 21: Samples of (a) processed 2D image pairs and (b) their 3D reconstruction structure.**

In premixed hydrocarbon flames, the visible chemiluminescence is mostly attributed to  $\text{CH}^*$  and  $\text{C}_2^*$ . Assuming that the segmented blue flame colour intensities are only contributed to by  $\text{CH}^*$  and  $\text{C}_2^*$  emissions. According to Eq. 4.8, the  $\text{CH}^*$  and  $\text{C}_2^*$

concentrations can be calculated. Therefore,  $C_2^*$  expression was considered  $1.79I_G$ , whereas  $CH^*$  was considered  $3.03I_B - 3.3I_G$ . Since each set of stereo image data includes two views of the flame and the flame colour in both views is the same, only the left view was used to calculate the  $CH^*$  and  $C_2^*$  concentration. The calculated  $CH^*/C_2^*$  ratios were then overlaid on the previously reconstructed 3D structures. Thus, the 3D  $CH^*/C_2^*$  ratio map can be obtained; an example is shown in Figure 4.22.

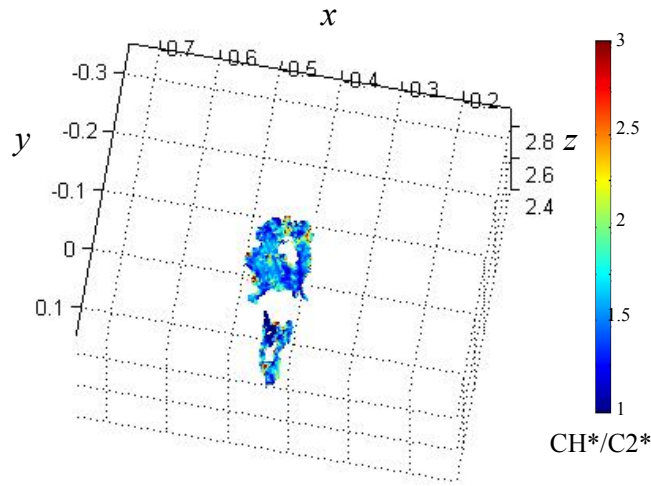


Figure 4. 22: A sample of a 3D  $CH^*/C_2^*$  ratio map.

## 4.5.4 Results and discussion

### 4.5.4.1 Structures analysis

The flame ignition dynamics were captured by high-speed stereo colour imaging measurement. Each set of image data includes two views of the measured flame, and the image colours of the flame profiles in both views are the same. Therefore, in the 2D image analysis, only the left view from each set of image data is discussed. In each image, two colour profiles exist in each flame structure during flame ignition to

impinging. Samples of 16.8L/min  $C_3H_8$  diffusion flame appearance from 44 ms to 128 ms after ignition at the bottom ignition location are shown in Figure 4.23. The blue profile is attributed to the radical chemiluminescence of the premixed flame portion, while the yellow profile is the diffusion signal attributed to the soot radiation. Their behaviours and relations are discussed below.

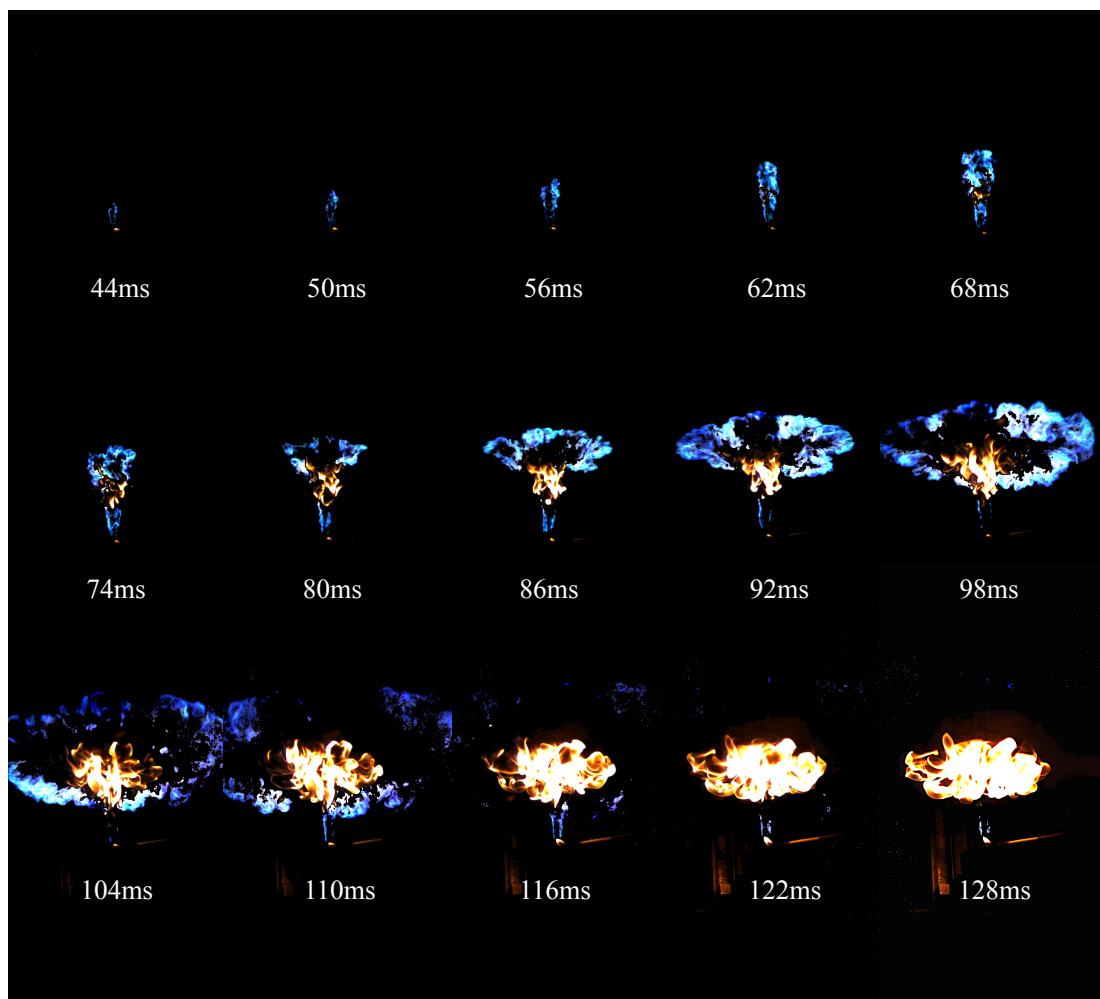


**Figure 4. 23: 2D flame appearance of 16.8L/min  $C_3H_8$  diffusion flame with bottom ignition location.**

From 44 ms to 68 ms, the flame is dominated by the blue colour because of the chemiluminescence emissions. The early flame propagation is spearheaded by the



premixed blue flame kernel as it propagates towards the plate. The flame structure is mostly developed in the vertical direction. No clear signals from the yellow flame can be seen until 68 ms (the yellow point at the bottom of flame is the tip of the ignitor, which was heated, presenting a yellow spot). Unlike the blue flame that appears near the nozzle after ignition, the yellow diffusion flame occurs in the blue flame some distance away from the nozzle exit.

From 74 ms to 98 ms, the flame profile is a combination of yellow and blue; the yellow flame exists in the middle region, while the blue flame occurs near the nozzle and plate. At 74 ms, the front of the blue flame is approximately planar, because it impinges the steel plate, and then it starts to travel outward along the radial direction of the plate. Unlike the blue flame's initial development behaviour, the yellow flame structure grows in all directions except downstream to the nozzle.

At 104 ms, the blue flame signal becomes weaker because the premixed flame reaches the plate boundary. Hence, it spreads until it disappears. At the same time, the yellow flame impinges the plate. Consequently, it gathers close to the plate and increases in both surface area and colour intensity. After 116 ms, the flame is dominated by yellow, and blue flame only occurs near the nozzle. By measuring the ignition to impinging from different flow rate cases, the flame development processes are similar to those described above. This means that this flame structure development in ignition-to-impinging behaviour would be affected little by flow rates.

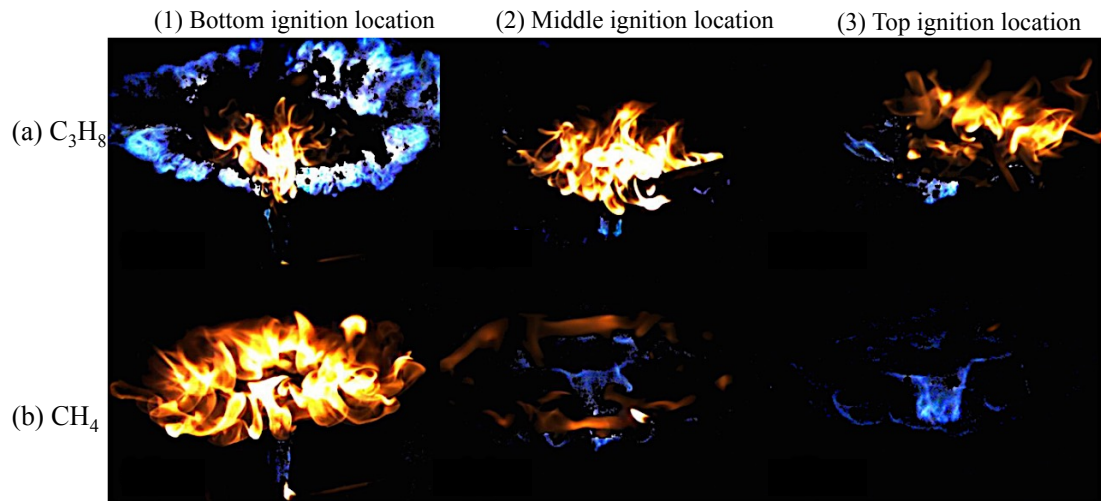


**Figure 4. 24: 2D Flame structure visualisation of  $C_3H_8$  and  $CH_4$  100 ms after ignition at the bottom, middle, and top, respectively.**

However, the fuel composition and the ignition location have a significant influence in flame ignition-to-impinging development. As shown in Figure 4.24, the flame structure samples of 16.8L/min  $C_3H_8$  and  $CH_4$  flames were captured 100 ms after ignition at different locations.  $C_3H_8$  is shown in Figure 4.24(a), while  $CH_4$  is shown in Figure 4.24(b). Ignition at the bottom, middle, and top locations are indicated by (1), (2), and (3), respectively.

For ignition at the bottom location in the  $C_3H_8$  case, as shown in Figure 4.24(a1), the blue flame position precedes the yellow flame position. Since, at the moment that this image was captured, the blue flame profile had already reached the plate's boundary, while the yellow flame profile was just impinging to the centre of the plate. However, in Figures 4.24(a2) and (a3), only a slight blue flame exists near the nozzle at the bottom of the image. The difference can be attributed to the ignition

locations. Since the images in Figure 4.24 were all captured at 100 ms after ignition, for higher ignition locations at the middle (a2) and top (a3), the blue flame had already travelled out of the plate boundary, thus the blue only occurred at the bottom. In addition, the observed flame intensity is less intense in higher ignition location cases. The reason could be that the local reactant state downstream would gradually become leaner with an increase in distance from the nozzle exit.

In contrast, in CH<sub>4</sub> cases, the flame profiles showed a more drastic change with a change in ignition location. As shown in Figure 4.24(b1), the observed flame profile is dominated by yellow flame, and the premixed blue flame had already travelled out of the captured image. Compared to Figure 4.24(a1), the flame in (b1) travelled faster. This is because CH<sub>4</sub> is lighter than C<sub>3</sub>H<sub>8</sub>. For the higher ignition locations at the middle (b2) and top (b3), the yellow flame intensity weakened. Especially in Figure 4.24 (b3), yellow flame can hardly be observed. This is similar to that in Figure 4.24(a2) and (a3). This is because the higher ignition locations can improve the levels of partial premixing before ignition. However, compared to Figure 4.24(a2) and (a3), the blue flame signals became stronger. As demonstrated in this investigation, this spatial burning influence is obviously fuel-specific, but this conclusion requires further research to confirm.

#### **4.5.4.2 Signal analysis**

To compare the yellow profile of the diffusion flame signal with the blue profile of the premixed flame signal quantitatively, a signal ratio of  $I_D/I_P$  is applied. Based on

this  $I_D/I_P$  signal ratio, the relations between a flame's colour signals and its area within the diffusion and premixed flame profiles can be observed.  $I_D$  is the total diffusion flame intensity, which indicates the mean intensity of the yellow signal and its spatial presence and  $I_P$  represents that for premixed blue flame signals. The logarithmic scale of the  $I_D/I_P$  signal ratio for the  $C_3H_8$  and  $CH_4$  flame ignition processes under different fuel flow rates and ignition locations are plotted in Figures 4.25 and 4.26, respectively. When the  $\log(I_D/I_P) = 0$ , it means that these two signals are equivalent, and  $\log(I_D/I_P) > 0$  means that the flame is dominated by diffusion signals, while  $\log(I_D/I_P) < 0$  means that it is dominated by premixed signals. The signal ratios of the different flow rates of 4.2, 8.4, and 16.8 L/min are plotted in red, blue, and black, respectively. Different ignition locations at the bottom, middle, and top are shown in sub-figures (a), (b), and (c) respectively.

Figure 4.25(a) shows the  $C_3H_8$  flame ignited at the bottom location. The ratio is below zero before 0.1s, which means that the flame was dominated by the premixed signals in the beginning of ignition. After 0.1s, the ratio increased significantly, which means that the diffusion signals increased after this time. Last, the ratio dropped and then stabilised. The moment that is assumed to be stable is when the  $\log(I_D/I_P)$  ratios under different flow rates are almost the same. A similar phenomenon is also found in Figure 4.25(b) and (c). It could be assumed that different ignition locations have little influence on the chemical reaction during  $C_3H_8$  flame ignition.

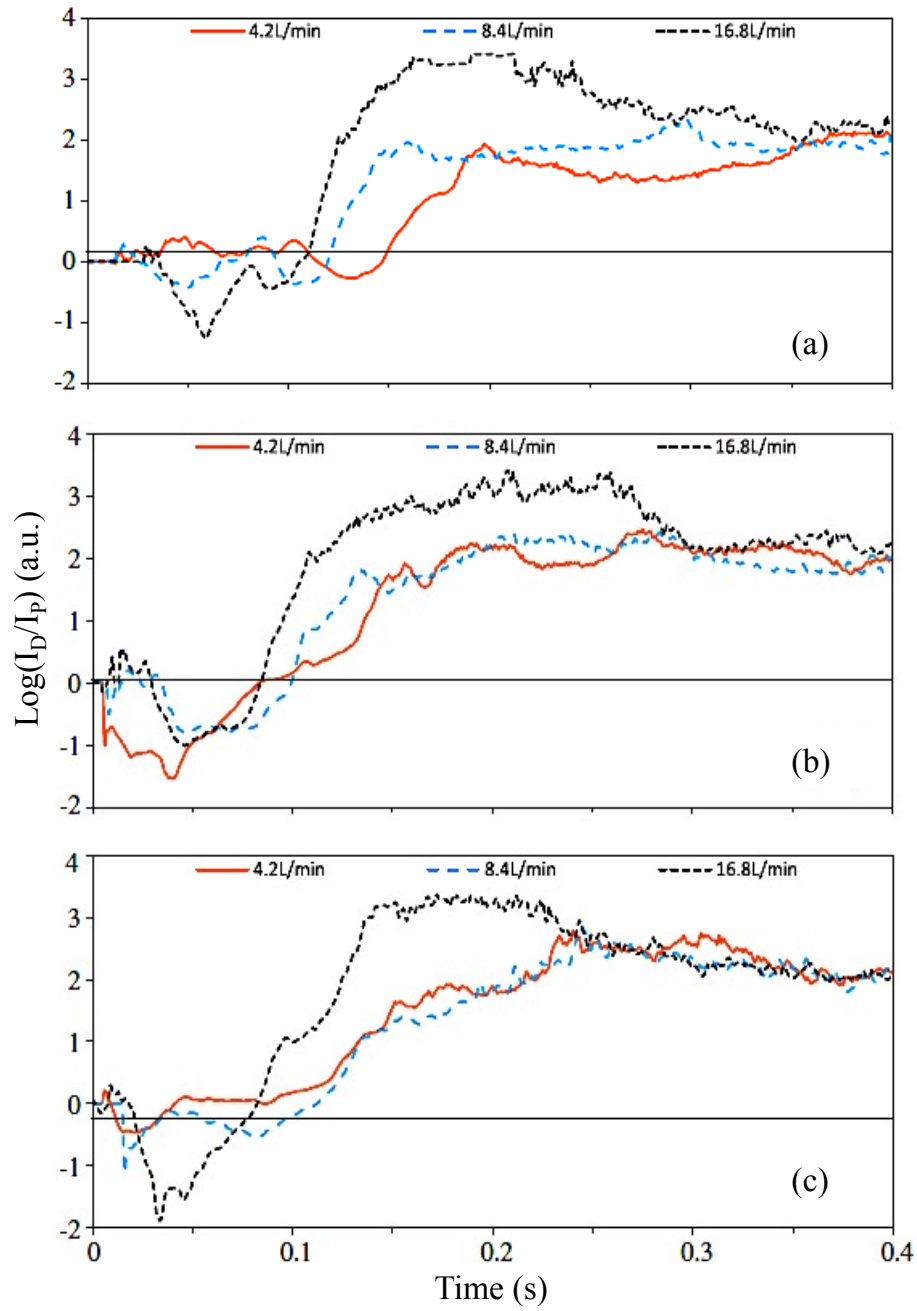


Figure 4. 25:  $\log(I_D/I_P)$  signal ratio of the  $C_3H_8$  flame ignition process under different flow rates

(4.2 L/min plotted in red, 8.4 L/min plotted in blue, and 16.8 L/min plotted in black) and

different ignition locations at the (a) bottom, (b) middle, and (c) top.

However, the higher ignition location would reduce the time delay with which the diffusion signal occurs. As shown in Figure 4.25(a), the  $\log(I_D/I_P)$  ratio becomes

positive at about 0.1s after ignition. This phenomenon occurred earlier, at about 0.008s and 0.007s, in Figure 4.25(b) and (c), respectively. A comparison of the different flow rate cases of 4.2L/min (red line), 8.4L/min (blue line), and 16.8L/min (black line) shows that the 16.8L/min case is always fastest in turning positive, which means that a higher flow rate could reduce the time to the diffusion signal.

As Figure 4.25 shows, the  $\log(I_D/I_P)$  ratio would finally become stable at a value of about 2. This means that the final  $\log(I_D/I_P)$  signal of  $C_3H_8$  ignition is constant, with little influence from changing flow rates and ignition locations. However, it seems that, with higher ignition locations, the period before the flame becomes stable becomes shorter, as the ratios reach a constant value of 2 at 0.35s, 0.3s, and 0.25s, as shown in Figure 4.25(a), (b), and (c), respectively.

However, in  $CH_4$  cases (Figure 4.26), the trends of the ratio were quite different from those in  $C_3H_8$  cases (Figure 4.25). The changed ignition locations shown in Figure 4.26 significantly increased the premixed flame signals. As shown from the sub-figures, the ratio in Figure 4.26(a) was negative before 0.12s; and in Figure 4.26(b), this period was about 0.03s longer; whereas in Figure 4.26(c), the ratio was almost negative all the time with a discontinuity signal that dropped to zero because of no yellow signal could be detected. In contrast of the flow rate influence, unlike  $C_3H_8$  ignition, the  $\log(I_D/I_P)$  ratios of the different flow rates do not reach the same value in the end. The reason may be that the captured sequences are not long enough to detect

the phenomenon. Furthermore, higher flow rates increased the premixed signal, as the ratios plotted in black were almost the lowest.

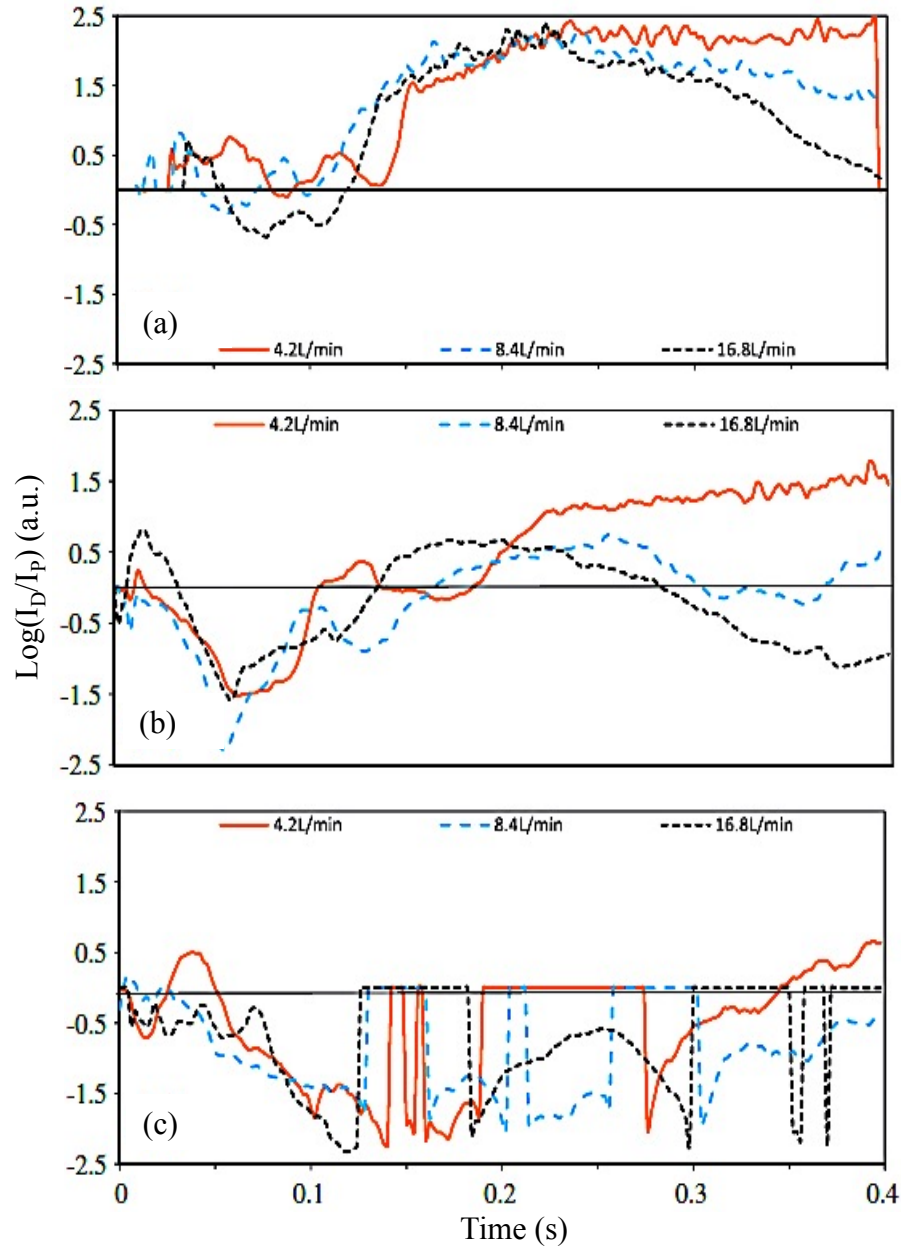


Figure 4. 26:  $\log(I_D/I_P)$  signal ratio of the CH<sub>4</sub> flame ignition process under different flow rates (4.2 L/min plotted in red, 8.4 L/min plotted in blue, and 16.8 L/min plotted in black) and different ignition locations at the (a) bottom, (b) middle, and (c) top.

The ignition locations and flow rates show very different effects on the ignition-to-impinging behaviours for both  $C_3H_8$  and  $CH_4$  diffusion flames. The reasons could be attributed to different fuel characteristics or different shutter speed settings. A higher shutter speed would cause blue flame signals to be lost in the  $C_3H_8$  cases. Further experiments need to investigate these two considerations.

#### **4.5.4.3 3D structures**

The 3D flame structures of the 16.8L/min  $CH_4$  and  $C_3H_8$  ignited at the bottom position were reconstructed. The blue and yellow flame profiles of  $CH_4$  are shown in Figures 4.27 and 4.28, while the corresponding  $C_3H_8$  cases are shown in Figures 4.29 and 4.30 respectively. These 3D reconstruction structures clearly indicate the variances between premixed blue and yellow diffusion signals.

For the  $CH_4$  case, the blue flame propagates vertically prior to reaching the plate from 80 to 92 ms, as shown in Figure 4.27. Evidence can be found that the structure colour (the depth of the flame structure) changes slightly. The flame kernel reaches the plate at 98 ms. Then it starts to spread across the plate surface, as a greater variance in depth in the flame structures can be seen (the top left corner of the flame turned green, and the top right corner turned orange). After that, from 104 to 122 ms, the flame reaches the plate boundary and begins to diminish, creating a discontinuous visualisation and becoming smaller fragmented structures. The different colour in the depth can be observed clearly around the flame boundary as the flame grows in  $z$  direction. The empty hole in the blue flame profile is where the yellow flame exists.



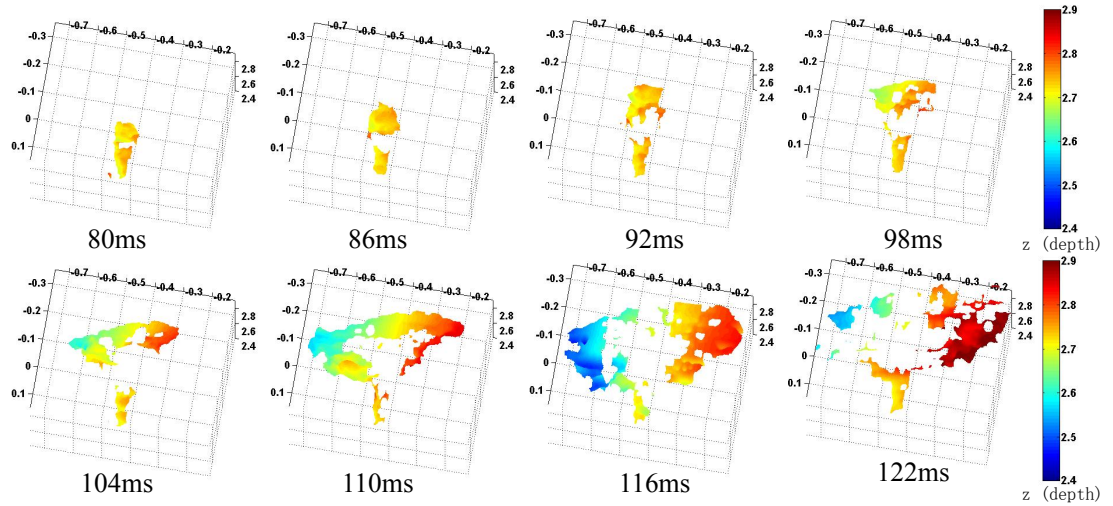


**Figure 4. 27: Premixed blue flame 3D structures of 16.8L/min CH<sub>4</sub> diffusion with ignition at the bottom location.**

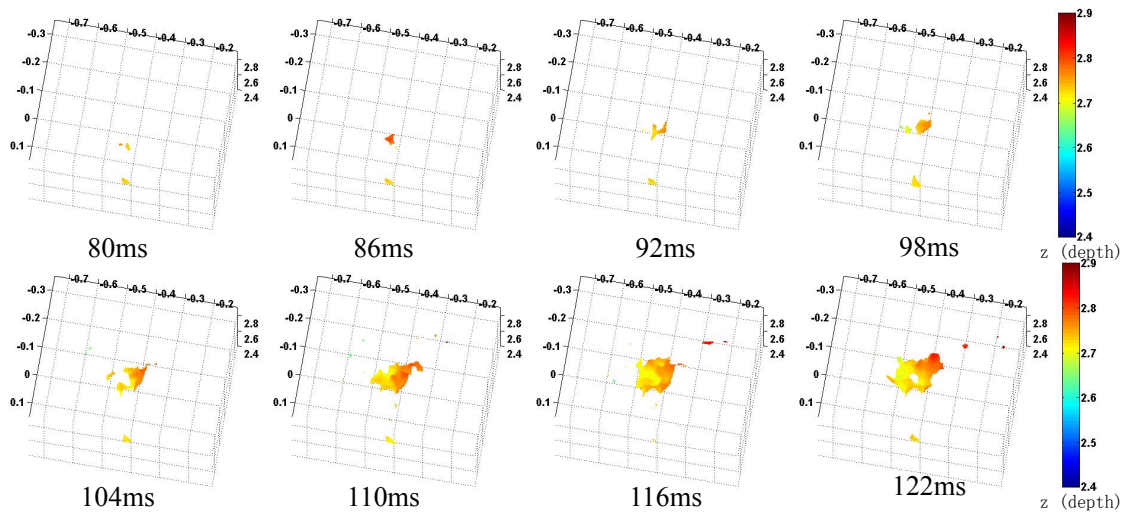


**Figure 4. 28: Yellow diffusion flame 3D structures of 16.8L/min CH<sub>4</sub> diffusion with ignition at the bottom location.**

However, the corresponding yellow flame structure in Figure 4.28 shows a very different behaviour. The yellow flame profiles are smaller when compared with those in Figure 4.27. The development of the yellow flame structure starts from a point and

expands in every direction. However, it grows slowly; the depth presented by the colour remains almost the same.

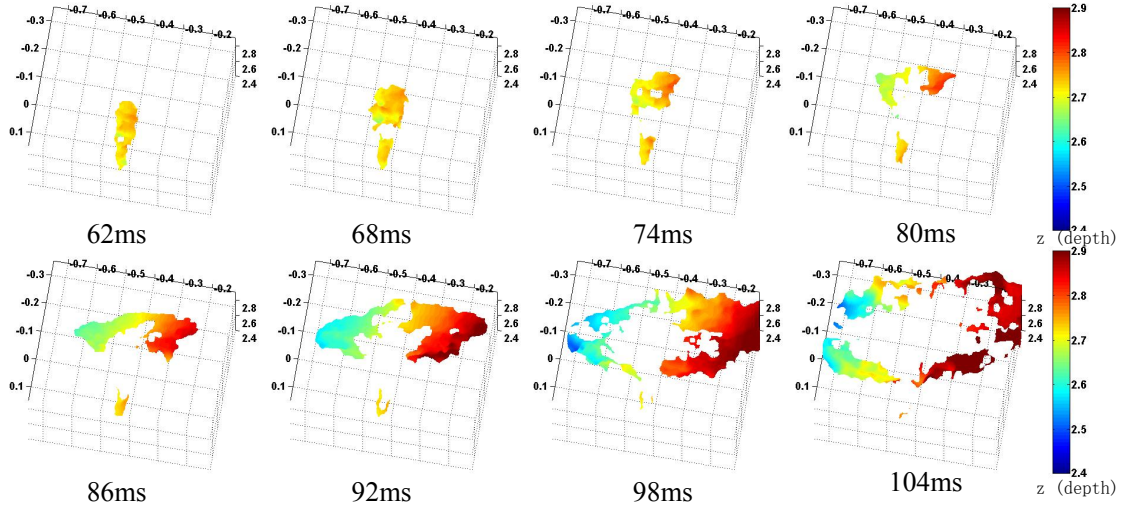


**Figure 4. 29: Premixed blue flame 3D structures of 16.8L/min  $C_3H_8$  diffusion with ignition at the bottom location.**

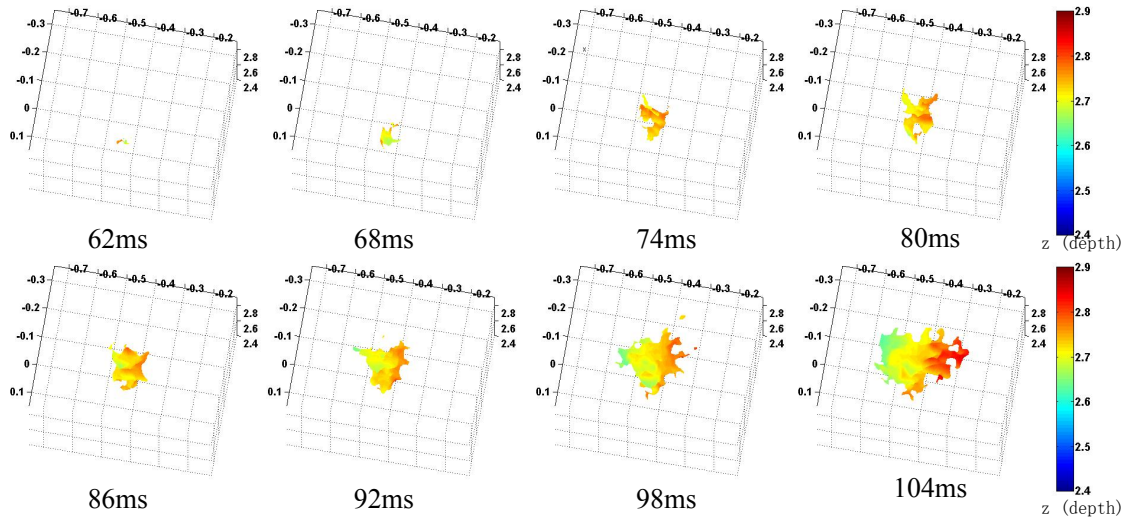


**Figure 4. 30: Yellow diffusion flame 3D structures of 16.8L/min  $C_3H_8$  diffusion with ignition at the bottom location.**

Comparatively, the flame 3D reconstruction for the  $C_3H_8$  case exhibits a similar phenomenon with that in the  $CH_4$  case. The blue flame occurs before the yellow

flame. Nevertheless, there are still some differences. 80 ms after ignition, the blue flame is already impinged against the plate and starts to travel along the surface of the plate in Figure 4.29 while in the corresponding CH<sub>4</sub> case shown in Figure 4.27, the blue flame is still propagating vertically. At 104 ms, the C<sub>3</sub>H<sub>8</sub> blue flame structure is similar to that of CH<sub>4</sub> at 122 ms. The temporal discrepancy between CH<sub>4</sub> and C<sub>3</sub>H<sub>8</sub> occurs because the flame propagation velocity of C<sub>3</sub>H<sub>8</sub> is faster than that of CH<sub>4</sub>. In addition, the observed flame profile of the C<sub>3</sub>H<sub>8</sub> yellow flame in Figure 4.30 is generally larger and grows in depth with a greater variation because of the variation in carbon content and the associated molecular density between CH<sub>4</sub> and C<sub>3</sub>H<sub>8</sub>.

#### 4.5.4.4 3D CH<sup>\*</sup>/C<sub>2</sub><sup>\*</sup> ratio

Further analysis of the difference in chemical reactions between C<sub>3</sub>H<sub>8</sub> and CH<sub>4</sub> ignition-to-flame processes is conducted in their 3D reconstruction; hence, the image colour-calculated local CH<sup>\*</sup>/C<sub>2</sub><sup>\*</sup> ratios were overlaid onto the reconstructed 3D flame surface. Figures 4.31 and 4.32 show the 3D CH<sup>\*</sup>/C<sub>2</sub><sup>\*</sup> ratio of C<sub>3</sub>H<sub>8</sub> and CH<sub>4</sub> at the 16.8 L/min flow rate ignited at the bottom location, respectively.

Since CH<sup>\*</sup>/C<sub>2</sub><sup>\*</sup> has a linear relation with the flame equivalence ratio, the 3D CH<sup>\*</sup>/C<sub>2</sub><sup>\*</sup> maps have potential in showing the dynamics of the fuel/air mixing state in the 3D space. The CH<sup>\*</sup>/C<sub>2</sub><sup>\*</sup> ratio values are denoted by the colour bar; the colour change from blue to red indicates the change in the CH<sup>\*</sup>/C<sub>2</sub><sup>\*</sup> ratio from a low value to a high value. As in the previous investigation of the relation between the CH<sup>\*</sup>/C<sub>2</sub><sup>\*</sup> ratio and

equivalence ratio described in Section 4.3.3, the flame 3D structure region presented by the blue colour indicates that more fuel exists in this flame mixture region, while the red colour means that there is less fuel in the region.

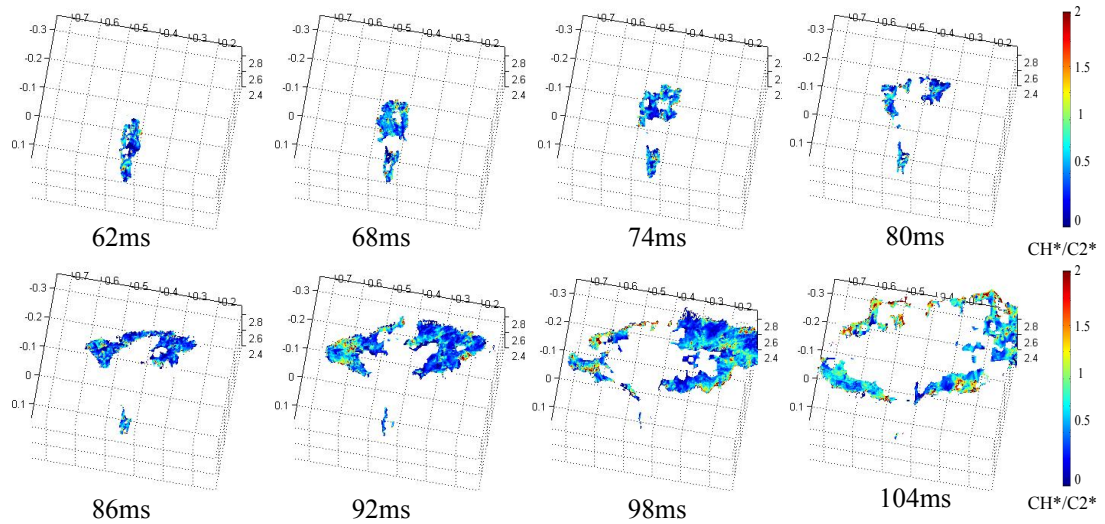


Figure 4. 31: 3D CH\*/C<sub>2</sub>\* ratio map of 16.8 L/min C<sub>3</sub>H<sub>8</sub> diffusion with bottom ignition for Fig.

4.29.

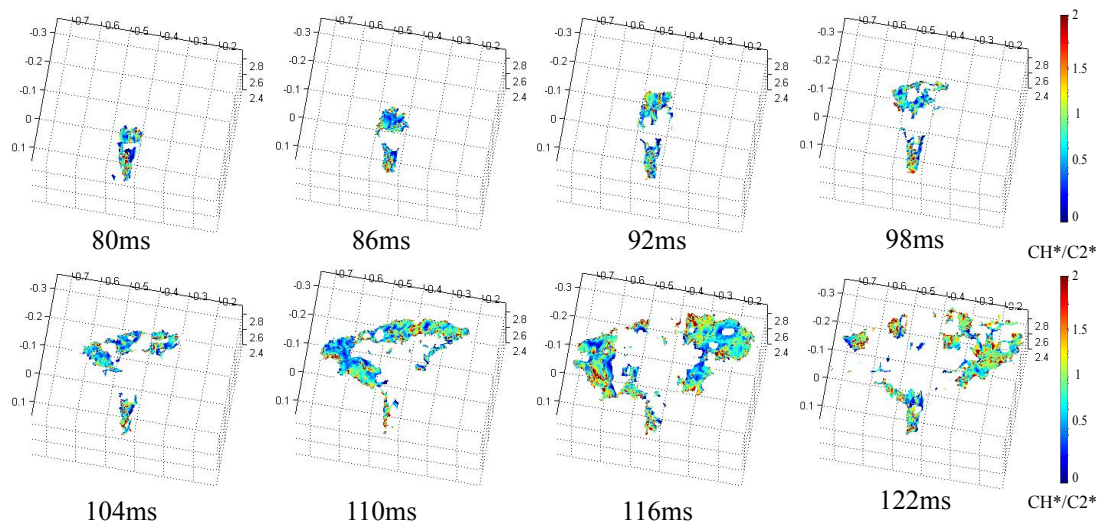


Figure 4. 32: 3D CH\*/C<sub>2</sub>\* ratio map of 16.8 L/min CH<sub>4</sub> diffusion with bottom ignition for Fig.

4.27.

Figure 4.31 shows the diffusion of  $C_3H_8$  ignition; from 62 to 80 ms, the colour of the 3D  $CH^*/C_2^*$  map is dominated by blue and greenish-blue, which means that the 3D  $CH^*/C_2^*$  ratio in this period is around 0.5, with a small variation. Then, most of the 3D  $CH^*/C_2^*$  map becomes pure blue at 86 ms; the ratio drops below 0.5 because, when the flame impinges to the steel plate at 86 ms, more unburned fuel is gathered at the plate surface. After that, the impinged flame begins to propagate to the boundary of the plate. When the flame reaches the plate's boundary at 92 ms, the  $CH^*/C_2^*$  ratio increases, so some parts of the 3D  $CH^*/C_2^*$  map turn greenish-blue and even red. This occurs because more air exists near the plate's boundary, which reduces the fuel/air mixture. At 98 ms, this phenomenon becomes clearer. At 104 ms, most parts of the 3D  $CH^*/C_2^*$  map become greenish-blue and green because more air exists in those regions. Thus, the average  $CH^*/C_2^*$  ratio increases to about 1. After that, the premixed flame signals diminish and disappear; only diffusion flame signals remain and dominate, as shown in Figure 4.23 at 122 and 128 ms. The reason could be that the impinging plate obstructs the  $C_3H_8$  travelling upward. The  $CH^*/C_2^*$  ratios increase from the centre to the boundary of the plate. This indicates that the highest concentration of the  $C_3H_8$  fuel/air mixture is at the plate centre, and the fuel/air concentration reduces linearly with the radius of the plate.

Figure 4.32 shows behaviour similar to that shown in Figure 4.31 for the  $CH_4$  ignition case. However, compared with Figure 4.31, the colour of the 3D  $CH^*/C_2^*$  maps for  $CH_4$  show more green. The global  $CH^*/C_2^*$  ratio in Figure 4.32 is higher.

Therefore, more  $\text{CH}^*$  is dominant in the premixed portion of the  $\text{CH}_4$  diffusion flame ignition. Before the flame impinges onto the plate, the colour of 3D  $\text{CH}^*/\text{C}_2^*$  map is dominated by a greenish-blue colour; the ratio is around 1. Similarly, the blue flame profile propagation also corresponds with a gradual increase in the  $\text{CH}^*$  concentration from 104 to 122 ms. The colour variation in the 3D  $\text{CH}^*/\text{C}_2^*$  map at 122 ms is smaller than that in the  $\text{C}_3\text{H}_8$  case at 104 ms because  $\text{CH}_4$  is lighter than  $\text{C}_3\text{H}_8$ , which causes less  $\text{CH}_4$  to be obstructed by the plate. The difference in the global  $\text{CH}^*/\text{C}_2^*$  ratios between  $\text{C}_3\text{H}_8$  and  $\text{CH}_4$  can certainly be attributed to the variation in their fundamental molecular structure. For example, the higher diffusivity of  $\text{CH}_4$  means that local air entrainment has a greater effect in the mixing of the fuel and air, resulting in a leaner local reactant mixture state. Obviously, many factors are involved in the complex combustion phenomenon that needs further investigation.

#### **4.5.4.4 Conclusion**

In this case study, the flame ignition-to-impinging behaviour of the  $\text{C}_3\text{H}_8$  and  $\text{CH}_4$  diffusion flames under different flow rates and ignition locations were investigated using a high-speed stereo colour imaging system:

- From the structure analysis, the yellow flame profile occurred with a time delay after ignition. The delay period of the diffusion flame signal in  $\text{CH}_4$  was shorter than that in  $\text{C}_3\text{H}_8$  because  $\text{CH}_4$  is lighter, leading to fast propagation, while the blue flame profile existed from the moment of ignition. With higher

ignition locations, the flame would impinge onto the plate faster. In contrast, a higher ignition location would reduce the yellow flame intensity; it is attributable to the fact that the partial fuel/air premixing time before burning is longer.

- The  $\log(I_D/I_P)$  ratio was proposed for the temporal and spatial quantitative analysis of the effect of variation of fuel, ignition location, and flow rate on the relations between diffusion and premixed signals.
  - For  $C_3H_8$ , a higher ignition location would reduce the delay period of the diffusion signal, so the flame signals would become stable sooner. The higher flow rates could also reduce the time delay of  $I_D$ .
  - For  $CH_4$ , higher ignition locations and flow rates both can enhance the premixed signals.
  - The difference in the effect on  $C_3H_8$  and  $CH_4$  could be a result of fuel differences or the imaging shutter speed setting difference, with the higher shutter speed for  $C_3H_8$  cases resulting in the loss of premixed signals.
- The 3D reconstruction structure development of the  $C_3H_8$  and  $CH_4$  flames was similar; the blue flame changed significantly in the  $z$  direction while travelling around the plate, while the yellow flame changed slightly in the  $z$  direction since it stayed in the centre of the plate instead of traveling around it.

- The proposed 2D image colour-based flame chemiluminescence measurement was combined with stereo imaging and 3D reconstruction. The 3D  $\text{CH}^*/\text{C}_2^*$  ratio map showed great potential in 3D chemical fuel/air mixture diagnostics for combustion. Before the flame impinged onto the plate, the  $\text{CH}^*/\text{C}_2^*$  ratio was constant at a lower value. After the flame impinged, the  $\text{CH}^*/\text{C}_2^*$  ratio increased while the flame travelled from the plate centre to the flame boundary, which means that the plate prevented the fuel from travelling farther after it impinged onto the plate.



### 4.5.5 Conclusion of image colour-based flame chemiluminescence measurement

In this chapter, a flexible image colour-based flame chemiluminescence measurement was proposed:

- This method is based on a developed model that links image colour information and flame chemiluminescence emissions. The relationship is expressed as follows:

$$\begin{cases} I_R = \alpha_{R_{430}} I_{CH^*} + \alpha_{R_{516}} I_{C_2^*} \\ I_G = \alpha_{G_{430}} I_{CH^*} + \alpha_{G_{516}} I_{C_2^*} \\ I_B = \alpha_{B_{430}} I_{CH^*} + \alpha_{B_{516}} I_{C_2^*} \end{cases}$$

- A camera sensor calibration process is needed to explore the spectral sensitivities of the G and B channels at wavelengths of 430 and 516 nm. For the employed multi-dimensional imaging system in this thesis,

$$\begin{cases} I_{C_2^*} = 1.79 I_G \\ I_{CH^*} = 3.03 I_B - 3.3 I_G \end{cases}$$

- High accuracy has been demonstrated in measuring  $C_3H_8$  premixed flame from  $\Phi = 0.93$  to 1.53 in Section 4.3. The maximum global  $CH^*/C_2^*$  ratio deviation is no greater than 2% from its characteristic global  $CH^*/C_2^*$  ratio predicted from the training data, meaning a maximum 1% deviation from the 99% CI range, and the measured 1D global  $CH^*/C_2^*$  ( $\mu_e$ ) is related to the  $\Phi$  of  $C_3H_8$  as follows:

$$\Phi = -0.0145\mu_e^3 + 0.1268\mu_e^2 - 0.43\mu_e + 1.6413$$

- The 2D local  $\text{CH}^*/\text{C}_2^*$  ratio was applied in the case study measuring flame propagation in tubes in Section 4.4. The results showed a clearly chemical oscillation in the flame front during the flame oscillation at  $1.1 < \Phi < 1.4$  in tubes open at both ends. It led to visible 2D chemical reaction diagnostics in the deflagration-to-detonation study.
- The method was combined with stereo imaging and 3D reconstruction to provide 3D chemical reaction visualisation. The obtained 3D  $\text{CH}^*/\text{C}_2^*$  ratio maps were demonstrated in the case study of the ignition-to-impinging process under variations in fuel, ignition position, and flow rates, in Section 4.5.

# 5

---

## IMAGE INTENSITY FLUCTUATION-BASED VIBRATION MEASUREMENT

---

### 5.1 Introduction

In this chapter, an image intensity fluctuation-based vibration dynamics measurement method is proposed. The methodology is introduced in Section 5.2. The vibration measurement comparison between this proposed method and the feature tracking-based method is discussed in Section 5.3. In Section 5.4, the proposed method is applied in industrial product rotating-vibration testing. The product rotating-vibration dynamics was analysed, and the vibration frequency signals were separated from the combined rotation-vibration signals' frequency spectra.

### 5.2 Methodology

#### 5.2.1 Introduction

Because machines vibrate to some degree during their operations, the vibration signal is related to the specific condition of a machine. In a rotating machine, the vibration signal is an important parameter that contains information on the machine's condition. Vision-based measurement has been successfully applied in detecting vibration signals by tracking points on the rotating objects, such as wind turbine

monitoring with a multi-camera system (Ozbek, Rixen, Erne, & Sanow, 2010). Vibration measurement by tracking points is suitable for measuring a rotating object that has clear markers/features that can be measured all the time. Thus, in the feature tracking method, the camera usually measures the front view of the rotating object; a sample is shown in Figure 5.1(a). As the object rotates, the red point on the object can always be captured. However, if the camera measures a side view of this rotating object, as shown in Figure 5.1(b), then the red marker cannot be detected in all the image data because the red marker would be hidden to the camera during rotation. Because of this issue, image intensity fluctuation-based vibration signal detection is proposed to detect vibration signals from the side view of a rotating machine.

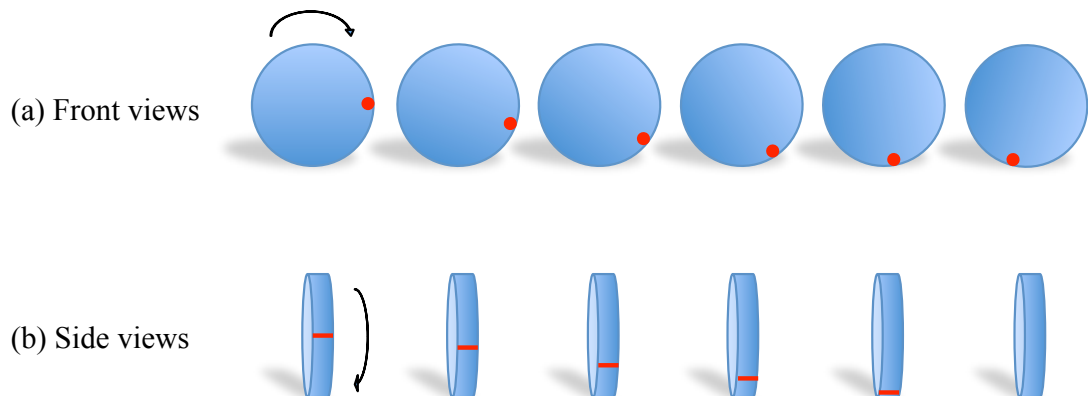


Figure 5. 1: Front view and side view measurements of an object during rotation.

### 5.2.2 Surface orientation

In the early 1970s, Horn proposed that the image intensity of a measured object's surface is the light flux reflected from the surface, which could be utilised to indicate the object's shape (Horn B. K., 1975). The surface orientation (the surface's normal

direction) of the measured object plays a major role in determining the light flux reflected (Horn B. K., 1975).

There are various ways of specifying the surface orientation of a plane. For example in Figure 5.2, the equation of a plane with nonzero normal vector  $n = (a, b, c)$  through a point  $x_0 = (x_0, y_0, z_0)$  is:

$$n \cdot (x - x_0) = 0, \quad (5.1)$$

where  $x = (x, y, z)$ . Hence, the general equation of a plane is defined as:

$$ax + by + cz = d. \quad (5.2)$$

where  $d = ax_0 + by_0 + cz_0$ .

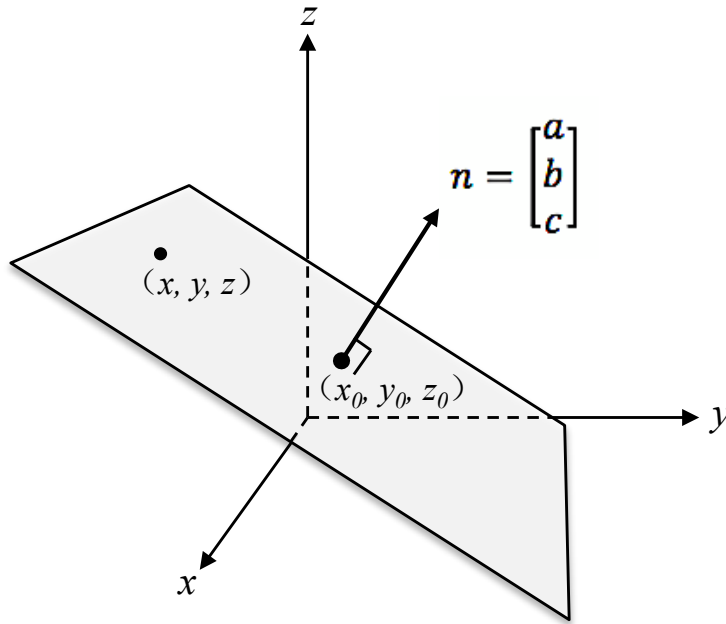


**Figure 5. 2: Definition of a plane.**

If considering a curved surface, the above definitions can be simply applied to a tangent plane of the curved surface, as shown in Figure 5.3.

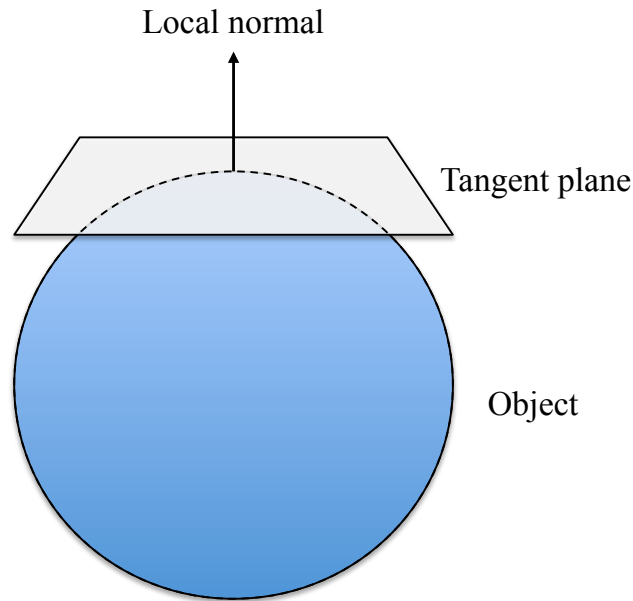


Figure 5. 3: Surface orientation of a curved object.

### 5.2.3 Light scattering

When a light ray impinges on the interface between two different media. A part of the incident light ray is turned back in the form of reflected light, while the remainder is transmitted across the boundary as refracted light. In general, because of irregularities on a surface, the incident rays propagating to a surface are not reflected just at single angle but at many angles. This phenomenon is called light scattering. Scattered reflection is also referred to as diffuse reflection, and it occurs when the surface irregularities are random and dense enough.

The distribution of reflected light from a surface is determined by the scattering that takes place at the surface and within the bulk of the material. The material type and the roughness of the surface govern the level of scattering. Figure 5.4 (Juds, 1988) depicts a model that demonstrates an incident light and its reflection on a glossy

surface. The diffuse reflection occurs because of irregularities on the surface. The general mechanism of diffuse reflection is attributed to the transmitted light reaching the so-called sub-surfaces that are inside the object. Then the light is reflected again as many specular reflections depending on the normal orientation of the sub-surfaces (Hanrahan & Krueger, 1993).

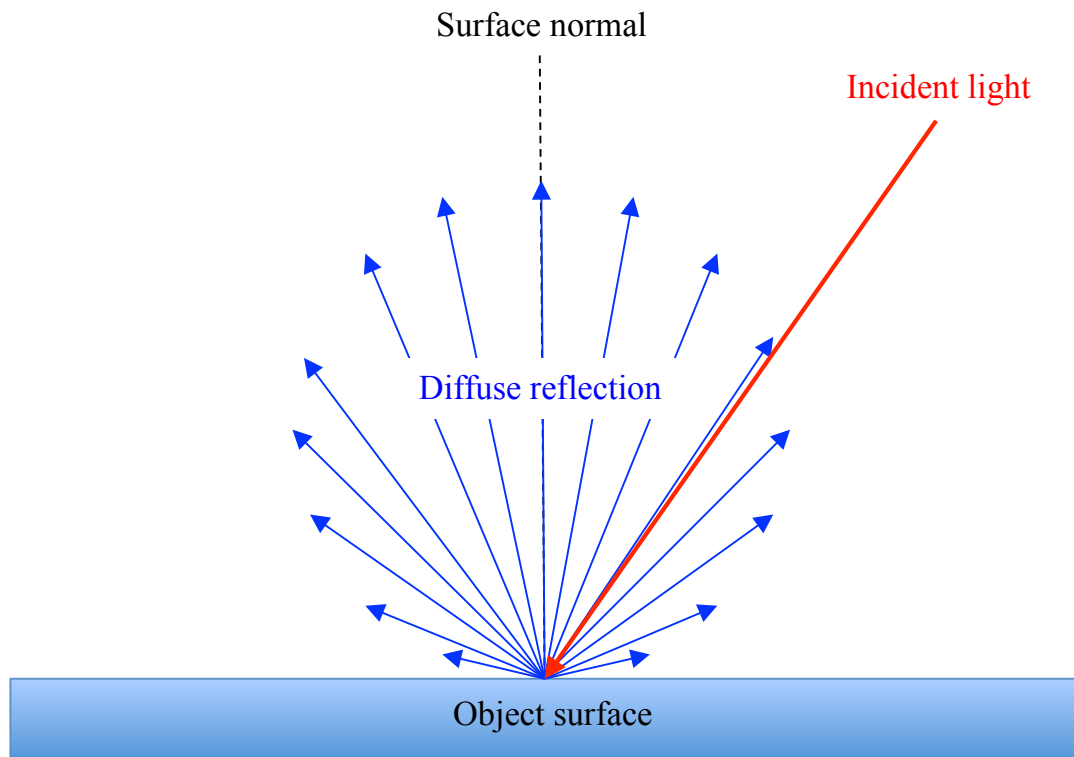


Figure 5. 4: Light reflection from a glossy surface [redrawn from (Juds, 1988)].

### 5.2.4 Reflectivity

The measured distribution of light reflected from an object's surface is attributed to the light scattering from the surface. The scattering is governed by the reflectivity of the measured surface. The reflectivity is the fraction of the incident light that is reflected into the camera per unit surface area with the per unit solid angle. To explain this, a model of light geometry is shown in Figure 5.5.

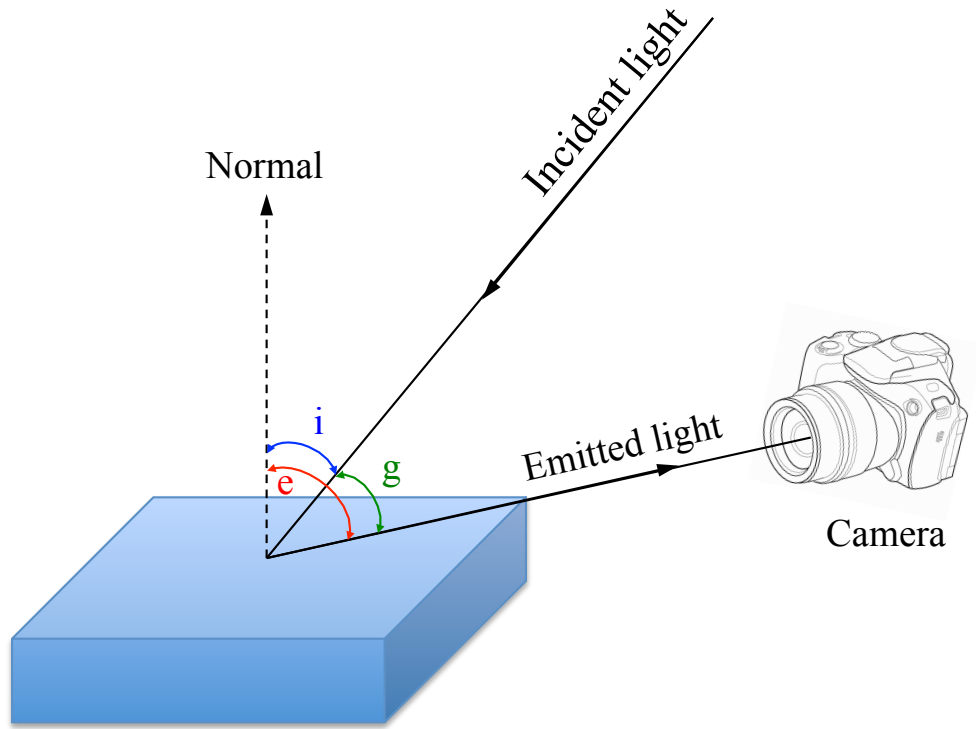


Figure 5. 5: Light geometry, using a single-point light source.

The model depicts the light geometry between a light source and a camera from a measured object's surface. The light geometry in this model is governed by three angles (Horn B. K., 1975): the incident angle ( $i$ ), between the incident light and surface normal; the emittance angle ( $e$ ), between the emitted light and surface normal; and the phase angle ( $g$ ), between the incident and emitted light. The reflectivity depends on the three angles within the light geometry, so it is defined as  $\varphi(i, e, g)$ . When the light geometry is changed, such as when an object is rotated or moved, the reflectivity would also change. Examples can be found in Figure 5.6.



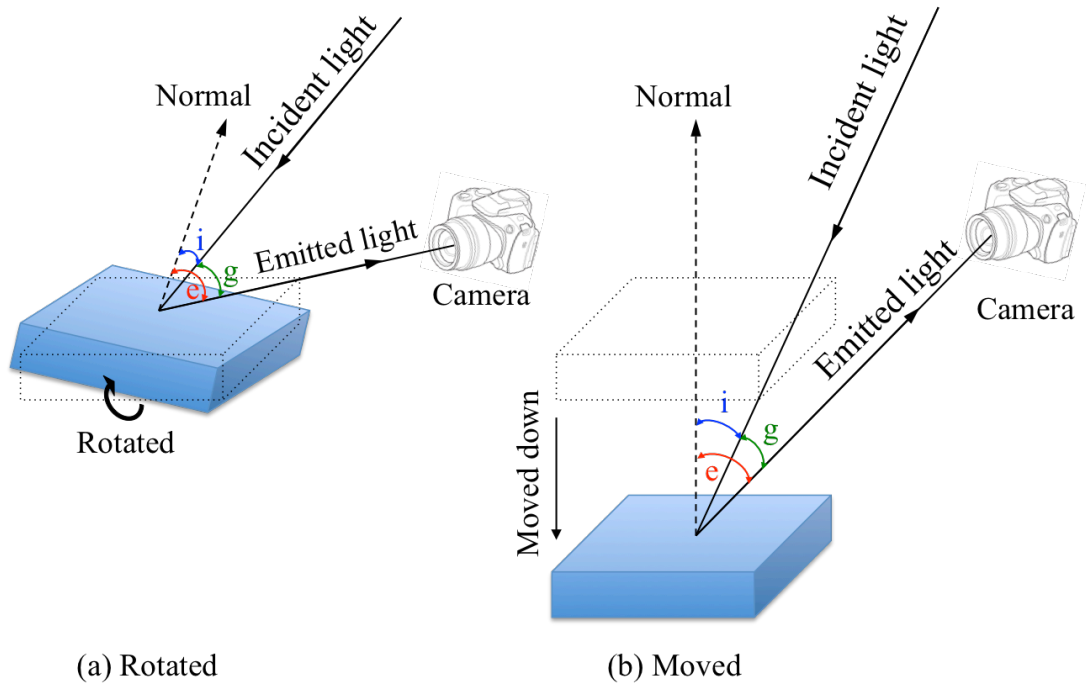


Figure 5. 6:  $\varphi(i, e, g)$  changed by object motion.

The object's previous positions are plotted by a dashed line, while the present positions are shown in blue. In Figure 5.6(a), the object is rotated, which changes the normal surface direction. Thus, the incident angle ( $i$ ) and emittance angle ( $e$ ) become smaller. In Figure 5.6(b), the object is moved down which changes all three angles within the light geometry. Whether the plane is rotated or moved, if the light geometry angles change, it leads to a corresponding change in reflectivity. Therefore, the measured image intensity would also change. If a flat plane is moved horizontally, then the angles may not change. To achieve that, the plane surface must be absolutely smooth because any irregularity on the surface would cause the surface normal to change, leading to different reflectivity to the camera. Of course, the

different colours and materials of the measured position would also cause different reflectivity to the camera.

### **5.2.5 Image intensity fluctuation-based vibration measurement**

The intensity of an object in an image is the light scattered from the observed surface in the direction of the camera. If the positions of the light source, camera, and measured object are fixed, then the light geometry among them is constant. The intensity variation of an image sequence can be attributed to scene alternation (Healey & Kondepudy, 1992). Therefore, to measure an object, if the light source and camera are fixed, any intensity variations within the image sequence could be related to the object motion.

To obtain the intensity variation, the intensities of pixels at the same position within an image sequence should be tracked. The measured intensities are in grey scale. Since the original image data are in the RGB model, the image sequence should be transformed to a grey scale image first. This process was conducted in Matlab using the `rgb2grey` function. Noise in the processed grey scale images is then reduced using the `wiener2` function. Not all the parts of an image contain useful information, so the measured windows are set in the area of interest in an image. Sometimes this area is on the object's surface, for reasons discussed below. To detect a clear motion signal, the measured position and the size of the measured window are two important factors that should be considered during image processing.

To explain these two factors, experimental image sequence data are employed. The data are obtained from the measurement of blade vibration at a frequency of 6.2 Hz using a high-speed stereo colour imaging system. Details of the measurements will be introduced and discussed in Section 5.3; here, the effects on the obtained results for different positions and sizes of the measured window are analysed. The frame rate was set at 125 fps with a 1/125 s shutter speed in order to capture non-blur images in a 12 second long sequence. This image sequence includes 1500 frames. Figure 5.7 is a sample stereo image in the employed image sequence.

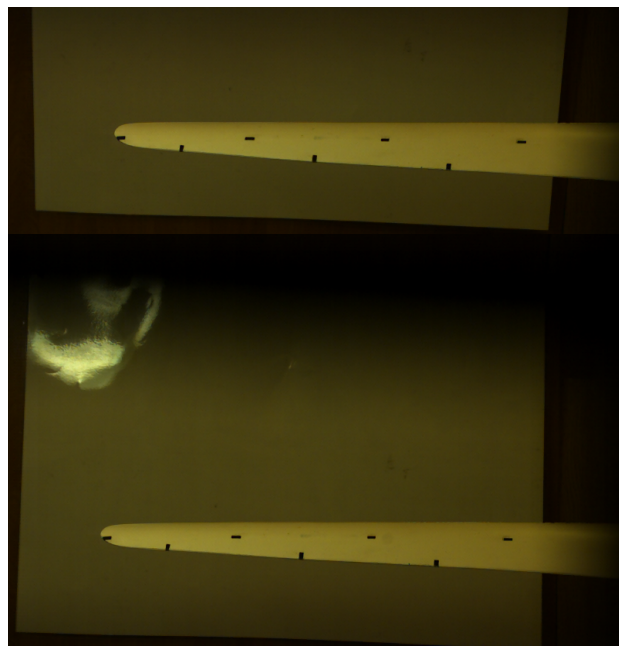


**Figure 5. 7: A sample stereo image in the employed image sequence.**

In this sample, two views of the blade are shown at the top and bottom parts of the image because the camera is connected to the four-mirror stereo adapter; thus, the image data can capture two views of an object in a single image. Only half of the image is used to detect intensity variation during image processing. It does not matter

which part of the image is employed because the two views are almost the same. Here we use the bottom part of the image only because it is brighter than the upper part.

### 5.2.5.1 Measured position

The measured window position is essential in detecting vibration motion signals. Figure 5.8 shows the processed image after the transformation to grey scale, reducing noise and cutting unnecessary parts. Different measured positions are chosen for comparison. The three selected measured window positions are marked as position a, position b, and position c; a is the position on the object's surface near an obvious feature (the obvious feature here is defined as the position with a large intensity difference from its neighbouring pixels; in this image, the obvious feature is the black square); (b) is also on the object's surface but without any obvious features; and (c) is positioned on the background outside the object's surface.

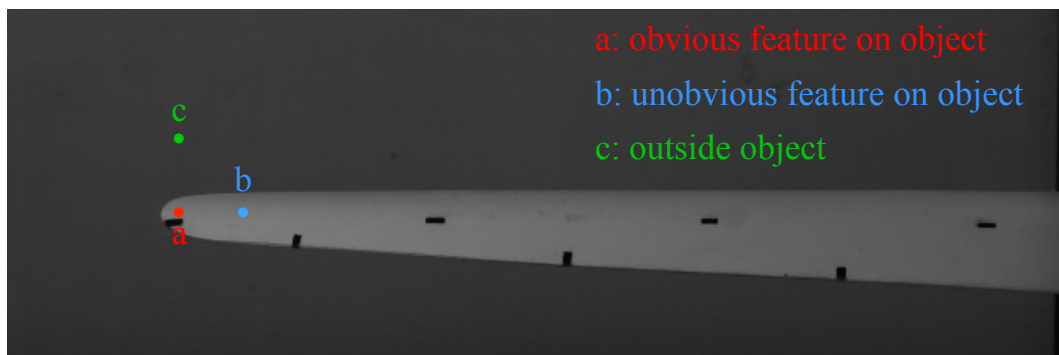
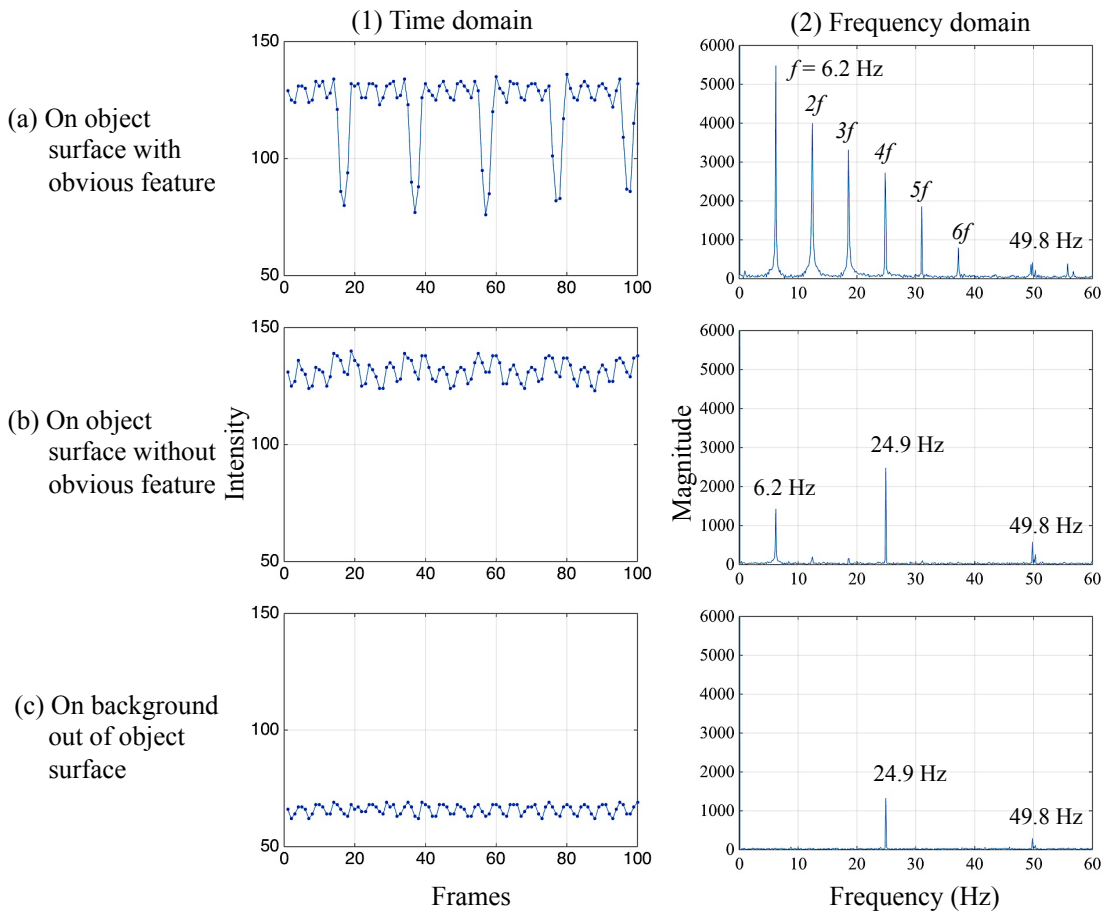


Figure 5. 8: Different measured positions on the blade.

In this comparison, the intensities of a single pixel at the three selected positions are tracked in the 1024-frame sequence. The tracked intensities are transformed into

their frequency domain by fast Fourier transformation (FFT). The results obtained for the tracked intensities and their frequency spectra are shown in Figure 5.9. To see the intensity fluctuation clearly, only the tracked intensity variations in the first 100 frames are plotted in the time domain, as shown in Figure 5.9(1). The corresponding intensities in the 1024 frames are transformed into the frequency domain by FFT, as shown in Figure 5.9(2).



**Figure 5. 9: Comparison of measured positions: (a) obvious features on object surface, (b) unobvious features on object surface and (c) outside of object.**

The blade vibration input frequency was set at 6.2 Hz; this frequency can be detected at both spectra in Figure 5.9(a2) and (b2). The detected vibration frequencies are at 6.2 Hz, which exactly matches the real blade vibration. Compared with (a2) and (b2), the amplitude of 6.2 Hz in (a2) is higher than that in (b2). It is because the obvious features can significantly enhance the intensity variation, as shown in (a1) the measured intensity dramatically drops from 125 to 75. The large intensity variation then results in a clearer vibration signal. Although the intensity variation in (b2) is small, the vibration frequency could still be detected. This demonstrates that the image intensity-based vibration measurement is very sensitive. Furthermore, clear harmonics (integral multiplies of vibration frequency) such as  $2f$ ,  $3f$ ,  $4f$ ,  $5f$ , and  $6f$  are shown in (a2), but the harmonics in (b2) are not obvious. The measurement of harmonics is useful, since high harmonics are usually associated with mechanical looseness (Bilsova & Bilos, 2012). Therefore, position (b) is not suitable for measuring vibration signals as at this position the light flicker signal is much stronger than the vibration signal.

Position (c) is measured outside the blade, so the vibration frequency cannot be detected in its frequency spectrum. However, the intensity in (c1) still fluctuates slightly, and the frequency is 49.8 Hz in (c2). This is the light source flicker frequency, which can be detected in all positions, as shown in (a2), (b2), and (c2). The frequency component 24.9 Hz is half the frequency of 49.8 Hz. Its amplitude is stronger than the one at 49.8 Hz because of the aliasing effect. This effect occurs

when the sampling frequency is not enough to realistically capture a fast action. Based on Nyquist criterion, the requirement for the correct sampling frequency should be 2.56 times of the maximum measured frequency (Bilosova & Bilos, 2012). Therefore, in this case, the sampling frequency of 125 Hz is not enough to measure light source flicker frequency of 50 Hz. The correct sampling frequency should be at least 128 Hz.

Clearly, the image intensity variation could detect the frequency of the light source flicker and object motion. The light source flicker frequency can be detected at every image pixel. It is important to detect this frequency, as this could help in separating the background frequency component in a complex frequency spectrum. The motion signals can only be measured at a position with something moving. An obvious feature would cause a large reflectivity difference, which can enhance the motion signal. Therefore, to measure any object motion, the measured position should be on the object's surface, and it would be better with an obvious feature. The measured position should be based on previous knowledge and experience. However, the flexibility of the measured position selection is an advantage in post-image processing and analysis since any area of interest could be processed after one shot. Furthermore, multiple positions could be measured at the same time; this would be very useful when one has no idea which position should be measured. The captured sampling frequency should be at least 2.56 times of the expected frequency.

### 5.2.5.2 Measured size

After the measured position is chosen, the measured size is another important element. Figure 5.10 shows the results measured at the position (a) in Figure 5.8 under different measured sizes. Subtitles a to f indicate 1,  $3\times 3$ ,  $5\times 5$ ,  $7\times 7$ ,  $9\times 9$ , and  $11\times 11$  pixels of measured sizes, respectively. The tracked intensity variations are the average intensity within these measured windows.

As shown in the figures, when the size of the measured window increases, the tracked intensity fluctuation amplitude decreases because the mean intensity reduces the intensity variation caused by the surface reflectivity difference. Hence, the frequency amplitudes are also reduced. Based on above discussion, the strongest frequency amplitude should be found in the single pixel measurement. However, the strongest frequency signal amplitude is found in the  $5\times 5$  and  $7\times 7$  pixels measurement. As discussed in the previous section, the sensitivity of this method depends greatly on the selected measured position. The selected position (a) was not the position with the most obvious feature. Although measuring more pixels would reduce the intensity variation caused by surface reflectivity difference, a large measured area could also cover more reflectivity signals. For example, the measured position doesn't in the black marker as shown in Figure 5.10(a), but since more pixels are measured in the size of  $5\times 5$  pixels and  $7\times 7$  pixels measurements, the part of the black marker is selected for inclusion in both measured sizes.



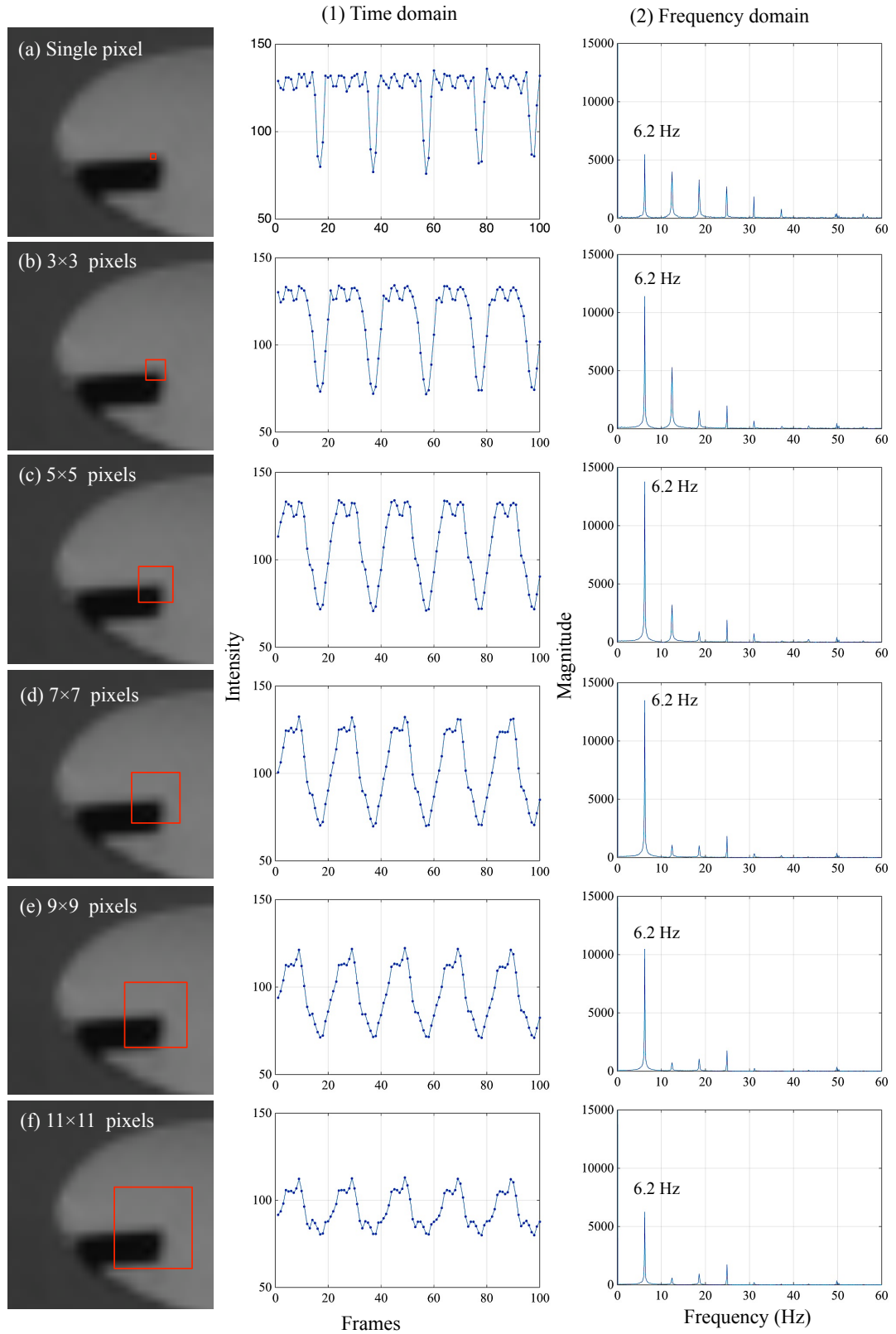


**Figure 5.10: Different measured sizes of measured position a in Figure 5.8; a) 1 pixel, b)  $3 \times 3$  pixels, c)  $5 \times 5$  pixels, d)  $7 \times 7$  pixels, e)  $9 \times 9$  pixels, and f)  $11 \times 11$  pixels.**

During the measured size increases, the obtained frequency harmonics almost decreases, except  $4f$  at 24.8 Hz. The amplitudes of frequency component at 24.8 Hz from Figure 5.10(a2) to (f2) are nearly the same, due to the amplitude at this position is the combination of both  $4f$  and the half frequency of light flicker (24.9 Hz) as detected in Figure 5.9(b2). As mentioned in previous section, the harmonics are useful to estimate mechanical looseness as a reference. Since the amplitudes of harmonics in  $7 \times 7$  pixels measurement are very small, in this test, the  $5 \times 5$  pixel measured size is chosen.

### 5.2.6 Conclusion

Image intensity is the result of the interaction among the light source, object surface, and camera. In this relation, the object's surface reflectivity plays the major role in determining the intensity values. When the light source and camera position are fixed, any intensity variation at the measured position is attributable to the object's motion. The position and size of the measured window are two important parameters to be considered. The measured position should be an obvious feature on the measured object. A larger measured area reduces the intensity variation caused by the surface reflectivity difference, but it also offers a greater opportunity to cover the position with the largest reflectivity difference, so the appropriate measured size is important and depends on experience.

The following two cases employ this method to detect vibration frequency. Case 1 aims to explore the potential of this method in wind turbine blade vibration

monitoring. The results are compared with the tracked point-derived vibration signal method. Case 2 applies this method in a real industrial product testing during rotation.

## **5.3 Case 1: wind turbine blade vibration monitoring**

### **5.3.1 Introduction**

The world's wind power generation capacity has grown at a fast rate of 20–30% per year (Amirat, Benbouzid, Al-Ahmar, Bensaker, & Turri, 2009). To increase the wind power acquisition and conversion rate, the size of wind turbine blades is becoming larger and larger. However, huge blade structures will increase the opportunity for failure. The long, thin, and elastic blade is the part that suffers the most complex forces, which can easily cause vibration (Lu & Chu, 2010). Frequent and violent vibrations can lead to the cracking of a blade, which adversely affects wind power generation. Moreover, unbalanced rotation caused by a damaged blade may result in serious secondary destruction, such as the collapse of the whole wind turbine (Ciang, Lee, & Bang, 2008). Detecting early signs of blade damage would allow the operators to better plan for maintenance.

The wind turbine blades vibrate during operation, and the vibration signature pattern will change with the development of structural damage. The conventional methods of blade vibration signal monitoring involve placing strain gauges or accelerometers on the blade. However, these approaches are sensitive to electro-magnetic fields and lightning, which will cause incorrect reporting of blade condition (Ozbek M. , Rixen, Erne, & Sanow, 2010). In addition, the extra installations may change the blade's original structure and dynamics. In addition, the number of sensors is usually limited because of the cost issue, but if the number of sensors is not enough to cover all the expected measured positions, it will lead to a lack of monitoring information (Lu & Chu, 2010).

Vision-based measurement is also considered for blade vibration monitoring. However, in the past, this method has been limited to visible inspection. If the damage is inside an object or cannot be seen on an image, then vision-based measurement is not suitable. With the development of high-speed digital cameras and computer capabilities, nowadays, both the visible (structure) and invisible (dynamics) parameters of a blade can be explored by using digital camera imaging and image processing techniques.

Many successful vibration measurements involving camera imaging have been published (Sabel, 1996; Ozbek, Rixen, Erne, & Sanow, 2010; Lu & Chu, 2010). They all employed a feature identification method to track marker displacement on the measured object. In this case study, the blade vibration signals are detected by both image intensity fluctuation-based measurement and the point tracking-based measurement, and the results are compared.

### **5.3.2 Experimental setup**

The schematic of the experimental setup is shown in Figure 5.11. Two 29-inch fiberglass low wind generator blades were employed for the vibration testing. It is assumed that both blades have the same properties and dynamics in their undamaged structural conditions. To compare the different blade structures, one blade was broken with a small crack. This blade is termed the damaged blade, and the other blade is referred to as the undamaged blade throughout the text.

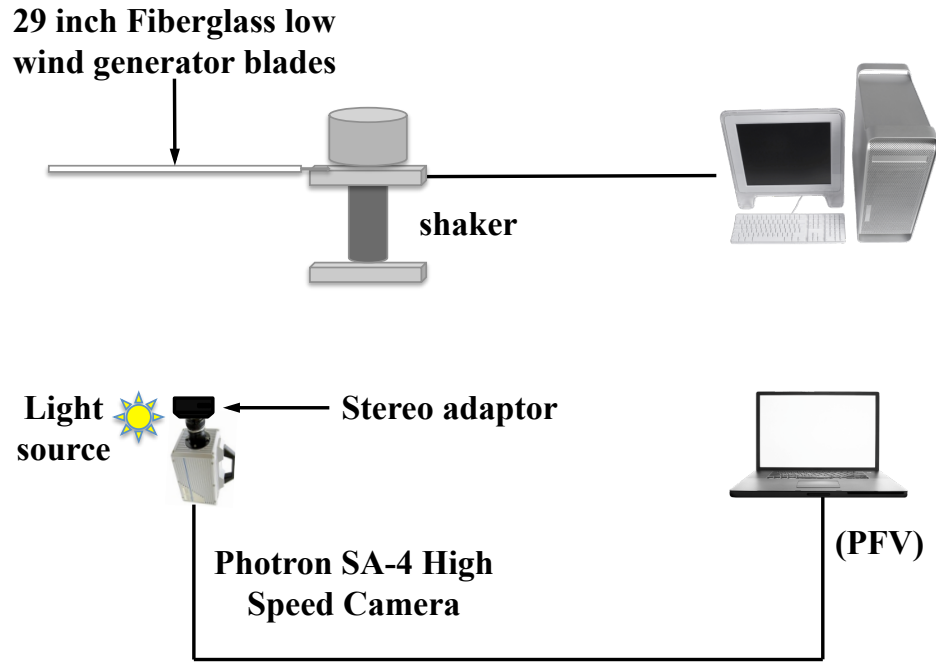


**Figure 5. 11: The schematic of blade vibration measurement.**

The experiments were carried out on a shaker, which can vibrate at different frequencies and amplitudes with the setting of various input frequencies (shaking frequency) and voltages (shaking power). Both blades were fixed on the same location on the shaker and vibrated separately at the corresponding input setting. The input frequencies were set from 6.0 to 6.4 Hz (with a 0.1 Hz interval). At each frequency, three voltages of 3, 4, and 5 V were employed to provide different vibration amplitudes.

For data acquisition, the high-speed stereo colour imaging system introduced in Section 3.2 was employed. A 30 W white light source was placed near the camera to supply sufficient illumination. Based on this, the frame rate was set at 125 fps with a  $1/125$  s shutter speed in order to capture non-blur image with sufficient brightness images. In each measurement, 1500 frames were recorded at a resolution of  $1024 \times 1024$  pixels. Typically, three measurements were performed for each condition. Since the camera was connected with a four-mirror stereo adapter, two views of the blade

were photographed in each set of image data. An example of the original stereo image is shown in Figure 5.12.



**Figure 5. 12: A sample stereo image and the markers' locations on the blade.**

Seven black paper markers were pasted on the blade surface. These markers can offer the obvious features to enhance the intensity variation caused by blade vibration in the image intensity variation-based method. Furthermore, they were also tracked to measure the blade vibration displacement in the compared method. For convenience, the markers are named Marker 1 to 7 from the blade tip to the blade bottom. The crack was located on the back of the damaged blade and between the positions of Markers 3 and 4. Since the crack exists on the back of the damaged blade, and the measurement was performed on the blade's front view; the crack cannot be seen directly on the measured image data. In this way, the sensitivity of the image intensity variation-based measurement in invisible damage detection can be tested.

### 5.3.3 Image processing

The image data were processed by both the intensity fluctuation-based method and the feature tracking displacement-based method. In the image intensity fluctuation-based method, only the down view of each image was processed. Seven measured windows on the blade surface were selected. The positions were measured near the seven markers because the black marker can offer a very different intensity that can enhance the obtained vibration signals. For each measured window, an area with  $5 \times 5$  pixels was measured (refer to the discussion in Section 5.2.5.2). The average intensity of each measured window was calculated and recorded. Since the intensity fluctuation is caused by blade vibration, the vibration signal can be related to the intensity fluctuation.

For the feature tracking displacement-based method, the movements of seven markers are tracked. To obtain the vibration displacement in 3D, the camera calibration process was performed before the experiments to determine the camera's intrinsic and extrinsic parameters. In the calibration procedure, five images of the calibration board from five different directions were captured. The intrinsic and extrinsic parameters were then obtained by processing these five images' data using a pre-written Matlab program. The calibration process is the same as that described in Section 3.3.4.2, so the details are not described here. After the experiments, the seven markers were tracked in both the upper and lower part of each image in the measured image sequences. Because the marker squares contain many pixels, only the right-top corner coordinates of each marker were recorded. The recorded corresponding coordinates were then matched between the corresponding upper and lower part of each image. The distance (the x-coordinate difference between the selected



coordinate in the upper part and its corresponding coordinate in the lower part) was selected as the disparity (the difference in the projected locations between different views). Using Eq. 2.21, the depth information can be calculated. The 3D reconstructed coordinates of each marker were then obtained. However, in this case study, the vibration displacement was tracked by the reconstructed  $y$  coordinates of each marker.

### **5.3.4 Results and discussion**

#### **5.3.4.1 Comparison between the intensity fluctuation-based method and feature tracking-based method**

The image processing procedures of both intensity fluctuation-based method and marker tracked displacement-based method are introduced in previous sections. The resulting samples of vibration at 6.2 Hz and 3V derived by the two methods are compared in Figure 5.13. The intensity-based results are shown in Figure 5.13(a), while the displacement-based results are shown in Figure 5.13(b).

As shown in Figure 5.13(a1), the intensity variations in this plot were obtained from the original measured intensities minus their median in this case. Hence, the intensities fluctuated around 0. The maximum and minimum intensities in each vibration cycle are not constant. For example, at 5s, the amplitude of the intensity fluctuations is about  $\pm 26$ , which is smaller than that at 1s, about  $\pm 30$ . Since the amplitudes of the intensity fluctuation in a short period are similar, it may be that the changed light source illumination caused voltage instability. This  $\pm 4$  intensity difference is quite small when compared to the total intensity variation, so it can be ignored.

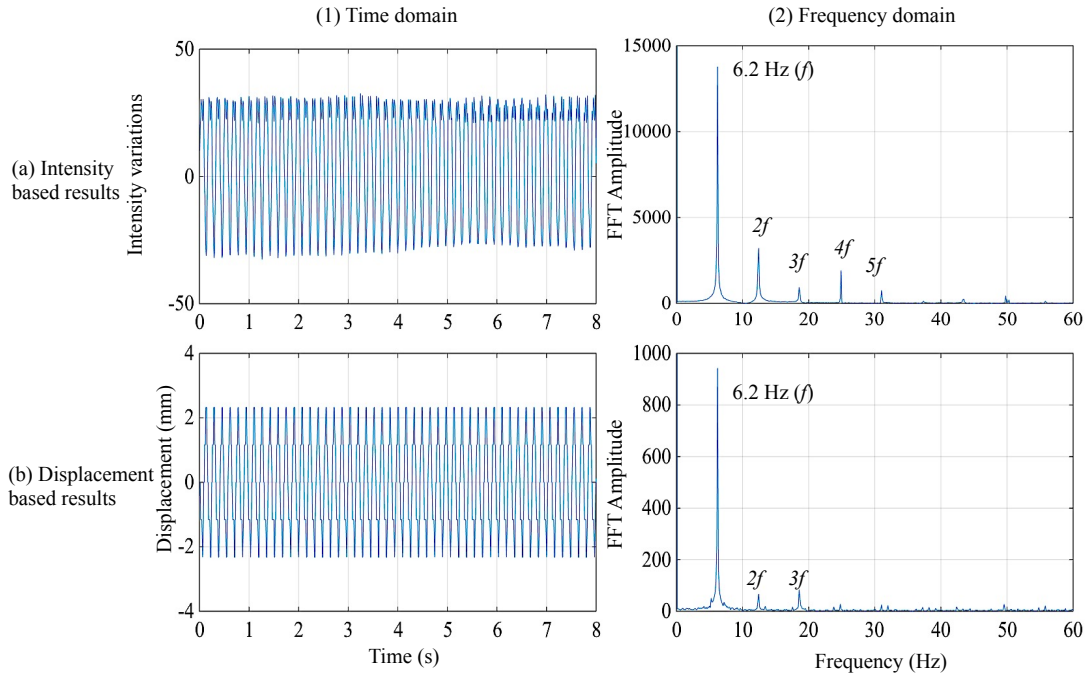


**Figure 5. 13: Vibration signal results of 6.2 Hz & 3 V sample derived by (a) intensity fluctuation and (b) marker displacement in the (1) time domain and (2) frequency domain.**

The intensity variation-based method is very sensitive to the surrounding conditions, so any intensity variation caused by the light source or noise should be considered. Therefore, the amplitude of the measured intensity fluctuation caused by object vibration should be sufficiently bigger; thus, the small intensity variation caused by the light source or noise could be ignored. On the contrary, the measured marker displacements plotted in Figure 5.13(b1) are not sensitive to the surrounding conditions. The tracked displacements only depend on the input voltages. Hence, in this case measurement, the displacements are about  $\pm 2.2$  mm.

The results in Figure 5.13(a1) and (b1) are transferred by FFT, the obtained frequency spectra are shown in Figure 5.13(a2) and (b2), respectively. Clearly, the 6.2 Hz frequency peak can be detected in both frequency spectra, which successfully demonstrates the good abilities of intensity fluctuation-based and marker displacement-based methods in vibration signal detection. Five harmonics can be

found in Figure 5.13(a2), while only two harmonics can be obtained in Figure 5.13(b2).

### 5.3.4.2 Blade condition monitoring

In this test, the vibrating blades were measured under various input frequencies and voltages ranging from 6.0 Hz to 6.4 Hz and 3V to 5V, respectively. The blade vibration frequency is determined by the input frequency, while the vibration amplitude is controlled by the input voltage power; the higher the voltages are, the larger the vibration amplitudes will be. To explain the relationship between the measured vibration signals and the corresponding input vibration settings, typical samples of vibration frequency spectra of the undamaged blade are presented in Figures 5.14 and 5.15. The frequency spectra were transformed from the mean intensity fluctuation within the measured window at the Marker 1 position by FFT.

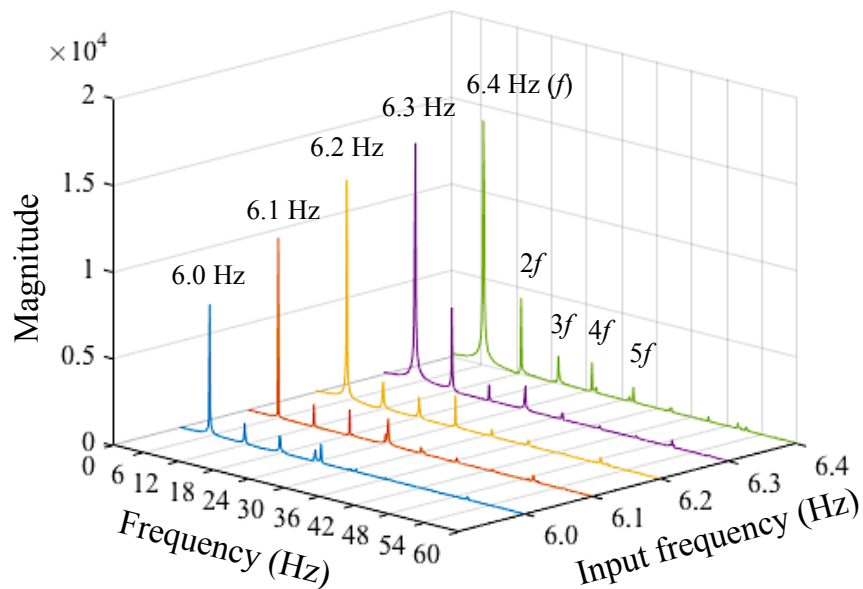


**Figure 5. 14: Intensity fluctuation derived vibration frequency spectra of the Marker 1 position on the undamaged blade at input settings of 6.0–6.4 Hz and 3 V.**

Figure 5.14 shows the frequency spectrum comparison under different input frequencies ranging from 6.0 to 6.4 Hz at a constant voltage of 3V. The obtained main frequency  $f$  in each spectrum matches exactly the input vibration frequency. For example, the measured frequency of the blade vibration at 6.0 Hz obtained frequency peaks at exactly 6.0 Hz. This indicates a good capability of the image intensity fluctuation-derived vibration frequency detection for vibration dynamics measurement. It is clear that the magnitudes of the main frequencies in each spectrum are not equal. The lowest frequency magnitude is found in the 6.0 Hz spectrum. As the vibration became faster, the magnitude of the measured driving frequency increased. The strongest frequency magnitude is found for 6.4 Hz. The harmonics phenomenon can be found in all frequency spectra. Take the 6.4 Hz case, for example, as plotted in violet; the harmonics of  $2f$ ,  $3f$ ,  $4f$ , and  $5f$  can be easily identified. The trend of the magnitude in harmonics is similar to the trend of the magnitude in the driving frequency described previously; as the input vibration frequency increases, the obtained magnitudes of their harmonics increase.

To explore the effect of input voltages, a comparison of different input voltages from 3 to 5 V at 6.3 Hz is plotted in Figure 5.15. It is obvious that, when the voltage input changes, the obtained driving frequency  $f$  is still found in the same position at exactly 6.3 Hz. This means that the voltage input would not affect the vibration frequency. During the voltage increases, the magnitude of frequency at 6.3 Hz increases as well. Although their harmonics can be found in their spectrum, no clear trends for them can be obtained. The highest magnitude of the second harmonic is found for 4 V.

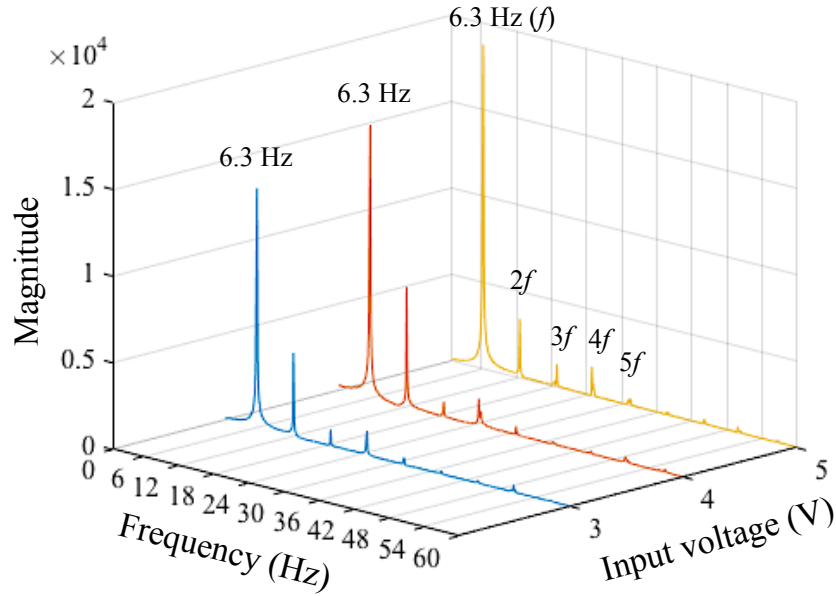


**Figure 5. 15: Intensity fluctuation-derived vibration frequency spectra of the Marker 1 position on the undamaged blade at input settings of 6.3 Hz and 3–5V.**

The magnitudes of the frequency peak components (driving frequency and its harmonics) are specific, and no clear trend can be found. However, the magnitudes of frequency always remain the same under the same vibration input setting. This was found by repeating tests at the same frequency and voltage setting and then comparing them with the obtained frequency spectra. In other words, the frequency spectrum of a specific blade depends on its structural condition. Hence, the achieved frequencies and their magnitudes can then be considered the signature pattern of the blade vibration dynamics. If there is a sufficient database of blade vibration frequency spectrum patterns in different conditions, the blade structure can be easily identified by finding a similar spectrum pattern in the database. According to this, damage can be predicted and condition-based maintenance can be better planned.

### 5.3.4.3 Damage detection

Damage detection is one of the key purposes of blade vibration monitoring. In general, damage is defined as changes in a system that adversely influences the current or future performance of the system. Therefore, damage is not meaningful without a comparison between two different conditions of the system, one of which is assumed to represent the undamaged condition (Farrar & Worden, 2007). Therefore, to demonstrate the effectiveness of the image intensity fluctuation-based vibration measurement in blade damage detection, the tracked mean intensity fluctuations from undamaged and damaged blades are compared. A sample of the comparison at 6.3 Hz and 4V is shown in Figure 5.16.

As shown, the time histories of the tracked mean intensity of the measured window at the positions of Markers 1 to 7 are plotted from the top of the figure to the bottom, respectively. The case of the undamaged blade is shown at left, while the corresponding damaged blade case is shown at right. It is clear that the intensity fluctuation amplitudes decrease from Marker 1 to 7. This phenomenon can be found in both the undamaged and damaged blades because the elasticity of the blade structure decreases from the top to the bottom. In the undamaged blade, the intensity amplitude is nearly constant, while in the damaged blade case, the amplitude shows a clear fluctuation, especially at Marker 1. Another difference is that the intensity fluctuations' amplitudes in the damaged blade are larger than those in the undamaged blade case at all the measured positions. This may have occurred because the damage decreases the ability of the blade to resist deformation.

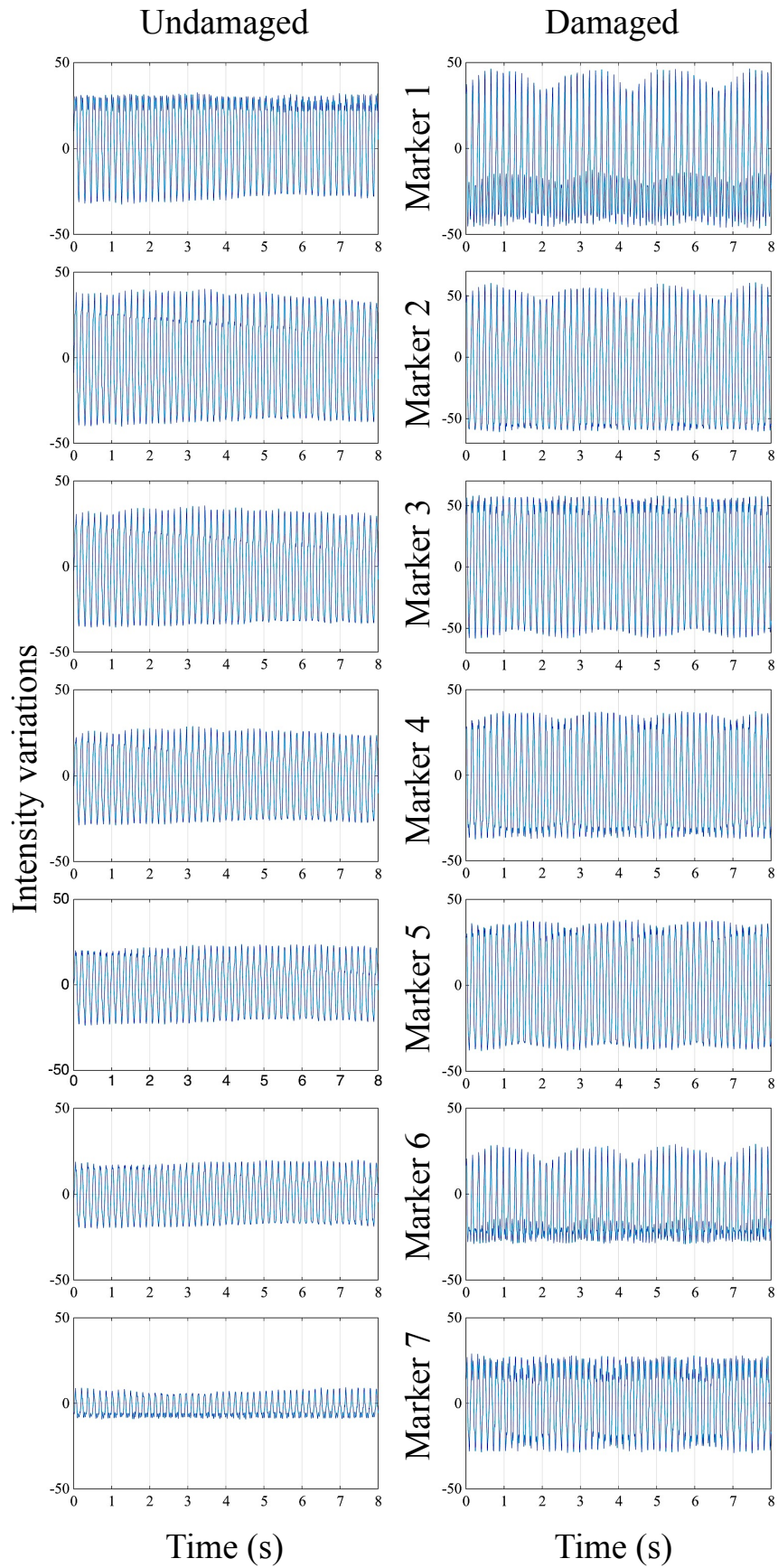
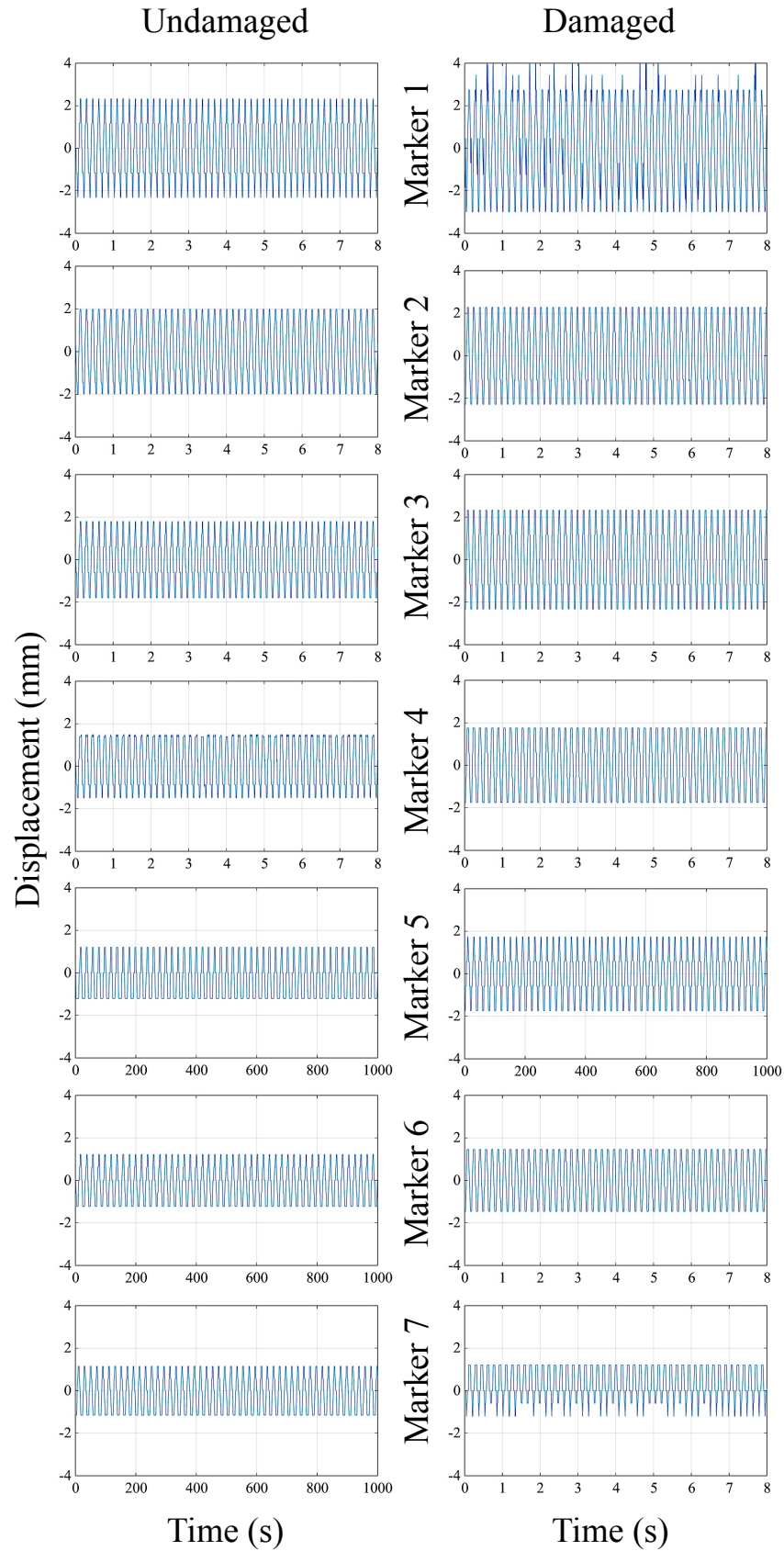


Figure 5. 16: Measured intensity variation of undamaged and damaged blades at 6.3 Hz and 4V.



**Figure 5. 17: Measured displacement variation of undamaged and damaged blades at 6.3 Hz and 4V by the photogrammetry method.**



The corresponding comparison of the measured vibration displacement is shown in Figure 5.17. The trajectories of the markers' vibration exhibit stable sinusoidal waves. The displacement amplitude drops from Marker 1 to 7, similar to that found in the reduced intensity fluctuation amplitude phenomenon. In the damaged blade case, although the trajectories still exhibit sinusoidal waves, the movements are unstable, especially in the case of Marker 1. Furthermore, similar to the findings for image intensity tracked fluctuation, the vibration displacements in the damaged blade are larger than those in the undamaged blade. However, the displacement increments between the undamaged and damaged blades are lower than the corresponding increments in intensity variations. This indicates that, in this case study of blade vibration, the intensity fluctuation-derived method is more sensitive than the tracked displacement-derived method.

There was no dissimilarity in the direct visualisations from the image data between undamaged and damaged blades. However, the difference in their vibration dynamics can be distinguished clearly by both the intensity fluctuation-derived and displacement-derived methods. It could be assumed that, if the displacement of the blade vibration is very small, then the intensity fluctuation-derived vibration signal measurement is more suitable than the displacement-based method.

The achieved frequencies and the magnitudes of their vibration signals can be considered the signatures of blade conditions. Then they can be utilised for blade damage detection by comparing the vibration spectrum of a damaged blade with a reference frequency spectrum from an undamaged blade. Hence, further analysis was carried out in the frequency domain. After being transformed by FFT, the frequency spectra of seven markers on both the undamaged and damaged blades were obtained.

The results shown in Figures 5.16 and 5.17 are transformed to the frequency domain in Figures 5.18 and 5.19, respectively.

In the frequency spectra obtained by both methods, the vibration frequency at 6.3 Hz could be found in both the undamaged and damaged blades. The vibration frequency amplitudes in the damaged blade case are much higher than that in the undamaged blade case. Since higher amplitude is a dangerous signal in a condition change, it demonstrates the good capacity of vision-based measurement for damage detection.

To see the vibration frequency harmonics, the spectra were plotted in their low-magnitude region. In Figure 5.18, considerably higher-order harmonics were apparent in the damaged blade. As higher-order harmonics is a typical feature of damage in many structural systems, the results also demonstrate the efficacy of the proposed intensity fluctuation method for blade damage detection in distinguishing between undamaged and damaged blade structures. Compared to the measured displacement-derived frequency in Figure 5.19, the harmonics of the vibration frequency can also be found, but the enhanced harmonics phenomenon was not found at all markers. Furthermore, some other frequency peaks appeared, which could indicate damage. This indicates that the intensity fluctuation-based method is more sensitive than the marker tracking-based method in damage signal detection.

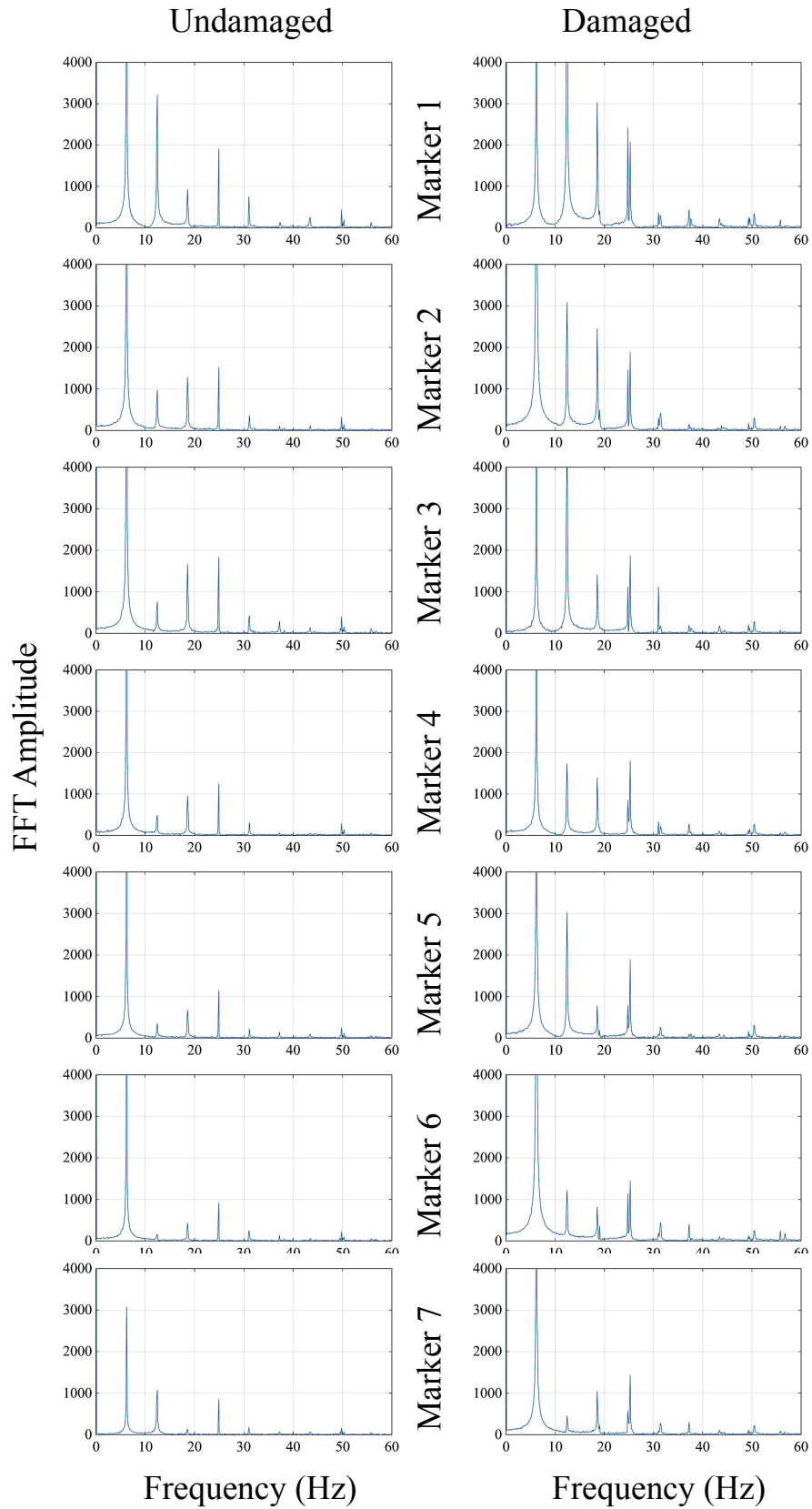


**Figure 5. 18: Intensity variation-derived frequency spectra of undamaged and damaged blades at the input settings of 6.3 Hz and 4V.**

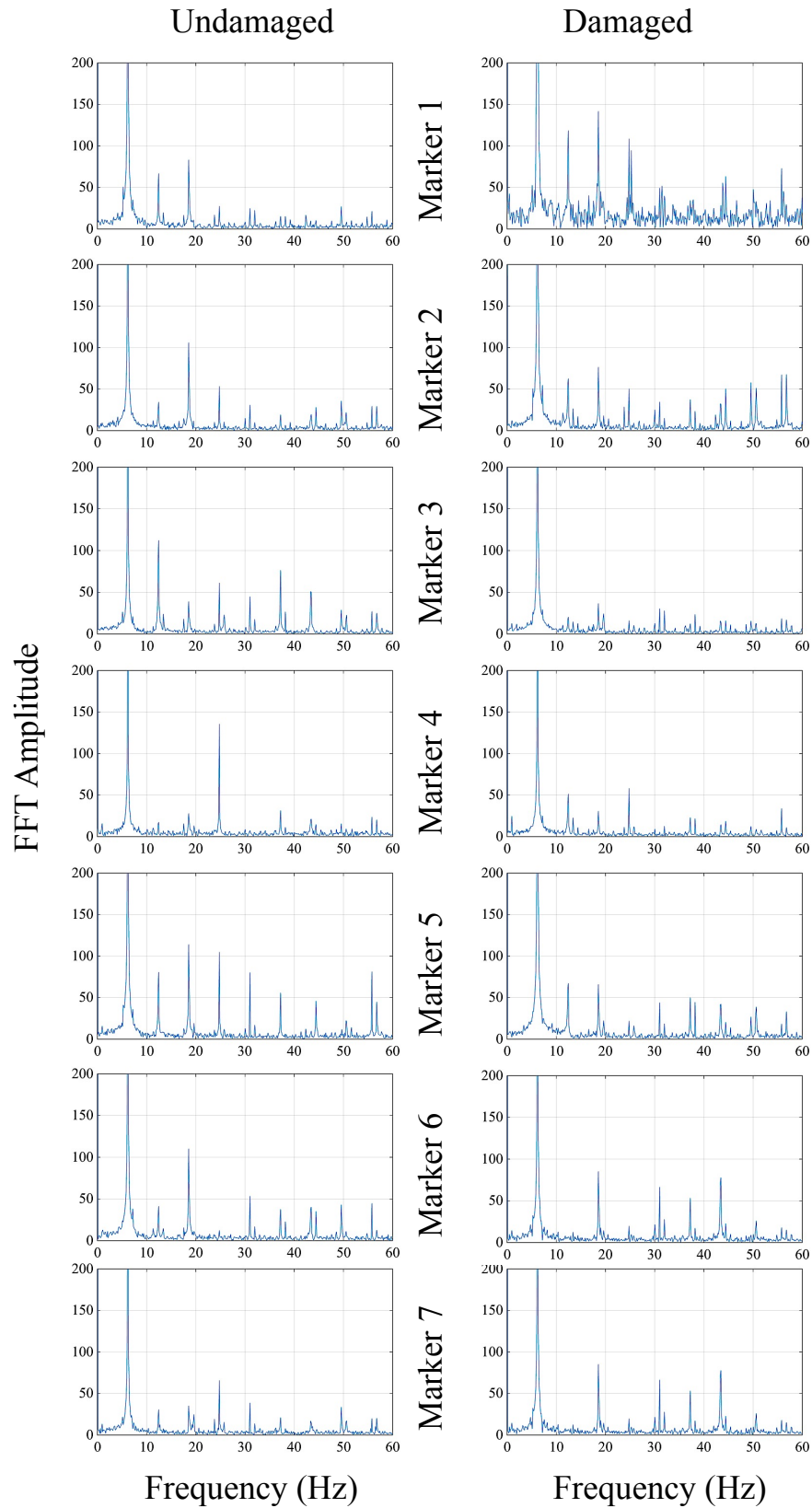


**Figure 5. 19: Displacement variation-derived frequency spectra of undamaged and damaged blades at the input settings of 6.3 Hz and 4V.**

### 5.3.5 Conclusion

In this case study, the vibrations of damaged and undamaged blades under different input frequencies and voltages were measured using a high-speed stereo imaging system.

- The vibration dynamics were obtained by employing two image processing methods, the intensity fluctuation-based method and the marker-tracking method. The intensity-based method is more sensitive to surrounding conditions and image noise. The vibration frequencies measured by the two methods exactly matched the input vibration frequencies. From 6.0 to 6.4 Hz, the highest amplitudes of the measured vibration frequency were found at 6.3 Hz, which may be one of the natural frequencies of the measured 29-inch fiberglass low wind generator blade. With higher input voltage, the obtained frequency amplitude dropped. This could be used to reduce the resonant frequency phenomenon.
- The vibration dynamic differences in the undamaged and damaged blades were distinguished by both the intensity-variation method and the displacement-tracking method. In the time domain measurement, since the blade vibration displacements were small, the intensity variation-based method was more sensitive in detecting structural change. In the frequency domain, the phenomenon of higher-amplitude harmonics in the damaged blade was found in the image intensity variation-based results. In the marker tracking-based results, no clear trend in harmonics was found. This indicates that the intensity fluctuation-based method is more sensitive than the marker tracking-based method in damage signal detection. However, some other

frequency peaks appeared in marker tracking-derived frequency spectra, which may be caused by the existing crack. Further experiments need to investigate this question.

## **5.4 Case 2: membrane coupling rotation-vibration measurement**

### **5.4.1 Introduction**

The alignment of pipes is crucial to ensure the optimum transfer of gases or liquids in a system of pipes. During system operation, any damage would be costly in terms of money, time, and labour. There is also an added disadvantage of a loss of production hours. The membrane coupling (see the red components in Figure 5.20), which connects with pipes, is a common solution to minimise the misalignment of reaction forces (Johnson, 1996). The membrane coupling is often designed with an infinite lifespan. Based on this, an overall test and measurement of membrane coupling performance in various simulated critical operating conditions is necessary to understand its dynamics. The information can be used in developing more knowledgeable design criteria before it becomes a product. Determining the natural frequency of the membrane coupling is also very important to avoid any damage caused by the resonant frequency phenomenon.

Vision-based measurement, as a non-intrusive and flexible measurement technique, can be an ideal diagnostic solution for acquiring multi-dimensional information without affecting key operating components and conditions. The dynamics of the coupling membrane can be easily obtained and analysed through a combination of a high-speed camera and powerful post-image processing algorithms.

Each pixel of the image is a light signal-recording channel. The pixel coordinates and its intensity are related to the geometry of the measured object's surface and its reflective luminous intensity. When the camera and light source positions are fixed,

any changes in the intensity of the image are related to the measured object's motion. Because the measured membrane coupling is made with the same material, any intensity variation is caused only by a change in surface reflectivity, so it can be used to identify motion.

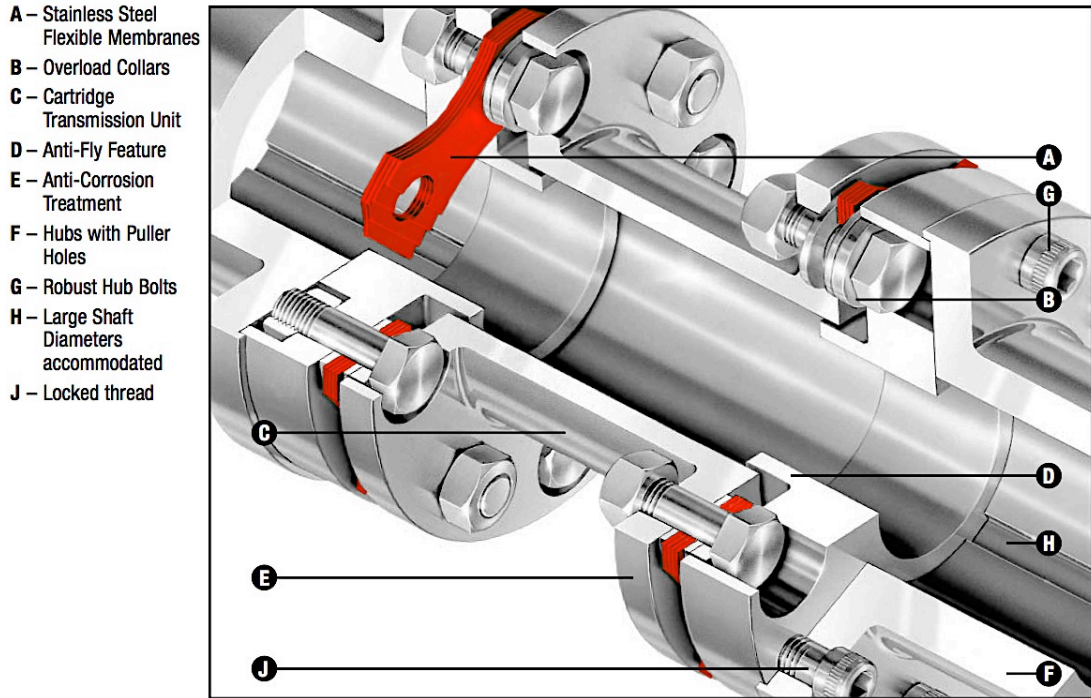


Figure 5. 20: Schematic of a membrane coupling connected with pipes.

An image is an inherently 2D radial signal. Therefore, the vertical and horizontal dynamics information can be recorded simultaneously using the light reflected from the measured object's surface. In this particular case, vision-based measurement and image intensity-based vibration measurement are applied to evaluate the vertical rotation and the horizontal vibration signal of the membrane coupling during its operation at variable conditions.

### 5.4.2 Experimental setup and process

The membrane coupling dynamics tests were conducted on the Dynamics Coupling Test Rig at John Crane Manchester. The schematic layout of the experimental



apparatus is illustrated in Figure 5.21. The capability of the rig in terms of its maximum speed, torque, and cyclic frequency is 3000 rpm (low-speed line), 12,000 Nm (low-speed line), and 15–20 Hz, respectively.

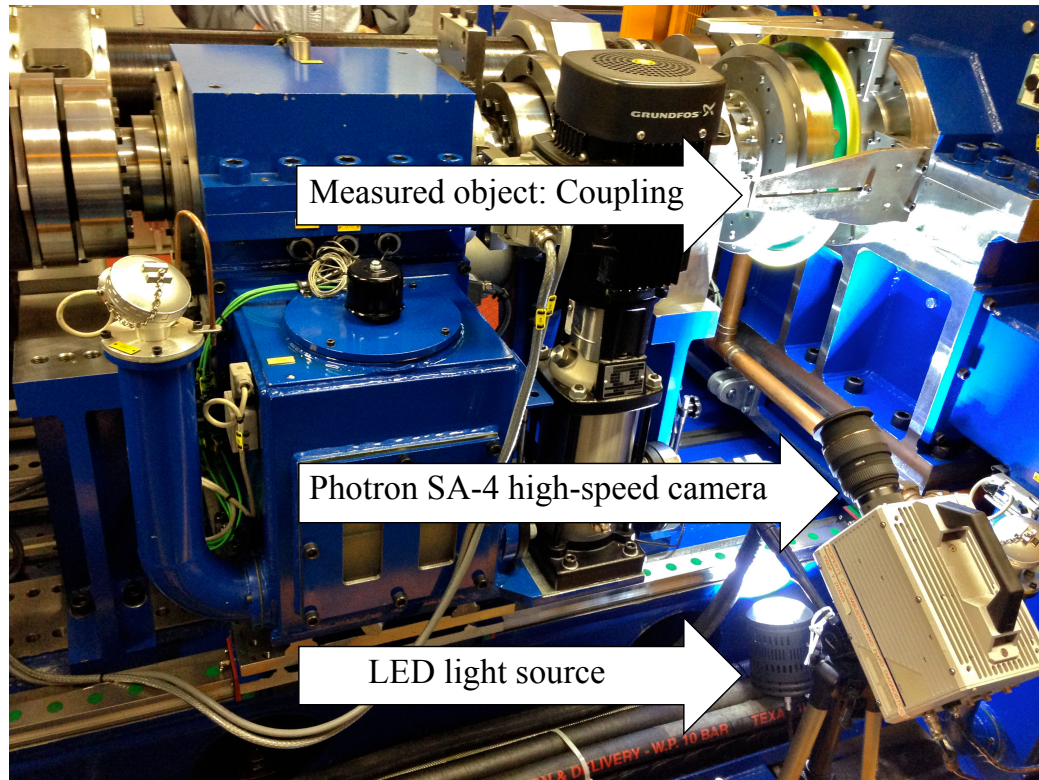


**Figure 5. 21: Schematic of testing setup.**

The test coupling membrane (GA/118640), whose structure is shown in Figure 5.22, can support a maximum speed of 15,900 rpm, maximum peak torque at 11,385 Nm, and maximum continuous torque at 7590 Nm, including a 1.5 FOS (factor of safety) for API (American Petroleum Institute) standard 671. Hence, the real maximum continuous torque is approximately 5060 Nm. The membrane bowing effect is designed to begin at approximately 40% of maximum continuous torque at around 3036 Nm.

On the test membrane coupling, there are six sides between the six adjacent bolt positions, as shown in Figure 5.22. Prior to testing, each side of membrane was

marked with a number (1 to 6). The membrane coupling was initially tested at of 2000 rpm and 1000 Nm steady torque. Then a steady increase in torque to 4000 Nm at a 1000 Nm interval was examined along with one additional case at 5500 Nm. The effect of cyclic frequency torque was also considered in a separate test conducted at 2000 rpm and 4000 Nm steady torque with cyclic torque variation from  $\pm 500$  Nm to  $\pm 1500$  Nm at a 500 Nm interval along with 5, 10, and 15 Hz for each cyclic torque level.

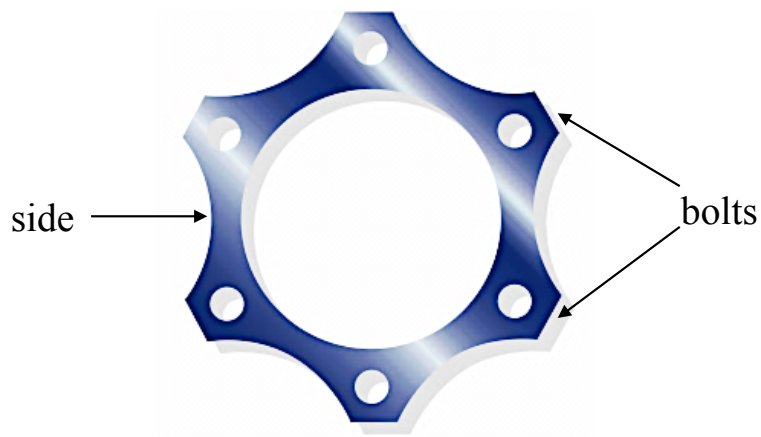


**Figure 5. 22: Six-bolt membrane coupling (GA/118640).**

For image data acquisition, a Photron SA-4 high-speed camera was employed. Since the rotation speed of the test was 2000 rpm, the corresponding frame rate was set to 3000 fps, which is dynamically sufficient to capture non-blurry images for the detection of frequencies up to 1500 Hz based on the Nyquist theorem. To obtain sufficient and steady illumination, a 60W IDT (Integrated Design Tools) LED light source was placed near the camera. Figure 5.23 shows a sample of image data captured at 2000 rpm with 5500 Nm steady torque, in which the membrane bowing is clearly apparent.

To analyse the dynamics of the coupling membrane, the intensity variation was tracked in the measured window; the position on an image is shown in Figure 5.24,

where the side length of the measured window is equal to the width of the membranes. The results were transformed to the frequency domain via FFT.

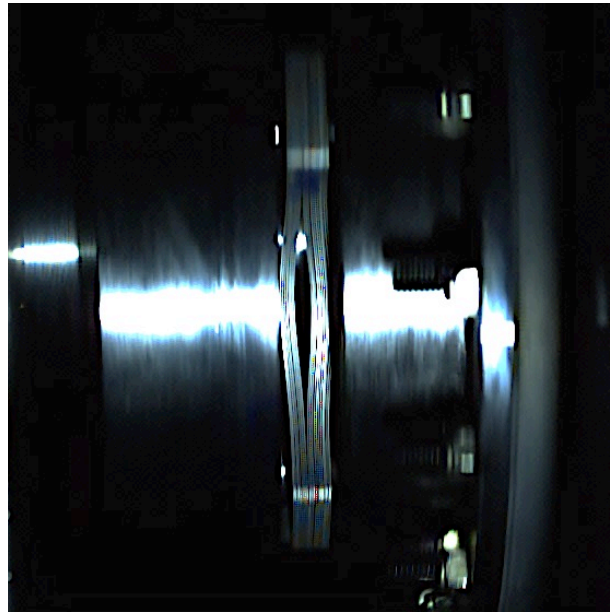


**Figure 5. 23:** A sample image of bowing occurred in the 2000 rpm and 5500 Nm steady torque test case.

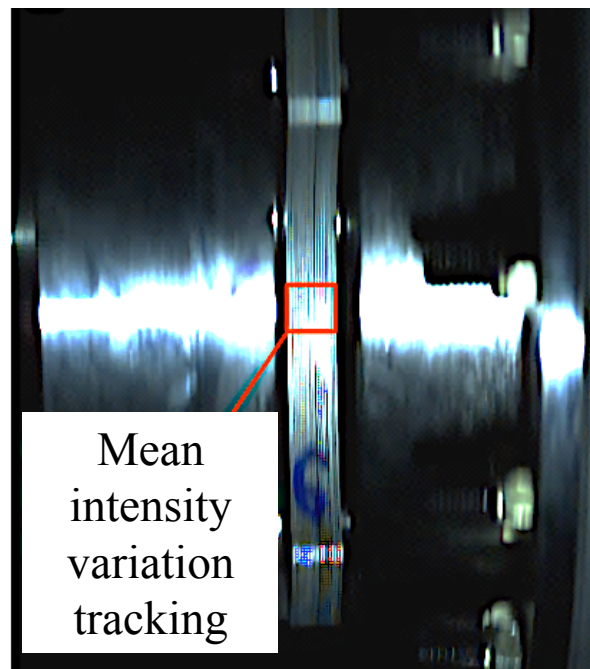


**Figure 5. 24:** Intensity variation tracked window position.

### 5.4.3 Results and analysis

#### 5.4.3.1 Vibration frequency identification

For consistency throughout this section, the symbol  $f_r$  is designated as the coupling rotation frequency and  $f_c$  is designated as the cyclic torque frequency, while  $f_v$  denotes other identified frequency components besides the aforementioned two. A sample frequency spectrum result is shown in Figure 5.25. It was obtained by measuring the mean intensity variation with 1024 images in the case of 1500 Nm cyclic torque at a 10 Hz cyclic frequency. The rotating  $f_r$  and its harmonics are shown; the  $3f_r$  and  $6f_r$  have higher amplitude in the frequency spectrum. The  $f_r$  was measured at 33.2 Hz, which is a good match to the expected rotation frequency of 33.33 Hz at 2000 rpm. In the low-frequency components,  $f_c$  is measured at 10 Hz, which also matches the 10 Hz input torque cyclic frequency well.

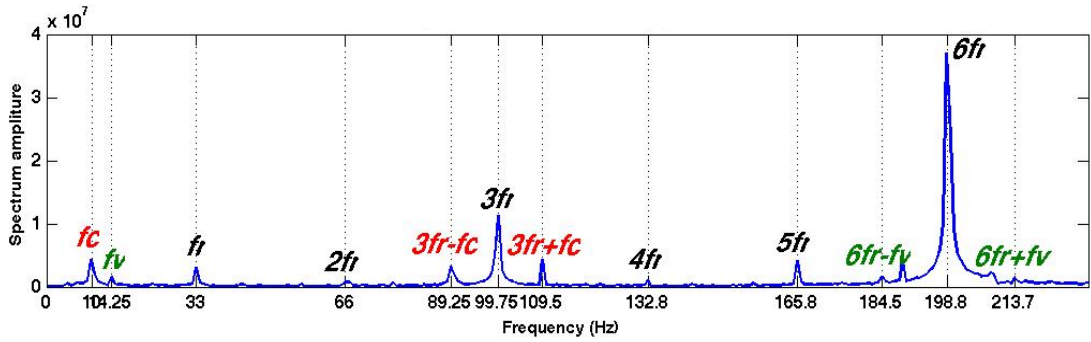


Figure 5. 25: A sample frequency spectrum.

In the coupling of two arbitrary signals,  $x_1(t) = X_1 \sin(w_1 t)$  and  $x_2(t) = X_2 \sin(w_2 t)$ , a component  $k \sin(w_1 t) \sin(w_2 t)$  may appear as a nonlinear response, where  $k$  is an arbitrary parameter. This component can be decomposed into harmonics using elementary trigonometry as follows:

$$k \sin(w_1 t) \sin(w_2 t) = k (\cos ([w_1 - w_2] t) - \cos ([w_1 + w_2] t))/2 \quad (5.5)$$

Therefore, in the case that two different frequency components are contained in the measured signal which originate from different sources (such as, rotation frequency and vibration frequency), their modulation takes place (Bilosova & Bilos, 2012). Modulation in a frequency spectrum appears as a series of side bands (the sum and difference of the two coupled frequencies). The phenomenon was previously observed in a buoyant diffusion flame under acoustic excitation (Huang, Wang, Tang, Zhu, & Zhang, 2012; Wang, Huang, Tang, Zhu, & Zhang, 2013) and fluid motion (Fenstermacher, Swinney, & Gollub, 1979).

In Figure 5.25,  $f_r$  and  $f_c$  were detected at 33.2 Hz and 10 Hz, as mentioned before. Several sub-frequency components also appeared clearly at the left and right sides of the  $3f_r$  and  $6f_r$  frequency components. Each sideband between the rotating frequency signals and their sub-frequencies is equal to 10 Hz. Thus, these sub-frequencies can be defined as  $nf_r \pm f_c$ . One can also find smaller sub-frequencies around  $f_r$  and its harmonics, whose sideband was 13 Hz. These sub-frequencies could be defined as  $nf_r \pm f_v$ .

The coupling rotation was in the  $y$  direction of the measured images. Therefore, it must be that  $f_r$  is a vertical signal. The bowing opening and closing relative to the axial  $x$  direction is caused by cyclic torque. This implied that  $f_c$  is a horizontal signal. The occurrence of a coupled signal frequency  $nf_r \pm f_c$  shows interaction between a signal in the vertical ( $y$  axis) relative to the horizontal ( $x$  axis) plane. Since the coupled signal frequencies  $nf_r \pm f_c$  and  $nf_r \pm f_v$  are both found in the frequency spectrum, this ensures that  $f_v$  is a signal in the same direction as  $f_c$ . Therefore,  $f_v$  is also a horizontal signal, which we hypothesise is the membrane coupling vibration signal.

### 5.4.3.2 Steady torque effect

Figure 5.26 illustrates the coupling rotation-vibration frequency spectra of the increasing steady torques obtained by the intensity variation-based motion detection approach. Although two frequency components,  $f_r$  and  $f_v$ , were expected to be presented based on the rotation-vibration mechanism, only  $f_r$  is clearly discernible in the full-scale frequency spectra. The harmonics of the  $f_r$  are also prominent in this frequency profile. In particular, the  $6f_r$  and its direct multipliers (12, 18, 24, 30, 36, and  $42 \times f_r$ ) are the main frequency components, which could be explained by the structure of the membrane coupling with six bolts that enhanced the  $6f_r$  frequency signal in intensity variations. In the low-frequency event, from  $f_r$  to the  $10f_r$  range, only harmonics exist. This means that no imbalance or misalignment phenomenon occurred. The highest peaks of frequency components occur at the  $12f_r$  positions in sub-figures (a), (d), and (e), while in sub-figures (b) and (c), the highest peaks at  $6f_r$  are observed. It is also interesting to note that, in the highest 5000 Nm torque case, the amplitudes of the  $3f_r$  and  $9f_r$  components became significant, as shown in sub-figure (e). Because, in the 5000 Nm torque case, three membrane bowings occurred at the sides of No. 1, 3, and 5, these additional structural parts enhanced the  $3 \times n$  ( $n=1, 2, 3, 4, 5 \dots$ ) of  $f_r$ . Based on the above measurement, it is demonstrated that the intensity fluctuation-based vibration detection depends greatly on the object's structure, as the principle of this method is to measure the object's surface reflectivity.

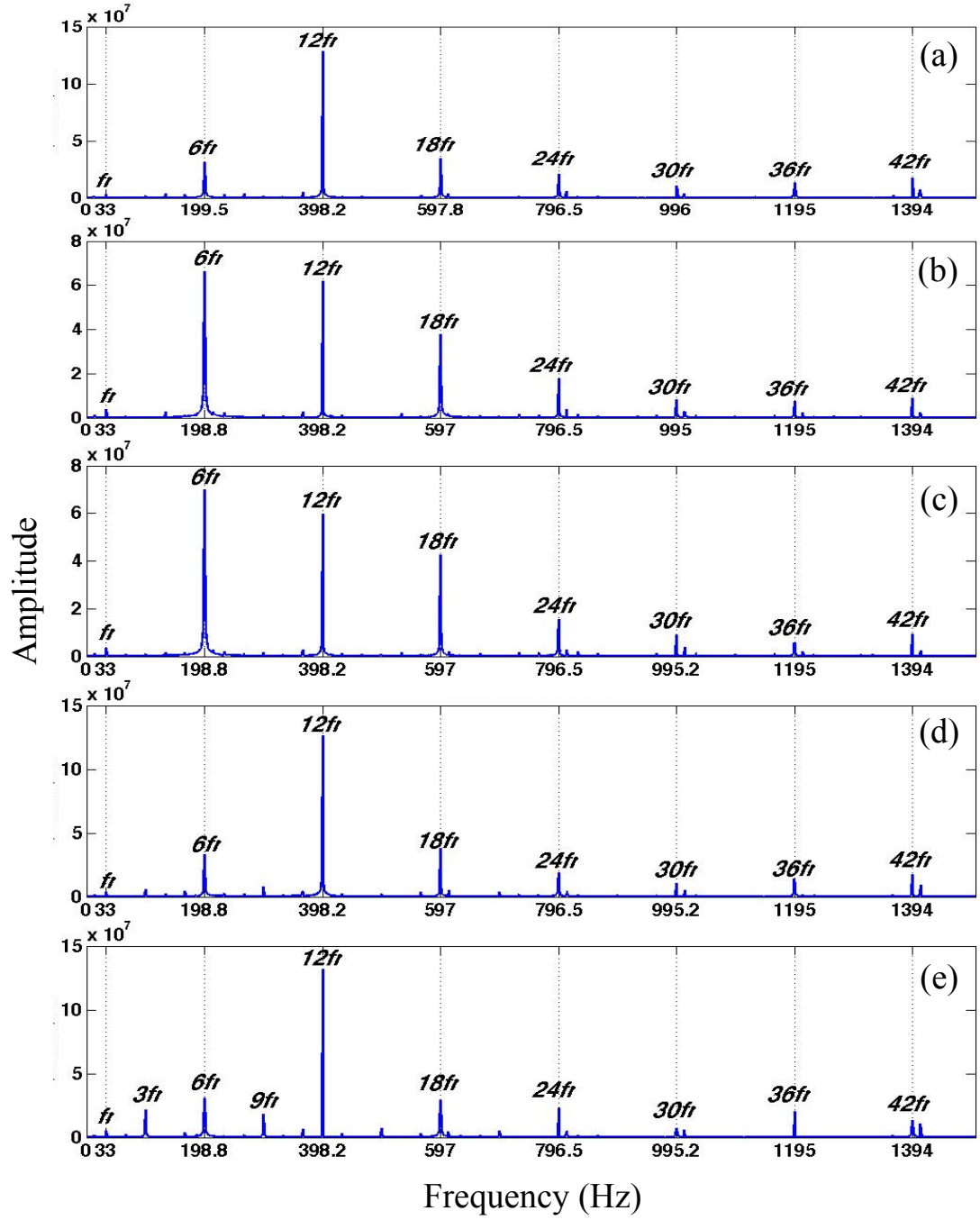


Figure 5.26: Intensity variation-derived frequency spectra for increasing steady torque from 1000 to 5000 Nm.

To find the membrane bowing effect on  $f_v$ , the corresponding sub-synchronous portion (the range below the rotation frequency) the frequency spectra in Figures 5.26 are magnified and shown in Figure 5.27. In these sub-synchronous frequency spectra, both  $f_r$  and  $f_v$  can be seen clearly. When the steady torque increased, the  $f_r$



was constant at 33 Hz because it depends only on the rotation speed of 2000 rpm.

However, the  $f_v$  fluctuated slightly between 12 and 14.25 Hz.

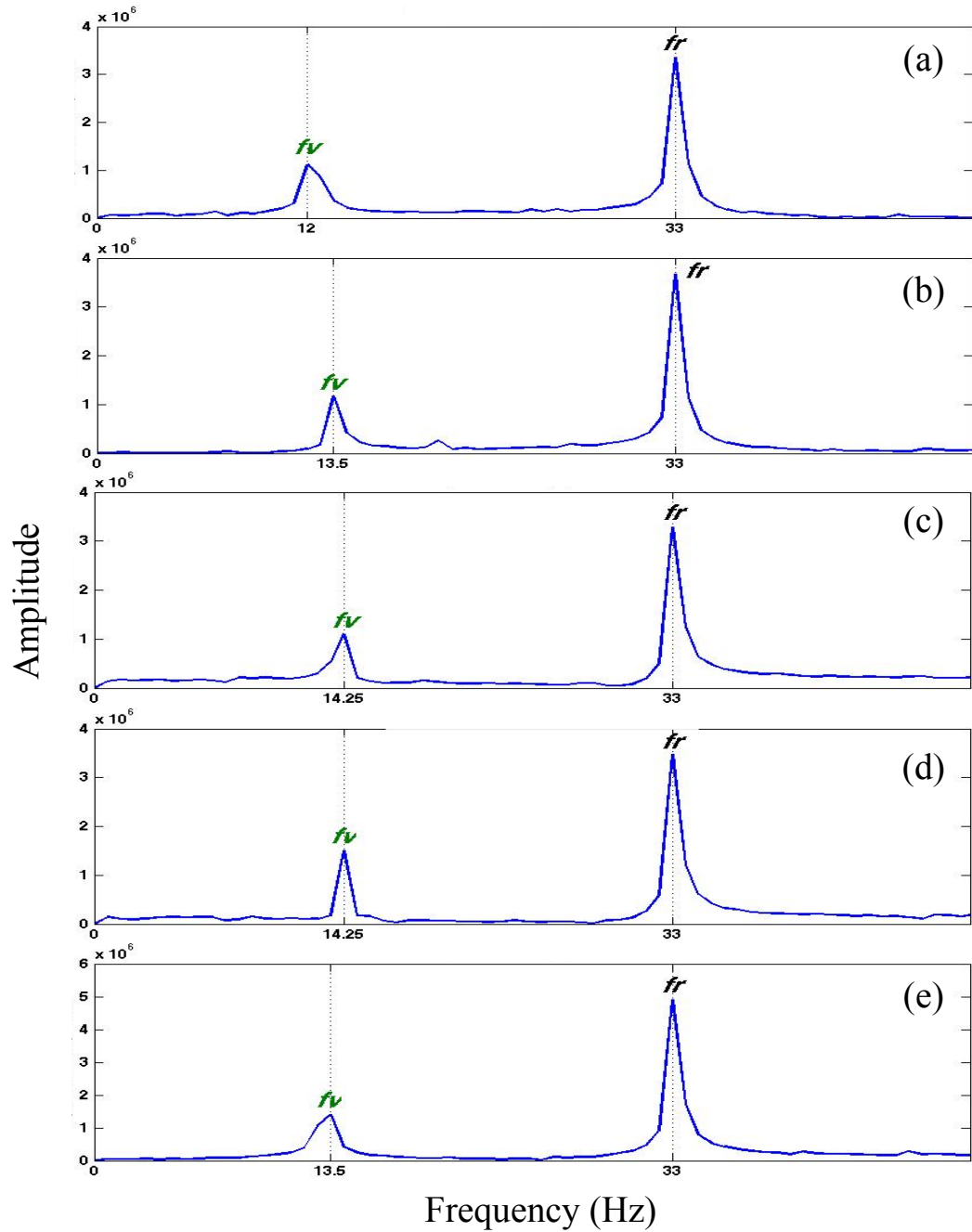


**Figure 5.27: Intensity variation-derived frequency spectra (sub-synchronous portion) for increasing steady torque from 1000 to 5000 Nm.**

To identify the relationship between the steady torque and the  $f_v$  clearly, the corresponding  $f_v$  variations at different torques were plotted in Figure 5.28. When



steady torque increased from 1000 to 3000 Nm, the  $f_v$  increased from 12 Hz to 14.25 Hz, respectively. The  $f_v$  profile had plateaus at 14.25 Hz between 3000 and 4000 Nm. After an increase to 5500 Nm steady torque, the  $f_v$  decreased to 13.5 Hz. This reductive trend from 4000 to 5000 Nm could be attributed to the emergence of membrane bowing that starts at 3036 Nm based on its design. The  $f_v$  may be one of the natural frequencies of the tested membrane coupling, which would be affected by the steady torque. With higher steady torque, the  $f_v$  increases slightly during membrane coupling rotation, but the opposite occurs with the presence of bowing along with a further increase in torque beyond a critical value. Further tests are still needed to ensure that the membrane bowing begins to occur at exactly 3036 Nm steady torque as it was designed to do, but the vision-based measurement with intensity variation-based vibration measurement method has already proven its ability in product vibration testing.

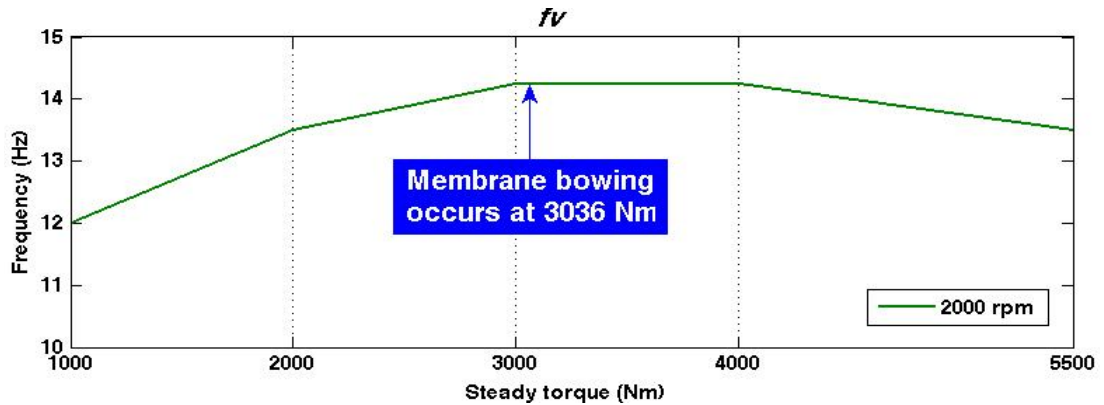


Figure 5. 28:  $f_v$  change during a steady torque increase.

#### 5.4.3.3 Cyclic torque and its frequency effect

The effect of cyclic torque and its frequency is discussed in this section. Figure 5.29 shows the frequency spectra of coupling operation at 4000 Nm steady torque with additional 10 Hz cyclic torques. From (a) to (d), the cyclic torques were set at 0,

$\pm 500$ ,  $\pm 1000$ , and  $\pm 1500$  Nm, respectively. Three types of signals of  $f_r$ ,  $f_v$ , and  $f_c$ , are found in the obtained intensity variation frequency spectra because the coupling dynamics contribute to three types of forces (rotating driving, steady torque, and cyclic torque). It is worth noting that the coupled oscillations of  $3f_r \pm f_c$  and  $6f_r \pm f_v$  are also observed on the left and right side of  $3f_r$  and  $6f_r$ , respectively. With increased cyclic torque, the amplitude of  $f_c$  also increased accordingly. This signifies that higher cyclic torque will induce greater disturbance, with its main oscillation mode matching the cyclic frequency.

The higher cyclic torque results in the elevation of the various frequency components. The frequency spectra under variable cyclic frequent variation at a particular cyclic torque were similar, so only the highest cyclic torque cases with  $\pm 1500$  Nm are discussed here. Figure 5.30 shows the frequency spectra of coupling rotation-vibration under 2000 rpm and 4000 Nm with  $\pm 1500$  Nm at frequencies from 5 to 15 Hz with 5 Hz intervals. Unlike the results with variable cyclic torque shown in Figure 5.29, the amplitude of frequency component is less affected by the cyclic frequency change. However, when the applied cyclic frequency was 15 Hz, the  $f_v$  was incorporated with  $f_c$  as a single-frequency component, as indicated in sub-figure (d). As resonance occurred, the amplitude increased. Based on the above, it can be assumed that the cyclic torque would not affect the frequency component caused by the steady torque; when they were close, resonance occurred.

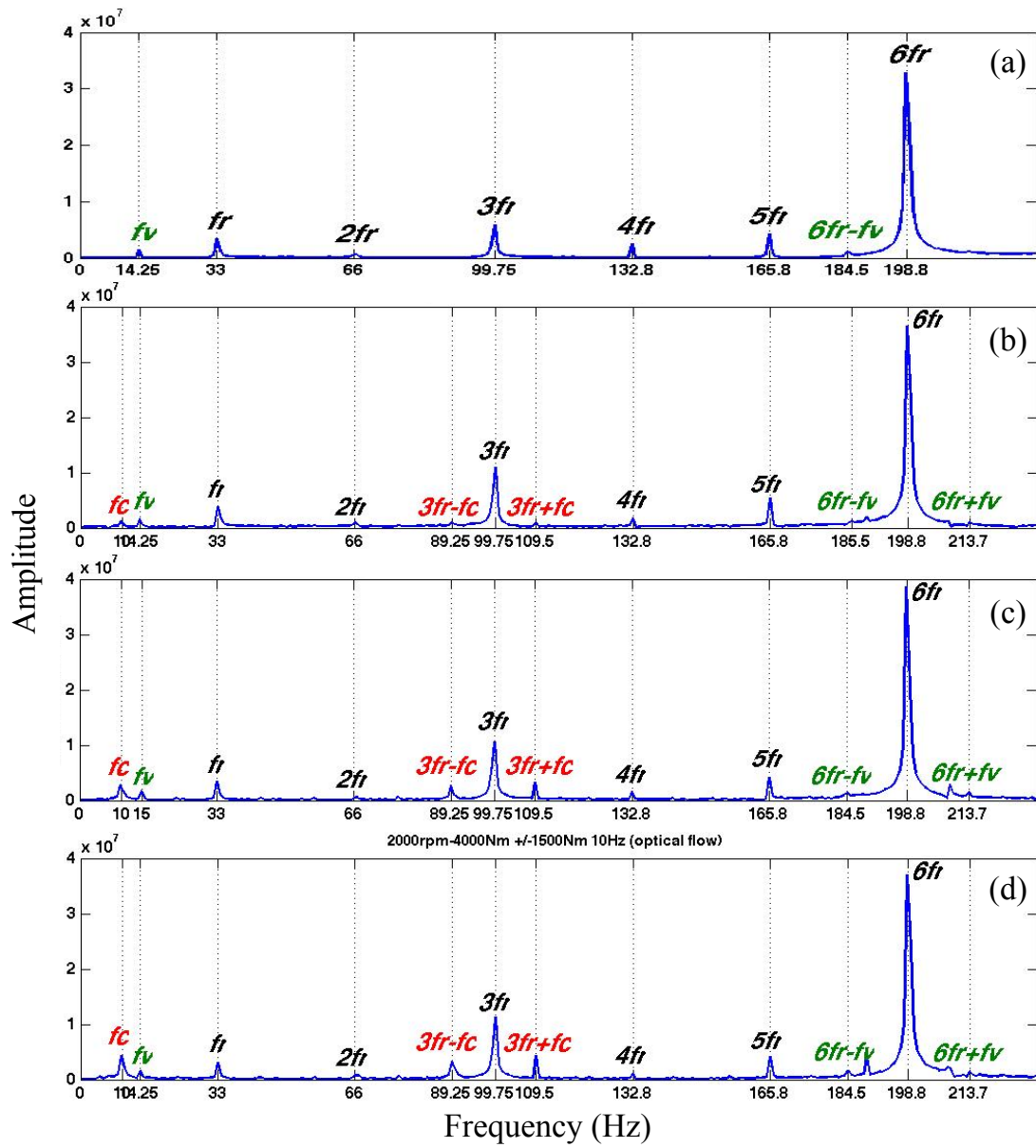
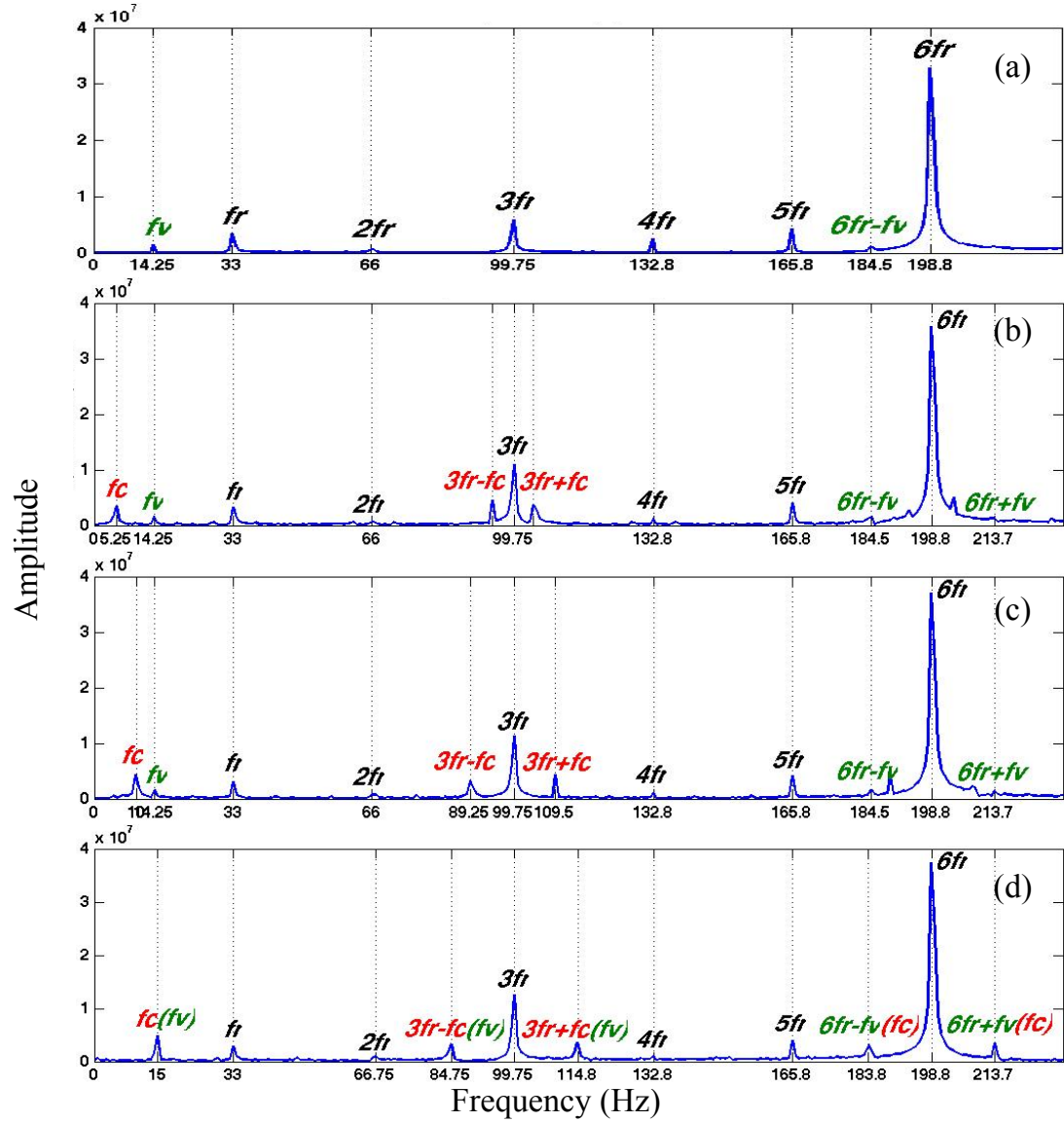


Figure 5. 29: Image intensity variation gained frequency spectra of coupling rotation-vibration under 2000 rpm and 4000 Nm steady torque with 10 Hz cyclic torques at 500, 1000, and 1500 Nm.



**Figure 5.30: Image intensity variation-derived frequency spectra of coupling rotation-vibration under 2000 rpm and 4000 Nm steady torque with 1500 cyclic torques at 5, 10, and 15 Hz.**

### 5.4.4 Conclusion

The image intensity fluctuation-based vibration measurement was successfully applied for industrial membrane coupling rotating-vibration dynamics testing. The membrane coupling dynamics was measured at a constant 2000 rpm rotation under different steady torques, cyclic torques, and cyclic torque frequencies.

- The measured intensity fluctuation was related to the two-dimensional motions of the membrane coupling in the vertical (rotation) and horizontal (vibration) directions. Hence, in this testing, the measured image intensity fluctuation-obtained frequency spectrum was combined with three types of frequencies caused by the rotation signal, steady torque-led vibration signal, and cyclic torque-caused vibration signal. These three types of frequency components ( $f_r$ ,  $f_c$ , and  $f_v$ ) were identified successfully in the combination frequency spectra. The nonlinear components of  $nf_r \pm f_c$  and  $nf_r \pm f_v$  were also detected.
- The relations between steady torques and vibration frequency were obtained. The natural frequency  $f_v$  was found. When the steady torques were increased, the vibration frequency  $f_v$  increased as well. However, if membrane bowing occurred, the vibration frequency decreased when the steady torques increased. Membrane bowing can reduce the natural vibration frequency effectively.
- The cyclic torques did not affect the rotation frequency  $f_r$ . When the cyclic torque frequency  $f_c$  differed from the steady torque  $f_v$ , cyclic torques did not affect the vibration frequency  $f_v$ . When  $f_c$  was close to  $f_v$ , the resonance occurred. The limitation of how  $f_v$  close to the frequency  $f_v$  would lead this resonance occurred needs more tests to be confirmed. Furthermore, a higher cyclic torque frequency increased the amplitude of  $f_c$ .

## **5.5 Conclusion of intensity fluctuation-based vibration measurement**

In this chapter, an image intensity fluctuation-based vibration detection method was proposed:

- The principle of the method is the use of image intensity fluctuation to detect vibration frequency. When the light geometry is fixed, the image intensity depends on the object's surface reflectivity. The surface reflectivity alternation is related to object motion. Thus, the vibration signals can be detected by the measured image's intensity fluctuation.
- A well-selected measured window is the key factor for vibration signal detection. The position and size are two important parameters in choosing the measured window. To obtain a strong vibration signal, the measured window should include an obvious feature, such as a different material or colour that would present a large difference in image intensity. The mean intensity of a measured window is recorded as the reflected light from the measured object. A large measured size leads to small intensity variation but can cover more of the vibration signal.
- The intensity fluctuation-derived vibration frequency method was compared with the marker displacement-derived vibration frequency method in monitoring blade vibration in Section 5.3. Both methods can detect vibration frequency exactly. The image intensity fluctuation-based method is more sensitive to vibration signals than the displacement-based method in measuring vibration with a small displacement and in detecting damage

signals. The method's ability and efficiency in vibration monitoring and damage detection were demonstrated.

- The proposed intensity fluctuation-based vibration frequency detection method was applied in an industrial membrane coupling rotation-vibration testing in Section 5.4. In this case, both the rotation frequency (in the vertical direction) and vibration frequency (in the horizontal direction) were obtained; this demonstrated that the method can detect motion in two directions simultaneously. The natural vibration frequency was detected. The membrane coupling effect was analysed. The vibration frequency was successfully separated from the rotation-vibration combination frequency spectrum.

# 6

---

## CONCLUSION AND FUTURE WORK

---

The main objective of this thesis is to carry out vision-based measurement for both combustion and vibration studies. Various suitable methodologies have been developed. The developed methodologies have been applied in different combustion and vibration case studies. The contributions of this research are summarised together with suggestions for future work.

### 6.1 Conclusion

- A high-speed stereo colour imaging system was employed in this work. It consists of a Photron SA-4 high-speed colour camera and a four-mirror stereo adapter. The calculated SNR indicates that this imaging system is of high quality with a very low noise level. It has been successfully applied in both combustion and vibration diagnostics studies. The flame colour and the light intensity reflected from the object were utilised to develop flame chemiluminescence measurement and vibration frequency detection, respectively.



- A novel flexible flame chemiluminescence measurement was proposed for combustion studies. The principle of this method was to use image colour to estimate the flame chemiluminescence emissions of  $\text{CH}^*$  and  $\text{C}_2^*$ . A camera sensor calibration process was employed in the proposed method to correct the sensor spectral sensitivity difference in different cameras. The  $\text{CH}^*$  and  $\text{C}_2^*$  expressions were built based on the spectral sensitivities of the B and G channels at the 430 nm and 516 nm wavelengths. The calculated  $\text{CH}^*/\text{C}_2^*$  ratio was correlated to the flame equivalence ratio. The 2D  $\text{CH}^*/\text{C}_2^*$  map demonstrates the good potential of the method in visualising local equivalence ratio variations.
- The proposed flame chemiluminescence measurement method was applied in the case study of propane flame propagation in tubes. In a closed tube, a flame was observed to propagate stably under all flammable equivalence ratio ranges, while, in an open tube, it becomes oscillatory when the fuel equivalence is between  $1.1 < \Phi < 1.4$ . The flame structure oscillation was analysed by tracking the flame's front point. The flame's local equivalence fluctuation was discussed using a 2D  $\text{CH}^*/\text{C}_2^*$  ratio map. Higher ratios were found at the flame front when the flame moved forward, which indicates 'better' combustion when the flame moved from burned gas to unburned gas. The flame equivalence fluctuation frequency was the same as the flame front displacement-derived oscillation frequency. The reason for the flame equivalence fluctuation needs further investigation.

- The proposed method was also applied in the case study of flame ignition-to-impinging with different fuels, ignition positions, and flow rates. A time delay of the diffusion flame signal (yellow-red flame) after ignition was observed in all cases. The  $\log(I_D/I_P)$  ratio was introduced to quantitatively analyse the relations between yellow-red flame and green-blue flame signals. The 2D  $\text{CH}^*/\text{C}_2^*$  ratio was successfully combined with stereo imaging and 3D reconstruction techniques. The 3D flame structure and the chemical reaction were analysed. The 3D  $\text{CH}^*/\text{C}_2^*$  map showed the potential of the proposed method in 3D flame chemical measurement.
- Image intensity fluctuation was proposed to detect vibration signals. The principle of this method is to measure the light intensity reflected from the object's surface. The image intensity variation depends on the measured surface's reflectivity. The image intensity fluctuation refers to the object's reciprocating motion when the light geometry is fixed. Two parameters, the measured position and size of the measured windows, were estimated. This method can be applied to evaluate vibration frequency by measuring a side view of a rotating object.
- The image intensity fluctuation-based vibration frequency detection was compared with feature tracking-based displacement measurement in a wind turbine blade vibration monitoring study. Undamaged and damaged blades were measured under different input vibration frequencies and amplitudes. The vibration frequency of 6.3 Hz has the strongest amplitude, as it is the natural frequency of the test wind

turbine blade. The difference between the undamaged blade and the damaged blade was obtained by both methods. The intensity-based method is more sensitive to small amplitude vibration than the displacement-based method. The image intensity fluctuation-based vibration measurement showed a good ability in vibration dynamics measurement and has great potential in blade condition monitoring and damage detection.

- This image intensity fluctuation-based vibration measurement method was also applied in industrial membrane coupling rotation-vibration testing. The coupling dynamics were measured under different steady torques, cyclic torques, and frequencies. The obtained frequency spectrum is a combination of the rotation frequency and the vibration frequency. The rotation frequency and two vibration frequencies were detected, which demonstrated the ability of the proposed method in 2D motion detection. The vibration frequency was successfully identified and separated from combined frequency spectra. The natural vibration frequency was found. The membrane bowing effects were discussed.

## 6.2 Scope of future work

- To develop the image colour-based flame chemiluminescence measurement method.
  - The image colour-based flame chemiluminescence method needs further development. The proposed method only employed  $C_2^*$  signals at 516.5 nm. Since, in the  $C_2^*$  Swan-band system, the  $C_2^*$  radiations

emit at the 473.7, 516.5, and 563.5 nm wavelengths, further investigation should estimate the effect of emissions at 473.7 and 563.5 nm.

- Considering the emissions at 473.7 nm and 563.5 nm may enable the development of a more accurate model. Because only the B and G channels are employed to calculate  $\text{CH}^*$  at 430 nm and  $\text{C}_2^*$  at 516.5 nm, the R channel may be useful in detecting other wavelengths, such as 563.5 nm. Therefore, further research should employ all colour channels to develop a more accurate model.
  - More comparisons between the proposed method and conventional methods, such as the spectroscopy method and the monochrome camera with filter method, could be considered. Another comparison between different cameras using the proposed image colour-based flame chemiluminescence measurement is worth studying.
- To investigate flame ignition by image colour-based flame chemiluminescence measurement and Schlieren imaging.
- The 2D local  $\text{CH}^*/\text{C}_2^*$  map can be combined with Schlieren imaging to investigate the relations between the local flame fuel/air mixture condition and flow density. As shown in Figure 6.1, the enhanced direct colour images are overlaid on Schlieren images. The blue flame portion can be processed to present  $\text{CH}^*$  and  $\text{C}_2^*$  concentrations. Then the  $\text{CH}^*/\text{C}_2^*$  ratio can show the local fuel equivalence. This combined measurement method can show a great potential for the analysis of flow density and fuel/air condition in the flame ignition process.

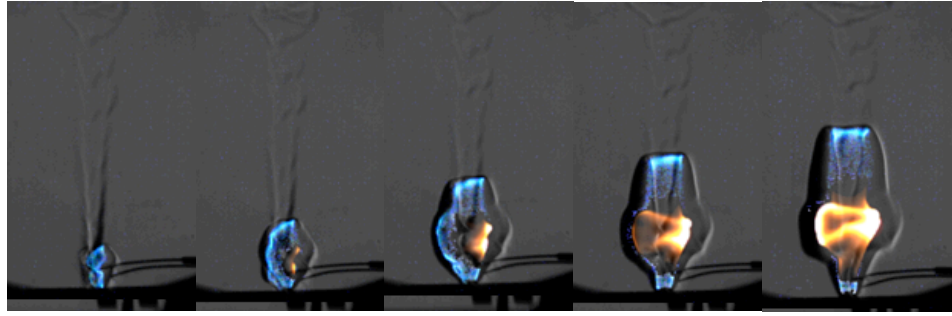
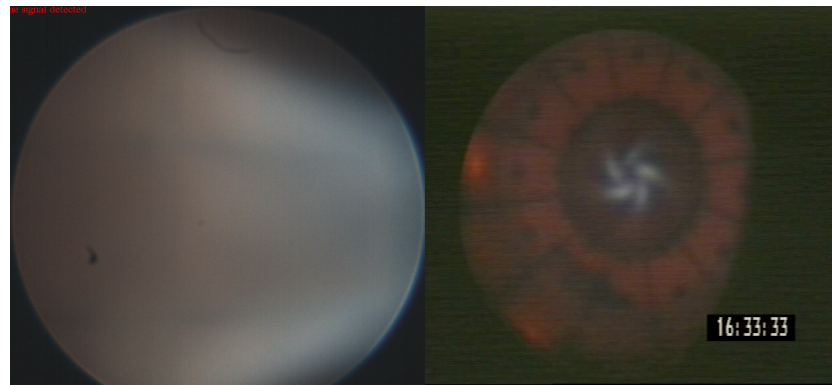


**Figure 6. 1: Enhanced colour images combined with Schlieren images for flame ignition measurement.**

- To measure the local fuel/air ratio in a real industrial gas turbine combustor.
  - Measurement of the fuel/air ratio within a gas turbine combustor is desirable in industry. In a combustor, the camera-measured flame colour is often affected by the red colour of the hot wall. As shown in Figure 6.2, the images of flames in a combustor were measured at Ansaldo Energy S.p.A. The flame colour signals are weak because of the strong red light emission from the hot wall, which makes it difficult to measure the correct flame chemiluminescence; hence, it cannot use the proposed flame chemiluminescence measurement directly to detect fuel/air ratio for developing the combustion reaction in the combustor. Therefore, removing or reducing the hot wall effect is important and worth studying.



(a) Side view

(b) Front view

**Figure 6. 2: Images of an industrial gas turbine combustor: (a) side view and (b) front view.**

- To develop 3D reconstruction of flames in tubes.
  - The distortion caused by a curved quartz tube wall is a serious problem for camera parameter calibration. The analysis was only conducted in two dimensions. Hence, further research could focus on solving this distortion problem, which would benefit analysis of the 3D chemical reaction during flame propagation.
- To combine the proposed two methods in gas turbine engines.
  - The proposed image colour-based flame chemiluminescence and image fluctuation-based vibration measurement could be combined in investigating gas turbine engines. Since a gas turbine has a combustor and a rotating blade, it is worth analysing their relations together. Because a flame is a self-illuminated object and a blade is reflected-illumination object, the imaging setting is an issue in measuring both objects clearly in one image.

## References

- Akkerman, V., Law, C. K., Bychkov, V., & Eriksson, L.E. (2010). Analysis of flame acceleration induced by wall friction in open tubes. *Physics of Fluids* , 22 , 053606.
- Aleiferis, P. G., Hardalupas, Y., Taylor, A., Ishii, K., & Urata, Y. (2004). Flame chemiluminescence studies of cyclic combustion variations and air-to-fuel ratio of the reaction mixture in a lean-burn stratified-charge spark-ignition engine. *Combustion and Flame* , 136, 72-90.
- Amirat, Y., Benbouzid, M. E., Al-Ahmar, E., Bensaker, B., & Turri, S. (2009). A brief status on condition monitoring and fault diagnosis in wind energy conversion systems. *Renewable and Sustainable Energy Reviews* , 13, 2629-2636.
- Arnold, H. (1977). William Henry Fox Talbot: pioneer of photography and man of science. *London: Hutchinson Benson*.
- Barnard, J. A., & Bradley, J. N. (1985). Flame and Combustion. *New York: Chapman and Hall*.
- Bartaud, T., & Heinze, T. (1992). Gasoline Distribution Measurements with PLIF in a SI Engine. *SAE Technical Paper* , 922355.
- Bayer, B. E. (1976). Colour imaging array. *Patent No. 3971065*. U.S.
- Bilsova, A., & Bilos, J. (2012). Vibration Diagnostics. Retrieved from [http://www.fs.vsb.cz/export/sites/fs/330/.content/files/VIBDI\\_skriptaEN.pdf](http://www.fs.vsb.cz/export/sites/fs/330/.content/files/VIBDI_skriptaEN.pdf)
- Boller, C., & Buderath, M. (2007). Fatigue in aerostructures - where structural health monitoring can contribute to a complex subject. *Philosophical Transactions of The Royal Society A* , 365, 561-587.
- Bradt, H. (2004). Astronomy Methods: A Physical Approach to Astronomical Observation. *Cambridge: Cambridge University Press*.
- Bruel, & Kjaer. (1982). Measuring Vibration. Retrieved from <http://www.bksv.co.uk/doc/br0094.pdf>.
- Bulewica, E. M., Padley, P. J., & Smith, R. E. (1970). Spectroscopic studies of C<sub>2</sub>, CH and OH Radicals in Low Pressure Acetylene + Oxygen Flames. *Proceeding of*

*the Royal Society of London. Series A, Mathematical and Physical Sciences* , 315, 129-147.

Buser, P. A., & Imbert, M. (1992). *Vision. MIT Press.*

Chou, T., & Patterson, D. J. (1995). In-cylinder measurement of mixture maldistribution in a L-head engine. *Combustion and Flame* , 101 (1-2), 45-57.

Chrisment, A. (1998). *Color & Colorimetry. Paris: Editions 3C Conseil.*

Ciang, C. C., Lee, J. R., & Bang, H. J. (2008). Structural health monitoring for a wind turbine system: A review of damage detection methods. *Measurement Science and Technology* , 19, 1-20.

Ciccarell, G., & Dorofeev, S. (2008). Flame acceleration and transition to detonation in ducts. *Progress in Energy and Combustion Science* , 34 (4), 499-500.

CIE. (1987). *International Lighting Vocabulary. CIE.*

Clark, T. P. (1958). Studies of OH, CO, CH and C<sub>2</sub> radiation from laminar and turbulent propane-air and ethylene-air flames. *National Advisory Committee for Aeronautics, technical note* 4266.

Clarke, H. (1974). *A first course in Quantum Mechanics. Internet Archive.*

Constant, M. (2009). Signal to Noise Ratio. Retrieved from [http://www.cctv-information.co.uk/i/Signal\\_to\\_Noise\\_Ratio](http://www.cctv-information.co.uk/i/Signal_to_Noise_Ratio).

Coward, H. F., & Hartwell, F. J. (1932). Studies in the mechanism of flame movement. Part II. The fundamental speed of flame in mixtures of methane and air. *Journal of the Chemical Society* , 1996, 2676-2684.

Cui, C., Matalon, M., & Jackson, T. L. (2005). Pulsating Mode of Flame Propagation in Two-dimensional Channels. *AIAA Journal* , 43 (6), 1284-1292.

Davies, E. R. (1997). *Machine Vision: Theory, Algorithms, Practicalities. London, United Kingdom: Academic Press.*

Dec, J. E., & Espey, C. (1998). Chemiluminescence Imaging of Autoignition in a DI diesel engine. *SAE Techniques paper* 982685.

Demler, M. J. (1991). *High-speed analog-to-digital conversion. Academic Press.*



- Devriendt, K., Van Look, H., Ceursters, B., & Peeters, J. (1996). Kinetics of formation of chemiluminescent  $\text{CH(A } 2\Delta)$  by the elementary reactions of  $\text{C}_2\text{H(X} 2\Sigma^+)$  with  $\text{O(} 3\text{P)}$  and  $\text{O}_2(\text{X} 3\Sigma^- \text{g})$ : a pulse laser photolysis study. *Chemical Physics Letters* , 261, 450-456.
- Docquier, N., & Candel, S. (2002). Combustion control and sensors: a review. *Progress in Energy and Combustion Science* , 28, 107-150.
- Dowling, J. E. (1987). The Retina: An Approachable Part of the Brain. *Belknap Press*.
- Drain, L. E. (1980). The Laser Doppler Technique. *New York: Wiley*.
- Endelman, L. L. (1988). A brief history of high speed photography 1851-1930. Retrieved from <https://people.rit.edu/andpph/text-hs-history.html>.
- Farrar, C. R., & Worden, K. (2007). An introduction to structural health monitoring. *Philosophical Transactions of The Royal Society A* , 365, 303-315.
- Fenstermacher, P. R., Swinney, H. L., & Gollub, J. P. (1979). Dynamical instabilities and the transition to chaotic Taylor vortex flow. *Journal of Fluid Mechanics* , 94, 103-128.
- Foat, T., Yap, K. P., & Zhang, Y. (2001). The Visualization and Mapping of Turbulent premixed impinging flames. *Combustion and Flame* , 125, 839-851.
- Francis, K. A., Sreenivasan, R., & Raghavan, V. (2011). Investigation of structures and reaction zones of methane-hydrogen laminar jet diffusion flames. *International Journal of Hydrogen Energy* , 36, 11183-11194.
- Gaydon, A. G. (1974). *The Spectroscopy of Flame*. London: Chapman and Hall.
- Gaydon, A. G., & Wolfhard, H. G. (1979). *Flames-their structure radiation and temperature* (4th ed.). London: Chapman and Hall.
- Gernsheim, H. (1986). A concise History of Photography. *New York: Dover Publications*.
- Gerstein, M., Levine, O., & Wong, E. L. (1951). Flame Propagation. II. The Determination of Fundamental Burning Velocities of Hydrocarbons by a Revised Tube Method. *Journal of The American Chemical Society* , 73 (1), 418-422.

- Giergiel, M., & Kohut, P. (2011). Analysis of Dynamics of Vibratory Machines Applying Vision Based Measurements. *Mechanics and Mechanical Engineering* , 15 (4), 43-51.
- Glassman, I. (1977). Combustion. *New York: Academic Press*.
- Gonzalez, R. Z., & Woods, R. E. (2002). Digital Image Processing using MATLAB. *New York: Prentice Hall*.
- Goshtasby, A., & Gruver, W. A. (1993). Design of a single-lens stereo camera system. *Pattern Recognition* , 26, 923-937.
- Guenoche, H. (1964). Nonsteady flame propagation, Ed. G.H. Markstein. *New York: Pergamon Press*.
- Guild, J. (1931). The colorimetric properties of the spectrum. *Philosophical Transactions of the Optical Society* , A230, 149-87.
- Haber, L. C. (2000). An investigation into the origin, measurement and application of chemiluminescent light emissions from premixed flames. *Master's thesis, Virginia Polytechnic Institute and State University, Blacksburg, Virginia, U.S.A.*
- Hameed, Z., Hong, Y. S., Cho, Y. M., Ahn, S. H., & Song, C. K. (2009). Condition monitoring and fault detection of wind turbines and related algorithms: A review. *Renewable and Sustainable Energy Reviews* , 13, 1-39.
- Hamins, A., Heitor, M., & Libby, P. A. (1988). Gravitational effects on the structure and propagation of premixed flames. *Acta Astronautica* , 17 (5), 503-514.
- Hanbury, A. (2002). The Taming of Hue, Saturation and Brightness colour Space. *Proceedings of the 7th Computer Vision Winter Workshop*, 234-243.
- Hanrahan, P., & Krueger, W. (1993). Reflection from layered surfaces due to subsurface scattering. *Proceedings of SIGGRAPH* , 27, 165-174.
- Hardalupas, Y., & Orain, M. (2004). Local measurements of the time-dependent heat release rate and equivalence ratio using chemiluminescent emission from a flame. *Combustion and Flame* , 139, 188-207.
- Healey, G., & Kondepudy, R. (1992). CCD Camera Calibration and Noise Estimation. *Proceedings of Computer Society Conference on Computer Vision and Pattern Recognition* , 90-95.

- Heavens, O. S., & Ditchburn, R. W. (1991). *Insight into Optics*. John Wiley & Sons.
- Hecht, E. (2002). *Optics* (4th Edition ed.). San Francisco: Addison Wesley.
- Higgins, B., McQuay, M. Q., Lacas, F., & Candel, S. (2001). An experimental study on the effect of pressure and strain rate on CH chemiluminescence of premixed fuel-lean methane/air flames. *Fuel* , 80 (11), 1583-1591.
- Higgins, B., McQuay, M. Q., Lacas, F., Rolon, J. C., Darabiha, N., & Candel, S. (2001). Systematic measurements of OH chemiluminescence for fuel-lean, high-pressure, premixed, laminar flames. *Fuel* , 80 (1), 67-74.
- Horn, B. K. (1975). *Image Intensity Understanding*. Massachusetts Institute of Technology. Retrieved from <http://people.csail.mit.edu/bkph/AIM/AIM-335-NEW-OPT.pdf>.
- Horn, B. K. (1977). Understanding Image Intensities. *Artificial Intelligence* , 8, 201-231.
- Hossain, M. M., Lu, G., Sun, D., & Yan, Y. (2013). Three-dimensional reconstruction of flame temperature and emissivity distribution using optical tomographic and two-colour pyrometric techniques. *Measurement Science and Technology* , 24 (7), 074010.
- Huang, H. W., & Zhang, Y. (2011). Digital colour image processing based measurement of premixed CH<sub>4</sub>+air and C<sub>2</sub>H<sub>4</sub>+air flame chemiluminescence. *Fuel* , 90, 48-53.
- Huang, H. W., & Zhang, Y. (2008). Flame colour characterization in the visible and infrared spectrum using a digital camera and image processing. *Measurement Science and Technology* , 19 (8), 085406.
- Huang, H. W., & Zhang, Y. (2012). Syngas combustion radiation profiling through spectrometry and DFCD processing techniques. *International Journal of Hydrogen Energy* , 37, 5257-5267.
- Huang, H. W., Wang, Q., Tang, H. J., Zhu, M., & Zhang, Y. (2012). Characterisation of external acoustic excitation on diffusion flames using digital colour image processing. *Fuel* , 94, 102-109.

- Huang, H. W., Yang, J., Wang, Q., & Zhang, Y. (2013). Variation of hydrocarbon compositions and ignition locations on the radiative flame initiation characteristics through multi-dimensional DFCD incorporated image analysis. *Fuel*, 103, 334-346.
- Inaba, M., Hara, T., & Inoue, H. (1993). A stereo viewer based on a single camera with view-control mechanism. *International Conference on Intelligent Robots and System*, 3, 1857-1865.
- Jain, R., Kasturi, R., & Schunck, B. G. (1995). *Machine Vision*. Singapore: McGraw-Hill.
- Jimenez, C., Quinard, J., Grana-Otero, J., Schmidt, H., & Searby, G. (2012). Unsteady response of hydrogen and methane flame to pressure waves. *Combustion and Flame*, 159 (5), 1894-1908.
- Johnson, C. M. (1996). The characteristics of multiple membrane couplings. *World pumps*, 12, 14-15.
- Juds, S. M. (1988). *Photoelectric sensors and controls: selection and application*. CRC Press.
- Katta, V. R., & Roquemore, W. M. (1993). Role of inner and outer structures in transitional jet diffusion flame. *Combustion and Flame*, 92, 274-282.
- Kiefer, J., & Ewart, P. (2011). Laser diagnostics and minor species detection in combustion using resonant four-wave mixing: a review. *Progress in Energy and Combustion Science*, 37 (5), 525-564.
- King, R. B. (1948). Relative Transition Probabilities of the Swan Bands of Carbon. *Astrophysical Journal*, 108, 429-433.
- Kojima, J., Ikeda, Y., & Nakajima, T. (2005). Basic aspects of OH(A), CH(A), and C<sub>2</sub>(d) chemiluminescence in the reaction zone of laminar methane-air premixed flames. *Combustion and Flame*, 140, 34-45.
- Kojima, J., Ikeda, Y., & Nakajima, T. (2000). Spatially resolved measurement of OH\*, CH\* and C<sub>2</sub>\* chemiluminescence in the reaction zone of laminar methane/air premixed flames. *Processing of the Combustion Institute*, 28, 1757-1764.
- Kon, S., Oldham, K., & Horowitz, R. (2007). Piezoresistive and Piezoelectric MEMS Strain Sensors for Vibration Detection. *Proceedings of SPIE*, 6529.

- Kumar, N. (2008). Comprehensive Physics XII. *Laxmi Publications*.
- Kuo, K. (2005). Principles of Combustion (2nd Edition ed.). *Hoboken: NJ: John Wiley and Sons*.
- Laufer, G. (1996). Introduction to Optics and Lasers in Engineering. *Cambridge: Cambriage University Press*.
- Lee, D., Kweon, I. (2000). A novel stereo camera system by a biprism. *IEEE Transactions on Robotics and Automation* , 16, 528-541.
- Lee., D. H., Kweon, I. S., & Cipolla, R. (1999). Biprism-stereo camera system. *Proceedings of the IEEE Computer Society Conference on Computer Vision and Pattern Recognition*, 1, 82-87.
- Lefebvre, A. H. (1999). Gas Turbine Combustion. *London: Taylor & Francis*.
- Li, G., Lu, G., & Yan, Y. (2014). Fire Detection using Stereoscopic Imaging and Image Processing Techniques. *IEEE International Conference on Imaging Systems and Techniques (IST)*, 28-32.
- Love, R. C. (1997). Surface Reflection Mode Estimation from Naturally Illuminated Image Sequences. *Leeds: The University of Leeds*.
- Lu, W., & Chu, F. (2010). Condition monitoring and fault diagnostics of wind turbines. *IEEE Prognosctis & Health Mangement Conference*, 1-11.
- Ma, Z., & Zhang, Y. (2014) High temperature measurement using very high shutter speed to avoid image saturation. *AIP Conference Proceedings*, 246-253.
- Mallard, E., & Le Chatelier, H. L. (1883). Recherches experimentales et theoriques sur la combustion des melanges gazeux explosifs. *Paris: H. Dunod et E. Pinat*.
- Maurice, L., & Adams, J. (2001). Rotating Machinery Vibration from Analysis to Troubleshooting. *New York: Marcel Dekker*.
- Maxwell, J. (1865). A Dynamical Theory of the Electromagnetic Field. *Phiosophical Transactions of the Royal Society of London* , 155, 459-512.
- McDaid, C. J. (2013). Developing and Implementing Advanced Optical Diagnostics for the Investigation of Fuel and Flow Effects on Impinging Jet Flames. *PhD Thesis* . *Sheffield, UK: The University of Sheffield*.

- McIntosh, A. C. (1995). Pressure-driven disturbances in fluid dynamic interactions with flames. *Modeling in Combustion Science* , 449, 176-192.
- McMains, O. D. (2000). What is Vision? Retrieved from <http://visionandlearning.org/whatisvision08.html>.
- Merzkirch, W. (1987). Handbook of Flow Visualization. *Orlando, Florida, USA: Academic Press Inc.*
- Mieder, K. H. (1992). A Dictionary of American Proverbs. *Oxford University Press.*
- Migliorini, F. S. (2014). Analysis of chemiluminescence measurements by grey-scale ICCD and colour digital cameras. *Measurement Science and Technology* , 25 (5), 055202.
- Nagase, K., & Funatsu, K. (1989). Spectroscopic analysis of diesel combustion flame by means of streak camera. *SAE Transactions* , 97, 1455-1463.
- Najm, H. N., Knio, O. M., Paul, P. H., & Wyckoff, P. S. (1998). A study of flame observables in premixed methane-air flames. *Combustion Science and Technology* , 140 (1), 369-403.
- Neitz, J., & Jacobs, G. H. (1986). Polymorphism of the long-wavelength cone in normal human colour vision. *Nature* , 323, 623-25.
- Newhall, B. (1949). The History of Photograph. *New York, United States of America: The Museum of Modern Art.*
- Ng, W. B., & Zhang, Y. (2003). Stereoscopic imaging and reconstruction of the 3D geometry of flame surfaces. *Experiments in Fluids* , 34 (4), 484-493.
- Ni, T. Q., & Melton, L. A. (1993). Fuel equivalence ratio imaging for methane jets. *Applied Spectroscopy* , 47 (6), 773-781.
- Nishimoto, Y., & Shirai, Y. (1988). A feature-based stereo model using disparity histograms of multi-resolution channels. *Advanced Robotics*, 3 (1), 17-33.
- Nori, V. N., & Seitzman, J. M. (2007). Chemiluminescence measurements and modeling in syngas, methane and jet-A fueled combustors. *45th AIAA Aerospace Sciences Meeting and Exhibit* , 0466.

- Nori, V. N., & Seitzman, J. M. (2008). Evaluation of chemiluminescence as a combustion diagnostics under varying operating conditions. *46th AIAA Aerospace Sciences Meetings and Exhibit*, 953.
- Oleari, C. (1987). Metamerism. *IL Nuovo Cimento* , 9 D (8), 979-985.
- Ostrom, H., & et al. (2015). Probing the transition state region in catalytic CO oxidation on Ru. *Science* , 347 (6225), 978-982.
- Ozbek, M., Rixen, D. J., Erne, O., & Sanow, G. (2010). Feasibility of monitoring large wind turbines using photogrammetry. *Energy* , 35, 4802-4811.
- Pal, G. K., & Pal, P. (2001). Textbook of Practical Physiology. *Chennai: Orient Blackswan*.
- Payri, F., Pastor, J. V., Garca, J. M., & Pastor, J. M. (2007). Contribution to the application of two-colour imaging to diesel combustion. *Measurement Science and Technology* , 18, 2579-2598.
- Petchenko, A., Bychkov, V., Akkerman, V., & Eriksson, L. E. (2006). Violent folding of a flame front in a flame-acoustic resonance. *Physical Review Letters* , 97, 164501.
- Prasad, A. K. (2000). Stereoscopic particle image velocimetry. *Experiments in Fluids* , 29, 103-116.
- Raynor, J. M., Seitz, P. (1997). A linear array of photodetectors with wide dynamic range and near photon quantum-noise limit. *Sensors and Actuators A: Physical*, 61 (1-3), 327-330.
- Reibel, Y., Jung, M., Bouhifd, M., Cunin, B., & Draman, C. (2003). CCD or CMOS camera noise characterisation. *The European Physical Journal Applied Physics* , 21, 75-80.
- Sabel, J. C. (1996). Optical 3D Motion Measurement. *IEEE Instrumentation and Measurement Technology Conference*, 367-370.
- Sawicki, M. (2007). *Filming the Fantastic: A Guide to Visual Effect Cinematography*. Amsterdam: Focal Press.
- Serridge, M., & Licht, T. R. (1987). Piezoelectric accelerometer and vibration preamplifier handbook. *Denmark: K Larsen & Sen A/S*.

- Sick, V. (2013). High speed imaging in fundamental and applied combustion research. *Proceedings of the Combustion Institute* , 34 (2), 3509-3530.
- Simonini, S., Elston, S. J., & Stone, C. R. (2001). Soot temperature and concentration measurements from colour charge coupled device camera images using a three-colour method. *Proceedings of the I MECH E Part C Journal of Mechanical Engineering Science* , 215, 1041-1052.
- Simth, A. R. (1978). Color gamut transform paris. *Proceedings of the 5th annual conference on computer graphics and interactive techniques*. 12, 12-9.
- Smith. (2006). Camera lense: from box camera to digital. *SPIE Press*.
- Smith, G. P., Luque, J., Park, C., Jeffries, J. B., & Crosley, D. R. (2002). Low pressure flame determinations of rate constants for OH(A) and CH(A) chemiluminescence . *Combustion and Flame* , 131 (1-2), 59-69.
- Smith, T., & Guild, J. (1931). The C.I.E. colorimetric standards and their use. *Transactions of the Optical Society* , 33, 73-134.
- Sonka, M., Hlavac, V., & Boyle, R. (1999). Image processing, analysis, and machine vision (2nd Edition ed.). *PWS Publication*.
- Sonka, M., Hlavac, V., & Boyle, R. (2015). *Image Processing, Analysis, and Machine Vision* (4th Eidition ed.). *CENGAGE Learning*.
- Steger, C., Ulrich, M., & Wiedemann, C. (2007). Machine Vision Algorithms and Applications. *Wiley*.
- Svaetichin, G., Negishi, K., & Fatehchand, R. (1965). Cellular Mechanisms of a Young-Hering Visual System. In Ciba Foundation Symposium-Colour Vision: Physiology and Experimental Psychology. *Chichester: John Wiley & Sons, Ltd*.
- Swan, W. (1857). On the prismatic sectra of the flames of compounds of carbon and hydrogen. *Transactions of the Society of Edinburgh* , 21, 411-430.
- Takeuchi, M., & Kubono, T. (1999). A spectroscopic detecting system for measuring the temperture distribution of silver breakng arc using a CCD color camera. *IEEE Transactions on Instrumentation and Measurement* , 48, 678-683.
- Taylor, A. (1993). Instrumentation for Flows with Combustion. *San Diego: Academic Press*.



- Teoh, W., & Zhang, X. (1984). An inexpensive stereoscopic vision system for robots. *IEEE Proceedings of International Conference on Robotics and Automation* , 186-189.
- Tovee, M. J. (2008). An Introduction to the Visual System. *Cambridge: Cambridge University Press*.
- Trussell, H., & Vrhel, M. (2008). Fundamental of Digital Imaging. *Cambridge University Press*.
- Turns, S. R. (2000). An introduction to combustion. *New York: McGraw Hill*.
- Velten, A., Raskar, R., & Bawendi, M. (2011). Picosecond camera for time-of-flight imaging. *Imaging and Applied Optics, OSA Technical Digest, Optical Society of America, IMB4*.
- Wang, Q., Gohari, D. H., Chen, L., & Zhang , Y. (2012). Vortex dynamics ans structure of methane/air jet diffusion flames with air coflow. *Experimental Thermal and Fluid Science* , 37, 84-90.
- Wang, Q., Huang, H. W., Tang, H. J., Zhu, M., & Zhang, Y. (2013). Nolinear response of buoyant diffusion flame under acoustic exciation. *Fuel* , 103, 364-372.
- Wang, Q., Yang, J., Huang, H. W., Zhang, Y., & Zhao, C. (2014). Three-dimensional investigation of the dynamics of a propane diffusion flame. *Fuel* , 116, 448-454.
- Wang, R. (2009). Digital stereo imaging and reconstruction of flame dynamics and structure. *PhD Thesis, Manchester: Manchester University*.
- Wang, R., Li, X., & Zhang, Y. (2008). Analysis and optimization of the stereo-system with a four-mirror adapter. *Journal of the European Optical Society* , 3, 08033.
- Warnatz, J. M., & Dibble, R. W. (2006). Combustion: physical and chemical fundamentals, modelling and simulation, experiments, pollutant formation (4th Edition ed.). *Berlin Heidelberg: Springer-Verlag*.
- Weigart, F. G. (1964). *Patent No. 3277302*. U.S.
- Wheatstone, C. (1838). Contributions to the Physiology of Vision.--Part the First. On Some Remarkable, and Hitherto Unobserved, Phenomena of Binocular Vision. *Philosophical Transactions of the Royal Society of London* , 128, 371-394.

- Wright, W. D. (1928). A re-determination of the trichromatic coefficients of the spectral colours. *Philosophical Transactions of the Optical Society* , 30, 141-164.
- Wu, W., Fuh, C. A., & Wang, C. (2015). Comparative study on microwave plasma-assisted combustion of premixed and nonpremixed methane/air mixtures. *Combustion Science and Technology* , 187 (7), 999-1020.
- Yamazaki, M., Ohya, M., & Tsuchiya, K. (1992). Detection of the air equivalence ratio of a burner from the flame emission spectra. *International Chemical Engineering* , 30 (28), 160-168.
- Yang, J., Mossa, F. M. S., Huang, H. W., Wang, Q., Woolley, R., and Zhang, Y. (2015) Oscillating Flames in Open Tubes. *Proceedings of Combustion Institute*, 35, 2075-2082.
- Yang, W. J. (1989). Handbook of Flow Visualization. *Hemisphere Publishing Corporation*.
- Young, Thomas. (1802). Bakerian Lecture: On the Theory of Light and Colours. *Philosophical transactions of the royal society of london* , 92, 12-48.
- Young, I. T., Gerbrands, J. J., & Vliet, L. J. (2007). Fundamentals of Image Processing. *The University of Edinburgh School of Informatics*: [http://homepages.inf.ed.ac.uk/rbf/CVonline/LOCAL\\_COPIES/TUDELFT/FIP2\\_3.pdf](http://homepages.inf.ed.ac.uk/rbf/CVonline/LOCAL_COPIES/TUDELFT/FIP2_3.pdf)
- Zajac, A. (1987). Opticas (2nd Edition ed.). *Addison-wesley Publishing Company*.
- Zhang, Y., & Bray, K. N. (1999). Characterization of impinging jet flames. *Combustion and Flame* , 116, 671-674.
- Zhang, Z. (2000). A Flexible New Technique for Camera Calibration. *IEEE Transactions on Pattern Analysis and Machine Intelligence* , 22 (11), 1330-1334.
- Zhang, Z. (2004). Camera calibration. In *Emerging topics in computer vision. NJ, USA: Prentice Hall PTR Upper Saddle River*, 4-43.